Tunnelling effects on capped piles and masonry buildings with shallow strip foundations

Chuanjin Tang

Department of Civil Engineering
University of Nottingham, UK

A dissertation submitted for the degree of
Doctor of Philosophy

August 2024

Declaration

I hereby declare that except where specific reference is made to the work of others, the contents of this dissertation are original and have not been submitted in whole or in part for consideration for any other degree or qualification in this, or any other university. This dissertation is my own work and contains nothing which is the outcome of work done in collaboration with others, except as specified in the text.

Chuanjin Tang
August 2024

Acknowledgement

I completed my PhD study at the University of Nottingham Centre for Geomechanics (NCG) under the guidance of Prof Alec Marshall and Dr Charlie Heron.

I extend my sincere appreciation to my main supervisor, Prof Alec Marshall, for his unwavering support, patience, and invaluable mentorship throughout my PhD journey. His guidance encouraged me to think critically and face challenges with confidence, contributing significantly to my growth as a researcher. I would also like to thank my second supervisor, Dr Charlie Heron, for his valuable suggestions and assistance with testing methods, centrifuge experiments, and data analysis.

I am thankful for the excellent technical support provided by NCG technicians, particularly Mr Senthil Prakash Selvaraj, Dr Mir Hashemi Afrapoli, Mr Steven Lawton, Mr Harry Hardy, Mr Mark Dale, Mr Lee Hickling, and Mr Andrew Maddison.

Gratitude also goes to all my fellow researchers at NCG for their kind assistance and camaraderie during my research. Additionally, I appreciate the previous NCG members, Dr Andrea Franza, Dr Geyang Song, Dr Ge Cui, Dr Jingmin Xu, and Dr Yalin Yu, for their important guidance and support at the outset of my PhD study.

I acknowledge the financial support from the China Scholarship Council (CSC) and the University of Nottingham, UK.

Lastly, I cherish the unforgettable moments spent with my new friends at Nottingham, and I express my heartfelt thanks to my parents and family for their unwavering support and encouragement.

Abstract

The increasing demand for infrastructure space in urban areas presents enormous prospects and challenges for the expansion and utilisation of underground spaces. Tunnels are a common way to utilise underground space, yet tunnel excavations are often situated close to existing underground and surface structures (such as piles, strip foundations, and masonry buildings) and bring potential risks to these structures. Therefore, it is important to understand soil-structure interaction mechanisms in tunnelling scenarios to provide a reference for designing new tunnels near deep pile foundations or under masonry buildings with shallow strip foundations. Nevertheless, due to the complexity of actual engineering projects, few studies have accurately investigated the comprehensive tunnel-soil-pile interaction (TSPI) and tunnel-soil-masonry building interaction with shallow strip foundation (TSBI) problems.

This thesis focused on three main areas to provide insights into TSPI and TSBI problems: (1) mechanisms of tunnelling under capped non-displacement piles (TSPI), (2) development of new approaches for studying tunnelling under masonry walls with shallow strip foundations (TSBI), and (3) TSBI mechanisms involving different types of masonry walls and material parameters. This study used geotechnical centrifuge testing as the primary method to simulate the tunnelling process under foundations in dense sand. In particular, based on the previous method for studying tunnel-pile-elastic framed building interaction problems developed at the University of Nottingham Centre for Geomechanics (NCG), an advanced coupled centrifuge-numerical modelling (CCNM) approach was developed (regarding the study of (2)). In the new CCNM approach, the displacements of a strip foundation affected by tunnelling measured in the centrifuge model are transferred to an Abaqus numerical model of a masonry wall, which predicts changes in structural loads within the wall and then feeds back the updated loads to the strip foundation in the centrifuge model. This iterative process continues between the centrifuge and numerical models until the system reaches stability. The new CCNM method combines the advantages of centrifuge models (providing soil stress/deformation data) with those of numerical models (capturing structural details along with associated load distributions and deformations) and achieves the use of non-linear materials and a continuous interface between physical and numerical domains in hybrid testing.

The study of (1) tunnelling under capped non-displacement piles (TSPI) focuses on the effect of a pile cap (representative also of a raft or grade beam) in contact with the soil surface on load transfer mechanisms. Experiments included loading tests to ascertain the foundation capacity and load-displacement response in the presence/absence of an underlying model tunnel. Individual 'reference' pile response is compared for cases with and without a pile cap, including pile displacements and load distributions between the head, shaft, and base; the case of 'friction' piles with a compressible base is also considered. Results show that uncapped piles with relatively large service loads experience 'geotechnical failure' (i.e. large settlements or a significant increase in settlement rate with tunnel volume loss) to mobilise base or shaft resistance, while pile caps can effectively prevent geotechnical failure.

The study of (2) tunnelling under masonry walls with shallow strip foundations (TSBI) verifies that the CCNM approach can effectively achieve load redistribution within masonry walls during tunnelling and its applicability in scenarios with different relative wall-to-tunnel positions. The CCNM test results, when compared with 'conventional' test outcomes where wall loads remain constant during tunnelling, highlight the importance of wall stress redistribution in risk assessments. The function of load redistribution is also well demonstrated in eccentric cases, where the location of tensile damage shifts from the lower part of the wall to the upper part (near the middle of sagging/hogging regions) when the wall-to-tunnel eccentricity e/L increases from 0 to 1/2. The bays nearest the tunnel centreline exhibit more bending behaviour with equivalent plastic strain areas (PEEQ) reducing with e/L, while bays above inflection points or further away from the tunnel show mixed bending and shear response with PEEQ for bays further away tending to increase with e/L.

The study of (3) TSBI mechanisms with different types of masonry walls and material parameters reveals the role of wall structural characteristics and material properties in TSBI problems by CCNM tests on tunnelling under standard masonry walls (with different heights and openings) and non-standard walls (with varying Young's modulus and density within a two-storey masonry wall with openings). The results show that high bending stiffness and low self-weight cause a dispersed distribution and horizontal connections (i.e. wall length direction) of tension damage areas within the walls and similar maximum bay angular distortions,

while low bending stiffness and high self-weight result in a concentrated distribution and vertical connections (i.e. wall height direction) of tension damage areas and higher maximum bay angular distortions. No gaps exist between the foundation and the surface, and more flexible or lighter walls produce greater differential settlements. This part also explores the impact of the existing walls on soil movements during tunnelling.

In short, this thesis makes innovative contributions to, in tunnel excavation scenarios, the load transfer mechanisms of cap piles, the testing approach for the response of masonry walls with shallow strip foundations, and the deformation and damage mechanisms of masonry walls.

Keywords: tunnel, pile, pile cap, strip foundation, masonry wall, centrifuge modelling, Abaqus, hybrid modelling

Contents

List of Figures

List of Tables

List of Notations

Roman Symbols

A	cross-section area (m^2)
A_s	effective cross-section area (m^2)
$A_{s,column}$	effective cross-section area of column (m^2)
A_{slab}	cross-section area of each slab of a building (m^2)
b_j	distance from the mid-point of the strip to the neutral axis (m)
C	cover depth above tunnel (mm, m)
C	column stiffening factor
d	pile diameter above surface (mm)
d_p	pile diameter below surface (mm)
D_{50}	average size of soil particle (mm)
D_t	tunnel diameter (mm)
DR	deflection ratio
$DR_{sag/hog,Bldg}$	building DR in the sagging/hogging zones
$DR_{sag/hog,GF}$	DR of the greenfield surface settlement trough in the sagging/hogging zones
e	eccentricity from wall centre to tunnel centreline (m)
$e_{max/min}$	maximum/minimum void ratio
E_a	Young's modulus of aluminium (GPa)
E_c	Young's modulus of column (GPa)
E_m	Young's modulus of masonry (GPa)
E_s	Young's modulus of soil (GPa)

EI	bending stiffness of building and/or foundation (MNṁ^2)
EI^*	bending stiffness per metre in the tunnel axial direction (MNṁ)
F	pile external load at z=0 (MN)
F_0	pile service load (MN)
F_f	foundation load from the wall load redistribution (N)
F_{f_0}	initial load from the wall self-weight (N)
F_i	pile axial force for at the specific FBG sensor position i (N)
F_t	concentrated loads (N)
F_w	concentrated (actuator) loads (N)
F_{w_node}	node reaction force at the Abaqus model base (N)
g	gravity (m/s^2)
G_s	specific gravity
GA_s	building shear stiffness (GN)
$GA_{s,i}$	total shear stiffness of each floor (GN)
$GA_{s,column}$	column shear stiffness (GN)
$GA_{s,wall}$	wall shear stiffness(GN)
GA_s^*	building shear stiffness per metre in the tunnel axial direction (GN/m)
$\overline{GS}_{max}$	maximum average slope at greenfield surface settlement curve
h_j	effective strip height (m)
h_m	soil height (m)
H	wall height (m)
H_c	thickness of pile cap (mm)
i	horizontal inflection point position relative to tunnel centreline (m)
I	second moment of area (m^4)
I_c	second moment of area of column (m^4)
I_d	relative density of sand (%)
I_j	second moment of area of strip (m^4)
I_{slab}	second moment of area of each slab (m^4)
K	pile global stiffness (MN)

K, K^*, K^{**}	trough width parameters based on i, x^*, and x^{**}, respectively
K_B	average stiffness of the beam line (= $(EI/L_u)_B$)
K_{LC}	average stiffness of the lower column (= $(EI/H_{storey})_{LC}$)
K_{UC}	average stiffness of the upper column (= $(EI/H_{storey})_{UC}$)
K_s^*, K_s^{**}	surface trough width parameters based on x^* and x^{**}, respectively
$K_{s,C/D_t}^{*(*)int}$	intercept of $K_s^{*(*)}$ with C/D_t
$K_{s,C/D_t}^{*(*)slope}$	slope of $K_s^{*(*)}$ with C/D_t
$K_{s,V_{l,t}}^{*(*)slope}$	slope of $K_s^{*(*)}$ with $V_{l,t}$
$K_{s,V_{l,t}}^{*(*)int,ln}$	intercept of $K_s^{*(*)}$ considering both C/D_t and I_d
$K_{s,V_{l,t}}^{*(*)slope,ln}$	slope of $K_s^{*(*)}$ considering both C/D_t and I_d
K_{FBG_j}	FBG calibration coefficient for pile axial force (N/pm)
K_t	FBG calibration coefficient for temperature (pm/°C)
l	wall thickness (m)
L	wall length (m)
L_{al}	length of aluminum base (mm)
L_c	side length of pile cap (mm)
L_p	pile length (mm)
L_{po}	polystyrene length (mm)
$L_{sag/hog}$	sagging or hogging length (m)
L_u	building unit (bay) length (m)
M^{DR}	modification factor of deflection ratio
$M^{DR,sag/hog}$	modification factor of deflection ratio in sagging/hogging regions
$M^{\epsilon h,c/t}$	modification factor of horizontal compressive/tensile strain
M^{β}	modification factor of angular distortion
N	scaling coefficient
N	axial force along the pile centreline (MN)
N_j	pile axial force at the FBG level j (N)
O	door and window opening percentage within walls (%)
Q	pile load capacity (MN)

R	pile head-to-greenfield surface settlement ratio (%)
R_a	arithmetic average of profile height deviations from the mean line (μm)
R_e	effective centrifuge radius (m)
R_q	root mean square average of the profile height deviations from the mean line (μm)
R_t	distance between the model top and rotation axis (m)
s	slope
s_0	FBG1 depth (mm)
s_1, s_2	FBG spacing (mm)
$s_{GF,max}$	maximum average slope along bay base positions at greenfield surface
s_T	temperature sensor spacing (mm)
S^*	pile settlement caused by pile external load (m)
S_f	foundation settlement (m)
S_{GF}	greenfield settlement (m)
S_{GF}^0	greenfield surface settlement (m)
S_h	horizontal displacement (m)
$S_{h,max}$	maximum horizontal displacement (m)
S_p	pile settlement (m)
$S_p^{pre\_tun}$	pile settlement in pre-tunnelling loading process (m)
$S_p^{post\_tun}$	pile settlement in post-tunnelling loading process (m)
S_p^{Tun}	pile settlement during tunnelling process (m)
S_v	vertical displacement (m)
$S_{v,bend}$	building settlement due to bending distortion (m)
$S_{v,max}$	maximum vertical displacement (m)
$S_{v,shear}$	building settlement due to shear distortion (m)
$S_{v,tilt}$	building settlement due to tilt (m)
$S_{v,tot}$	relative vertical displacement (m)
S_{w_node}	node settlement at the Abaqus model base (m)
$S_{w\_node\_ref}$	reference node settlement at the end of the preceding volume loss increment (m)
$\lvert S_{f,tol} \rvert$	LVDT displacement threshold (μm)

SF	pile safety factor
U_c	uniformity coefficient
V_0	nominal cross-sectional area of tunnel
$V_{l,s}$	soil volume loss (%)
$V_{l,t}$	tunnel volume loss (%)
V_s	volume of the ground surface settlement trough per metre length in tunnel axial direction
V_t	volume loss of the soil around the tunnel periphery per metre length in tunnel axial direction
x^*	horizontal positions on fitted settlement curve where $S_v(x^*) = 0.606S_{v,max}$ (m)
x^{**}	horizontal positions on fitted settlement curve where $S_v(x^{**}) = 0.303S_{v,max}$ (m)
WL	pile working load level
WL^*	capped (friction) pile working load level based on CP1
y_i	storey height (m)
z	depth under surface (m)
z_t	tunnel depth (m)

Greek Symbols

α^*	relative building-to-soil axial stiffness
α^*_{mod}	modified relative building-to-soil axial stiffness
β	angular distortion
β_{max}	maximum angular distortion
γ	shear strain
$\delta_{bending/shear}$	deflection due to bending/shear distortion (m)
Δ	relative deflection (m)
ΔF	temperature change (°C)
ΔGS	change in greenfield surface slope
ΔN_{exp}	load offset introduced during centrifuge testing (N)
$\Delta N_{exp,1}$	difference between FBG1 readings and the theoretical axial load at the surface (N)
$\Delta N_{exp,2}$	difference between the constants for the estimated and measured axial forces (N)

ΔS_v	differential settlement (m)
ΔT	difference in pile axial forces for the two FBG sensors at each level (N)
$\Delta\lambda_{FBG_j}$	average wavelength shift of two FBGs at the same level j (pm)
$\Delta\lambda_{T_j}$	temperature-induced average wavelength offset of two FBGs at the same level j (pm)
ε^t	building tensile strain
ε^t_{99}	the strain not exceeded in 99% of the total volume of the masonry wall
$\varepsilon_{b/d,max}$	maximum bending/diagonal strain
$\varepsilon_{crit,b/d}$	limiting total bending/diagonal strain
ε_d	diagonal strain
ε_h	average horizontal strain
$\varepsilon_{h,c/t,Bldg}$	maximum building compressive/tensile strain
$\varepsilon_{h,c/t,GF}$	maximum greenfield compressive/tensile strain
$\varepsilon_{h,top/base}$	top/base horizontal strain
ε_{max}	maximum strain
ε_{xx}	horizontal strain
ε_{xy}	diagonal strain
ε_{yy}	vertical strain
ε_θ	tension strain at any angle θ
$\eta_{sag/hog}$	relative building-to-soil bending stiffness in sagging/hogging zones considering shear behaviour
θ	rigid body tilt
κ	relative soil-to-building shear stiffness
ρ^*	relative building-to-soil bending stiffness
ρ^*_{mod}	modified relative building-to-soil bending stiffness
τ_s	pile shaft resistance (kPa)
$\rho_{sag/hog}$	relative building-to-soil bending stiffness in sagging/hogging zones
χ	curvature
ω	centrifuge rotational velocity
ω	local tilt

Chapter 1

Introduction

1.1 Background

Urbanization necessitates the expansion of infrastructure to accommodate various needs such as housing, production, and transportation. In this context, underground spaces, particularly tunnels, have gained prominence for their potential to alleviate surface traffic congestion and enhance travel efficiency. Given the dense urban infrastructure, tunnels are often constructed beneath or in proximity to existing buried structures (such as piles, shallow foundations, pipelines, and basements). Tunnel excavation activities would induce stress relief and movements of the surrounding soil, which brings potential risks of damage to nearby underground infrastructure and corresponding surface buildings.

The designs of new tunnels require a comprehensive assessment of the impact on neighbouring infrastructure to mitigate potential damage and minimize the risk of accidents. In addition, engineers commonly employ strategies such as compensation grouting and protective walls, which should be based on a precise evaluation of how structures respond to tunnelling to ensure economically viable plans are implemented. In practice, the designs and protective measures tend to be over-conservative to ensure safety due to insufficient understanding of tunnelling effects, resulting in increased costs and reduced space utilization efficiency.

Pile foundations have been widely used by mankind for centuries to support buildings (including residentials, historical heritages, high-rise buildings, and bridges) in areas with unstable soil (Mandolini et al., 2005; Klaassen and Creemers, 2012). Masonry buildings on shallow foundations make up a substantial proportion of the building stock of many countries around the world (see, for example, Piddington et al. (2020) for the United Kingdom). Tunnel-soil-pile interactions (TSPI) and tunnel-soil-masonry building (with shallow strip foundations) interactions (TSBI) are therefore commonplace scenarios that have received considerable attention from practitioners.

First, for the TSPI problems related to piles (a typical deep foundation), tunnelling under piles may reduce pile load capacities and alter the axial load distributions along the pile shaft (Marshall and Mair, 2011; Franza and Marshall, 2018; Song and Marshall, 2020). The load capacities and load transfer mechanisms of piles are influenced by pile configurations (including pile diameter, shaft length, and elements like pile cap and base), pile installation methods (including driven piles and bored piles), pile positions relative to tunnels (for example, tunnelling under pile tips and near pile shafts), and external conditions (such as applied loads and tunnel excavations). Field and laboratory tests (Jacobsz et al., 2004; Kaalberg et al., 2005; Lee and Chiang, 2007) and theoretical and numerical analyses (Chen et al., 1999; Cheng et al., 2007) have been conducted to explore the TSPI issues. Among these, geotechnical centrifuge testing stands out as an effective method to model TSPI scenarios by employing scaled-down physical models at elevated acceleration-level (gravity-level) environments to replicate full-scale scenarios with realistic stress conditions, yielding comprehensive and dependable data encompassing tunnelling-induced soil movements and building/foundation reactions. For example, the tests on tunnelling under piles carried out using the 50 g-tone geotechnical centrifuge at the University of Nottingham Centre for Geomechanics (NCG) provided a lot of useful insights into TSPI problems (Franza, 2017; Song, 2019). The TSPI mechanisms serve as an important reference for more complex scenarios, such as tunnelling beneath piled structures.

Second, for the TSBI problems related to shallow foundations (including raft and strip foundations), applying greenfield surface settlement to the bottom of equivalent beams for theoretical calculation is a simplified method in building damage assessments (Mair et al., 1996), and subsequent improvements have incorporated additional factors like building self-weight and shear stiffness (Potts and Addenbrooke, 1997; Franzius et al., 2006) or using the Timoshenko beam to replace the Bernoulli–Euler beam or developing new equivalent beam methods (Pickhaver et al., 2010; Franza et al., 2017) to minimize errors. Geotechnical centrifuge modelling, similar to what was mentioned above, can provide valuable insights by replicating realistic deformations and failure characteristics of buildings induced by tunnelling, however the utilization of centrifuge-compatible physical models of masonry buildings (such as small-scale models, plate models, 3D printed models) might oversimplify complex building attributes, leading to inadequate evaluations of building responses (Mair, 2013; Farrell et al., 2014; Ritter et al., 2017, 2018; Franza and Marshall, 2018). Numerical simulations of entire scenarios (encompassing soil, tunnel, and buildings with foundations) are capable of simulating detailed distortion and damage within full-scale building models (Burd et al., 2000; Son and Cording, 2005; Yiu et al., 2017), but the credibility of results should be verified with real on-site or experimental data. These limitations hinder a comprehensive understanding of the TSBI mechanisms. Hybrid testing methods dissect complex problems into components suited for physical or numerical model domains, integrating the strengths of both model domains, with the key data within two model domains interacting through a shared boundary. The real-time coupled centrifuge-numerical modelling (CCNM) approach developed at NCG achieved modelling tunnelling under elastic framed buildings (considering only building stiffness) with pile foundations in plane strain conditions (Idinyang et al., 2019; Franza and Marshall, 2019a; Song and Marshall, 2020) which might provide some inspirations for studying TSBI problems.

Despite significant progress in elucidating the mechanisms of TSPI and TSBI, accurately predicting the impact of tunnelling on buildings and foundations remains challenging due to the intricate nonlinear behaviours of both soil and structures. Current simulation or prediction methods typically involve over-simplification or homogenization assumptions about the research objects, which may lead to under- or overestimation of the responses of the target assets. Therefore, conducting an in-depth study of the TSPI and TSBI mechanisms is imperative.

For the TSPI problems, one notable gap is the limited understanding of how pile caps influence single-pile response to tunnelling activities. In this thesis, a capped pile is defined as an isolated pile topped by a rigid cap that is in contact with the soil. These foundations, when subjected to large vertical displacements (such as those caused by tunnelling), will behave as a hybrid foundation, where both the cap and the pile transmit load to the underlying soil (the response to tunnelling of a capped pile is distinct from that of a piled raft, which would be able to transfer loads through the raft to other piles within the raft without mobilising significant additional bearing stress beneath the raft).

For the TSBI problems, there is a need for more advanced and accurate simulation methods to better understand the complex mechanisms that are involved. In this thesis, isolated masonry walls are selected for investigating building response to tunnelling using an advanced modelling approach (i.e. the coupled centrifuge-numerical modelling (CCNM) approach; introduced later) which currently applies to planar scenarios. In this thesis, masonry walls with strip foundations that rest on the soil surface are considered, which differs from the real cases where shallow foundations are typically buried at a shallow depth. Despite this difference, outcomes still provide significant insights into the main soil-structure interaction mechanisms, in particular the effect of load redistribution within the walls, which is a novel contribution of this work.

1.2 Aims and objectives

The TSPI and TSBI problems are common scenarios related to tunnelling, which can be investigated using similar methods such as geotechnical centrifuge modelling. The pile caps are essentially derived from shallow foundations to improve the mechanical response of piles, thus understanding these mechanisms can help not only estimate the impacts of new tunnels on existing piles and/or shallow foundations but also the design of new foundations to compensate building loads or excavation needs.

The aim of this thesis is, concerning the lacking research aspects of TSPI and TSBI problems, to investigate the effect of pile caps on tunnelling-induced pile load transfer mechanisms in centrifuge tests and develop a new coupled centrifuge-numerical modelling (CCNM) approach (based on the pioneering work of Idinyang et al. (2019)) to further accurately study the effect of tunnelling on masonry walls with shallow strip foundations. The main study objectives are as follows:

- Investigate the load transfer mechanisms of non-displacement capped piles before, during, and after tunnel volume loss with reference to uncapped pile (i.e. reference pile) and raft foundation (with the same size as the pile cap) behaviour and including an evaluation of the effect of initial pile load distribution (TSPI problem). Establish a correlation between tunnelling-induced changes in pile settlement, influenced by levels of pile external loads, and greenfield surface settlement. Innovative fibre Bragg Grating (FBG) strain sensors within the piles were used to evaluate load transfer mechanisms.

- Develop a new version of the coupled centrifuge-numerical modelling (CCNM) approach to enable the study of shallow strip foundations (for TSBI problem). The new CCNM development includes a novel implementation of non-linear masonry wall behaviour. The new CCNM approach achieves the simulations of realistic walls (considering gravity, structural characteristics, and non-linear materials) and the establishment of a continuous interface between the centrifuge and numerical domains. The rationality and progressive nature of the CCNM approach is validated by comparing test results using CCNM and the mere conventional constant dead-load method. The new CCNM technique is extended to different wall-to-tunnel eccentricities ($e/L = 0$-1/2, considering different settlement profiles).
- Study the tunnel-soil-masonry wall interaction mechanisms using the CCNM approach (TSBI problem). Study the scenarios of tunnelling directly underneath masonry walls ($e/L = 0$), with various wall heights (1-3 storeys), opening ratios (0-27%), Young's modulus (reproducing the bending stiffness of one- and three-storey masonry walls within the reference two-storey wall), and density (reproducing the self-weight of one- and three-storey masonry walls within the reference two-storey wall). The outcomes of these tests will contribute to the understanding of building/foundation/soil responses to tunnelling.

1.3 Thesis outline

This thesis comprises the following seven chapters:

- Chapter 1 introduces the background, aims, objectives, and structure of the thesis.

- Chapter 2 presents a review of the existing literature concerning the effects of tunnelling on soils, piles, and masonry buildings.
- Chapter 3 describes the methodology and experimental setup for the TSPI and TSBI studies, including the development of the new coupled numerical-centrifuge modelling (CCNM) approach for shallow strip foundations.
- Chapter 4 investigates the tunnelling effect on non-displacement capped piles in dense sand considering pile components (cap versus no cap, and soft base) and different working load levels (TSPI problem).
- Chapter 5 verifies the progressiveness of the CCNM method by comparing CCNM results with constant dead-load test results and extends the CCNM applicability on TSBI scenarios with different relative tunnel-to-wall positions (TSBI problem).
- Chapter 6 investigates the mechanisms of tunnel-soil-masonry wall interactions with shallow strip foundations through the advanced CCNM method, emphasizing the roles of building height, openings, bending stiffness, shear stiffness, and self-weight (TSBI problem).
- Chapter 7 summarises the major findings of this study and provides some suggestions for future work.

Chapter 2

Literature review

This chapter systematically reviews research related to the impacts of underground tunnel excavation activities on surrounding ground movements and the responses of adjacent pile foundations and low-rise buildings with shallow foundations. First, the chapter introduces surface and subsurface soil movements induced by tunnelling in greenfield conditions (where there are no existing structures), along with related theories describing and predicting soil movements. Next, studies on settlement patterns and load transfer mechanisms of pile foundations (including single piles, pile groups, and piles under buildings) in various tunnelling conditions, with a focus on findings from geotechnical centrifuge modelling tests, are presented. Subsequently, studies on masonry building deformations and the assessment methods of building damage when tunnelling occurs beneath or nearby are reviewed. Finally, the existing literature is briefly summarised and identified study gaps are discussed, which informed the direction of this research project.

2.1 Greenfield tunnelling

Greenfield refers to a scenario where there are no existing infrastructure both above and below the ground surface. Excavations for underground tunnels in greenfield inevitably disturb the surrounding soil, resulting in soil stress relief and ground movement, and ultimately causing surface settlement (Fig. 2.1). This section presents an overview of the understanding of tunnel-soil interaction mechanisms, which can provide a reference for risk assessments in scenarios involving tunnel excavations near surface and subsurface assets in urban areas.

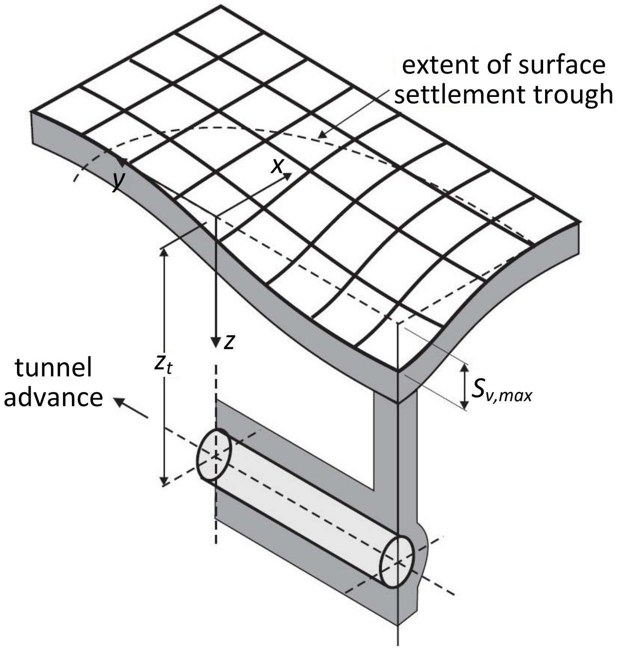

Fig. 2.1. Greenfield surface settlement induced by tunnelling (modified from Franza et al. (2016), based on image from Attewell et al. (1986), with symbols adapted for consistency within this thesis)

Mair and Taylor (1997) summarised five primary factors contributing to soil movement in the vicinity of tunnels associated with the shield tunnelling method, as shown in Fig. 2.2:

(1) Ground movement towards the tunnelling face due to stress relief, which is typically considered the primary cause of ground movement, particularly in open-faced tunnelling in clays;

(2) Radial ground movement resulting from an over-cutting edge along with potential plough

or yaw during shield passage;

(3) The presence of a tail void between the shield tailskin and the installed lining;

(4) Lining deformation induced by ground loading; and

(5) Changes in effective stress of soil due to consolidation (especially soft clay).

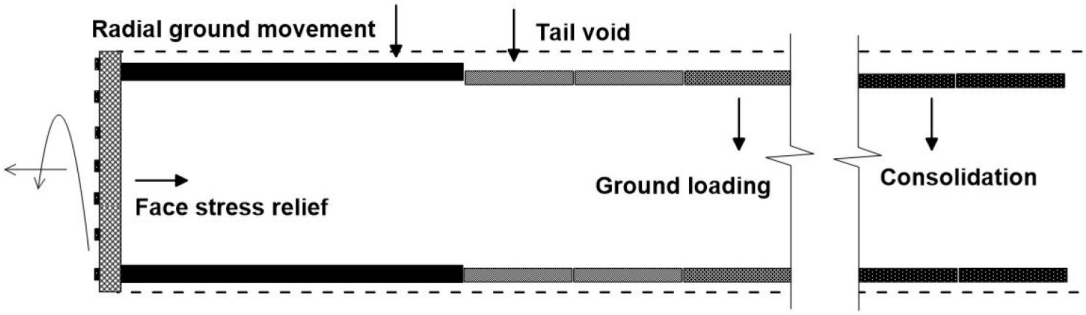

Fig. 2.2. Five main reasons of ground movement during shield tunnelling (Song (2019), based on image from Cording (1991); Mair and Taylor (1997))

Tunnelling-induced soil movement patterns might be quite different in clays and sands, as shown in Fig. 2.3. The soil movements tend to propagate horizontally within a wide range in clays while a vertical propagation of soil movement from the tunnel crown within a narrow range, resembling a chimney shape, exists in sands.

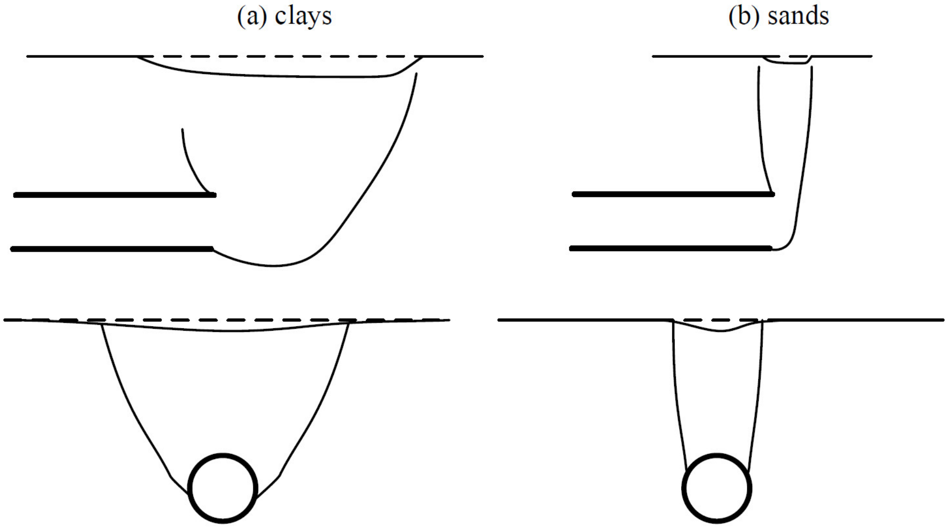

Fig. 2.3. Observed soil movement patterns according to centrifuge tunnelling tests (Mair, 1979; Franza, 2017)

2.1.1 Soil transverse settlement

Tunnelling-induced transverse ground settlements (determined after stabilisation for clays) under plane strain conditions (i.e. in the transverse plane perpendicular to the tunnel axis) are commonly described using empirical formulas, such as the standard Gaussian curve (Peck, 1969) and modified Gaussian curve (Vorster et al., 2005a). The typical ground loss distributions around the tunnel and the resulting surface settlement trough are illustrated in Fig. 2.4.

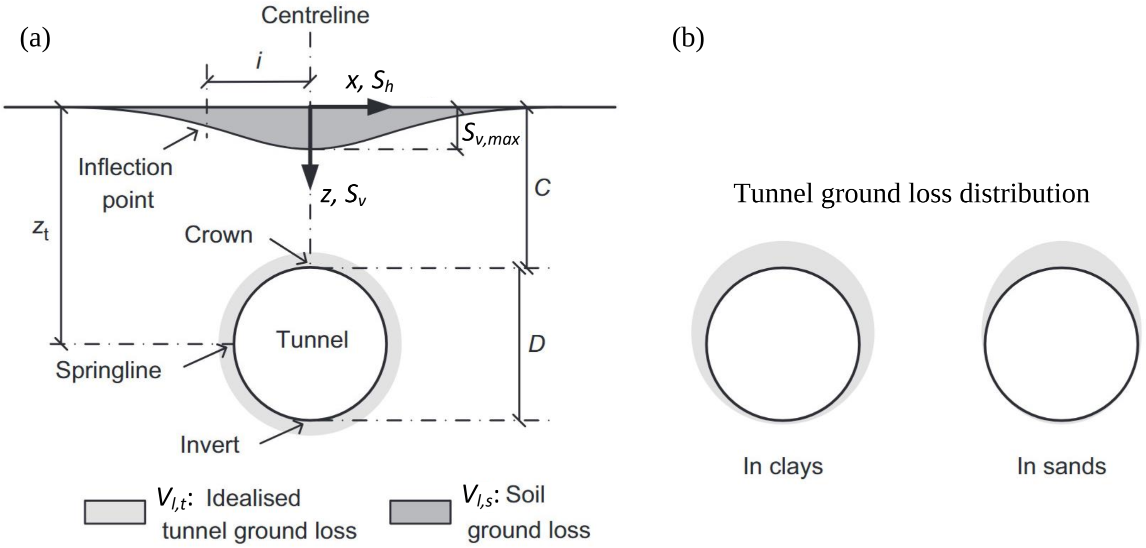

Fig. 2.4. Illustration of (a) transverse tunnel and soil volume losses; (b) typical tunnel ground loss distributions for shallow tunnels (Franza et al., 2019)

Peck (1969) proposed the adoption of the standard Gaussian distribution curve to match the shape of transverse surface settlement troughs caused by tunnelling in clays under drained conditions:

$$S_v = S_{v,max} \cdot \exp\left(-\frac{x^2}{2i^2}\right) \tag{2.1}$$

where S_v is the surface settlement, $S_{v,max}$ is the maximum surface settlement, i is the horizontal distance between the tunnel centreline and the inflection point of the fitted curve, and x is the horizontal distance from the tunnel centreline. Therefore, the volume of the transverse surface settlement trough per unit length in the tunnel axial direction, V_s, can be described as:

$$V_s = \sqrt{2\pi} i S_{v,max} \tag{2.2}$$

The shape of the standard Gaussian curve in Eq. 2.1 is jointly determined by the maximum surface settlement $S_{v,max}$ and the inflection point i. For the parameter i, O'Reilly and New (1982) found that i is an approximately linear function of the tunnel depth z_t:

$$i = Kz_t \tag{2.3}$$

where K is a width parameter of the settlement trough, and Mair and Taylor (1997) suggested K equals 0.4-0.6 for clays and 0.25-0.45 for sands and gravels.

Subsurface settlement profiles exhibit certain similarities to surface settlement troughs. To predict subsurface settlements, Mair et al. (1993) adopted the standard Gaussian curve (Eq. 2.1) and found that the inflection point i is proportional to the distance between the target depth and the tunnel depth level, where the proportion K is calculated by the ratio of the target depth to tunnel depth z/z_t:

$$\begin{aligned} i &= K(z_t - z) \\ K &= \frac{0.175 + 0.325(1 - z/z_t)}{1 - z/z_t} \end{aligned} \tag{2.4}$$

Jones (2010) reported that Eq. 2.4 would overestimate the width parameter K for deep tunnel cases. Instead, the author proposed a logarithmic formula Eq. 2.5 to define the width parameter K of subsurface settlement curves based on field monitoring data:

$$K = -0.25\ln(z_t - z) + 1.234 \tag{2.5}$$

Several authors reported that i is also a function of the tunnel diameter D_t, especially for shallow tunnels (Clough and Schmidt, 1981; Moh et al., 1996; Lee et al., 1999). For example, Lee et al. (1999) suggested using Eq. 2.6 to establish the relationship between i and the tunnel diameter D_t based on centrifuge tests of tunnelling in soft clays:

$$2\frac{i}{D_t} = 1 + 0.58\frac{z}{D_t} \tag{2.6}$$

The standard Gaussian curve method provides good assessments of soil movements induced by tunnelling in clays (Peck, 1969; O'Reilly and New, 1982; Mair et al., 1993). However, when tunnelling in sands, soils exhibit different movement modes and surface/subsurface settlement trough shapes compared with clays (see Figure 2.4(b)) due to complex soil dilation and contraction behaviours, which are associated with changes in cover-to-tunnel diameter ratio C/D_t, soil relative density I_d, and tunnel volume loss $V_{l,t}$ (Marshall et al., 2012; Zhou et al., 2014; Franza et al., 2019). Several researchers reported that the standard Gaussian curve (Eq. 2.1) cannot always adequately fit surface settlements resulting from tunnel excavations in sands (Mair and Taylor, 1997; Celestino et al., 2000; Jacobsz et al., 2004; Marshall et al., 2012). For example, O'Reilly and New (1982) and Mair and Taylor (1997) reported more scatter in the data for parameter K related to settlement trough width using the standard Gaussian curve Eq. 2.1 and Eq. 2.3 to interpolate field data. Based on the work from Clough and Schmidt (1981), Moh et al. (1996) proposed Eq. 2.7 to characterize the field subsurface settlement troughs from the Tapei Mass Transit system in silty sands:

$$i = \left(\frac{D_t}{2}\right)\left(\frac{z_t}{D_t}\right)^{0.8}\left(\frac{z_t - z}{z_t}\right)^{m} \tag{2.7}$$

where the author suggested m is 0.4 for silty sands and 0.8 for silty clays.

To describe tunnelling-induced surface settlement troughs quantitatively and accurately, a yield-density type curve (Eq. 2.8) (Celestino et al., 2000), a slightly different form of the Gaussian curve (Eq. 2.9) (Jacobsz et al., 2004), and a modified Gaussian curve (Eq. 2.10) (Vorster et al., 2005a) were proposed:

$$\begin{aligned} S_v(x) &= \frac{S_{v,max}}{1 + (|x|/a)^b} \\ i &= a\left(\frac{b-1}{b+1}\right)^{1/b} \end{aligned} \tag{2.8}$$

where a is a length dimension and b is dimensionless.

$$S_v(x) = S_{v,max}\exp\left[-\frac{1}{3}\left(\frac{|x|}{i}\right)^{1.5}\right] \tag{2.9}$$

$$\begin{aligned} S_v &= \frac{nS_{v,max}}{(n-1)+\exp[\alpha(x^2/i^2)]} \\ n &= \exp(\alpha)\frac{2\alpha-1}{2\alpha+1}+1 \end{aligned} \tag{2.10}$$

where the parameter α controls the shape of settlement troughs and maintains the definition of i, i.e. inflection point, consistent with the standard Gaussian curve Eq. 2.1. The inclusion of three variables ($S_{v,max}$, α, i) complicates the calculation process of Eq. 2.10 (compared with the standard Gaussian curve (Eq. 2.1) with two variables ($S_{v,max}$, i)), and Eq. 2.10 becomes Eq. 2.1 when $n = 1$. Marshall et al. (2012) provided evidence to support the universality of the modified Gaussian curve (Eq. 2.10) by analysing centrifuge test data of greenfield tunnelling in dense sand using Eq. 2.1 and Eqs. 2.8-2.10, with results demonstrating that Eq. 2.10 is capable of providing an excellent fit with varying depth of interest z and tunnel volume loss $V_{l,t}$.

Despite the improved fitting accuracy of the modified Gaussian curve to settlement troughs, the parameter α lacks direct physical meaning. Marshall et al. (2012) proposed an alternative approach to describing the shapes of settlement curves using two specific points, $(x^*, 0.606S_{v,max})$ and $(x^{**}, 0.303S_{v,max})$, where $(x^*, 0.606S_{v,max})$ is based on the position of the inflection point at the standard Gauss curve $(i, 0.606S_{v,max})$. Combining Eq. 2.10 and Eq. 2.4, Marshall et al. (2012) proposed Eq. 2.11 to predict ground surface and subsurface settlement trough shapes in dense sand with varying cover-to-tunnel diameter ratio C/D_t and tunnel volume loss $V_{l,t}$:

$$\begin{aligned} K^{*(*)} &= \frac{K_s^{*(*)}+\left(\partial x^{*(*)}/\partial z\right)(z/z_t)}{1-z/z_t} \\ K_s^{*(*)} &= K_{s,C/D_t}^{*(*)int}+K_{s,C/D_t}^{*(*)slope}(C/D_t)+K_{s,V_{l,t}}^{*(*)slope}\left(V_{l,t}\right) \end{aligned} \tag{2.11}$$

where $K_{s,C/D_t}^{*int} = 0.440$, $K_{s,C/D_t}^{*slope} = 0.055$, $K_{s,V_{l,t}}^{*slope} = -0.041$, $\partial x^*/\partial z = -0.436$, $(\partial x^{**}/\partial z) = (\partial x^*/\partial)z - 0.20$, $K_s^{**} = K_s^* + 0.29$. The authors assumed a linear relationship between the settlement trough parameters and cover-to-tunnel diameter ratio C/D_t and tunnel volume loss $V_{l,t}$. Following Marshall et al. (2012), Franza and Marshall (2019b) extended the analysis of centrifuge tunnelling test data, incorporating the influence of cover-to-tunnel diameter ratio C/D_t and soil relative density I_d, and proposed a set of equations (Eq. 2.12) to calculate the settlement trough parameters due to the non-linear effect of C/D_t:

$$\begin{aligned}
\partial x^{*}/\partial z &= \frac{(+0.81I_d - 0.93)\ln(C/D_t) - 0.60I_d - 0.07}{1 + z/z_t} \\
\partial x^{**}/\partial z &= \frac{(+1.50I_d - 1.55)\ln(C/D_t) - 0.96I_d - 0.28}{1 + z/z_t} \\
K^{*slope,ln}_{s,V_{l,t}} &= (+0.35I_d - 0.30)\ln(C/D_t) - 0.22I_d + 0.07 \\
K^{**slope,ln}_{s,V_{l,t}} &= (+0.41I_d - 0.35)\ln(C/D_t) - 0.22I_d - 0.01 \\
K^{*int,ln}_{s,V_{l,t}} &= (-0.84I_d + 0.95)\ln(C/D_t) + 0.45I_d + 0.07 \\
K^{**int,ln}_{s,V_{l,t}} &= (-1.16I_d + 1.36)\ln(C/D_t) + 0.47I_d + 0.42
\end{aligned} \tag{2.12}$$

2.1.2 Soil transverse horizontal movement

It has been observed that soil horizontal displacements are typically much lower than vertical displacements (Marshall and Mair, 2011; Standing and Selemetas, 2013; Farrell et al., 2014; Yiu et al., 2017; Franza et al., 2019). However, there is still a potential for the tunnelling-induced soil horizontal movements to impact nearby structures or structure groups during tunnel excavation activities. Although soil horizontal displacements and strains can be derived from numerical or physical modelling tests, directly measuring soil horizontal movements in field sites is challenging (time-consuming). Therefore, researchers tried several methods to estimate soil horizontal displacements based on the available settlement data.

O'Reilly and New (1982) proposed an estimation formula to describe the horizontal movement S_h of clays with the assumption that the width parameter K of settlement troughs does not change with depth and the displacement vectors point to the tunnel axis:

$$S_h(x) = \frac{x}{z - z_t} \cdot S_v(x) \tag{2.13}$$

Soil horizontal strains ε_h can be derived by taking the derivative of Eq. 2.13, in conjunction with Eq. 2.1:

$$\varepsilon_h(x) = \frac{S_{v,max}}{z_t - z} \cdot \exp(-\frac{x^2}{2i^2}) \cdot (1 - \frac{x^2}{i^2}) \tag{2.14}$$

The illustration of surface settlement and predicted horizontal displacements and strains are shown in Fig. 2.5. $\widehat{\varepsilon}_{hc}$ and $\widehat{\varepsilon}_{ht}$ represent the maximum compressive and tensile strains in the transverse horizontal direction, respectively. Note the false mirror symmetry of the horizontal displacement curve (which should exhibit point symmetry, representing soil on both sides of the tunnel moving in opposite horizontal directions), as it originates from the axisymmetric settlement curve without considering the issue of horizontal directions.

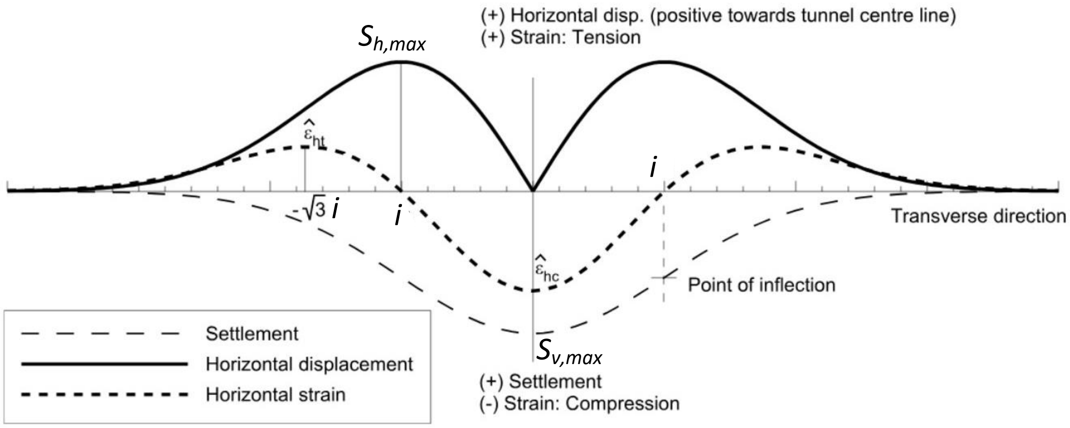

Fig. 2.5. Surface horizontal displacement and strain in the transverse direction along with settlement trough (Franzius, 2003)

Attewell and Yeates (1984) introduced a constant n into Eq. 2.13 to accommodate various tunnelling scenarios:

$$S_h(x) = \frac{nx}{z - z_t} \cdot S_v(x) \tag{2.15}$$

The authors suggested $n = 1$ is applicable for cohesive soils and $n < 1$ for granular soils (indicating that the displacement vectors of the soil point to a location below the tunnel axis). Marshall (2009) also reported that a representative value of n within 0.46-0.91 based on centrifuge tunnelling tests in sand.

Taylor (1995b) proposed an alternative method to estimate soil horizontal displacements based on a constant volume condition and the changes in K with depth z in Eq. 2.4:

$$S_h(x) = \frac{x}{(1+0.175/0.325)z_t} \cdot S_v(x) \tag{2.16}$$

where the displacement vectors point to the tunnel centreline depth of $0.175z_0/0.325$ below the tunnel axis. This estimation method was validated by centrifuge test results in clay (Grant and Taylor, 2000).

2.1.3 Tunnel volume loss and soil movements

Under plane-strain conditions transverse to the tunnel axis, tunnel volume loss $V_{l,t}$ is the ratio of soil loss area at the tunnel periphery V_t to the initial excavation area V_0, whereas soil volume loss $V_{l,s}$ represents the ratio of the settlement trough area V_s to the tunnel excavation area V_0. The magnitudes and relationship between $V_{l,t}$ and $V_{l,s}$ are usually adopted to assess the effects of tunnelling on ground movements, as shown in Fig. 2.4:

$$V_{l,t} = \frac{V_t}{V_0} \times 100\% \tag{2.17}$$

$$V_{l,s} = \frac{V_s}{V_0} \times 100\% \tag{2.18}$$

Engineers usually substitute $V_{l,s}$ for $V_{l,t}$ (i.e. assuming $V_{l,t} = V_{l,s}$) to estimate the ground surface V_s for clays, taking into account the short-term undrained conditions of tunnel excavation. Tunnel excavations typically occur in clays, and Mair and Taylor (1997) summarised the experience in ground volume loss of the following cases: approximately 1-2% in stiff clays (such as London clay) using open-face tunnelling techniques; 0.5-1.5% in London clay with sprayed concrete linings (NATM); a high degree of settlement control with volume losses of 0.5% for sands and 1-2% for soft clays (excluding consolidation settlements) when using earth pressure balance (EPB) and slurry machines; in mixed face conditions volume loss may be higher for EPB and slurry machines. However, ground conditions and volumetric strains affect the relationship of magnitudes of $V_{l,s}$ and $V_{l,t}$ in sands (drained conditions) due to soil contraction and dilation behaviours (Marshall et al., 2012).

In experimental studies, model tunnel contraction methods are widely adopted to simulate ground loss, that is, $V_{l,t}$ can be obtained by dividing the reduced cross-sectional area of the model tunnel by the initial cross-sectional area of the model tunnel (Marshall et al., 2009; Song and Marshall, 2020). Franza et al. (2019) reported the relationships between $V_{l,s}$ and $V_{l,t}$ in centrifuge tests of tunnelling in sand, as shown in Fig. 2.6. The results indicate that the surface soil volume loss $V_{l,s}$ increases with the cover-to-tunnel diameter ratio C/D_t and decreases with soil relative density I_d at a given tunnel volume loss $V_{l,t}$; soil volume loss tends to contract at the beginning (for all conditions), and then to dilate under conditions of lower C/D_t and higher $V_{l,t}$ and I_d.

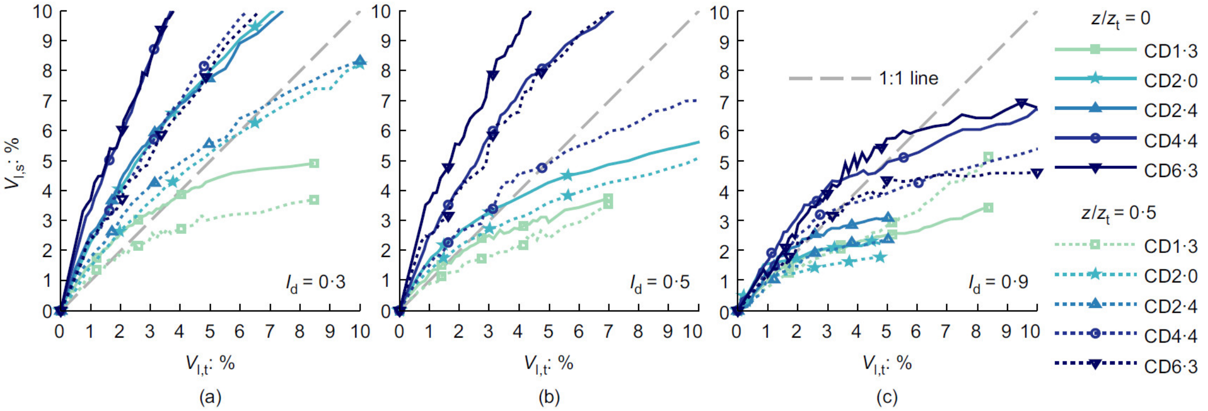

Fig. 2.6. Soil volume loss $V_{l,s}$ against tunnel volume loss $V_{l,t}$ under different soil relative density I_d and cover-to-tunnel diameter ratio C/D_t (Franza et al., 2019)

As shown in Fig. 2.4, the tunnel ground loss is distributed around the tunnel in clays (Loganathan and Poulos, 1998) but in sands it is concentrated at the tunnel crown (Marshall et al., 2012). Franza et al. (2019) proposed the soil arching mechanism to explain the effects of sand density and tunnel depth on shear strains and soil arching, as shown in Fig. 2.7. When tunnelling in dense and medium dense sands, a closed arch forms above the tunnel crown, where the soil within the arch range moves vertically and significantly and the soil above the arch is characterized by movements propagating upwards and outwards towards the surface. In loose sands, ground loss propagates from near the tunnel shoulders towards the surface both vertically and laterally. Shallow-buried tunnels tend to form a chimney-like displacement field with narrow settlement troughs.

Song and Marshall (2020) reported that soil shear behaviours are also affected by the shrink-

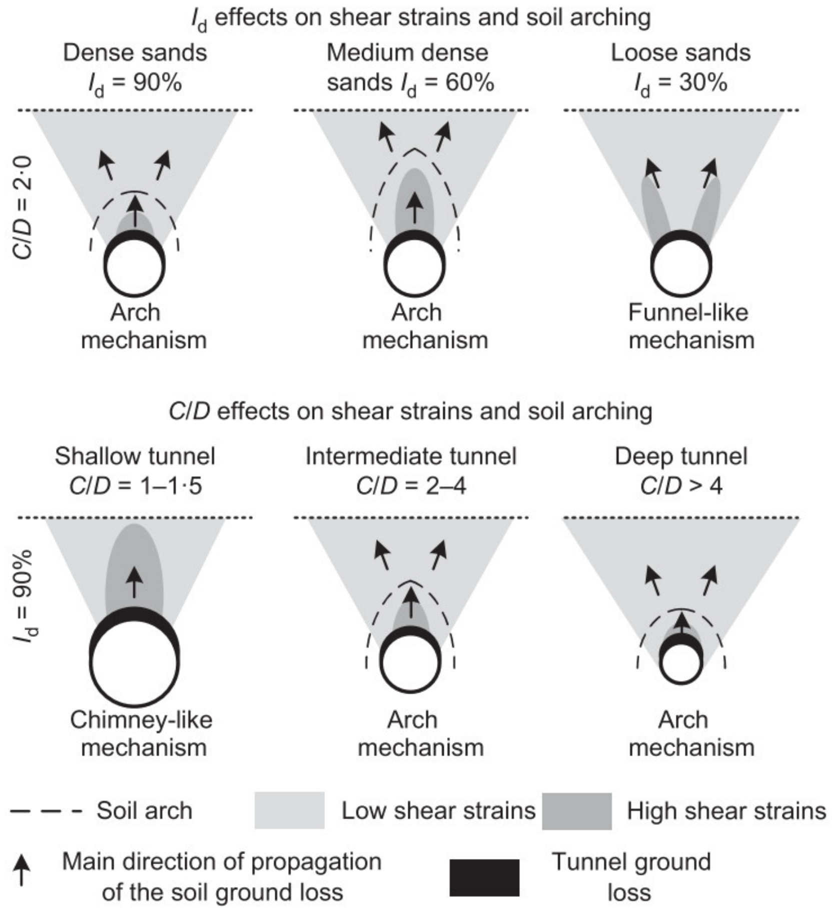

Fig. 2.7. Sketches of soil strains, arching mechanism, and ground loss propagation (Franza et al., 2019)

age principles of tunnel models in centrifuge tunnelling tests. The authors conducted a series of centrifuge tests of tunnelling in fine-grained silica sand at 80 g using an eccentric flexible membrane (eFM) tunnel model (controlled by the tunnel inner pressure; this kind of tunnel model was also adopted by Marshall et al. (2012) and Franza et al. (2019)) and an eccentric rigid boundary mechanical (eRBM) tunnel model (controlled by the fixed changes in the tunnel boundary). As shown in Fig. 2.8, shear regions (along with dilation zones) are concentrated around the tunnel boundary, specifically, near the tunnel crown/shoulder for the flexible membrane (eFM) tunnel model and closer to the tunnel springline for eccentric rigid boundary mechanical (eRBM) tunnel model. Additionally, the magnitudes of shear strain and dilative volumetric strain of the eRBM test are significantly higher than the eFM test. The authors also reported that the eRBM model always provides a wider settlement trough than the eFM model.

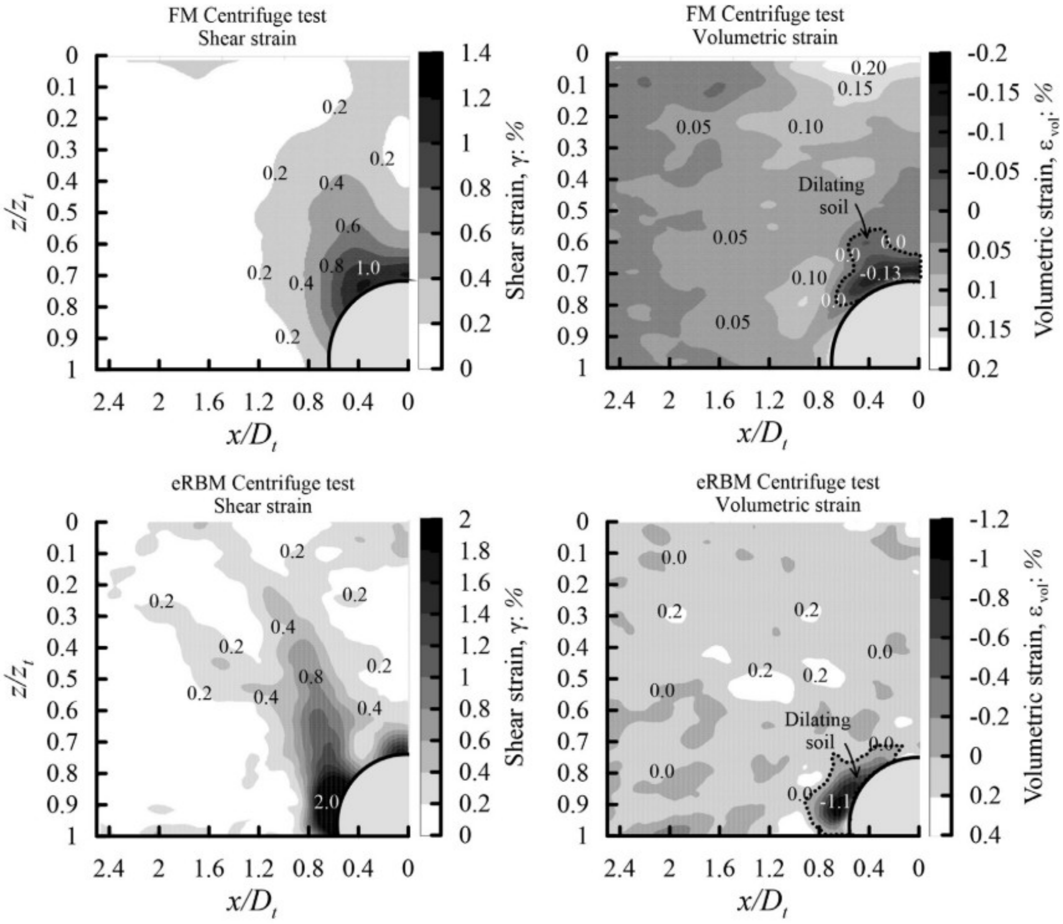

Fig. 2.8. Contours of shear and volumetric strain for centrifuge tunnelling tests in sand with $C/D_t = 2$ at $V_{l,t} = 2\%$ (Song and Marshall, 2020)

2.2 Tunnelling effects on pile foundations

Pile foundations are critical in Civil engineering developments to support heavy loads and minimise differential settlement of buildings and other structures, and help withstand lateral and uplift forces during extreme loading scenarios such as earthquakes and storms. In general application scenarios, shaft friction and base load jointly withstand vertical service loads at the pile head. Pile installation methods influence the load transfer mechanisms and displacement performance of piles, according to which piles are divided into two types: displacement piles (i.e. driven or jacked piles), where shaft friction increases to cope with higher service loads, with base load capacity (partly) mobilized during the subsequent loading process; and non-displacement piles (i.e. bored piles), where both shaft friction and base load play important roles, with the base load capacity not being mobilized during installation.

The restricted availability of urban areas increases the demand for underground construction. In this circumstance, tunnel excavations often come close to or pass directly beneath existing pile foundations, posing uncertain risks to these deep foundations and associated buildings (Mair et al., 1993; Jacobsz et al., 2004; Teparaksa et al., 2006; Phienwej et al., 2006). To mitigate or avoid potential risks to surrounding structures with pile foundations, practitioners typically adopt relatively conservative designs of tunnel excavations and/or implement additional protective measures. It is therefore crucial to understand how tunnelling activities affect pile load capacities through changing the state of the soil around the pile, so as to guarantee the safety and serviceability of structures (both superstructures and buried foundations) and simultaneously avoid waste of space, manpower, and money. This section presents an overview of geotechnical centrifuge modelling and field studies of tunnel-soil-pile interaction (TSPI) problems, focusing on load transfer mechanisms and settlements of piles under different tunnelling scenarios.

2.2.1 Centrifuge modelling studies

Small-scale physical models at 1 g (gravity) can provide indications of the important relationships and trends in structural elements affected by tunnelling scenarios (Lee and Bassett, 2007; Shahin et al., 2016; Moussaei et al., 2019; Zhu et al., 2023), however the direct applicability of results to full-scale scenarios is questionable because of the mismatch in stress conditions (where the 1 g model stresses are much less than the full-scale). Numerical models are able to reproduce, in detail, many aspects of the construction and material complexities involved in real tunnelling projects (Mroueh and Shahrour, 2002; Pang et al., 2005; Lee and Jacobsz, 2006; Cheng et al., 2007; Lee, 2013; Nematollahi and Dias, 2019), however the reliability/fidelity of results is difficult to verify unless corresponding experimental/full-scale data are available. In contrast, geotechnical centrifuge simulations at high g-levels (representing relatively realistic full-scale stress conditions) provide reliable data for the study of pile responses to tunnelling, even though model structures/dimensions are simplified/reduced accordingly.

2.2.1.1 Response of displacement piles and pile groups

Jacobsz et al. (2004) investigated the effects of tunnelling on single piles at different positions related to the tunnel centreline in dense sand through centrifuge tests at 75 g. The experimental setup replicated a real-world scenario featuring a 4.5 m diameter tunnel excavated at a depth of 21.5 m with 0.9 m diameter and 15-18.75 m deep (below the surface) single piles in the vicinity. After centrifuge spin up to 75 g, the piles with 60° conical tips were pushed from the initial 175-225 mm depth (in model scale) to the target positions of 200-250 mm depth at 15 mm/min to mobilise the base bearing capacity, representing displacement piles. The working loads of the piles weas constant, with a safety factor of 2, during the tunnel volume loss process. Jacobsz et al. (2004) explained the tunnelling-induced pile load transfer mechanisms, as is commonly believed, that soil stress relief around the pile base reduces pile base loads and the altered loads are transferred to pile shaft friction; upon reaching the maximum shaft friction capacity, high levels of pile settlements and movement speeds occur at further tunnel volume loss to balance the state of resisting pile working loads, ignoring the minor impacts of pile bending behaviours.

Jacobsz et al. (2004) defined influence zones around the tunnel using data obtained at a tunnel volume loss of 1.5% (where large settlements, i.e. ≥ 20 mm in prototype scale, are expected), as shown in Fig. 2.9.

- Zone A: pile settlement exceeded surface settlement; pile base loads reduced quickly during $V_{l,t} = 0\text{-}1.5\%$ and then remained constant with rapid pile settlement; shaft friction was fully mobilised within settlement of 1% pile diameter ($S_p/d_p = 1\%$).
- Zone B: pile settlement exceeded surface settlement; pile base loads reduced with a similar rate to Zone A; shaft friction was mobilised quickly at $V_{l,t} = 1.5\%$, and then gradually increased due to increased confining stress induced by high shear and dilation strains.
- Zone C: pile settlement approximated surface settlement; pile base loads reduced with a relatively slow rate; shaft friction was initially negative (i.e. downwards) and not fully mobilised.
- Zone D: pile settlement was less than surface settlement; pile base loads increased slightly and then remained constant after $V_{l,t} = 1.5\%$; minimal changes were observed in negative shaft friction.

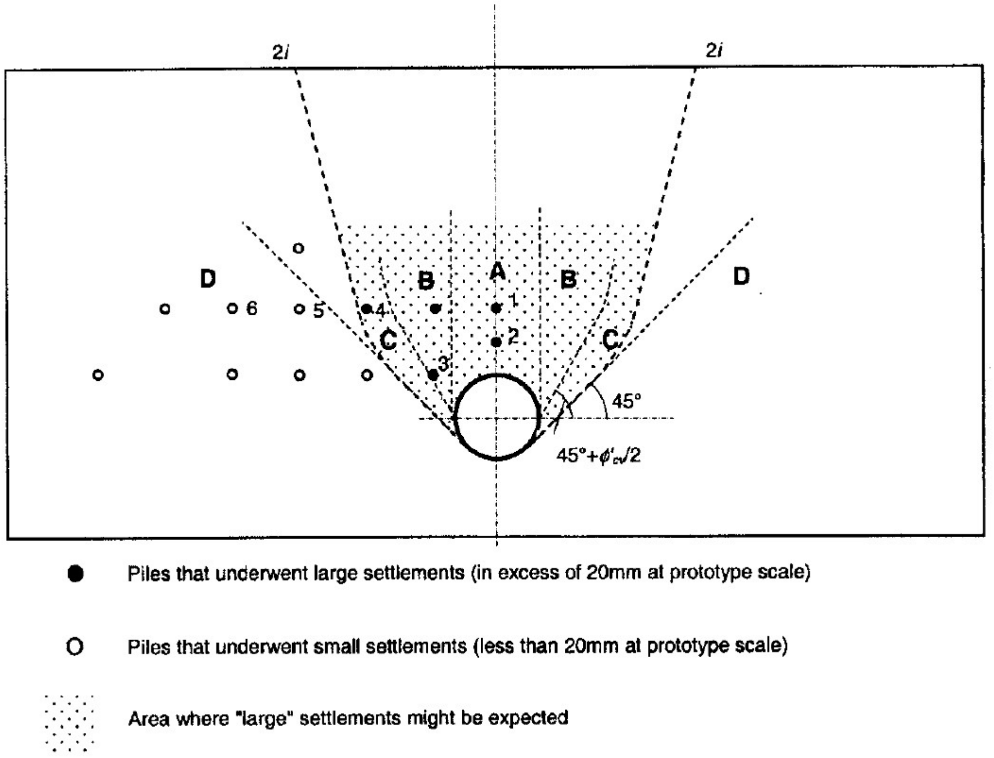

Fig. 2.9. Different influence zones of tunnelling excavations for piles (Jacobsz et al., 2004)

To validate the rationality of the influence zones around a tunnel proposed by Jacobsz et al. (2004), Marshall and Mair (2011) carried out two groups of centrifuge tunnelling tests on displacement piles in dry dense sand with a relative density of 90%; the test layout is shown in Fig. 2.10, along with a greenfield tunnelling test. The first set included a pile directly above the tunnel and the other pile away from the tunnel centreline by $2.1D_t$; the second set involved two nearly symmetrically located piles offset by about $1D_t$ related to the tunnel centreline. The aluminium piles, half piles precisely, had a semi-circular cross-section perpendicular to the pile axis, and the pile axis cross-section was aligned with the inner face of the acrylic wall of the strongbox, assuming no friction at the contact surfaces. The piles were jacked a distance of approximately two times the pile diameter $2d_p$ into the sand after centrifuge spin up to the target g-level (75 g), with a final C/D_t of 2, to reproduce realistic stress conditions around the piles. The pile working loads were set with a safety factor $SF = 1.6$ before the tunnel volume loss process commenced.

Marshall and Mair (2011) reported the difference between pile and greenfield settlements

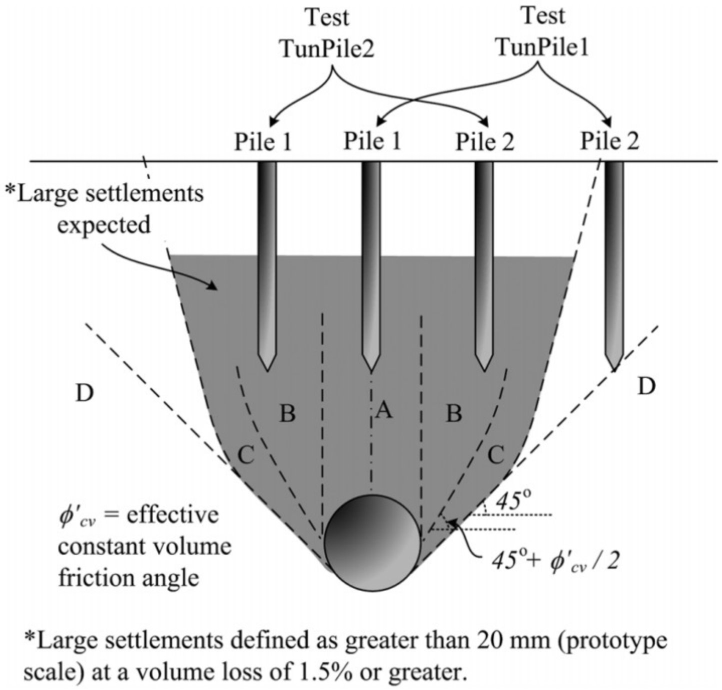

*Large settlements defined as greater than 20 mm (prototype scale) at a volume loss of 1.5% or greater.

Fig. 2.10. Tested piles (Marshall and Mair, 2011) located in different influence zones defined by Jacobsz et al. (2004)

(normalised by pile diameter) during tunnel volume loss, as depicted in Fig. 2.11. The difference in settlements was negligible at initial low tunnel volume loss ($V_{l,t} \leq 0.2\%$), after which the settlement difference became more obvious under tunnel-soil-pile interactions. The soil beneath piles tended to undergo vertical compression–horizontal extension, while the soil along the pile periphery experienced vertical extension–horizontal compression. Large pile settlements would occur to counteract the loss in confining stress induced by tunnelling. The authors also cautioned against adopting greenfield data (typically applicable for non-displacement pile analysis) as an input for analytical analysis of tunnel-soil-pile interactions for driven or jacked piles due to the effects of pile installation. These results confirmed the definition and interaction mechanisms of the influence zones of tunnel excavation proposed by Jacobsz et al. (2004).

2.2.1.2 Responses of non-displacement piles and pile groups

Loganathan et al. (2000) performed three centrifuge tests to study the influence of tunnelling depth on adjacent single piles and 2×2 pile groups (with piles sealed by a plastic cap) in stiff

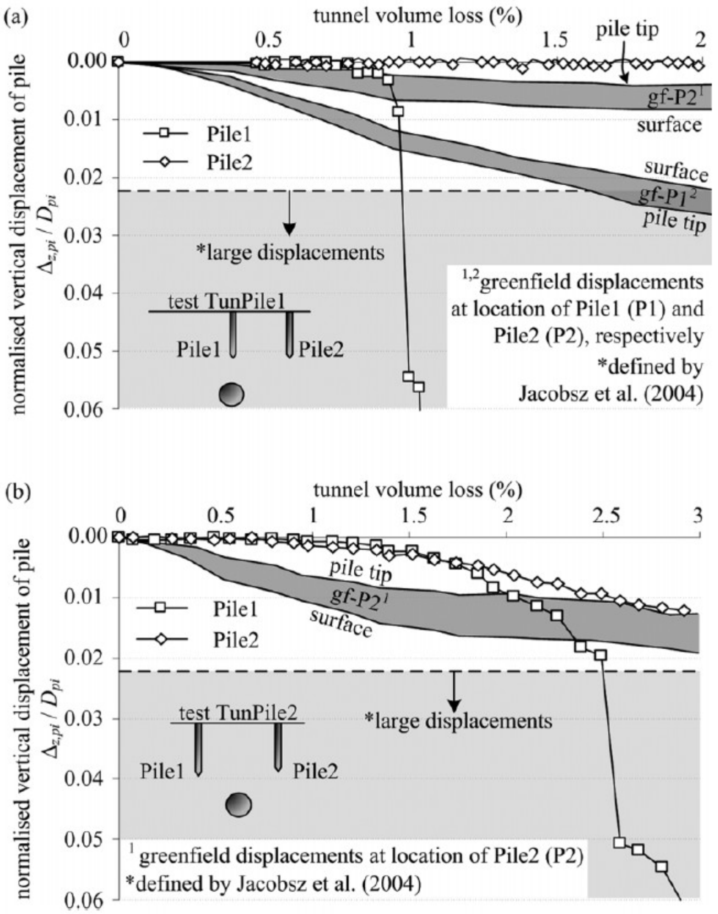

Fig. 2.11. Comparison of normalised pile settlement and greenfield settlement (Marshall and Mair, 2011)

clay, as shown in Fig. 2.12. The piles were pushed into the preconsolidated kaolin clay at a rate of 0.5 mm/s prior to the centrifuge spin-up and loaded with a safety factor $SF = 2$ at 100 g; tests were intended to consider non-displacement piles. The results show that pile horizontal deformations (including bending moments and lateral deflections) were critical when the tunnel centreline was situated near the pile tip level, whereas tunnelling occurring below the pile tip level would result in critical pile axial force (especially pile base load). The effects of tunnelling depth on bending moments and lateral deformations of both single piles and piles in a group at an identical distance from the tunnel were similar. The authors also reported a nearly linear relationship between maximum bending moments of piles and ground loss values, which confirmed the applicability of elastic analysis in predicting tunnelling-induced pile behaviours (within $V_{l,s} \leq 5\%$).

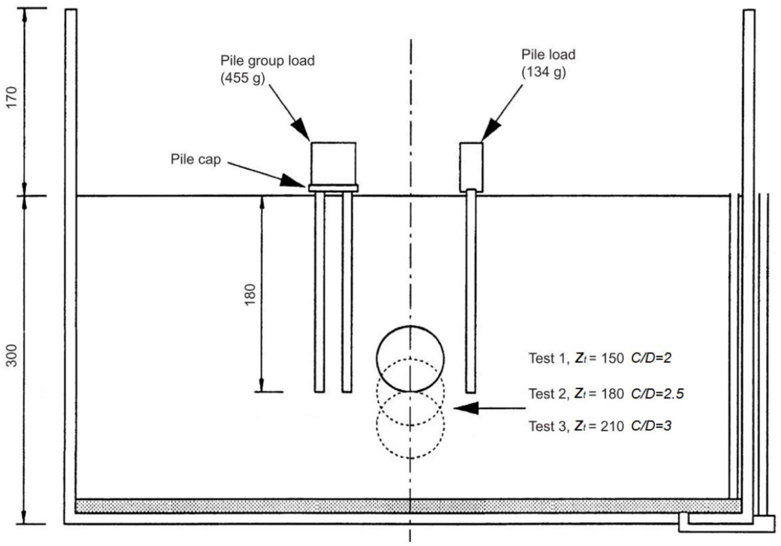

Fig. 2.12. Centrifuge model configuration (Loganathan et al., 2000)

Williamson (2014) conducted a series of centrifuge tests (at 75 g) to investigate the impact of pile offsets from the tunnel centreline when tunnelling beneath bored piles in stiff clay. The results of pile settlements, at different locations and working loads, were consistent with previous studies. Piles exhibited a reduction in shaft friction when subjected to negative displacements (upwards relative to soil) and an increase in shaft friction when subjected to positive displacement (downwards relative to soil). Pile stiffening effects, compared with greenfield soils, altered soil movements close to the pile shafts, resulting in greater shear strains in the soil zone between piles than in areas distant from the piles. Furthermore, the author reported that there was no pile failure even at high volume loss; instead, higher pile settlements occurred to generate sufficient positive friction to maintain pile-soil equilibrium.

Lee and Chiang (2007) investigated the response of single bored piles buried with a depth of 27 m (in prototype scale) under various working loads to nearby tunnelling activities (tunnel diameter D_t = 6 m; at various cover-to-tunnel diameter ratios C/D_t = 1-4) in saturated sandy ground through centrifuge tests. Strain gauges were affixed to the outer surface of the piles to measure pile axial force and bending moment during the tunnelling process. The piles were placed in predetermined positions during sand preparations and were not further driven after the centrifuge reached the target g-level (100 g), representing bored piles. The results indicate that, during tunnelling volume loss, pile shaft friction between the tunnel axis level and approximately $1.5D_t$ above the tunnel axis rapidly decreased for shallow tunnelling scenarios (i.e. C/D_t = 1-2), and a significant loss of pile base load capacity resulted in large pile settlements when tunnelling near pile tips (i.e. C/D_t = 4) (see Fig. 2.13). The pile-tunnel depth ratio significantly affects pile bending and axial load/deformation, with the latter also being influenced by pile working loads. Higher working loads, as expected, caused more severe pile settlements.

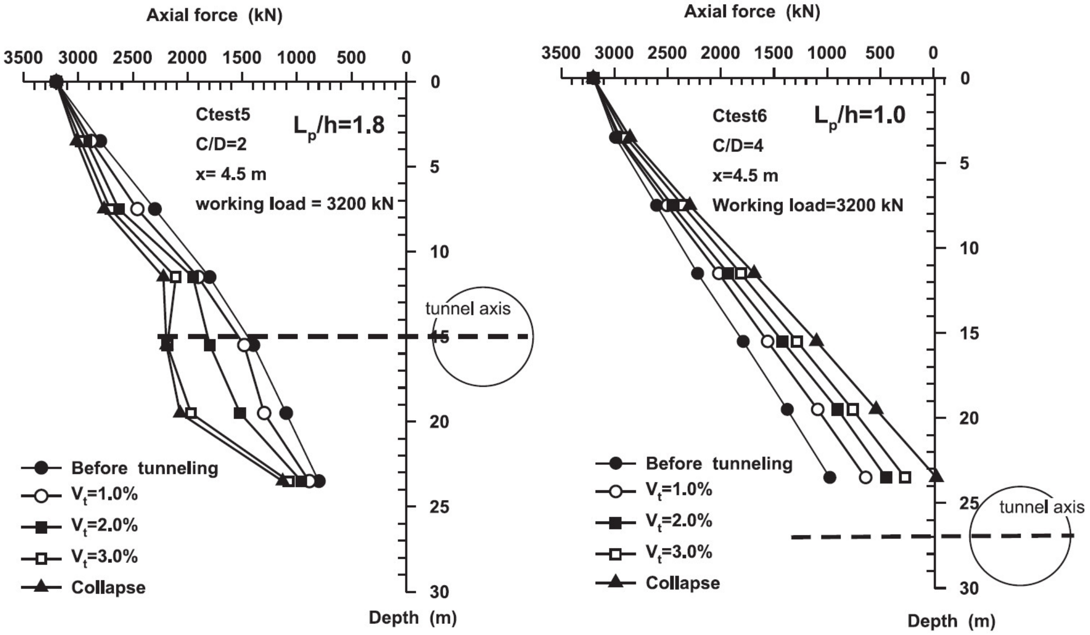

Fig. 2.13. Pile axial force and friction profiles with a working load of 3200 kN (Lee and Chiang, 2007)

Song and Marshall (2020) evaluated changes in pile stiffness and load capacities after nearby tunnelling activities in dense sand in 80 g centrifuge tests. The authors reported an important finding that the post-tunnelling pile-jacking responses were similar to the pile-jacking response in greenfield scenarios, as shown in Fig. 2.14. This similarity was attributed to local soil contraction behaviours (especially near the tunnel) during tunnel volume loss in dense sand, which countered the detrimental effects of stress relief induced by tunnelling.

Ng et al. (2014) investigated complex 3D scenarios of twin tunnelling near 2×2 pile groups (connected to a cap) in dense sand in centrifuge tests (40 g). The adopted tunnel model included five chambers when the water could be drained away from each chamber sequentially to achieve 3D tunnelling, with a maximum volume loss of $V_{l,t}$ = 1% for each segment. The tunnels were

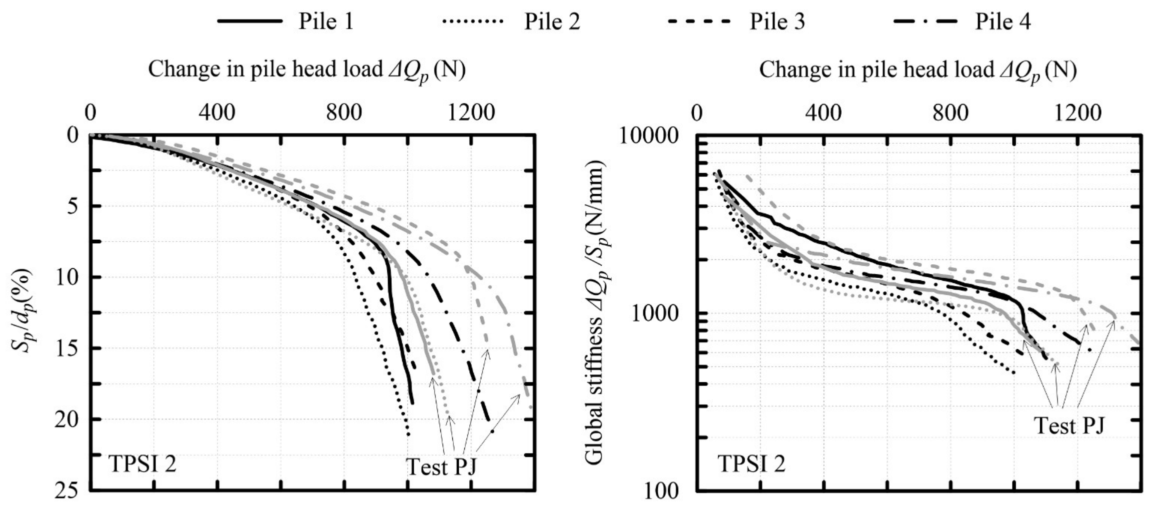

Fig. 2.14. Post-tunnelling (TPSI 2) and greenfield (Test PJ) pile-jacking responses: pile head load versus (a) normalised settlement and (b) global stiffness (Song and Marshall, 2020)

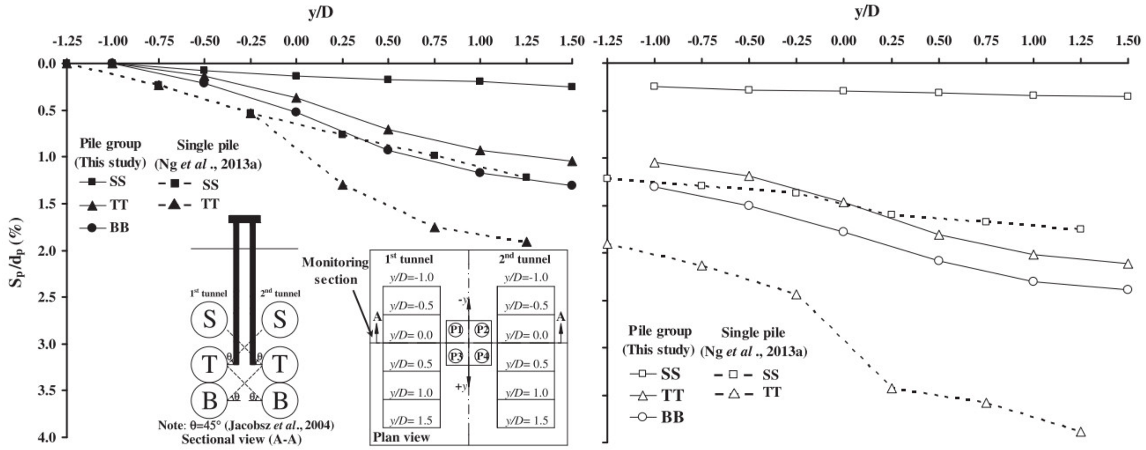

(a) (b)

Fig. 2.15. Settlement of pile group during twin tunnelling: (a) the first tunnel (i.e., tunnels S, T and B); (b) the second tunnel (i.e., tunnels S, T and B) (Ng et al., 2014)

positioned on both sides of the pile group at the same levels (near the mid-depth of pile shaft, Test SS; next to pile toe, Test TT; and below pile toe, Test BB) and were excavated one after another. The most significant transverse tilting was observed after the excavation of the first tunnel, attributed to a larger difference in soil stress release around the piles. Twin tunnelling under piles (Test BB) caused the largest settlement of the pile group, as shown in Fig. 2.15, resulting in an apparent loss of pile base capacity. Furthermore, Ng et al. (2015) and Soomro et al. (2020) studied the impacts of construction positions and sequences of twin stacked tunnels on the load transfer mechanisms and movements of neighbouring pile groups. These findings contribute valuable insights into the construction of twin tunnels in proximity to pile groups.

2.2.1.3 Responses of piled structures

Franza and Marshall (2018) performed 80 g centrifuge tests in loose dry fine silica sand (I_d = 30%) to investigate tunnel-soil-pile-structure interactions, as illustrated in Fig. 2.16. A 90 mm diameter tunnel model was buried with a cover-to-tunnel diameter of $C/D_t = 2$. Aluminium plates with varying thicknesses (representing structures using the equivalent beam approach) were rigidly connected to seven aluminium alloy rods with a layer of sand bonded to the outer surface (representing piles). A 38 mm gap (in model scale) existed between the plate and the soil surface to replicate a piled structure rather than a piled-raft foundation. The results revealed that pile foundations increased the potential for damage to flexible structures. The assumption of fully flexible structures with self-weight in preliminary damage assessment procedures would lead to overestimating structure deflection ratios and horizontal strains. However, an acceptable and conservative estimate of maximum settlement was expected before reaching pile failure. The authors also highlighted the dependence of structure settlements on the relationship between structure stiffness and weight, as well as the safety factor of the piles.

Simulation of superstructures using plates, however, still cannot provide highly accurate data in tunnel-soil-pile-structure interaction scenarios due to the over-idealised simplifications in accounting for building bending and shear stiffness during tunnel volume loss. To better reproduce the response of buildings during tunnelling, Idinyang et al. (2019) developed a real-time coupled centrifuge-numerical modelling (CCNM) testing method, where a framed building was simulated in a numerical domain (e.g., Matlab or Abaqus), the tunnel-soil-pile system was included in centrifuge model, and the real-time coupling of data between the numerical (i.e. frame base) and centrifuge models (i.e. pile top) was achieved through a Labview data exchange interface. This technique enables the redistribution of pile loads under the influence of frame stiffness (in this case an elastic frame, without self-weight) in centrifuge testing.

Franza and Marshall (2019a) employed the CCNM method (mentioned above) to investigate how framed buildings on pile foundations respond to tunnelling in loose sand (I_d = 30%) within

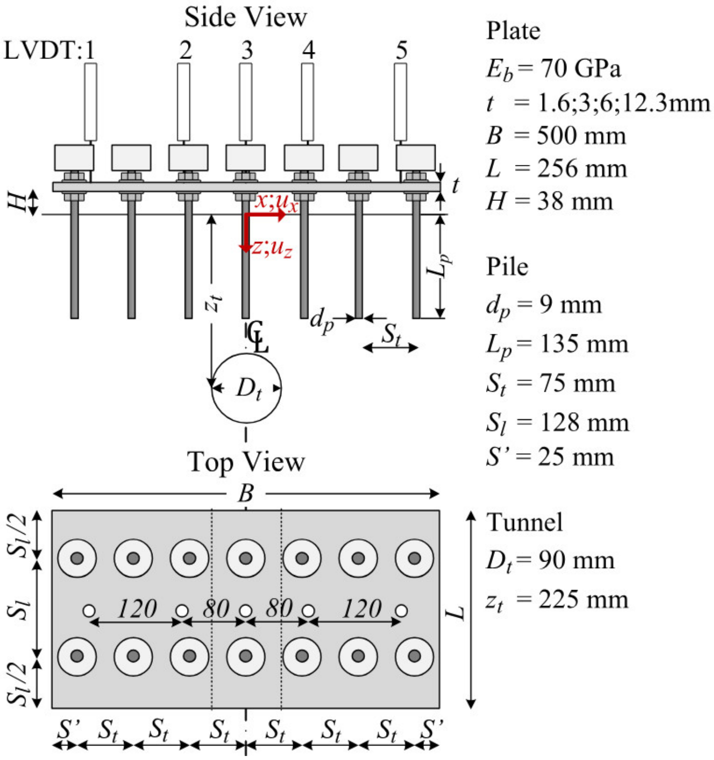

Fig. 2.16. Test layout (in model scale) of tunnelling beneath piled plate (Franza and Marshall, 2018)

a centrifuge setup at 60 g (see Fig. 2.17). The framed buildings, consisting of beam and column elements of different square cross sections (0-0.7^2 m^2 in prototype scale), were simulated in the Matlab software through a simple and computationally efficient stiffness matrix method for structural analysis (i.e. a first-order elastic analysis) based on the finite-element method. The findings indicated that structural stiffness can effectively redistribute building loads among piles and reduce the level of building deformation (which also depends on pile type, i.e. displacement or non-displacement pile foundations). A limited relative reduction in the pile load during tunnel volume loss could prevent geotechnical failure of piles directly above the tunnel. This way, traditional tunnel-single pile analysis with constant head load conditions that neglects load redistribution due to structure action may result in an overly conservative assessment of global tunnel-piled structure interaction.

Song and Marshall (2020) also utilized the CCNM approach to examine tunnelling proximity to piled structures in dense sand (I_d = 90%) at 80 g, different from Franza and Marshall

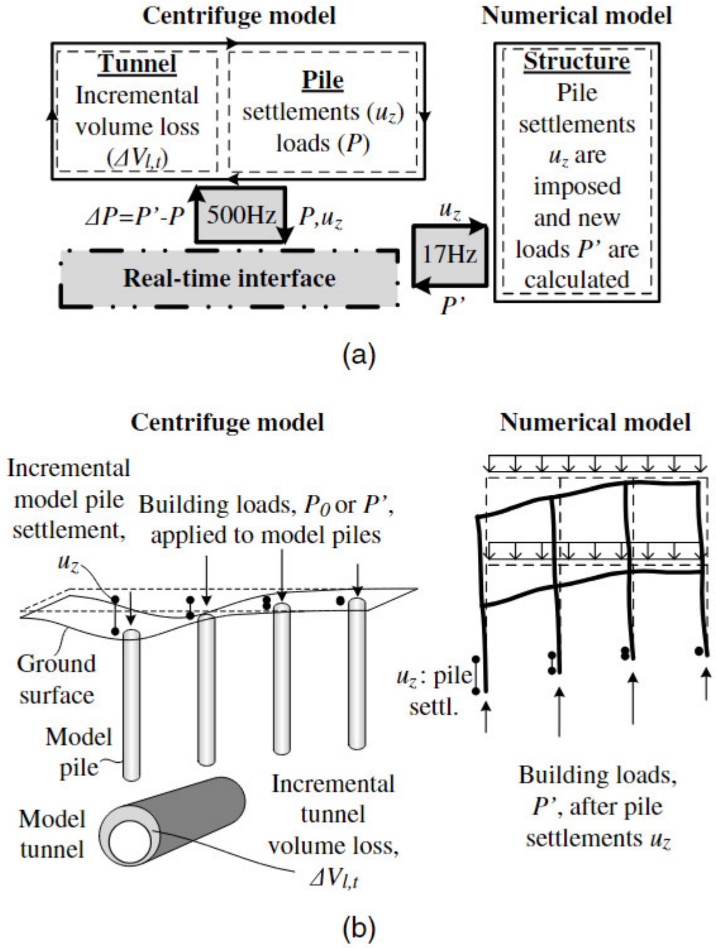

Fig. 2.17. Coupled centrifuge-numerical model: (a) diagram of the coupling loop and (b) decoupled geotechnical and structural domains (Franza and Marshall, 2019a)

(2019a) in employing an eccentric rigid boundary mechanical model tunnel (vs a flexible membrane model tunnel), stepper motors for loading on piles (vs servo actuator apparatus and lever system), and Abaqus simulations for framed buildings (vs Matlab simulation). Fibre Bragg grating (FBG) sensors were installed within the pile models (constructed with hollow aluminium tubes) to measure loads along the pile axis. The pile load capacity was first tested (Fig. 2.18(a)) to serve as a baseline for subsequent tunnelling tests (Fig. 2.18(b)). For the pile nearest to the tunnel, the pile head load was reduced due to the structure stiffness and the pile base resistance diminished owing to tunnelling activities (Fig. 2.19). Excavation significantly impacted piles situated close to the tunnel, while all piles were influenced by the structure stiffness.

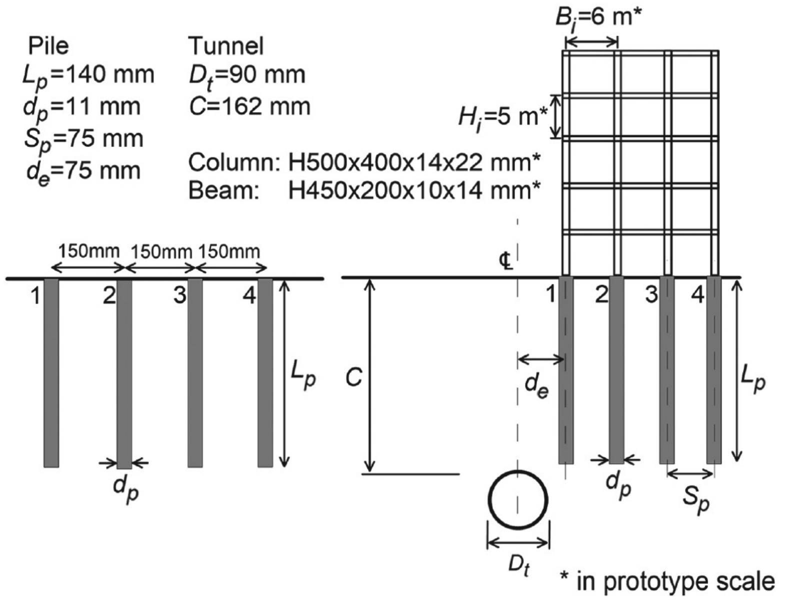

Fig. 2.18. Tunnel-pile interaction test configuration: jacking (left) and tunnelling (right) (Song and Marshall, 2020)

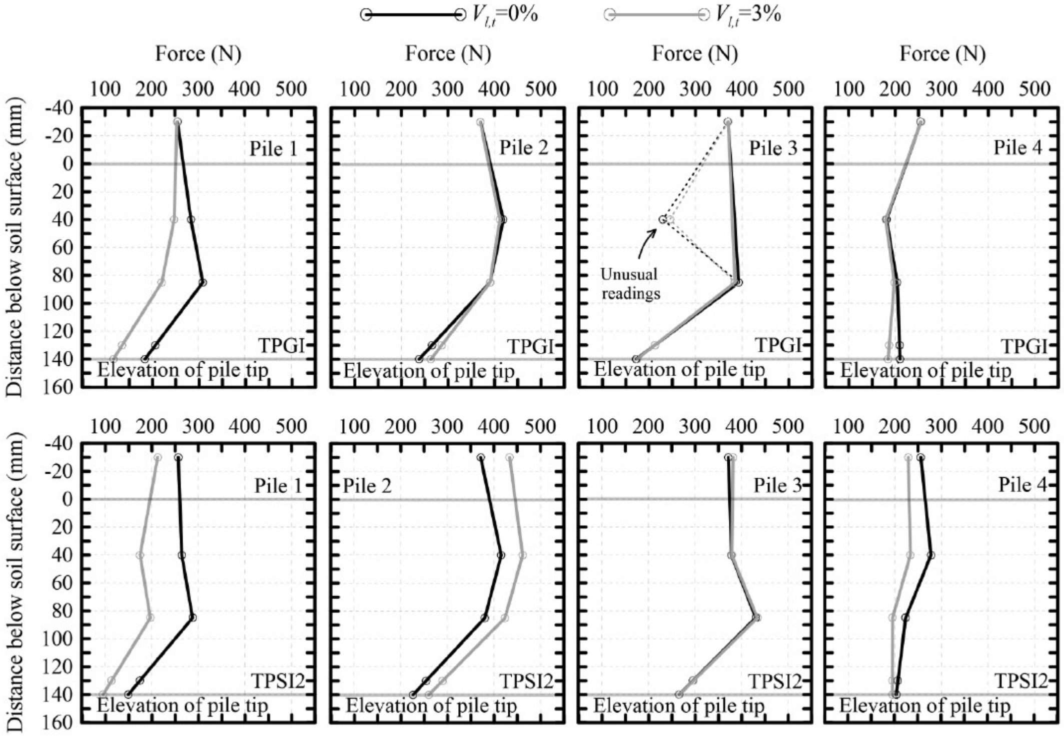

Fig. 2.19. Changes in pile axial force after tunnelling (TPGI: tunnel-pile group interaction, TPSI2: the second test of tunnel-pile-structure interaction) (Song and Marshall, 2020)

2.2.2 Field studies

Kaalberg et al. (2005) conducted full-scale tests on representative timber and concrete piles at the Second Heinenoordtunnel project, including two tunnels (tunnel outer diameter was 8.3 m, tunnel centre to centre distance was 16.3 m, tunnel lining to lining distance was 8.3 m), to furnish a benchmark for designing a new North-South metro line with piled-buildings in the vicinity in Amsterdam. The tested strata comprised a 4 m layer of soft clay underlain by fine sand. Pre-installed clay columns were constructed to reproduce similar geotechnical conditions in Amsterdam, and the piles were subsequently driven within the pre-installed clay columns, ensuring a reasonable reproduction of the ratio between pile base capacity and shaft friction. The test layout is shown in Fig. 2.20.

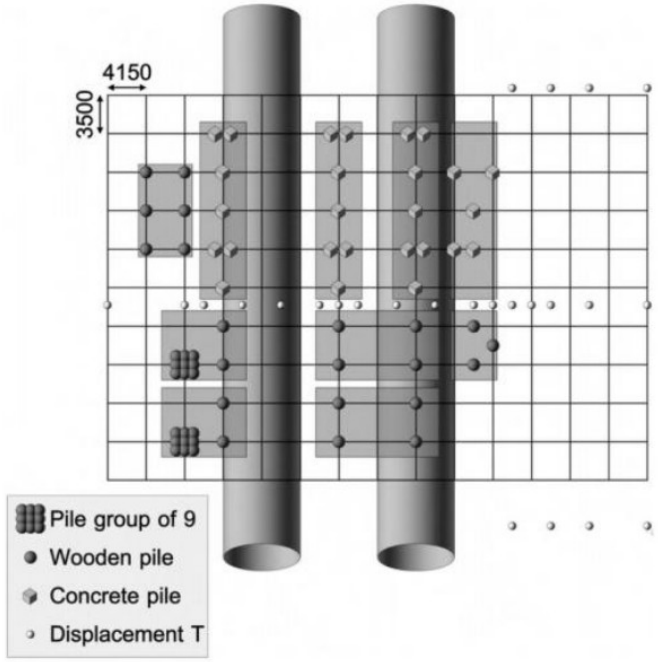

Fig. 2.20. Overview test field with two tunnel tubes (the left tube is drilled first; grid dimension is in mm; gray areas are loaded regions on pile foundations) (Kaalberg et al., 2005)

Selemetas (2006) carried out full-scale field trials to investigate the pile response to tunnelling in London Clay in the Channel Tunnel Rail Link (CTRL) project. The study involved the excavation of two parallel tunnels, each with a diameter of 8.15 m. These tunnels were bored at a depth of 19.5 m, using Earth Pressure Balance (EPB) shields with a spacing of 16 m. Four

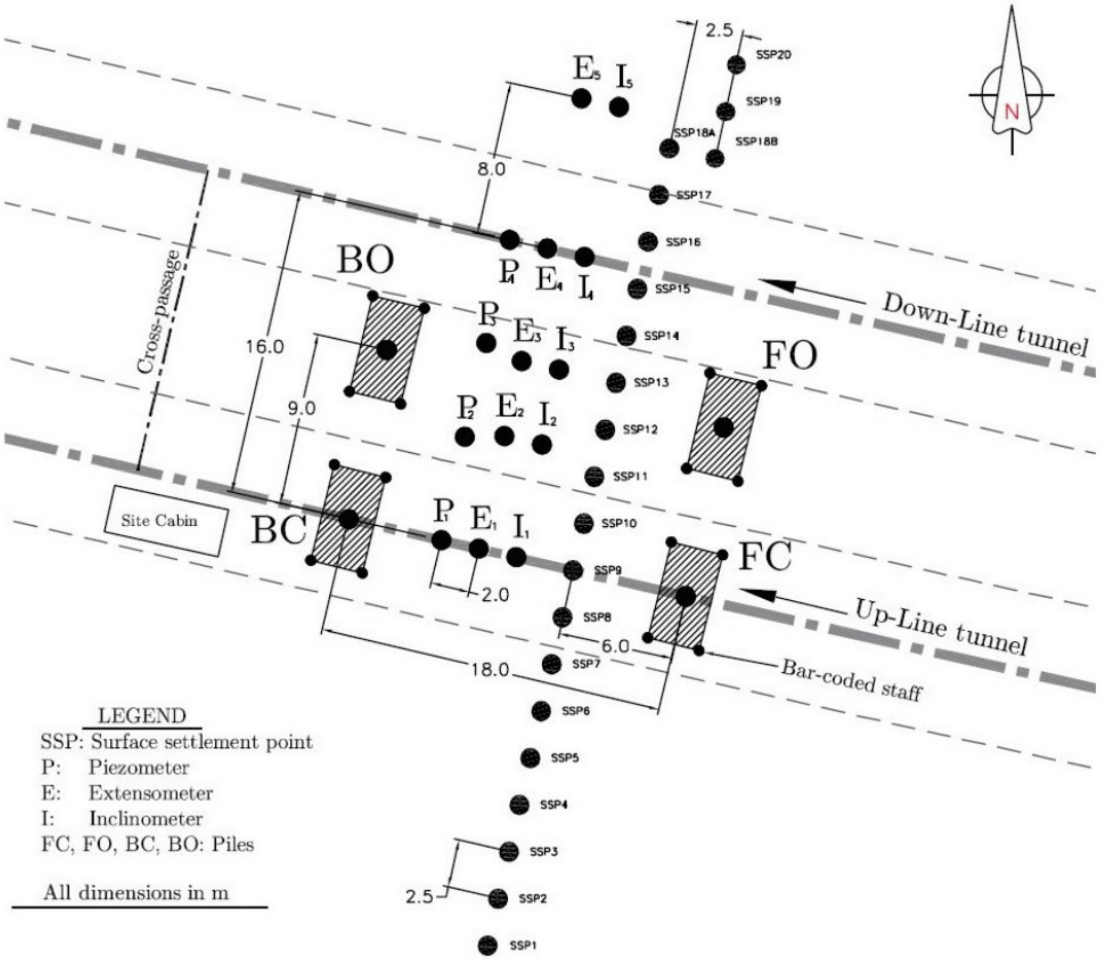

Fig. 2.21. Positions of piles and instrumentation in field trial (Selemetas, 2006)

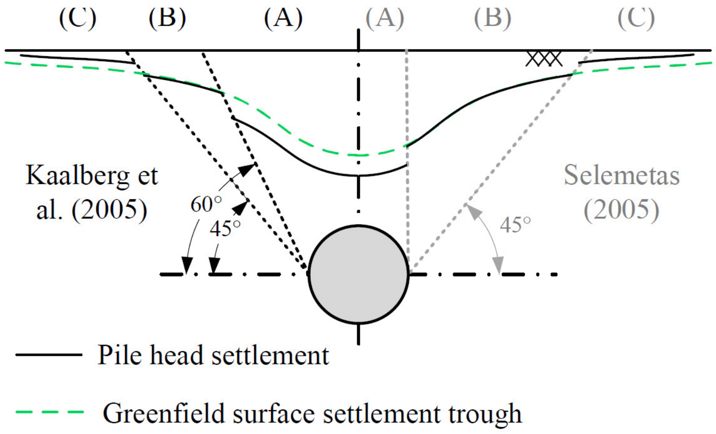

Fig. 2.22. Comparison of tunnelling influence zones in terms of pile settlement and greenfield surface settlements (Kaalberg et al., 2005; Selemetas, 2006), redrawn by Franza (2017)

driven-cast-in-situ piles were embedded at different depths (8.5 m depth, pile base in Terrace Gravels; 13 m depth, pile base in London Clay) and offsets from the tunnel longitudinal axis (pile directly above the tunnel; 9 m away from the tunnel). The piles were subjected to loading equivalent to half of their ultimate load capacity. The test layout is shown in Fig. 2.21.

Fig. 2.22 summarises the distribution of tunnelling-influence regions based on relationships between pile and ground surface settlements in the studies by Kaalberg et al. (2005) and Selemetas (2006). The delineation of influence areas exhibits similarities: when pile tips are located in Zone A (approximately directly above the tunnel), Zone B (adjacent to Zone A), and Zone C (further from the tunnel), the pile settlement is respectively greater than, similar to, and smaller than the greenfield surface settlement. Results from centrifuge testing by Jacobsz et al. (2004); Marshall and Mair (2011) align well with these distributions of tunnelling influence areas. However, Dias and Bezuijen (2015) pointed out that factors beyond the relative position of the tunnel and pile tip, such as pile working load, pile base load-to-shaft friction ratio, and tunnel volume loss, also influence the division of regions and warrant consideration.

2.2.3 Capped piles

Capped piles, also known as hybrid foundations, combine the characteristics of both piles and caps (i.e. beams or plates that are connected to pile heads, sometimes linking multiple piles, which are designed to distribute building loads to piles but typically do not cover the entire base of the buildings). Capped piles in which the caps are not in contact with the underlying soil are typically used for offshore platforms (Li et al., 2017; Wang et al., 2023), while those with caps in contact with the soil are employed to support structures such as buildings (Hussien et al., 2014; Liu et al., 2021), viaducts (for highways or railways) (Yuan et al., 2021; Tawadros et al., 2022), and embankments (Wang et al., 2018). Another somewhat similar foundation is the piled raft foundation, where piles and rafts work together (i.e. rafts contact soil) to support significant load and reduce differential settlement in buildings. Unlike the pile cap of capped piles, the rafts of piled raft foundations can cover the entire base of the buildings and are generally larger. In addition, because of the size of a piled raft, piles situated directly above a tunnel would be less susceptible to large settlements from tunnelling which would be required to mobilise significant additional earth pressure beneath the foundation - the loads would get "shed" to other piles within the raft in tunnelling scenarios. Although capped pile foundations and pile raft foundations have different focuses, their basic working principles are similar, for example assessing the load capacity and settlement response of a foundation composed of a single pile and a single cap or raft that contacts the soil (Poulos, 2001).

Lee and Chung (2005) conducted a series model tests in sand at 1 g (Figure 2.23), where piles were loaded vertically by a hydraulic jack at a constant rate of settlement of approximately 1 mm/min, to investigate the interaction among bearing components (i.e. pile and cap). The study found that the pile load capacity could be increased due to the superimposed densification of soil between neighbouring piles at the narrow spacing up to $3d_p$ compared with a single pile in Figure 2.23(a), and wider spacings of 4-$5d_p$ further enhanced the pile capacity through higher shaft friction. The pile capacity of capped piles was affected by pile location and spacing; notably, pile capacity increased remarkably at narrow spacings of 2-$3d_p$ and then decreased dramatically at wider spacings of 4-$5d_p$. Additionally, the pile cap of capped piles (Figure 2.23(e)) and single cap (Figure 2.23(c)) demonstrated similar mechanical behaviours, which might be attributed to installation errors.

Horikoshi and Randolph (1996) performed centrifuge tests at 100 g to examine the behaviour of capped piles in clay, as shown in Figure 2.24. The capacity of capped piles was significantly higher than uncapped piles due to the presence of a thin sand layer on top of the clay, and the load capacity of piles was higher when capped than uncapped presumably due to increased horizontal effective stress acting on the pile shaft. The authors reported that, for the capped pile compromised of one cap and nine piles, the different settlement of the pile cap was less than 30% of that of a single cap (or raft), and the piles were loaded to 70% of the capacity under the ultimate foundation load.

Wang et al. (2023) conducted 50-g centrifuge tests (see Figure 2.25) and complementary numerical modelling to investigate the influence of pile number, diameter, and loading height on the lateral capacity of pile groups (with piles being connected by a cap) for offshore wind turbines. The authors reported that the lateral capacity of pile groups was improved by increasing pile number and diameter, whereas the increasing loading height would weaken the capacity.

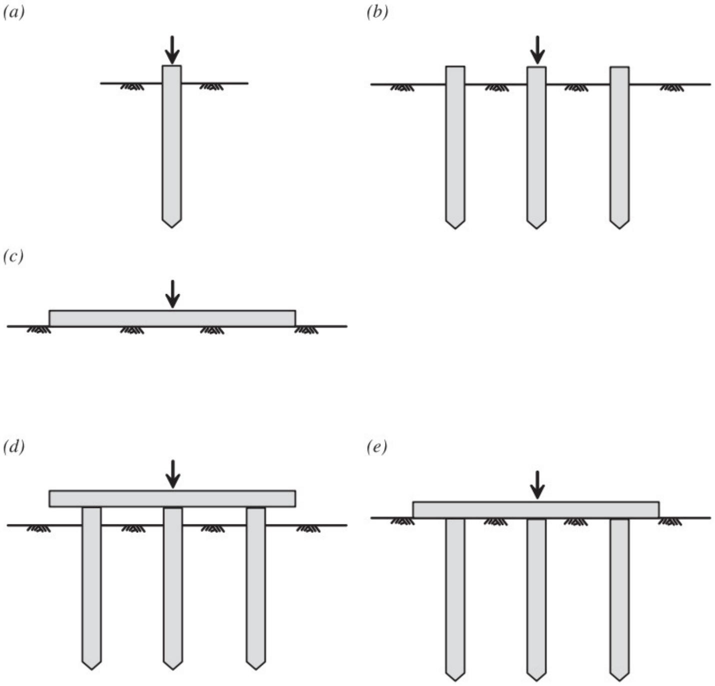

Fig. 2.23. Schematics of pile models: (a) single pile, (b) pile groups, (c) raft (cap), and (d)-(e) capped pile (cap away from/contacting the surface) (Lee and Chung, 2005)

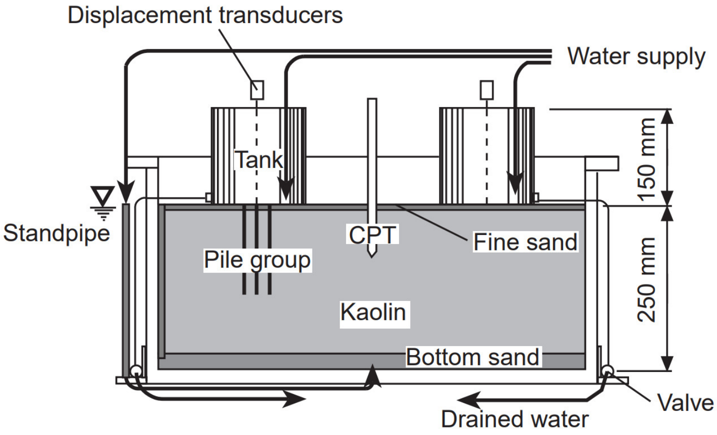

Fig. 2.24. General section of centrifuge package (Horikoshi and Randolph, 1996)

Leung et al. (2003) carried out 50-g centrifuge tests in dense sand to study the effect of deep excavations on capped piles (including free-head and capped-head pile groups consisting of two, four, and six piles), as illustrated in Figure 2.26. The results revealed that piles closer to the retaining wall would mitigate the adverse effect of soil movements on piles situated farther away. Pile caps would help to resist the soil lateral force by transferring the bending movement

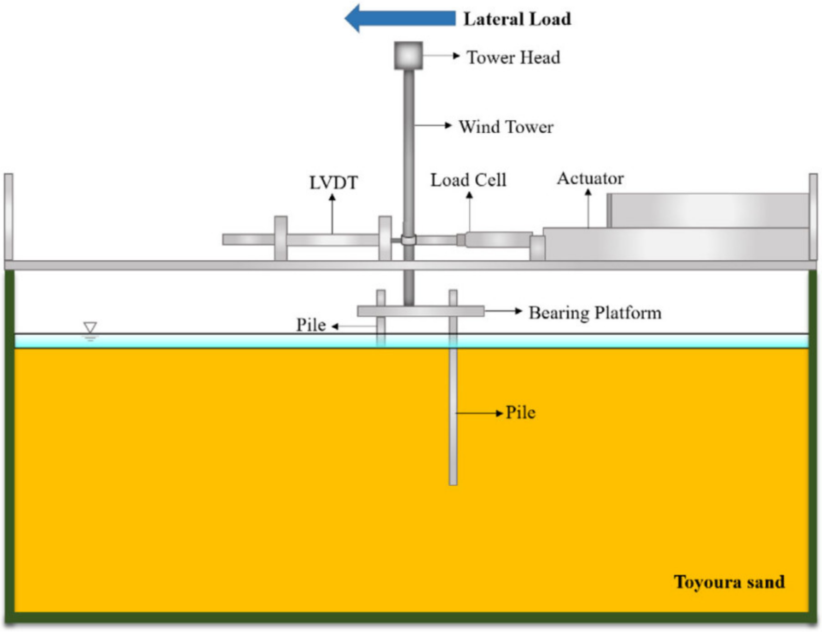

Fig. 2.25. Centrifuge test configuration of pile lateral response (Wang et al., 2023)

induced by soil movements from the closer piles to those further away.

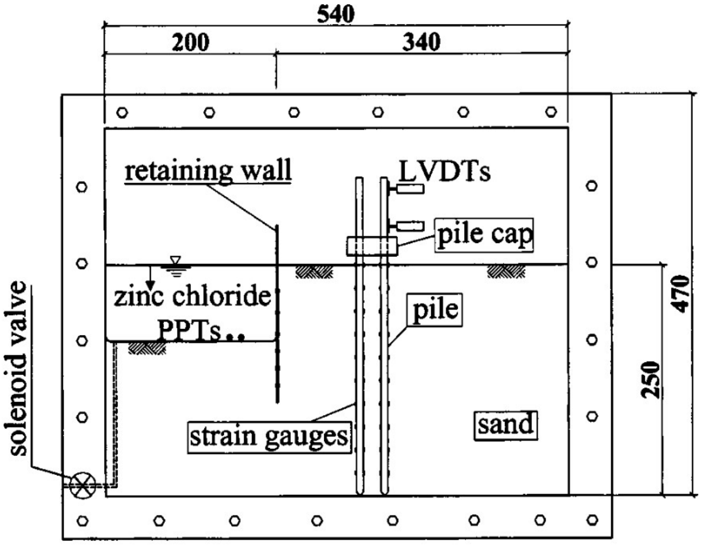

Fig. 2.26. Schematic centrifuge model setup (unit in mm) (Leung et al., 2003)

Field and experimental studies on the capacities and load transfer mechanisms of capped piles in tunnelling scenarios remain limited. As capped piles become more prevalent, it is essential to incorporate the role of pile caps into risk assessments for new tunnels nearby, thus understanding the interactions between tunnels, soil, and capped piles is particularly important. Specifically, investigating the behaviour of the capped piles consisting of a pile and a cap would provide valuable insights, currently lacking, for analyzing more complex scenarios involving tunnelling beneath or near pile groups connected through caps.

2.3 Tunnelling effects on buildings with shallow foundations

Tunnel excavation activities often disrupt adjacent soils, leading to ground movements that may further induce surface building deformations and, in certain cases, structural damage. Therefore, it is important to understand how buildings respond to the nearby tunnelling activities and to employ appropriate approaches to forecast building deformation behaviours, which is helpful in engineering design and maintenance and ultimately ensures the safety of both individuals and property.

2.3.1 Building deformation and damage

Camós et al. (2014) reported the structural response of a group of masonry buildings subjected to ground movements induced by the nearby construction of the L9 Metro tunnel in Barcelona, bored by an earth pressure balance (EPB) tunnel boring machine (TBM). The studied one-storey small dwellings represented a common building typology frequently used in those days in Barcelona's outskirts. The damage to the masonry buildings manifested in diagonal and vertical cracks, originating from the corners of window and door openings and extending to the exterior boundaries of the building (see Figure 2.27).

Farrell et al. (2014) carried out a series of geotechnical centrifuge modelling tests to investigate the interactions between tunnels and masonry buildings with fine dry Leighton Buzzard Fraction E sand. Various simplified building models were employed, including aluminium plates of different thicknesses (1.6 mm, 5 mm, 10 mm, and 20 mm, referred to as STR-1, STR-2 (see Figure 2.28), STR-3, and STR-4, respectively), as well as micro-concrete models and masonry models. Figure 2.29 presents the settlement profiles of the aluminium plates (STR-1-4, located on the surface directly above the tunnel) and greenfield surface at a tunnel volume loss

Fig. 2.27. Photographs of damage in buildings due to tunnelling (Camós et al., 2014)

of $V_{l,t}$ =2%. The results illustrate that the existence of buildings reduced the ground surface differential movements, with stiffer buildings (i.e. thicker aluminium plates, such as STR-4) exhibiting a more rigid response to tunnelling (characterised by the minimum deflection). Farrell et al. (2014) also reported that cracks occurred through the mortar in sagging zones at small tunnel volume loss ($V_{l,t}$ ≈1.1-1.5%), while cracks appeared through both mortar and bricks in hogging regions at larger tunnel volume loss ($V_{l,t}$ ≈4-5%) for the non-linear masonry building models (Figure 2.30).

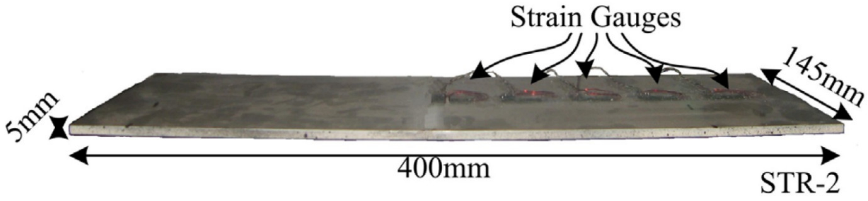

Fig. 2.28. Aluminium plate model with strain gauges (Farrell et al., 2014)

Ritter et al. (2017, 2020) reported a series of 75 g centrifuge test results of 3D printed building models on the surface when tunnelling in dry dense sand (Leighton Buzzard Fraction E silica sand, with a relative density of I_d =90%) with a cover-to-tunnel diameter ratio of $C/D_t = 1.35$. These building models, depicted in Figure 2.31, featured various tunnel eccentricity-to-building length ratios (e/L), building length-to-height ratios (L/H), and opening percentages (O), with

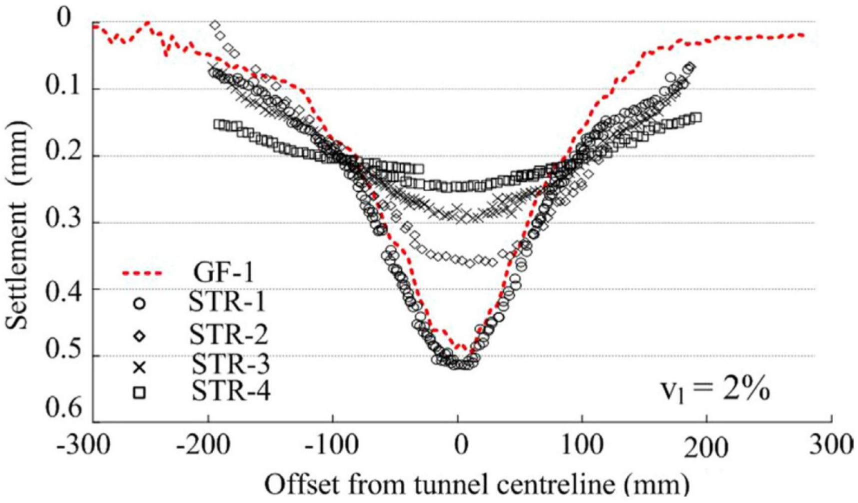

Fig. 2.29. Settlement profiles of the aluminium plate models (Farrell et al., 2014)

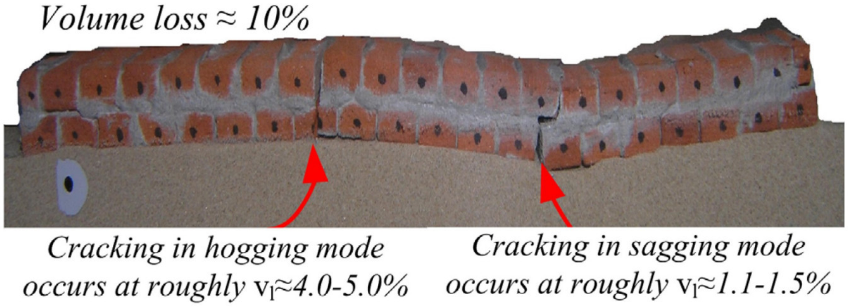

Fig. 2.30. Observed cracking of masonry model in centrifuge testing (Farrell et al., 2014)

powder-based 3D printing employed to create scaled-down structural models incorporating building details such as façade openings, strip footings, rough soil-structure interfaces, and intermediate walls at a scale of 1/75 of the prototype. Ritter et al. (2017) found the existence of buildings altered ground deformation characteristics, such as widening the soil settlement trough and restraining the horizontal surface displacement, consistent with the centrifuge test results reported by Farrell et al. (2014) (Figure 2.29). Figure 2.32 illustrates the positions of crack propagations within the buildings and the corresponding tunnel volume loss at the onset of visible cracking. Similar patterns emerged, with cracks initiating at the top of the building models and vertically propagating toward the base. Buildings spanning both the greenfield hogging and sagging regions with significant window openings (i.e., 40%) exhibited heightened susceptibility to cracking damage (Figure 2.32(f)). These results underscore, for buildings

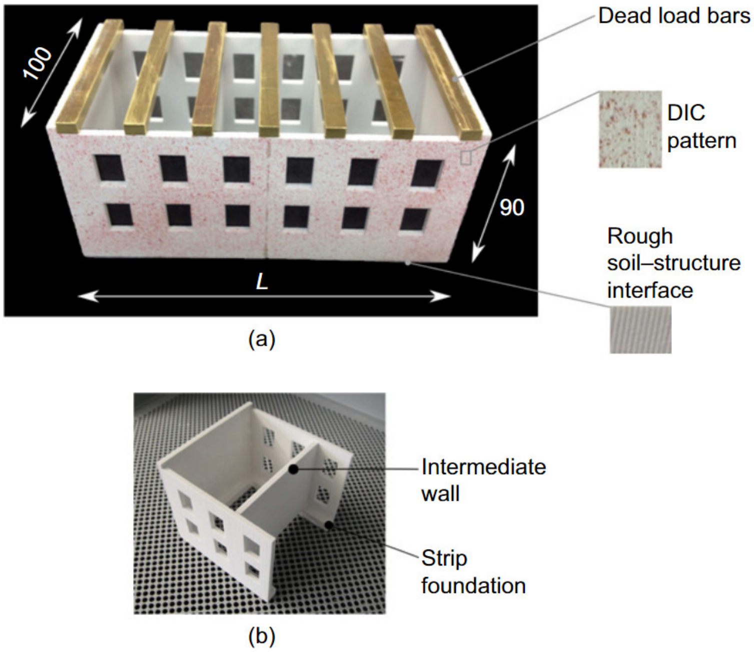

Fig. 2.31. 3D printed building model (dimensions in mm) (Ritter et al., 2017)

(a) e/L=0, L/H=2.2, O=20% (b) e/L=0.8, L/H=2.2, O=20%

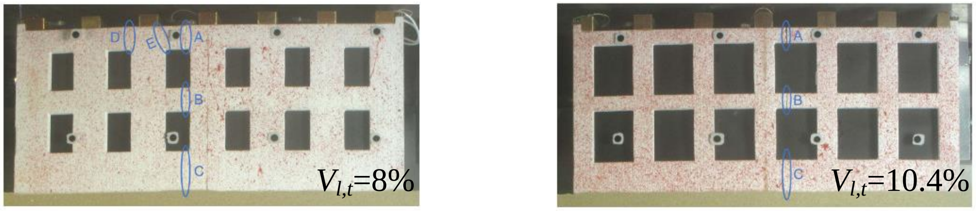

(c) e/L=0.5, L/H=2.2, O=20% (d) e/L=0.8, L/H=2.2, O=40%

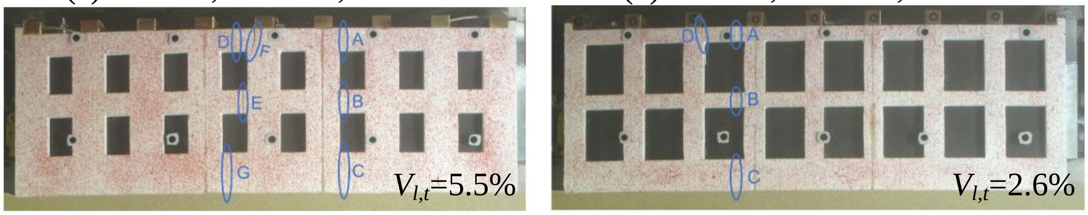

(e) e/L=0.5, L/H=2.9, O=20% (f) e/L=0.5, L/H=2.9, O=40%

Fig. 2.32. Cracking positions (letters indicate order of crack propagation) and the tunnel volume loss when visible cracking appears (Ritter et al., 2020)

spanning both sagging and hogging regions, the importance of considering the effect of the building sagging aspect when evaluating building damage in hogging regions during tunnelling activities (because the widely accepted assessment framework divides buildings into individual sagging and hogging parts that may lead to an underestimation of the hogging damage, despite the sagging damage assessment being reasonable).

2.3.2 Global building damage assessment

Determining the levels of building damage is crucial for risk assessment. Yet, relying solely on macroscopic qualitative or semi-quantitative descriptions of observable deformations, such as building settlement and cracks, may fall short in accurately evaluating building damage. The complex characteristics inherent in buildings (such as structural features, material properties) compound these challenges in defining and classifying damage levels. Consequently, researchers have explored various building deformation parameters to more effectively assess the severity of damage of buildings.

2.3.2.1 Sagging and hogging deformation parameters

According to the settlement troughs along the building base, the entire building can be characterized into sagging and/or hogging zones, and the corresponding main parameters are as follows (defined by Burland et al. (1977); see Figure 2.33):

- Settlement S_v indicates the vertical displacement of the building;
- Differential settlement ΔS_v represents the relative settlement between two points;
- Slope s denotes the slope of a straight line connecting two points;
- Relative deflection Δ is determined by the maximum settlement concerning a straight line connecting two points;
- Deflection ratio $DR = \Delta / L$ represents the ratio of the relative deflection between two points Δ and the corresponding initial (horizontal) distance (such as L);

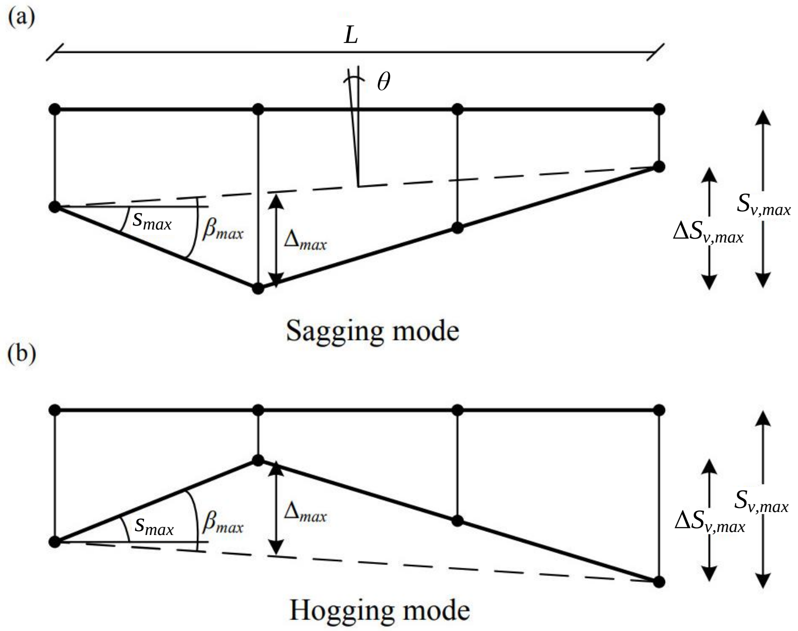

Fig. 2.33. Building deformation parameters in (a) sagging and (b) hogging regions (Burland et al., 1977; Franza, 2017)

- Tilt θ describes the rigid body rotation of the building;
- Angular distortion β is the rotation of a line joining two points relative to building tilt θ.

2.3.2.2 Empirical damage criteria

Polshin and Tokar (1957) adopted deflection ratio DR to evaluate the limit states before damage within plain brick walls under different length-to-height ratios (L/H) and soil conditions. Specifically, for walls with $L/H \leq 3$, the criteria were $DR < 0.0003$ for sand and hard clay and $DR < 0.0004$ for soft clay; for walls with $L/H \geq 5$, the limits were $DR < 0.0005$ for sand and hard clay and $DR < 0.0007$ for soft clay. The authors also suggested maximum slopes of 0.002 for steel and reinforced concrete frame structures in sand and hard/soft clays, and 0.007 and 0.001 for end rows of columns with brick cladding in sand/hard clay and soft clay, respectively.

While these empirical criteria offer a valuable framework for assessing building damage levels, it is essential to recognize that they only consider the effect of building self-weight (Burland and Wroth, 1974; Rankin, 1988). This limitation means that these empirical criteria might not reliably predict building damage induced by tunnel excavations, as the dynamic conditions of tunnelling scenarios can vary significantly.

2.3.2.3 Tensile strain approaches

Tensile strains are considered for building risk assessment. Burland and Wroth (1974) and Polshin and Tokar (1957) suggested the critical tensile strain range of 0.0005 and 0.00075 corresponding to very slight damage, marked by the onset of visible cracking of buildings. Boscardin and Cording (1989) extended this work by relating critical tensile strains to various degrees of building damage, summarized in Table 2.1. Mair et al. (1996) also supported the important link between tensile strains and potential damage categories, however, the authors pointed out that none of the cases provided by Boscardin and Cording (1989) indicated that tensile strains of ≤ 0.003 would result in severe damage and suggested the tensile strain range of 0.0015-0.003 should represent moderate damage (category 3).

Table 2.1. Damage category and limiting tensile strain (after Boscardin and Cording (1989))

Category of damage	Degree of severity	Limiting tensile strain (%)
0	Negligible	0-0.05
1	Very slight	0.05-0.075
2	Slight	0.075-0.15
3-4	Moderate to severe	0.15-0.3
4-5	Severe to very severe	> 0.3

Burland et al. (1977) simplified buildings as a simply supported beam with linear, elastic, and weightless properties, and the possible modes of deformation and cracking are shown in Figure 2.34. The authors related the maximum bending strain $\varepsilon_{b,max}$ and diagonal strain $\varepsilon_{d,max}$ to deflection ratio DR through the Timoshenko beam theory (Timoshenko, 1955), given as:

$$DR = \frac{L}{12h_{axis}}\left(1+\frac{18EI}{L^2HG}\right)\varepsilon_{b,max} \tag{2.19}$$

$$DR = \left(1+\frac{L^2HG}{18EI}\right)\varepsilon_{d,max} \tag{2.20}$$

where E is Young's modulus, G is shear modulus, I is the second moment of area of the equivalent beam, and h_{axis} is the location of the neutral axis. The neutral axis is typically assumed in the middle of the 'isotropic beam' (i.e. $h_{axis} = H/2$), however Burland and Wroth (1974) and

Burland et al. (1977) reported that, in brick wall model tests and field observations, it may be more realistic to take the neutral axis at the foundation level (i.e. $h_{axis} = H$) due to the significant restraint of raft foundations or in cases subjected to hogging with weak bending behaviours compared with shear response (e.g. $E/G = 0.5$).

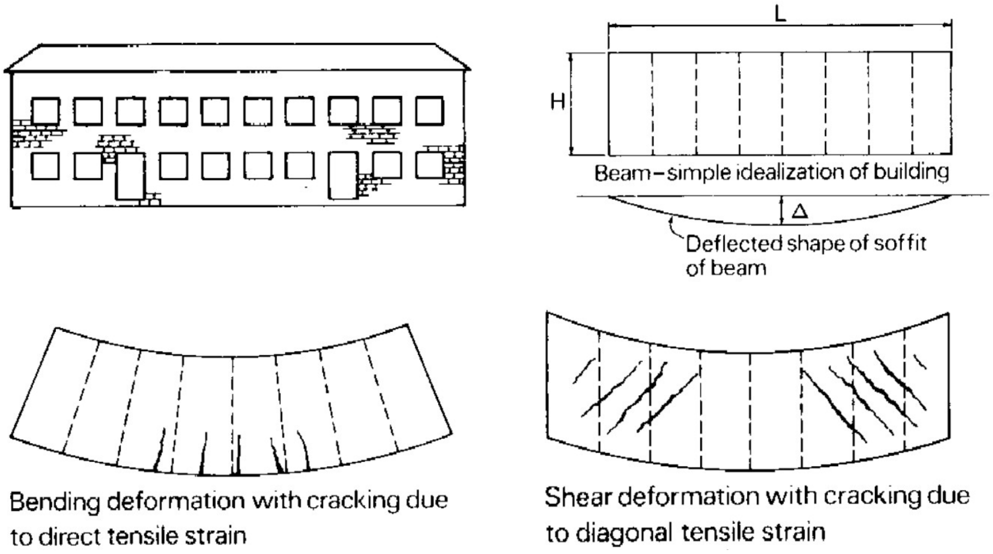

Bending deformation with cracking due to direct tensile strain

Shear deformation with cracking due to diagonal tensile strain

Fig. 2.34. Bending and shear deformation with cracks for idealised beam (Burland et al., 1977)

Macroscopic building deformation modes are closely related to the inherent damage mechanisms of the buildings. Figure 2.34 illustrates pure bending deformation of the building with vertical cracks induced by direct tensile strains, and pure shear deformation of the building with cracks in the diagonal direction induced by diagonal tensile strains. The predominant types of deformation of buildings are related to building length-to-height ratio L/H, Young's modulus-to-shear modulus ratio E/G, and the positions of the neutral axis (Burland and Wroth, 1974; Burland et al., 1977). Long buildings (with large L/H) are more prone to direct tensile strains, whereas short buildings (with small L/H) are more susceptible to diagonal tensile strains. For masonry buildings, E/G is typically equal to 2.6 (i.e. Possion's ratio $\nu = 0.3$) based on the assumption of isotropic behaviour, and E/G should be increased to 12.5 or higher for buildings with a low shear stiffness (such as masonry buildings with larger openings and framed buildings) to recognize anisotropic behaviour (Burland and Wroth, 1974; Cook, 1994; Mair et al., 1996; Son and Cording, 2007).

Apart from the settlement-induced damage, horizontal ground strains due to tunnel constructions may also contribute to potential building damage (Boscardin and Cording, 1989; Mair et al., 1996; Geddes, 1991). The average horizontal strain is given by $\varepsilon_h = \Delta L/L$, thus the critical tensile strain due to bending $\varepsilon_{crit,b}$ is given by the superposition of bending $\varepsilon_{b,max}$ and horizontal ε_h strains (Boscardin and Cording, 1989):

$$\varepsilon_{crit,b} = \varepsilon_{b,max} + \varepsilon_h \tag{2.21}$$

For the case of diagonal tension with horizontal extension, the tension strain ε_θ, at an angle θ from the horizontal direction can be given:

$$\varepsilon_\theta = \varepsilon_h \cos^2\theta + 2\varepsilon_{d,max}\cos\theta \sin\theta \tag{2.22}$$

The maximum value of ε_θ (i.e. $\varepsilon_{crit,d}$), is given by:

$$\varepsilon_{crit,d} = \varepsilon_{\theta,max} = \varepsilon_h \cos^2\theta_{max} + 2\varepsilon_{d,max}\cos\theta_{max} \sin\theta_{max} \tag{2.23}$$

where θ_{max} is the direction of crack formation and the angle of the plane where $\varepsilon_{crit,d}$ acts. Son and Cording (2005) proposed substituting β for $2\varepsilon_{d,max}$ and $\tan(2\theta_{max}) = \beta/\varepsilon_h$. If $\beta = 0$, $\varepsilon_{crit} = \varepsilon_h$ acts on the vertical plane ($\theta_{max} = 0$) and vertical cracks form; if $\varepsilon_h = 0$, $\varepsilon_{crit,d} = \beta/2$ acts on the plane at $\theta_{max} = 45°$ and cracks develop following 45° planes. This is a semiempirical criterion based on both strain theory and field observations. The critical tensile strains corresponding to various degrees of damage based on data from field observations, physical model tests, and numerical parametric studies are summarised in Figure 2.35.

Alternatively, Mair et al. (1996) reported the maximum diagonal strain $\varepsilon_{crit,d}$ using Mohr's circle of strain with a Poisson's ratio of $\nu = 0.3$ as follows:

$$\varepsilon_{crit,d} = 0.35\varepsilon_h + \sqrt{(0.65\varepsilon_h)^2 + \varepsilon_d^2} \tag{2.24}$$

Mair et al. (1996) proposed a procedure for preliminary risk assessment of buildings above tunnels based on the assumptions of plane strain conditions, where the building-foundation system is represented as an equivalent linear elastic beam and the building is divided into inde-

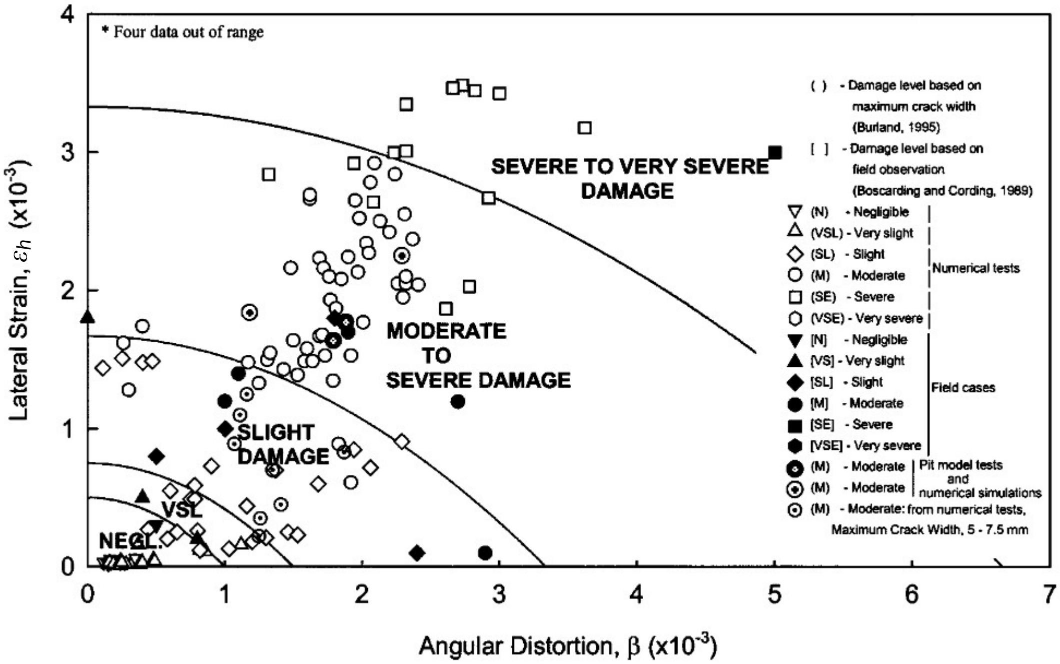

Fig. 2.35. Building damage estimation criterion and damage levels from field observations, physical model tests, and numerical parametric studies (Son and Cording, 2005)

pendent parts according to the greenfield sagging and hogging zones. This assessment method consists of the following three steps (summarised in Figure 2.36):

1. In the initial assessment, the greenfield surface profile is fitted by a Gaussian curve. Cases experiencing deformations with a maximum rotation greater than 1/500 or settlement over 10 mm are flagged as at risk and require the second risk assessment step. Tunnel-building interactions are not considered in the first step and thus the results might be conservative.

2. For the buildings identified as at risk from the first step of assessment, the building base is constrained to displace by imposing the greenfield surface settlement profile (i.e. a fitted Gaussian curve) and the maximum tensile strain of the buildings ($\varepsilon_{max} = \max(\varepsilon_{crit,b/d})$) can be calculated through Eqs. 2.21 and 2.24. Subsequently, damage levels are determined by comparisons between the maximum tensile strain ε_{max} and the classification of damage degrees of buildings in Table 2.1. If the resulting damage category is moderate or higher (category ≥ 3), the third step is needed for further assessment. Again, the second step might overestimate building damage levels due to the oversight of contributions from

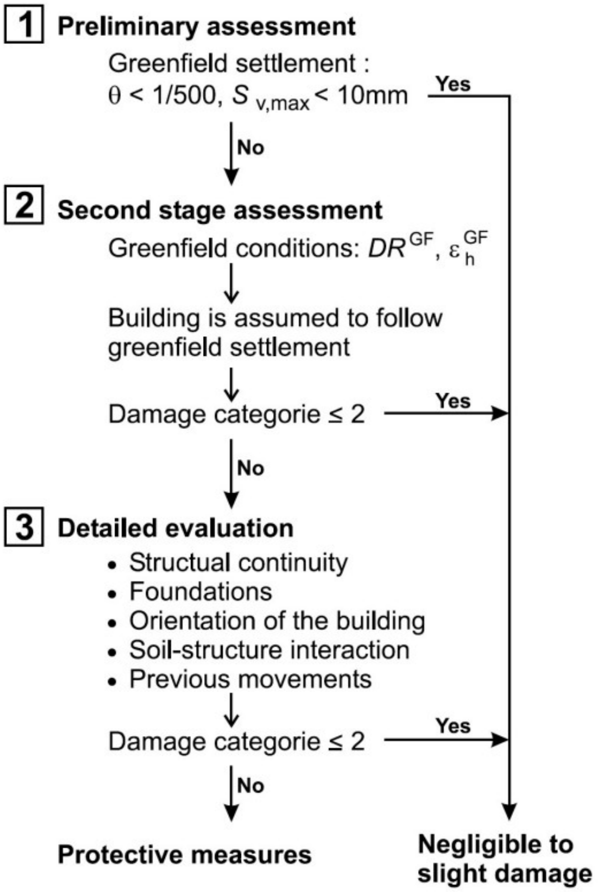

Fig. 2.36. Framework of building damage assessment (Mair et al., 1996; Franzius, 2003)

building stiffness and self-weight in reducing building deformation.

3. For the buildings with a risk level ≥ 3 from the second step of assessment, a more detailed evaluation should be carried out considering the soil-structure interaction and 3D geometries of structures and tunnels. This may result in a lower damage level compared to step 2.

The evaluation results help guide decision-making regarding the necessity and extent of protective measures required for buildings under the influence of tunnelling.

2.3.2.4 Modification factor methods

Potts and Addenbrooke (1997) introduced a modification factor method to establish a correlation between the tunnelling-induced building deformations and the corresponding greenfield surface movement caused by tunnelling activities through a parametric study involving plane-strain numerical analyses. Detailed parameters are shown in Figure 2.37, where the buildings in hogging and sagging zones are presumed to be independent. The deflection ratio modification factors in sagging and hogging regions ($M^{DR,sag}$, $M^{DR,hog}$) are determined based on the corresponding maximum deflection ratios of building settlement profiles ($DR_{sag,Bldg} = \Delta_{sag,Bldg}/L_{sag,Bldg}$, $DR_{hog,Bldg} = \Delta_{hog,Bldg}/L_{hog,Bldg}$) and greenfield surface settlement trough ($DR_{sag,GF} = \Delta_{sag,GF}/L_{sag,GF}$, $DR_{hog,GF} = \Delta_{hog,GF}/L_{hog,GF}$):

$$\begin{aligned} M^{DR,sag} &= \frac{DR_{sag,Bldg}}{DR_{sag,GF}} \\ M^{DR,hog} &= \frac{DR_{hog,Bldg}}{DR_{hog,GF}} \end{aligned} \tag{2.25}$$

The spans of sagging/hogging zones of buildings were assumed to be equal to those of corresponding greenfield surface conditions ($L_{sag,Bldg} = L_{sag,GF}$, $L_{hog,Bldg} = L_{shog,GF}$) (Potts and Addenbrooke, 1997; Goh and Mair, 2011; Mair, 2013). However, Franza et al. (2020b) suggested using actual spans of buildings, as illustrated in Figure 2.37 to acquire a narrower or more concentrated region of data in Eqs. 2.25 and 2.29.

A similar way of modification factors can be applied to the maximum horizontal tensile and compressive strains of the buildings ($M^{\varepsilon h,t}$, $M^{\varepsilon h,c}$), calculated by the maximum horizontal building strains ($\varepsilon_{h,t,Bldg}$, $\varepsilon_{h,c,Bldg}$) and the corresponding maximum horizontal greenfield surface strains ($\varepsilon_{h,t,GF}$, $\varepsilon_{h,c,GF}$) (Potts and Addenbrooke, 1997):

$$\begin{aligned} M^{\varepsilon h,t} &= \frac{\varepsilon_{h,t,Bldg}}{\varepsilon_{h,t,GF}} \\ M^{\varepsilon h,c} &= \frac{\varepsilon_{h,c,Bldg}}{\varepsilon_{h,c,GF}} \end{aligned} \tag{2.26}$$

To evaluate the impact of changes in building stiffness and soil stiffness during tunnelling on building deformations, Potts and Addenbrooke (1997) defined relative structure-to-soil bending stiffness ρ^* and relative building-to-soil axial stiffness α^*:

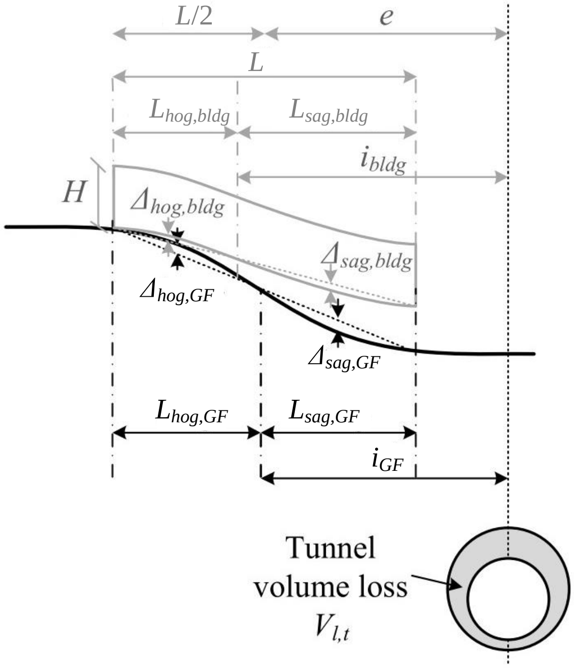

Fig. 2.37. Definition of sagging and hogging parameters in tunnel-building scenarios (Franza, 2017)

$$\begin{aligned} \rho^* &= \frac{EI}{E_s\,(L/2)^4} \\ \alpha^* &= \frac{EA}{E_s\,(L/2)} \end{aligned} \tag{2.27}$$

where L is the building length, EI is the building bending stiffness, EA is the building axial stiffness, and E_s is the representative soil stiffness at a depth of $z_t/2$ (z_t is tunnel axis depth) that is estimated by the soil secant stiffness at 0.01% axial strain in triaxial compression tests. The relative bending stiffness ρ^* has a dimension of m^{-1} and the relative axial stiffness α^* is dimensionless under plane strain conditions. The definitions of ρ^* and α^* are similar to those adopted by Fraser and Wardle (1976); Boscardin and Cording (1989); Potts and Bond (1994).

Figure 2.38 illustrates an example of design curves regarding relative bending stiffness-deflection ratio modification factor (ρ^*-$M^{DR,sag/hog}$) and relative axial stiffness-maximum horizontal strain (α^*-$M^{\varepsilon h,c/t}$). These design curves can be used for modifying deflection ratio or horizontal strain, thus serving for risk assessment (i.e. the second step in Figure 2.36).

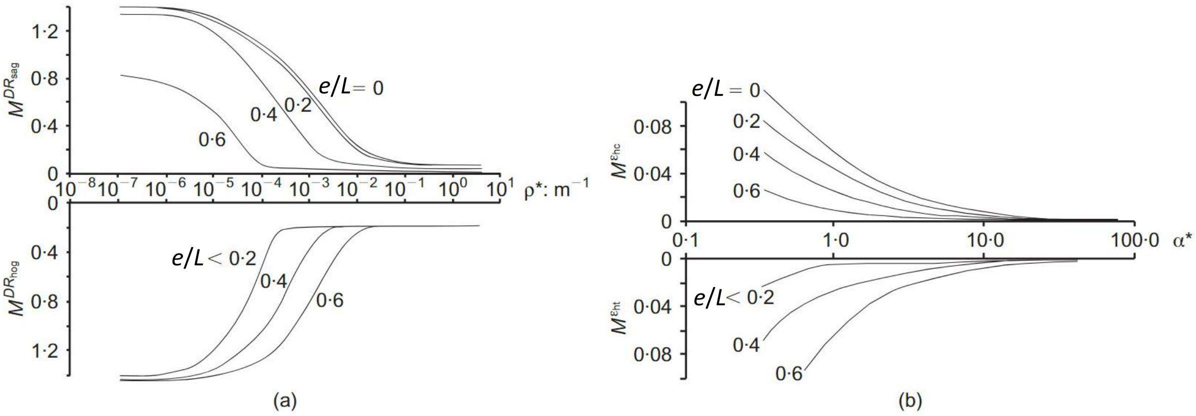

Fig. 2.38. Design curves for modification factors of (a) deflection ratio and (b) maximum horizontal strain (Franzius et al., 2006)

Eq. 2.27 only considers the building transverse length L, however, the effects of other factors such as tunnel depth z_t and building longitudinal length l are overlooked. To address this limitation, Franzius et al. (2006) extended Eq. 2.27 to obtain a more universal definition, given as:

$$\begin{aligned} \rho^*_{mod} &= \frac{EI}{E_s z_t L^2 l} \\ \alpha^*_{mod} &= \frac{EA}{E_s L l} \end{aligned} \tag{2.28}$$

where both ρ^*_{mod} and α^*_{mod} are dimensionless. Franzius et al. (2006) pointed out that the use of L, which is more consistent with expressing the degree of eccentricity e/L, replacing $L/2$ has no implication for the relative position of the results to each other when plotting against a logarithmic scale of relative stiffness.

To further generalise the design chart suggested by Franzius et al. (2006) and reduce level of scatter, Farrell (2011) and Goh and Mair (2011) proposed the following modified equations of relative bending stiffness:

$$\rho_{sag} = \frac{EI}{E_s L_{sag}^3 l} = \frac{EI^*}{E_s L_{sag}^3}$$
$$\rho_{hog} = \frac{EI}{E_s L_{hog}^3 l} = \frac{EI^*}{E_s L_{hog}^3} \tag{2.29}$$

where EI^* is the bending stiffness of the building per running metre (along the tunnel axis direction), and L_{sag} and L_{hog} are the building lengths in sagging and hogging zones of greenfield conditions, respectively. The tunnel depth z_t is not considered in Eq. 2.29. The findings presented by Mair (2013) demonstrate a clear relationship between the relative bending stiffness and the building deflection ratio modification factor ($\rho_{sag/hog}$-$M^{DR,sag/hog}$) for field cases, as depicted in Figure 2.39. Notably, higher relative bending stiffness correlates with lower modification factors, whereas lower relative bending stiffness is associated with higher modification factors. Based on these observations, Mair (2013) proposed envelopes to encapsulate these data points (also applicable to centrifuge testing and numerical results (Potts and Addenbrooke, 1997; Franzius et al., 2006; Goh and Mair, 2011)).

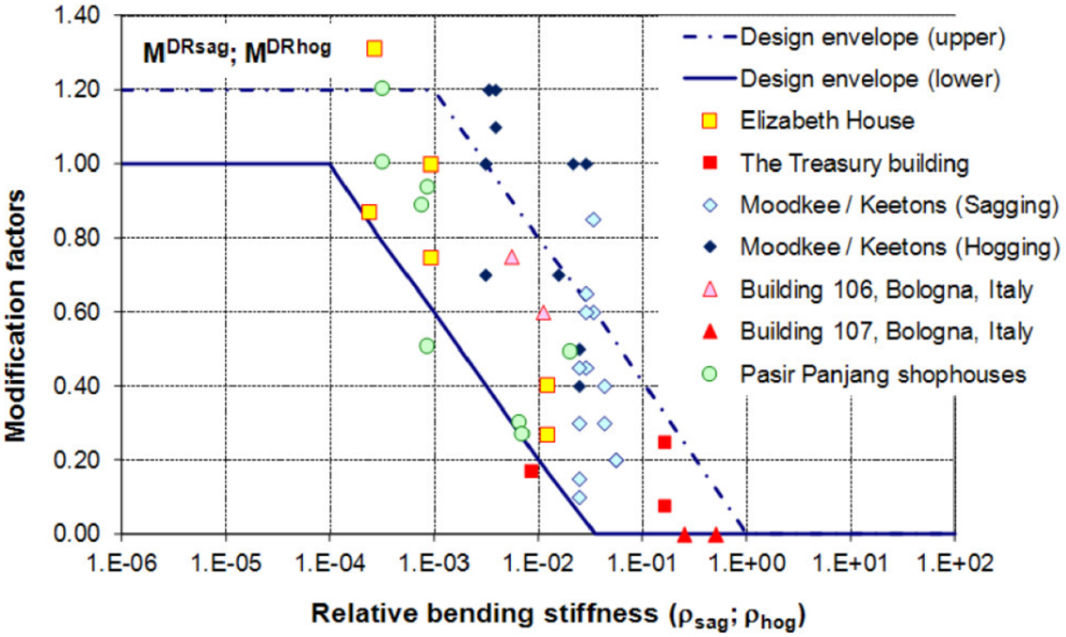

Fig. 2.39. Field data of building deflection ratio modification factor-relative bending stiffness (Mair, 2013)

The assumption or simplification of buildings as pure bending beams might lead to problematic results when ignoring the localised shear behaviours within the buildings induced by tunnel excavations. To account for the effect of building shear behaviours, Pickhaver et al. (2010) and Finno et al. (2005) suggested modelling buildings using equivalent Timoshenko beams and laminated beams. Franza et al. (2020a) modified the calculation of the relative building-to-soil bending stiffness ($\rho_{sag/hog}$ in Eq. 2.29) considering building shear stiffness GA_s based on the assumption of a simply supported Timoshenko beam, expressed as:

$$\begin{aligned} \eta_{sag/hog} = \frac{\rho_{sag/hog}}{1 + aF_{sag/hog}} &= \frac{EI^*}{E_s L^3_{sag/hog}(1 + aF_{sag/hog})} \\ F_{sag/hog} &= \frac{EI}{L^2_{sag/hog,GF} GA_s} \end{aligned} \tag{2.30}$$

where $aF_{sag/hog} = \delta_{shear}/\delta_{bending}$ is the ratio of shear deflection (δ_{shear}) to bending deflection ($\delta_{bending}$), $F_{sag/hog}$ is dimensionless, and the coefficient a is determined solely by loading conditions (a = 12 for a central concentrated load, a = 9.6 for a uniform load). In general, $F_{sag/hog} < 1/25$ represents bending-dominated behaviour, $F_{sag/hog} > 1$ indicates shear-dominated behaviour, and $1/25 < F_{sag/hog} < 1$ signifies mixed bending and shear responses.

To enhance the applicability of the EI^* to describe tunnelling-induced deformations of buildings with raft and strip foundations, Franza et al. (2020b) suggested:

$$EI^* = \frac{EI}{\chi l} \tag{2.31}$$

where χ is the ratio of the foundation bottom area to the wall bottom area, $\chi = 1$ for raft foundations and $\chi < 1$ for strip foundations.

2.3.3 Localised building damage assessment

Unlike the global building damage assessments, which primarily consider the bending deformations of the entire building during tunnel excavation activities, local evaluation methods focus on assessing damage in specific areas of the building, placing particular emphasis on the effects of local shear behaviours within buildings.

2.3.3.1 Bay deformation parameters

Buildings can be subdivided into bays (i.e. building units) according to their structural characteristics for localised assessments (refer to Figure 2.42(a)-(b)). Figure 2.40 presents a building unit with the horizontal S_h and vertical S_v displacements of the corners, the height H, and the length L_u. Based on this information, the following bay deformation parameters can be calculated (Son and Cording, 2005; Ritter et al., 2020):

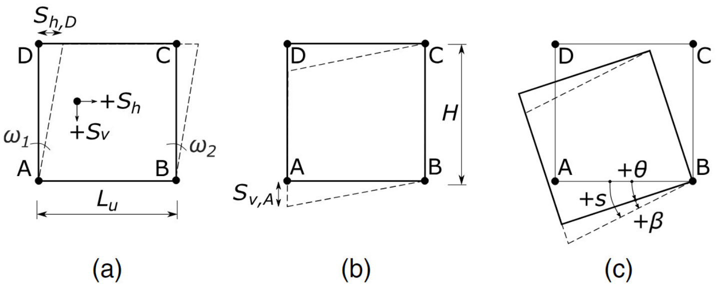

Fig. 2.40. Building bay deformation parameters (Ritter et al., 2020)

- Base horizontal strain $\varepsilon_{h,base} = \left(S_{h,B} - S_{h,A}\right) / L_u$;
- Top horizontal strain $\varepsilon_{h,top} = \left(S_{h,C} - S_{h,D}\right) / L_u$;
- Slope $s = \left(S_{v,A} - S_{v,B}\right) / L_u$;
- Tilt $\theta = \left((S_{h,A} - S_{h,D}) - (S_{h,B} - S_{h,C})\right) / (2H)$;
- Angular distortion $\beta = s - \theta$.

Ritter et al. (2020) suggested this calculation approach can be applied for estimating both entire buildings (using the displacements of the corner points) and localised building units. However, applying this approach to entire structures might oversimplify complex local behaviours (which may be problematic), despite its potential for more suitable application in localised architectural contexts.

Skempton and MacDonald (1956) utilized angular distortion β (with an assumption of no tilt of bays, i.e. $\theta = 0$, thus $\beta = s$ in Figure 2.40(c)) to assess the extent of building damage. The authors summarised data from ninety-eight buildings (among which fifty-eight suffered no damage and forty were damaged) and proposed the threshold values indicative of building damage: cracking happens in walls and partitions when $\beta > 1/300$, particularly sensitive brick structures experience cracking when $\beta > 1/1000$, and structural damage is evident when $\beta > 1/150$.

Cook (1994) introduced a method to distinguish tilt, bending, and shear displacements and deformations of a building unit based on the total vertical displacement $S_{v,tot} = (S_{v,A} - S_{v,B})$. Figure 2.41 presents the sign convention and tilt and bending deformation, and the calculations are as follows:

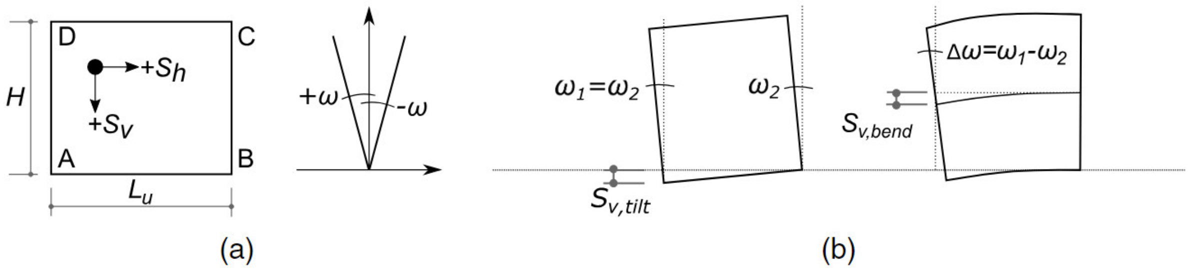

Fig. 2.41. Building deformations: (a) reference condition; and (b) tilt and bending deformations (Cook, 1994; Ritter et al., 2020)

- Tilt displacement $S_{v,tilt} = \omega_2 L_u$;
- Bending displacement $S_{v,bend} = \chi L_u^2/2 = (\omega_1 - \omega_2)L_u/2$, where χ is average curvature;
- Shear displacement $S_{v,shear} = S_{v,tot} - S_{v,tilt} - S_{v,bend}$;
- Shear strain $\gamma = S_{v,shear}/L_u = s - (\omega_1 + \omega_2)/2$, note that γ equals angular distortion β.

Ritter et al. (2020) distinguished bay bending and shear deflections in centrifuge modelling tests. The results, depicted in Figure 2.42, revealed that the greater building transverse length increases the bending deflections, with minimal impact on shear deflections, and larger opening areas tend to increase the building shear deflections rather than bending deflections.

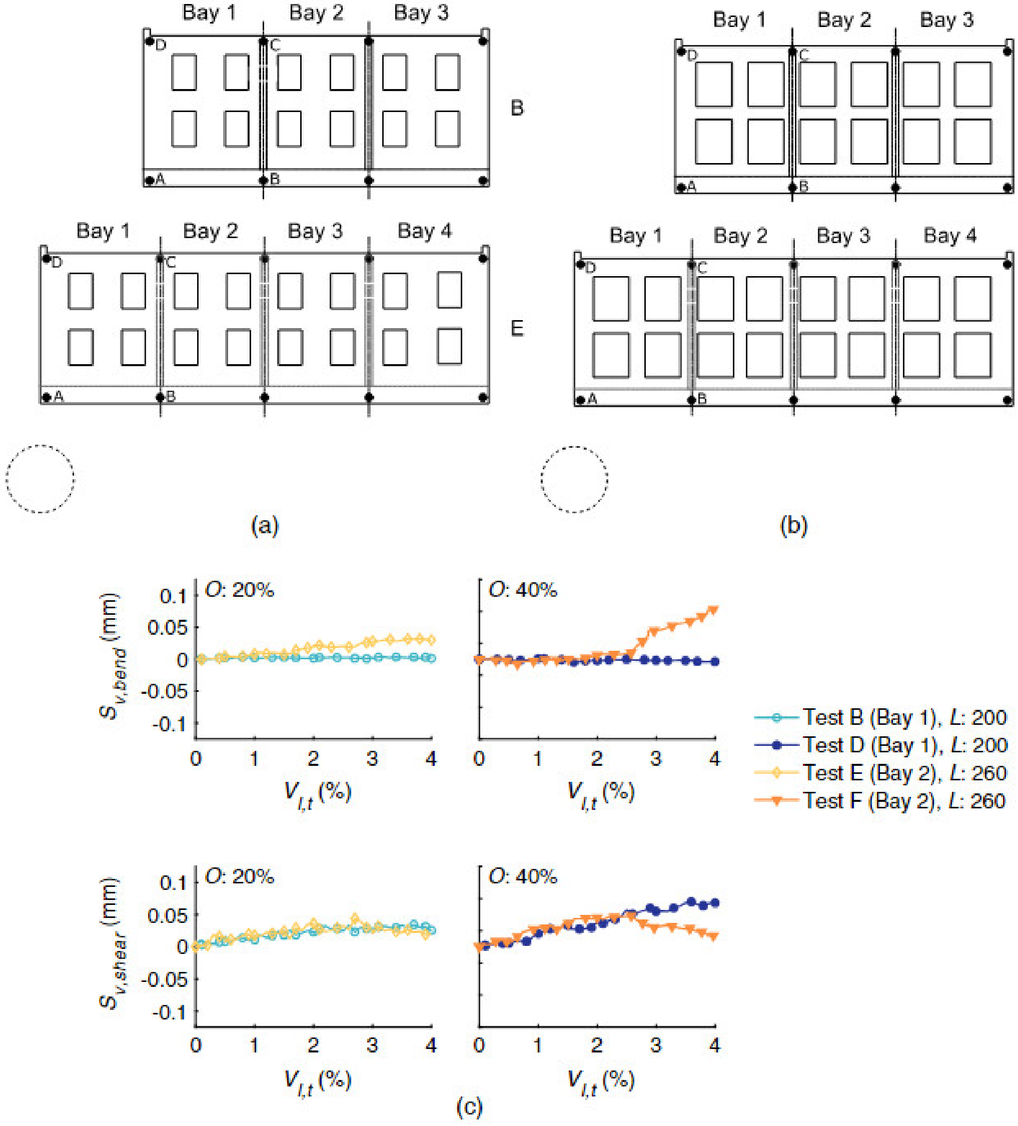

Fig. 2.42. Effect of length-to-height and opening percentage on bending and shear settlements (Ritter et al., 2020)

Boone (1996) and Elkayam and Klar (2019) also looked at distinguishing the panel distortions. For example, Elkayam and Klar (2019) described the in-plane horizontal and vertical displacements of a building unit, excluding bending, as follows:

$$\begin{aligned} \delta_x &= S_{h,A} + \left(S_{h,B} - S_{h,A}\right)\frac{x}{L_u} + \left(S_{h,D} - S_{h,A}\right)\frac{y}{H} + \left(S_{h,A} - S_{h,B} + S_{h,C} - S_{h,D}\right)\frac{xy}{L_u H} \\ \delta_y &= S_{v,A} + \left(S_{v,B} - S_{v,A}\right)\frac{x}{L_u} + \left(S_{v,D} - S_{v,A}\right)\frac{y}{H} + \left(S_{v,A} - S_{v,B} + S_{v,C} - S_{v,D}\right)\frac{xy}{L_u H} \end{aligned} \tag{2.32}$$

where δ_x and δ_y are the in-plane displacements, and $S_{h,i}$ and $S_{v,i}$ are the horizontal and vertical displacements at the four corners (i = A, B, C and D) of a building unit. The horizontal ε_{xx}, vertical ε_{yy}, and diagonal ε_{xy} strains can be estimated using these displacements:

$$\begin{aligned}
\varepsilon_{xx} &= \frac{\partial \delta_x}{\partial x} = \frac{\left(S_{h,B} - S_{h,A}\right)}{L_u} + \left(S_{h,A} - S_{h,B} + S_{h,C} - S_{h,D}\right) \frac{y}{L_u H} \\
\varepsilon_{yy} &= \frac{\partial \delta_y}{\partial y} = \frac{\left(S_{v,D} - S_{v,A}\right)}{H} + \left(S_{v,A} - S_{v,B} + S_{v,C} - S_{v,D}\right) \frac{x}{L_u H} \\
\varepsilon_{xy} &= \frac{\partial \delta_x}{2\partial y} + \frac{\partial \delta_y}{2\partial x} = \frac{\left(S_{v,B} - S_{v,A}\right)}{2L_u} + \left(S_{v,A} - S_{v,B} + S_{v,C} - S_{v,D}\right) \frac{y}{2L_u H} \\
&\quad + \frac{\left(S_{h,D} - S_{h,A}\right)}{2H} + \left(S_{h,A} - S_{h,B} + S_{h,C} - S_{h,D}\right) \frac{x}{2L_u H}
\end{aligned} \tag{2.33}$$

Thus, the maximum principal in-plane strain can be evaluated by:

$$\varepsilon_{max} = \frac{\varepsilon_{yy} + \varepsilon_{xx}}{2} + \sqrt{\frac{1}{4}\left(\varepsilon_{yy} - \varepsilon_{xx}\right)^2 + \varepsilon_{xy}^2} \tag{2.34}$$

2.3.3.2 Modification factor methods

Son and Cording (2005) reported the relationship between normalised angular distortion $\beta/\Delta GS$ (i.e., the ratio of the building angular distortion β to the changes in corresponding greenfield settlement slope ΔGS) and the relative soil-to-structure shear stiffness $E_s L/GHl$ (l is b in Figure 2.43). The effective cross-section area of the wall was assumed to be equal to the wall height multiplied by the thickness ($A_s = Hl$), which means the shear stiffness of walls with openings GHl would be overestimated. Son and Cording (2005) summarised results from a series of field observations, physical model tests, and numerical model parametric studies, as well as results from elastic analysis, in Figure 2.43. It was observed that the normalised angular distortion typically increases with the relative soil-to-structure shear stiffness, indicating that building distortion more closely matches ground movement when building shear stiffness decreases. The slopes of the $\beta/\Delta GS$ - $E_s L/GHl$ curves are small when there are few cracks or cracking, while significant normalised angular distortion occurs when large cracks develop due to decreased building shear stiffness.

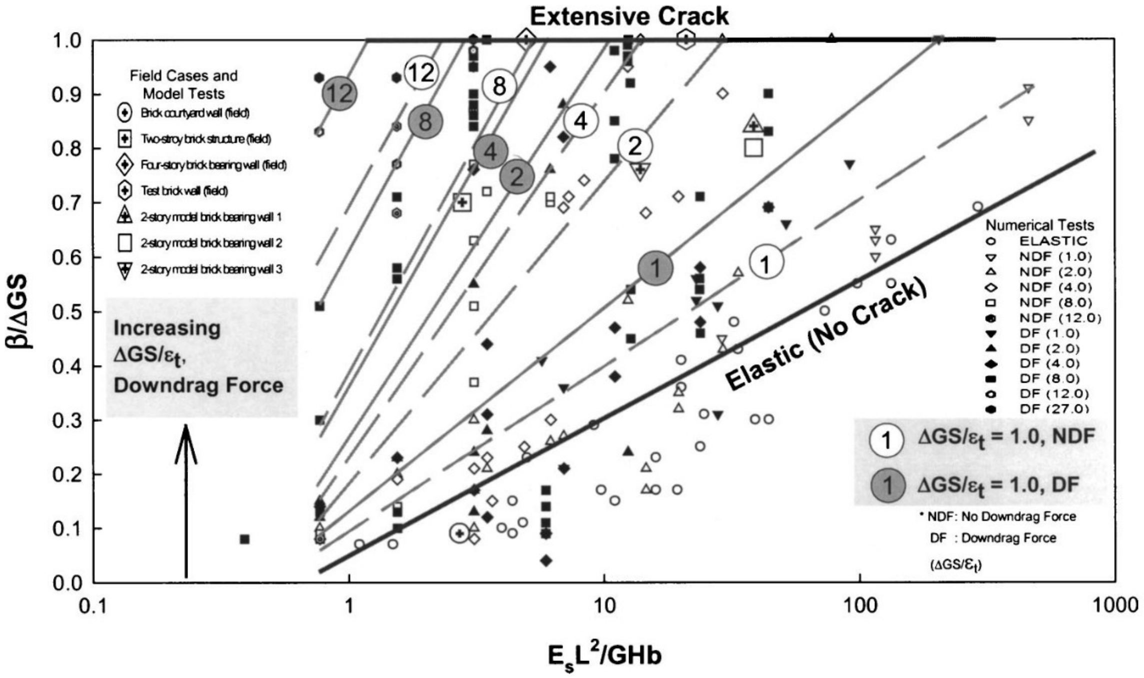

Fig. 2.43. Relationship between normalised angular distortion and relative soil-structure stiffness (Son and Cording, 2005)

Xu et al. (2020b) modified the $\beta/\Delta GS$-E_sL/GHl approach, adopting angular distortion modification factor M^{β} (i.e. the maximum bay angular distortion β_{max} normalised the maximum average slope of from the greenfield settlement curve $\overline{GS}_{max}$; Eq. 2.35) and relative soil-to-structure shear stiffness κ (with more effective building cross-section area A_s; Eq. 2.36). In Xu et al. (2020b), the possible average slope was obtained using a line of length equal to the building bay length (L_u) moved along the greenfield settlement curve; the maximum average slope obtained was referred to as $\overline{GS}_{max}$. The data reported by Xu et al. (2020b) in Figure 2.44 is roughly consistent with the findings of Son and Cording (2005) (Figure 2.43), even though the acquisition of $\overline{GS}_{max}$ is different.

$$M^{\beta} = \frac{\beta_{max}}{\overline{GS}_{max}} \tag{2.35}$$

$$\kappa = \frac{E_s L_u l}{G A_s} = \frac{E_s L_u}{G A_s^*} \tag{2.36}$$

where GA_s^* is the shear stiffness of the building per metre in the tunnel axial direction.

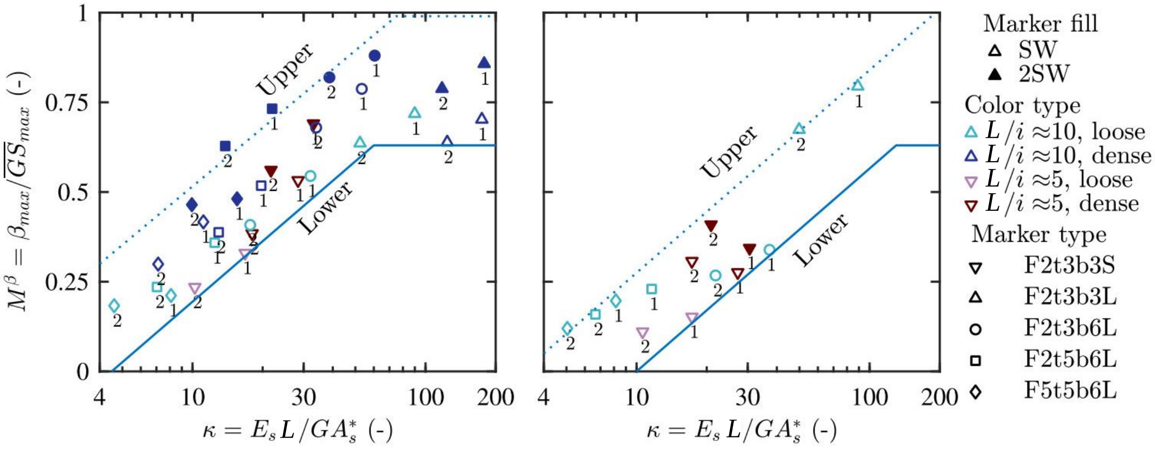

(a) (b)

Fig. 2.44. Angular distortion modification factor against relative soil-to-structure shear stiffness (numbers beneath markers indicate percentage of tunnel volume loss, $V_{l,t}$) (Xu et al., 2020b)

Franza et al. (2022) adopted a different approach for normalisation within M^{β} by using the maximum of average slope values calculated from a line of length equal to the building bay length L_u connected to points on the greenfield settlement curve corresponding to the building bay corners, denoted as $s_{GF,max} = \Delta S_{v,GF,max}/L_u$; in this approach β_{max} is normalised by $s_{GF,max}$. It can be argued that this approach, compared with Xu et al. (2020b), is more rational since values of β_{max} are normalised against a greenfield slope parameter that is more relevant to the building being evaluated:

$$M^{\beta} = \frac{\beta_{max}}{s_{GF,max}} \tag{2.37}$$

2.3.4 Building stiffness evaluation

The stiffness of buildings is crucial in tunnel-soil-building interaction scenarios as it directly impacts building deformation and damage levels. Thus, the accuracy of building stiffness determines the credibility of the results obtained through modification factor methods in both global and local assessments of building risk. Due to the complex structural characteristics and material properties involved, it is challenging yet essential to evaluate building stiffness in different aspects (including bending, shear, and axial stiffness). The following outlines several calculation methods for framed buildings and masonry buildings, noting that framed buildings are generally more flexible compared to masonry buildings thus the suitability of these methods must be carefully assessed depending on the structural characteristics.

Potts and Addenbrooke (1997) calculated the overall structure axial EA and bending stiffness EI using the parallel axis theorem, with an assumption that the equations for the axial and bending stiffness of a structure with n storeys comprise entirely of $n+1$ slabs:

$$EA = (n+1)EA_{slab} \tag{2.38}$$

$$EI = E\sum_{1}^{n+1}\left(I_{slab} + A_{slab}b^2\right) \tag{2.39}$$

where A_{slab} is the cross-sectional area of each slab, I_{slab} is the second moment of area of each slab, and b is the vertical distance between the structure's neutral axis and the slab's neutral axis. Potts and Addenbrooke (1997) acknowledged this would overestimate the building stiffness.

Mair and Taylor (2001) directly used the algebraic sum of the individual bending stiffness of all floor slabs EI_{slab} to evaluate the entire bending stiffness of a 10-storey reinforced concrete frame structure with two basement levels, the Elizabeth House, given as:

$$EI = E\sum(I_{slab}) \tag{2.40}$$

Meyerhof (1953) obtained an approximate estimate of the flexural rigidity of a rigidly framed structure, involving an open multi-storey frame with approximately equal bays and deflecting into the shape of a trough with a maximum central deflection and with similar curvature at each floor level. The author reported that columns increased the flexural rigidity of the entire frame (beam model) with a column stiffening factor, assuming points of contra-flexure in the columns at the mid-storey height and solving the structural analysis equations. Based on the work by Meyerhof (1953), Goh and Mair (2014) proposed a column stiffening factor C using slope deflection equations and rewrote the frame bending stiffness (from Eq. 2.40) considering the column contributions, given as:

$$
\begin{aligned}
EI &= CE\sum(I_{slab}) \\
C &= \left[1+\left(\frac{L_{sag/hog}}{L_u}\right)^2\left(\frac{K_{LC}+K_{UC}}{K_{LC}+K_{UC}+K_B}\right)\right]
\end{aligned}
\tag{2.41}
$$

where $K_{LC} = (EI/H_{storey})_{LC}$, $K_{UC} = (EI/H_{storey})_{UC}$, and $K_B = (EI/L_u)_B$ are the average stiffness of the lower column, the upper column, and the beam line, respectively.

These evaluation approaches for building stiffness mentioned above, however, lack the ability to distinguish between shear and bending stiffness. Son and Cording (2005) suggested carrying out separate pure bending and shear tests subjected to the given bending moment M and shear force τA in numerical models to acquire the shear and bending stiffness of masonry walls (see Figure 2.45).

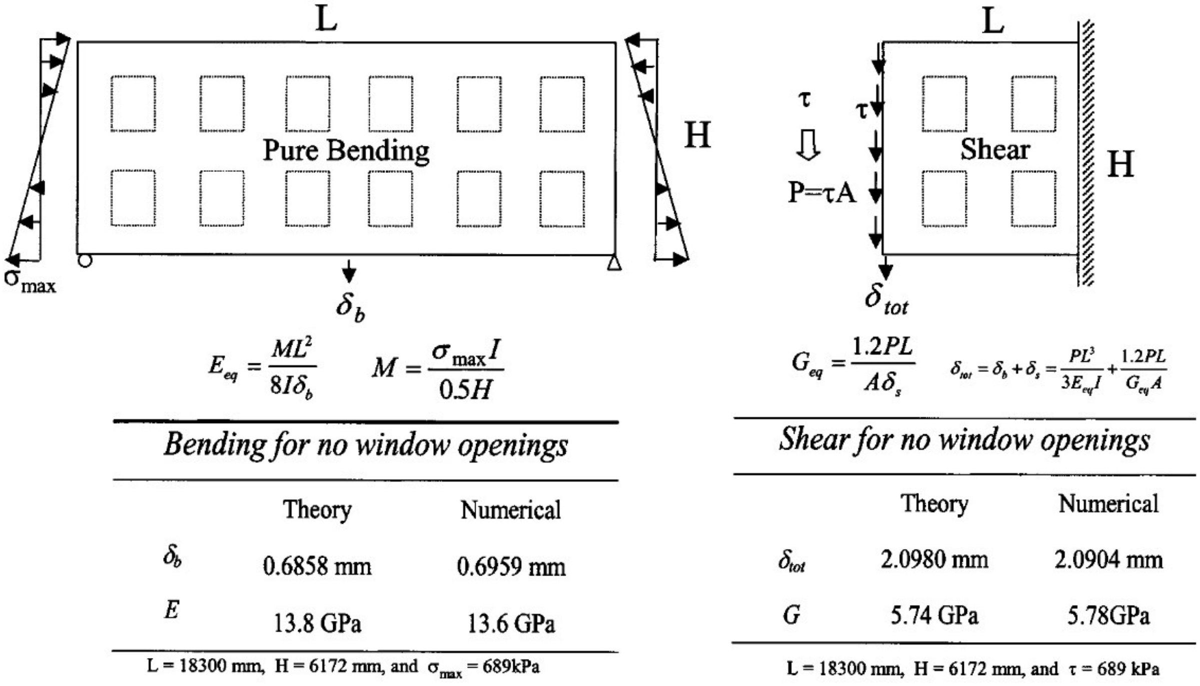

$$E_{eq} = \frac{ML^2}{8I\delta_b} \qquad M = \frac{\sigma_{max} I}{0.5H}$$

Bending for no window openings

	Theory	Numerical
δ_b	0.6858 mm	0.6959 mm
E	13.8 GPa	13.6 GPa

L = 18300 mm, H = 6172 mm, and σ_{max} = 689kPa

$$G_{eq} = \frac{1.2PL}{A\delta_s} \qquad \delta_{tot} = \delta_b + \delta_s = \frac{PL^3}{3E_{eq}I} + \frac{1.2PL}{G_{eq}A}$$

Shear for no window openings

	Theory	Numerical
δ_{tot}	2.0980 mm	2.0904 mm
G	5.74 GPa	5.78GPa

L = 18300 mm, H = 6172 mm, and τ = 689 kPa

Fig. 2.45. Estimation of building bending and shear stiffness (Son and Cording, 2005)

For framed buildings with infill shear walls, Finno et al. (2005) adopted a laminate beam (Figure 2.46) to represent a multi-storey building and estimate the building shear stiffness with an assumption that the infill wall provides shear resistance and the floor offers bending distortion. As shown in Figure 2.46, the laminate beam includes layers of plates (representing floors) and layers of core material (representing walls). Assuming the infill walls are compliant or not designed to function as shear walls, the stiffness of columns can significantly influence the shear stiffness of each floor level, especially if they feature moment-resisting connections at both ends. In this scenario, it is assumed that the columns are fixed at both the top and bottom, which may slightly overestimate their stiffening effect. The stiffness of each column $GA_{s,column}$ is as follows:

$$GA_{s,column} = \frac{12E_cI_c}{y_i^2} \tag{2.42}$$

where $A_{s,column}$ is the efective shear area of the column, E_c is Young's modulus of the column, I_c is the second moment of inertia of the column in the plane of the wall, and y_i is storey height. Since column ends experience small rotation, the factor of 12 may be reduced as much as 25%. The stiffness of each column in the section that is being analyzed should be summed and added to the wall stiffness of each floor level, and thus the total shear stiffness of each floor $GA_{s,i}$ is given by the sum of the column ($GA_{s,column}$) and wall ($GA_{s,wall}$) stiffness:

$$GA_{s,i} = \sum \left(GA_{s,column} + GA_{s,wall}\,(1-O)\right) \tag{2.43}$$

where O is the percentage opening in a wall. Finally, the equivalent shear stiffness GA_s of the laminate beam representing the entire structure is determined by:

$$\overline{GA_s} = \frac{1}{\sum_{i=1}^{n} \frac{y_i}{H}\frac{V_i}{V}\frac{1}{GA_{s,i}}} \tag{2.44}$$

where H is the building height, and V_i and V are the shear force of a storey and the entire beam, respectively.

Pickhaver et al. (2010) proposed a similar strip method to determine the equivalent bending and shear stiffness of masonry walls (especially the effective second moment of area I and shear area A_s) for in-plane bending using Timoshenko beam theory. For the estimation of I, the facade is divided into a set of imaginary horizontal strips (Figure 2.47(a)), and the equivalent second moment of area of the building I is given by the sum of the equivalent second moment

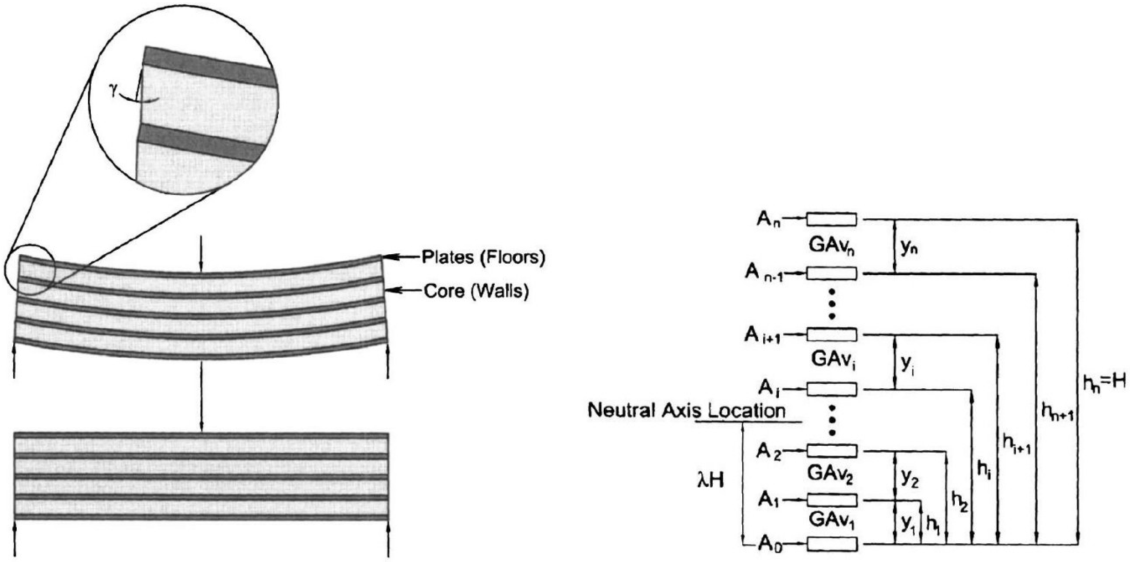

Fig. 2.46. Laminate beam representing structure (Finno et al., 2005)

of area contributed by each strip I_j:

$$I_j = \frac{lh_j^3}{12} + lh_j b_j^3 \tag{2.45}$$

$$I = \sum I_j \tag{2.46}$$

where l is the wall thickness, $h_j = a_j / L$ represents effective strip height, and b_j is the distance from the mid-point of the strip to the neutral axis. The location of the neutral axis depends on the boundary conditions of the building base, i.e. at the centroid of the building cross-section for a smooth-based building (neglecting the effect of any openings that may be present); coinciding with the ground surface for a rough-based building.

To determine A_s, the facade is segmented into a series of imaginary vertical strips (Figure 2.47(b)), and the equivalent cross-sectional area of the building (in the y–z plane, where z-axis is perpendicular to the x-y plane) is computed by assuming that the building compliance is given by the sum of the compliances of these vertical strips (Pickhaver et al., 2010), expressed as:

$$\frac{L}{A_s} = \sum \frac{L_i}{A_i} \tag{2.47}$$

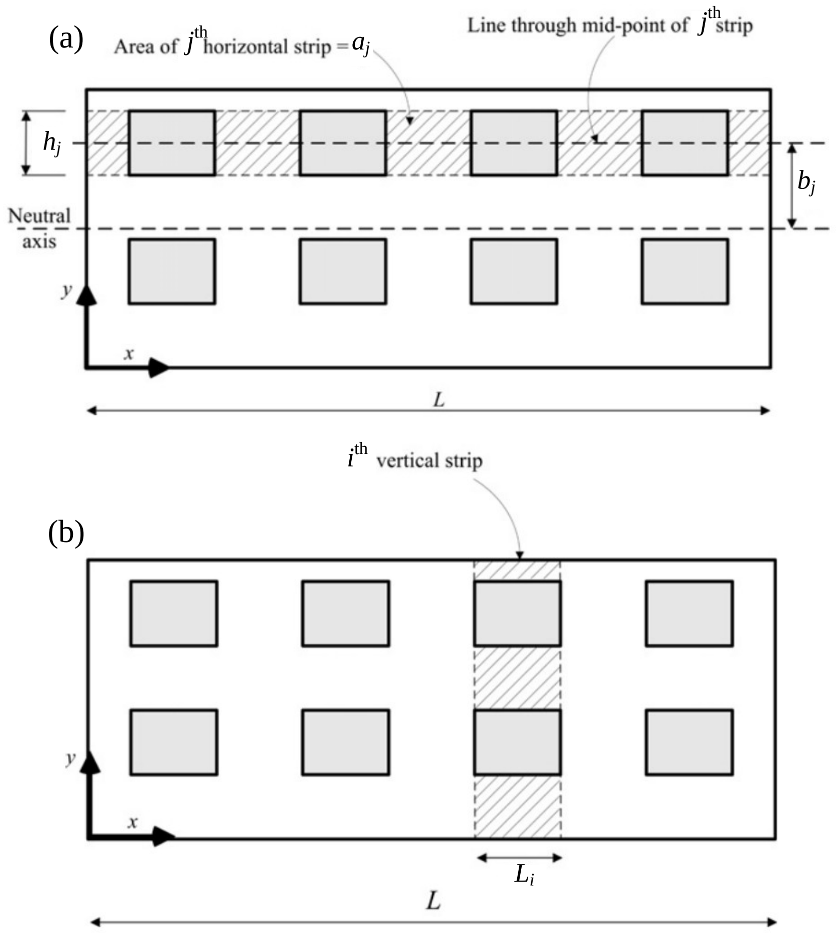

Fig. 2.47. Assessment of equivalent area (a) second moment of area and (b) shear area (Pickhaver et al., 2010)

where L_i the strip length (in x direction) and A_i the effective cross-sectional area of each vertical strip.

Pickhaver et al. (2010) summarised a large number of numerical modelling results and suggested that bending EI and shear stiffness GA_s should be multiplied by a coefficient $(L/H)/3$ for short buildings with a length-to-height ratio of $L/H < 3$ to avoid over-stiff responses.

Moreover, the overall bending and shear stiffness of the entire building, assuming it behaves like a Timoshenko beam, can be estimated by analysing the relationships between maximum deflections ($\delta_{bending}$, δ_{shear}) and loads (F_t) in three-point, four-point, and cantilever beam loading tests (Figure 2.48) using Eqs. 2.48-2.50:

Three-point loading (Figure 2.48(a)):

$$\begin{aligned}\delta_{tot} = \delta_{shear} + \delta_{bending} &= \frac{F_t L}{4GA_s} + \frac{F_t L^3}{48EI} \\ \frac{\delta_{shear}}{\delta_{bending}} = \frac{12EI}{L^2 GA_s} &= 12F_{sb}\end{aligned} \tag{2.48}$$

Four-point loading (Figure 2.48(b)):

$$\begin{aligned}\delta_{tot} = \delta_{shear} + \delta_{bending} &= \frac{F_t L_l}{GA_s} + \frac{F_t L_l (3L^2 - 4L_l^2)}{24EI} \\ \frac{\delta_{shear}}{\delta_{bending}} = \frac{24EI}{(3L^2 - 4L_l^2)GA_s} &= \frac{24L^2}{3L^2 - 4L_l^2} F_{sb}\end{aligned} \tag{2.49}$$

Cantilever beam testing (Figure 2.48(c)):

$$\begin{aligned}\delta_{tot} = \delta_{shear} + \delta_{bending} &= \frac{F_t L}{GA_s} + \frac{F_t L^3}{3EI} \\ \frac{\delta_{shear}}{\delta_{bending}} = \frac{3EI}{L^2 GA_s} &= 3F_{sb}\end{aligned} \tag{2.50}$$

where $F_{sb} = EI/(L^2 GA_s)$ is a constant.

2.4 Summary and research gap

Tunnelling in greenfield conditions has received considerable attention in the research community, with empirical methods being proposed to describe or predict ground movements in field conditions and geotechnical centrifuge tests. Compared to clays, tunnelling in sand requires special attention due to the impact of volumetric changes in the sand on ground movements. The reviewed studies on tunnelling in sands focus on the transverse settlement and the influence factors including tunnel volume loss, cover-to-tunnel diameter ratio, soil relative density. The contraction mechanisms of different tunnel models (for example, the eccentric flexible membrane (eFM) tunnel model (Marshall et al., 2012) and the eccentric rigid boundary mechanical (eRBM) tunnel model (Song and Marshall, 2020)) in centrifuge tests also affect results

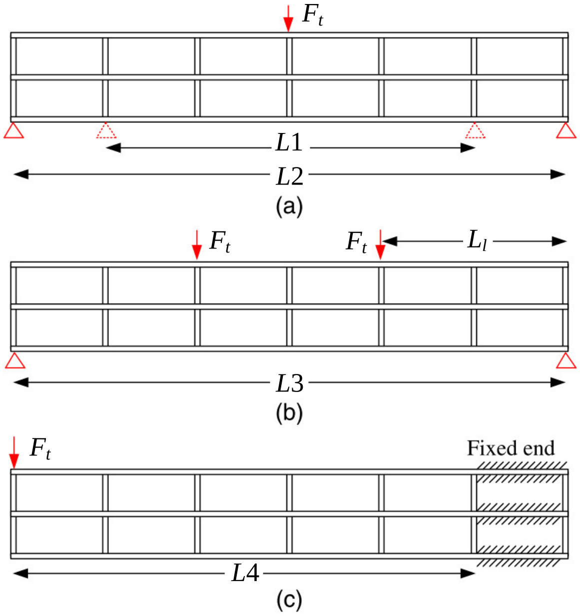

Fig. 2.48. Configuration of (a) three-point, (b) four-point, and (c) cantilever loading tests (Xu et al., 2020b)

and need careful assessment. The findings from studies on greenfield tunnelling provide a valuable reference for risk assessments of designing new tunnels near existing infrastructure such as piles and surface buildings.

Studies on tunnel-soil-pile interactions (TSPI) are crucial for understanding tunnelling effects on piles. Researchers attempted to divide the influencing zones of tunnelling (in relation to the location of the pile tips) based on field and centrifuge test data, and the influence zone patterns indicate that tunnelling has a diminishing effect on piles at greater distances from the tunnel. However, TSPI problems are quite complex due to various factors, such as soil types, pile installation methods (displacement piles, non-displacement piles), pile working loads (or safety factor), load distribution along the piles (potentially influenced by pile cap, rigid connection to other piles), tunnel volume loss, and issues related to force sensors. Among these, the influence of pile caps on load transfer mechanisms of piles affected by tunnelling lacks comprehensive studies, which will be part of this work.

Tunnelling may induce superstructure deformation or damage due to tunnel-soil-building interactions (TSBI), which is essential to quantitatively evaluate to avoid or mitigate risks. Empirical formulas and centrifuge modelling tend to simplify buildings as beams or slabs primarily subjected to bending deformations for parametric studies. This might lead to inaccurate estimations or predictions of building deformations that are also affected by shear stiffness (impacted by nonlinear building materials and structural characteristics such as openings). Some 3D building models adopted in centrifuge tests offer better structural details than beam models, yet the building mechanical behaviours are still limited by model materials and sizes. The coupled centrifuge-numerical modelling (CCNM) (Idinyang et al., 2019) method provides a reliable approach, where framed buildings are modelled in a numerical domain during centrifuge tests. However, there has been little to no work on CCNM for strip foundations (representing a continuous interface) and masonry buildings, which make up a large proportion of buildings in many cities around the world. As one objective of this work, developing a new powerful CCNM approach will improve human knowledge in tunnelling under masonry buildings with shallow strip foundations.

Chapter 3

Methodology and experimental setup

This chapter introduces the experimental setup, preparation, and procedures, including two centrifuge testing packages: tunnel-soil-pile interactions (TSPI) and tunnel-soil-masonry building interactions (TSBI) with shallow strip foundations.

First, the geotechnical centrifuge modelling technique, universal experimental package (for greenfield tunnelling), and detailed testing configurations for TSPI are provided. The general centrifuge testing package developed by Song (2019) was adopted for these tests. This group of tests involves capped and uncapped non-displacement piles with and without soft bases.

Subsequently, this chapter provides the development of an advanced coupled centrifuge-numerical modelling (CCNM) approach for shallow strip foundations (Tang et al., 2024c), which is used to study the TSBI mechanisms, followed by introducing detailed configurations for TSBI tests. This group of tests involves the validation of the new CCNM method and the effects of building positions and inherent characteristics on TSBI scenarios.

3.1 Geotechnical centrifuge modelling technique

A thorough grasp of the complex soil-structure interactions induced by tunnel excavations is vital for engineering designs. Field tests and on-site monitoring are capable of providing valuable data on soil and structure responses, however their practical application is constrained by high costs and limited data range from the existing assets. Numerical modelling methods rely heavily on realistic field or experimental data to validate the accuracy and precision of the results. Taking these factors into consideration, the geotechnical centrifuge testing technique offers a useful approach for investigating the tunnel-soil-foundation-building interactions through the use of small-scale ($1/N$) physical models subjected to N times Earth's gravity (Ng), enabling replication of full (prototype) scale scenarios with realistic stress levels.

3.1.1 Scaling principle of centrifuge simulation

When the centrifuge spins up, the centripetal acceleration Ng induces stress conditions in the scaled-down centrifuge model that closely replicate those of a prototype-scale scenario. The scaling coefficient N can be determined using Eq. 3.1:

$$Ng = \omega^2 R_e \tag{3.1}$$

where ω is the rotational velocity of the centrifuge and R_e is the effective radius from the centrifuge model to the centrifuge rotation axis. Note that due to the non-negligible size of the centrifuge model, the distances from the specific local regions within the centrifuge model to the centrifuge rotation axis are not identical, and consequently different local regions of the centrifuge model experience different g-levels. Taylor (1995a) provided Eq. 3.2 to calculate the effective radius R_e for the areas of interest (e.g., the soil within a strong box):

$$R_e = R_t + h_m/3 \tag{3.2}$$

where R_t is the distance from the top of the area of interest (e.g., soil surface) to the centre of the centrifuge rotation axis and h_m is the height of the area of interest (e.g., soil height).

The scaling factor between the parameters in the small-scale centrifuge model and the corresponding full-scale prototype scenario are summarised in Table 3.1.

Table 3.1. Centrifuge scaling laws (Taylor, 1995a)

Parameter	Metric unit	Model scale	Prototype scale
Gravity	$\mathrm{m/s^2}$	N	1
Length	m	1	N
Area	$\mathrm{m^2}$	1	N^2
Volume	$\mathrm{m^3}$	1	N^3
Force	$\mathrm{N = kgm/s^2}$	1	N^2
Density	$\mathrm{kg/m^3}$	1	1
Stress	$\mathrm{Pa = N/m^2 = kg/\left(ms^2\right)}$	1	1
Strain	-	1	1
Axial Stiffness (EA)	N	1	N^2
Bending stiffness (EI)	$\mathrm{Nm^2}$	1	N^4

3.1.2 Influence factors of centrifuge modelling

Compared to prototype-scale scenarios, centrifuge tests using small-scale models have three important factors which should be considered: stress magnitude (i.e. g-levels at different depths, as mentioned above), size effects, and boundary effects. These potential effects in all tests of this study are the same due to the identical test configurations, thus they would not affect the comparison of the results.

In centrifuge modelling tests, the soil used is typically the same as in the prototype scenarios to ensure consistent soil properties (such as Young's modulus and particle-scale characteristics). This raises awareness of the effect of soil particle size (characterised by the average size of soil particle D_{50}) without complying with the scaling rules in Table 3.1 since the ratios of model structure sizes to soil particle diameter (D_{50}) have altered. Kutter et al. (1994) performed a series of centrifuge tests to observe the sand collapse behaviours into cavities and reported that the soil particle size effect would reduce after the ratio of cavity diameter to average soil grain size exceeded 350. Marshall (2009) suggested the limit ratio should be 500 to minimise the grain size effect considering the contraction and dilation behaviours of sands under drained conditions. Bolton et al. (1999) reported that the cone resistance would not be affected when the ratio of cone diameter to average soil particle size exceeded 28 in cone penetration tests with fine Leighton Buzzard sand. Toyosawa et al. (2013) suggested surface model footing-to-average soil particle diameter ratio being over 50. In this study, the ratios of tunnel diameter (D_t =90 mm), pile diameter (d_p =12.6 mm), and minimum strip foundation size (32 mm), to average sand particle diameter (D_{50} =0.14 mm) are D_t/D_{50} =643 (> 500), d_p/D_{50} =90 (> 28), and 229 (> 50), respectively, indicating negligible size effects.

Marshall et al. (2009) reported that the friction along the inner surface of the transparent front acrylic wall of the strongbox would not obviously affect the soil movements based on a comparison between soil settlements at the box boundaries and within the centre of the box. Zhou (2015) also demonstrated that the discrepancy between settlements at the boundaries and those from the middle of the strongbox width (specifically, 130 mm from the front/back walls) was below 10% in centrifuge tests for dense sand ($I_d = 90\%$). These results provide reassurance regarding the attainment of plane-strain conditions in this study. Bolton et al. (1999) suggested that the distance from cone to the wall boundary should be at least 10 times the cone diameter to minimize the boundary effect on cone resistance. In this study, the ratio of the minimum distance from the pile shaft to the wall boundary (75 mm) to the pile diameter (d_p =12.6 mm) is 6 (< 10; see Fig. 3.1), which may result in a slight overestimation of the results for TSPI tests. For TSBI tests, where the strip foundation model is placed in close proximity to the acrylic wall, the ground movements near the surface level in particle image velocimetry (PIV) analysis would be affected (discussed later).

3.2 Universal experimental package (for greenfield tunnelling)

3.2.1 Centrifuge

Experiments were conducted at a nominal centrifuge acceleration of Ng on the 2 m radius, 50 g-tonne geotechnical centrifuge of the University of Nottingham Centre for Geomechanics (NCG), as shown in Fig. 3.2. At the effective radius of 1.7 m, the centrifuge is capable of carrying a maximum payload of 500 kg under 100 g, and it can achieve a maximum acceleration of 150 g with a payload of 333 kg. The swing cradle at one end of the beam can support a pay-

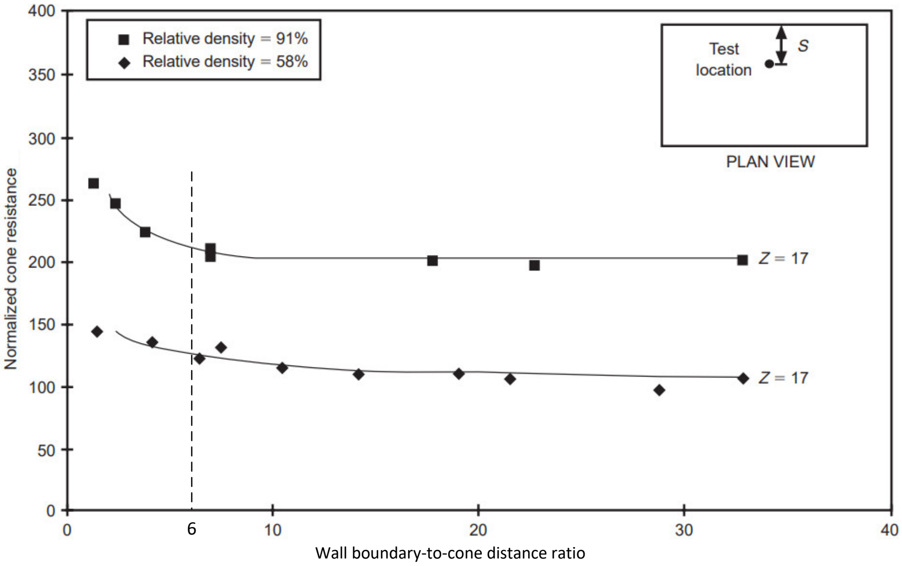

Fig. 3.1. Boundary effect in centrifuge cone penetration tests (where Z is the model penetration depth normalised by cone diameter; Bolton et al. (1999))

load of 200-500 kg, which is counterbalanced by a counterweight located at the other end of the beam. Additionally, the centrifuge is equipped with oil containers in the beam to automatically adjust the unbalanced force at both ends, maintaining it within 30 kN. The Data Acquisition System (DAS) cabinet houses a network switch and a Fiber Bragg Grating (FBG) interrogator, which are connected to and remotely controlled from the centrifuge control room (Zhou, 2015).

3.2.2 Strongbox

The centrifuge model strong box consists of an aluminium U-channel, a transparent acrylic front wall, and a back aluminium wall. The interior length × width × height dimensions of the strongbox are 700 mm × 150 mm × 500 mm, respectively (refer to Figs. 3.11-3.12). Subsurface images through the acrylic wall were taken using two Dalsa Genie Nano-M4020 12.4 megapixel cameras with monochromatic amber LED light strips; subsurface soil displacements in the greenfield (GF) tunnelling test were measured using GeoPIV-RG (Stanier et al., 2016).

The GeoPIV-RG technique enables the conversion of pixel space coordinates of the measured object into object space coordinates using a series of photographs. The object space

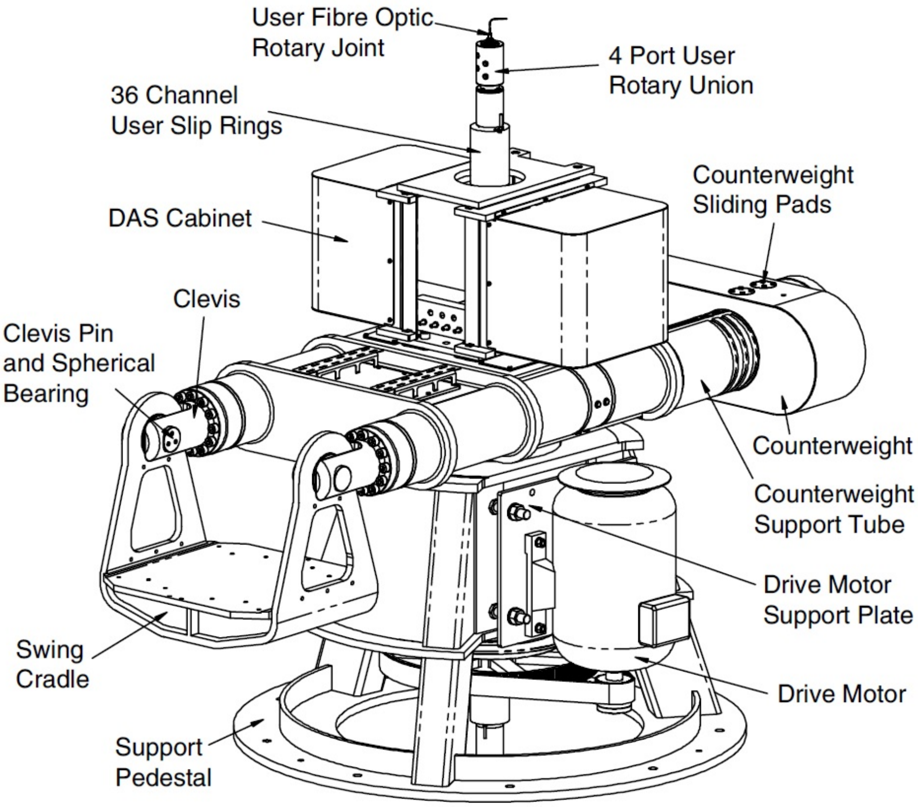

Fig. 3.2. Structure diagram of geotechnical centrifuge (Ellis et al., 2006)

coordinates were calibrated through specific reference points painted on the inner surface of the acrylic wall. The precision of the GeoPIV-RG technique was evaluated by Song (2019), who reported a standard deviation of 4.6 µm in horizontal displacement and 6.4 µm in vertical displacement. This suggests that the vertical data is more influenced by the tunnel model during centrifuge spinning, which aligns with the findings of Marshall and Mair (2011).

3.2.3 Soil

A uniform dry fine silica sand known as Leighton Buzzard Fraction E was adopted in this study, with a typical average diameter D_{50} of 0.14 mm, a uniformity coefficient U_c of 1.58, a specific gravity G_s of 2.65, and maximum e_{max} and minimum e_{min} void ratios of 1.01 and 0.61, respectively (Lanzano et al., 2016). The dense sand with a relative density $I_d = 90\%$ was adopted for all centrifuge tests. To prepare uniform sand for the tests, the strongbox was placed with its acrylic wall facing downwards, a temporary plate was fixed at the target soil surface, the tunnel was fixed vertically, and sand was poured in the direction of the tunnel longitudinal axis from the hopper of the NCG automatic sand pourer to achieve a relative density $I_d = 90\,\% \pm 3\,\%$. This model preparation method (pouring in-line with the tunnel axis; consistent, for example, with Jacobsz et al. (2004); Vorster et al. (2005a)) avoids "shadowing" issues which would occur if the sand was poured with the box in its upright position and which would cause non-uniform sand density around the tunnel.

Fig. 3.3 shows the NCG automatic sand pourer. Three stepper motors enable manual control or pre-set movement of the hopper in 3 axes. A laser sand level sensor is installed on the side of the hopper to check whether there is enough sand within the hopper, and another laser sensor installed below the hopper is used to monitor the vertical distance from the hopper to the sand surface within the strongbox, allowing automatic control of the height of sand pouring. A nozzle connected beneath the hopper contains an pneumatic pinch valve and houses plates containing a number of apertures of a specific size (4-6 mm) to control the flow rate, as well as two layers of sieves positioned below the nozzle (the lower sieve was positioned 0.8-1 m above the surface of the sand samples) to distribute the pluviated sand. Two schemes were adopted (because the sand pourer was modified during the study): one 6 mm aperture with the lower sieve at 1 m height for the tests of tunnelling under piles; and three 4 mm apertures with the lower sieve at 0.8 m height for the tests of tunnelling masonry buildings. This study employed a horizontal speed of 20 mm/s and a vertical speed of 3 mm/s. The sand pourer is within a dedicated enclosed room with a dust extractor to eliminate/reduce operator exposure to dust particles.

3.2.4 Tunnel

A 90 mm diameter (D_t) eccentric rigid boundary mechanical model tunnel developed by Song and Marshall (2020) provides uniform ground loss across the width of the strongbox, with a maximum tunnel volume loss of 3.5%. The central axis of the tunnel comprises a bidirectional screw shaft, which is driven by a stepper motor equipped with a 10:1 ratio gearbox. This arrangement enables the movement of five tunnel segments towards the tunnel centreline, resulting in a contraction of the overall volume. It is worth noting that the segment located

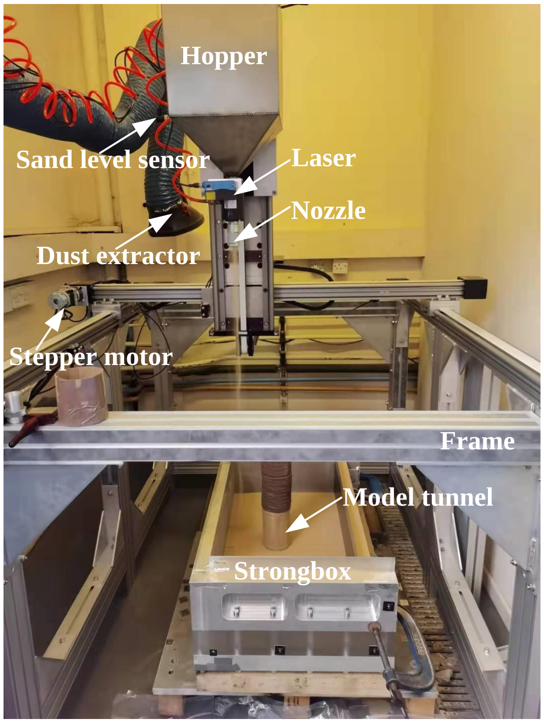

Fig. 3.3. Sand pourer at NCG

at the tunnel invert remains unchanged throughout this process. Each incremental tunnel volume loss is equivalent to 0.1125% and corresponds to a horizontal displacement of 0.625 mm for each hexagonal wedge-shaped shaft, which is measured by a Linear Variable Differential Transformer (LVDT) positioned in front of the model tunnel (refer to Figs. 3.11-3.12).

3.3 Centrifuge modelling of tunnel-soil-pile interactions

3.3.1 Test configuration

Experiments were conducted at 60 g. A greenfield test, seven foundation loading tests, and eight tests of tunnelling directly beneath a single foundation (either raft only, uncapped pile, or capped pile) were conducted. Fig. 3.4(a) shows the general layout of tests while Fig. 3.4(b) sketches the five types of tested foundations: namely, raft, uncapped reference pile, capped pile, uncapped friction pile, capped friction pile. All piles were either pushed or buried in the sand during model preparation at 1 g and can therefore be considered as ‘wished in place’ piles.

Whilst not completely representative of bored piles (which, depending on installation method, will have some installation effects), the tests presented here should be considered to be more reflective of a bored pile condition than a driven pile.

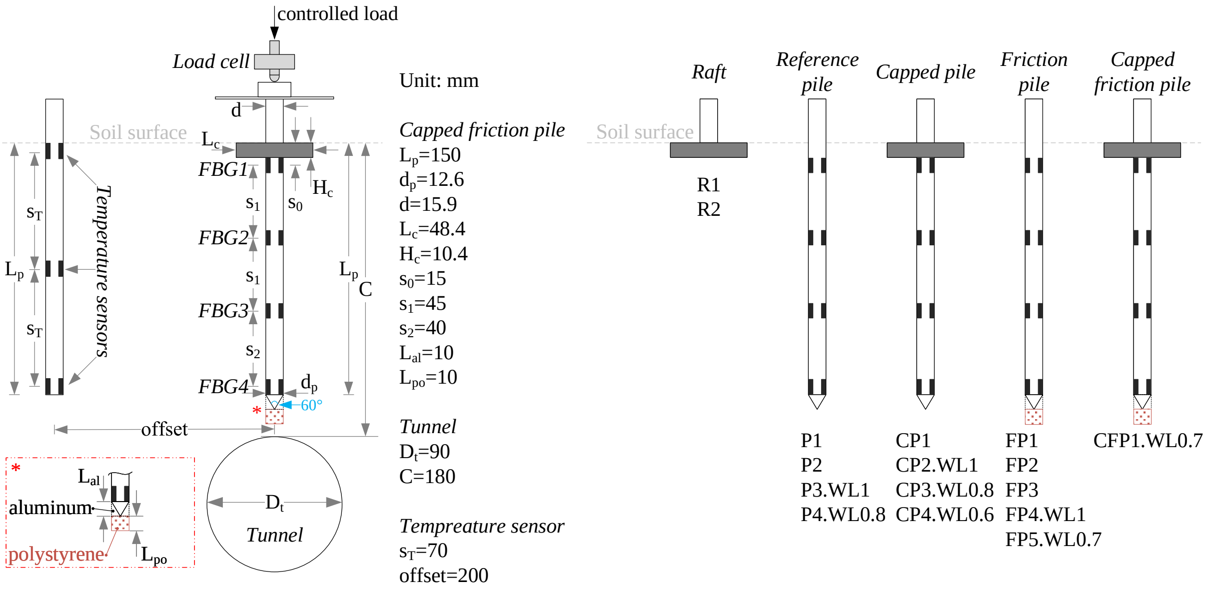

(a) (b)

Fig. 3.4. Illustration of (a) layout of capped friction pile in tunnelling test and (b) foundation types

3.3.2 Pile models

A thin layer of sand was bonded to all foundation surfaces in contact with the soil to achieve a ‘rough’ interface, except for the additional aluminium piece added to the pile base to create the friction piles (see magnified view at bottom-left of Fig. 3.4); all stated pile/cap/raft dimensions include this bonded layer. Model piles had a shaft length L_p = 150 mm, final diameter d_p = 12.6 mm (aluminium tube with 12 mm outer diameter and 1.35 mm thickness, having an external 0.3 mm rough interface), and were fitted with a 60° conical tip. The pile cap was fixed in place using a step in pile shaft diameter at the soil surface (piles were machined from 15.9 mm external diameter aluminium tubes with a thickness of 3.3 mm). The raft and the pile caps were square with 48.4 mm side length and 10.4 mm thickness, and were fully embedded in the ground.

Friction piles were created by fitting cylindrical pieces of aluminium and relatively soft polystyrene foam to the base of the reference pile, with the aim of reducing resistance mobilised at the pile base (similar to Gutiérrez-Ch et al. (2021)). Based on lab tests of the polystyrene under radially constrained conditions (similar to an oedometer test), a maximum base load of 12 N was expected (see Table 3.3).

The intention of the friction pile tests was to obtain data that more closely aligned with design assumptions (where little to no base capacity is assumed for capped piles (Poulos, 2001)). However, as demonstrated in Chapter 4, though effective in reducing the base loads to some degree, higher base loads were mobilised in the friction piles than expected. As such, even for the friction piles, test outcomes relate to a more conservative scenario of tunnel-pile interaction, where base capacity is proportionally higher than generally assumed for capped piles in design.

The pile was instrumented using two fibre optic cables on opposite sides of the pile, each with 4 FBG strain sensors, as shown in Fig. 3.4(a). The FBG sensors were calibrated to infer axial load along the pile through a positive correlation between pile axial force, strain, and FBG wavelength shift suggested by Song and Marshall (2020). The wavelength shifts of two FBG sensors at the same level were averaged to minimise the impact of pile bending. Measurements from the load cell and FBG sensors enable the estimation of: *external load F* as the pile axial force N at the ground surface $z = 0$, given by the load cell reading plus the self-weight of components between the load cell and the soil surface; *heading load* as the difference between the external load at the soil surface and FBG1 (for capped pile tests this represents the load carried by the cap); *shaft load* as the difference in axial force between FBG1 at a depth of 0.9 m (prototype-scale) and FBG4 at the pile base; and *base load* as the axial force at FBG4.

The centrifuge experiments consider a full-scale prototype scenario with 0.756 m diameter, 9 m deep piles equipped, where applicable, with a square pile cap with 2.904 m side length and 0.624 m thickness located directly above a 5.4 m diameter tunnel with a cover depth of 10.8 m.

3.3.3 Setup and calibration of piles with FBG strain sensors

3.3.3.1 Influence of the connection at the pile head

Fig. 3.5 illustrates the standard model piles, as well as the two types of connection methods between the pile head and the load cell above it: a "rigid connection", where the lower part of the load cell is threaded onto the pile head, and a "point-to-surface contact", where a hemispherical base of the lower part of the load cell makes contact with the top plane of the pile head. The upper end of both load cells is threaded to the loading device above, delivering only vertical force. Fig. 3.6(a) shows the difference in pile axial forces for the two FBG sensors at each level (i.e. $\Delta F = F_i - F_{(i+1)}$, where i and $i+1$ refer to the FBGs on opposite faces, Fig. 3.5(a)). The difference in axial force serves as an indicator of the magnitude of pile bending (Tang et al., 2024b).

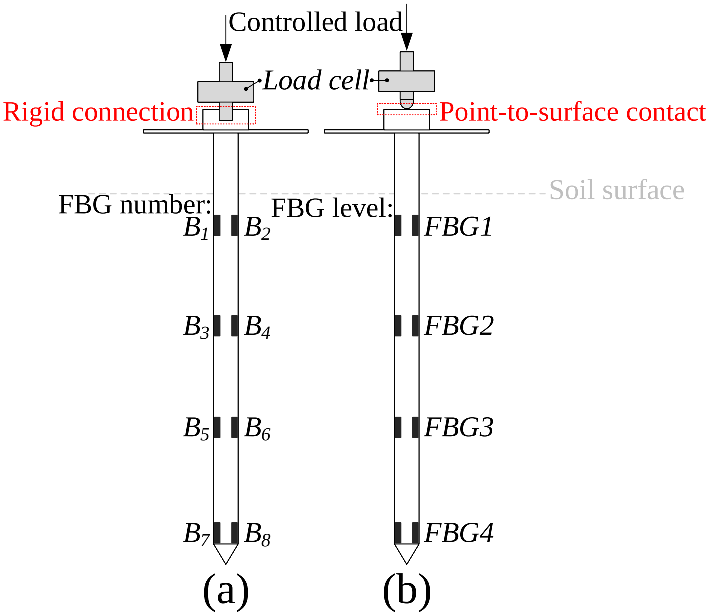

Fig. 3.5. Diagrams of (a) rigid connection and (b) point-to-surface contact between load cell and pile head

The rigid connection increased the pile bending. In contrast, the point-to-surface contact reduced the force difference ΔF compared with the rigid connection. Whilst in theory using the average FBG readings of the two sensors on opposite faces should still provide an accurate measurement of axial force, this relies on precise positioning and alignment of the sensors,

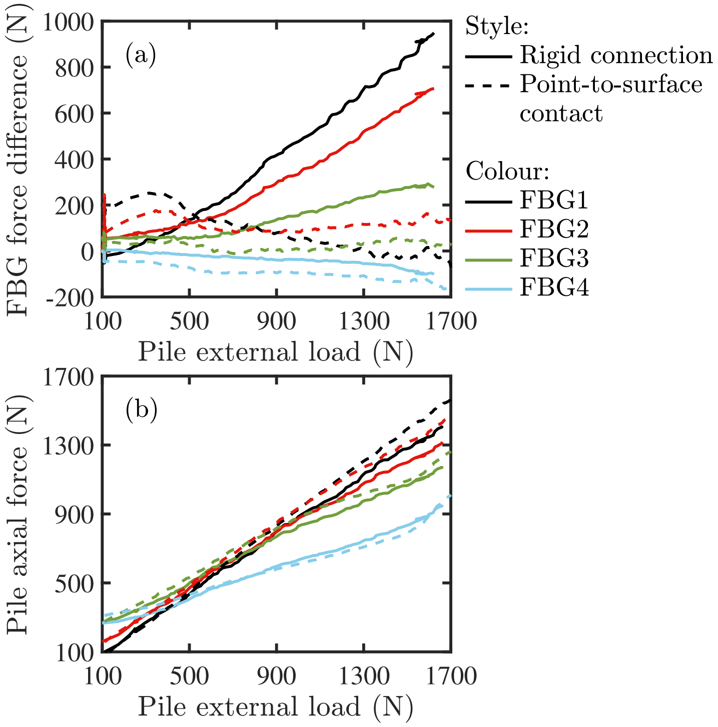

Fig. 3.6. (a) FBG force difference between opposite positions at same level and (b) pile axial force with rigid connection and point-to-surface contact during loading

which is difficult to achieve in practice. Fig. 3.6(b) shows that the point-to-surface contact tended to give higher FBG load readings.

3.3.3.2 FBG strain sensor calibration

In this study, the axial force along the pile N_j is inferred from the average wavelength shift $\Delta\lambda_{FBG_j}$ of two FBGs at the same level (at FBG_j, Fig. 3.5(b)) as:

$$N_j = K_{FBG_j} * (\Delta\lambda_{FBG_j} - \Delta\lambda_{T_j}) + \Delta N_{exp} \tag{3.3}$$

where j is the FBG level reference number, K_{FBG_j} (in N/pm, pm=picometre) is FBG calibration coefficient, $\Delta\lambda_{T_j} = K_t * \Delta T$ is the temperature-induced wavelength offset proportional to the change in temperature ΔT by a factor K_t = 32-41 pm/°C estimated for no mechanical strains, and ΔN_{exp} is an offset introduced during centrifuge testing to correct for the disturbance resulting from the loading system. $\Delta\lambda_{T_j}$ and ΔN_{exp} are zero during K_{FBG_j} calibration tests performed at constant temperature.

(1) Coefficient calibration

Table 3.2 shows the range, mean, and standard deviation (STD) of K_{FBG} from five sets of routine lab compression tests at 1 g within a standard loading frame (Lab C, two cycles from 0-600-0 N with an increment of ±100 N; a small cylindrical aluminium block with a conical recess matching the shape of the pile tip provides a surface for loading), two sets of compression tests using a loading/fixing system that fits on the centrifuge done at both at 1 g and 60 g (Cen 1 g, Cen 60 g, as above), and seven lab tension tests at 1 g (Lab T, from 0-200-0 N with an increment of ±20 N). After each cycle of loading-unloading, the position of the pile was altered through translation and/or rotation.

The deviation in 1-g lab compression coefficient K_{FBG} is likely caused by pile bending due to misalignment within the loading frame, despite attempts to reduce its effects. Overall, the lab compression coefficients K_{FBG} are stable and satisfactory, supported by the results of the centrifuge and tension tests discussed below. Next, the centrifuge compression coefficient K_{FBG} under 1 g and 60 g levels are discussed. K_{FBG} at 60 g was slightly smaller (by $\approx 2.1\%$ on average) than the results obtained at 1 g (conducted prior to and after the 60 g tests, without adjusting any components), which implies a slight (and acceptable) overestimation of the pile axial force when using K_{FBG} from 1 g lab compression tests. To minimise the effect of pile bending on K_{FBG}, lab tension tests were performed. The pile was fixed at the top and weights were hung from the pile via a clamp that was attached to the pile base, close to FBG4 (thus, FBG4 readings are unreliable). Neglecting the outliers for FBG1, $K_{FBG_{1-3}}$ are consistent with the compression results.

(2) Offset at elevated gravity

The tunnel-pile interaction tests included “stabilisation cycles” in which the centrifuge was repeatedly spun up/down to achieve a more uniform stress distribution within the soil and at soil-structure interfaces, and ensuring consistency between tests (Song et al., 2022).

To minimise deviations in FBG readings due to misalignments and bending, $\Delta N_{exp} = \Delta N_{exp,1} + \Delta N_{exp,2}$ in Eq. 3.3 is estimated for each test in two steps: (i) $\Delta N_{exp,1}$ is estimated during the stabilisation cycles of a specific test as the difference between the readings of FBG1

Table 3.2. FBG calibration coefficients from lab compression (C), centrifuge compression, and lab tension (T) tests

		FBG1	FBG2	FBG3	FBG4
Lab C	K_{FBG}	2.5-2.6	2.5-2.6	2.5-2.6	2.4-2.6
	Mean	2.53	2.54	2.57	2.52
	STD	0.048	0.052	0.024	0.064
Cen 1 g	K_{FBG}	2.6-2.7	2.7-2.8	2.7-2.8	2.8-2.9
	Mean	2.63	2.74	2.71	2.83
	STD	0.016	0.043	0.043	0.090
Cen 60 g	K_{FBG}	~2.6	~2.7	2.6-2.7	2.7-2.8
	Mean	2.59	2.70	2.66	2.73
	STD	0.022	0.040	0.037	0.044
Lab T	K_{FBG}	2.3-3.0	2.5-2.7	2.5-2.8	/
	Mean	2.62	2.54	2.62	/
	STD	0.229	0.070	0.080	/

at 15 mm beneath the surface and the theoretical axial load at the surface (neglecting the shaft friction between FBG1 and the soil surface); next, (ii) $\Delta N_{exp,2}$ is a constant for the instrumented pile estimated at a given g-level in tests without soil to account for the (minor) effects of the self-weight of FBG sensors and the glue covering them when g-level is increased.

Fig. 3.7 illustrates the uncorrected changes in pile axial forces (when $\Delta N_{exp} = 0$) in two centrifuge tests during stabilisation cycles from 1-60-10-60-10-60 g. Two scenarios are included: subplot (a) for a pile positioned directly above the tunnel; subplot (b) for a pile located 150 mm away from the tunnel centreline ("no tunnel"). The pile axial forces showed good repeatability subsequent to the first spin-up to 60 g. Specifically, in Fig. 3.7(a)-(b), the axial force at FBG1 was 15/-30 N at the 1st 10 g, whereas it was 2/-60 N for the subsequent 2nd and 3rd 10 g.

In these tests, the "theoretical surface load" (i.e. theoretical pile load at the soil surface) is equal to 22 N and 110 N at 10 g and 60 g respectively: e.g. at 60 g it consists of 105 N from the self-weight of the components above the soil surface (adjusted for distance from centre of rotation of the centrifuge) and a constant load of 5 N applied by the stepper motor (controlled load in Fig. 3.5).

The FBG correction of $\Delta N_{exp,1}$ = 20 N and 82 N were estimated, respectively, at the last

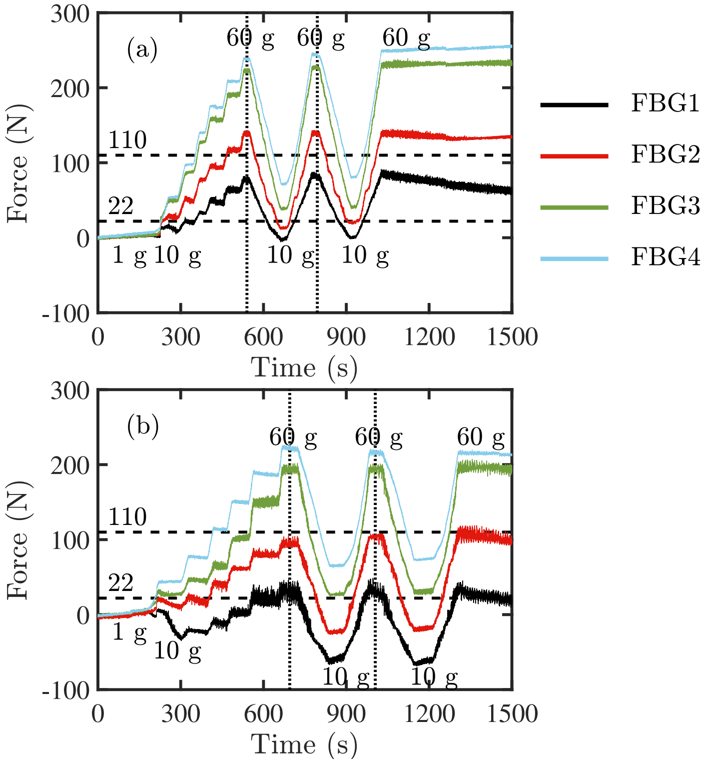

Fig. 3.7. Changes in pile axial forces during centrifuge spin up/down for pile (a) above tunnel and (b) no tunnel

spin-down to 10 g in Fig. 3.7(a)-(b), so that the FBG1 load matched the theoretical surface load of 22 N. Note that $\Delta N_{exp,1}$ estimated for FBG1 is applied to all other FBG loads while considering $\Delta N_{exp,2} = 0$.

Next, $\Delta N_{exp,2}$ is added to measurments at the end of the spin-up (or stabilisation cycles) once the final target 60 g is reached. This second offset $\Delta N_{exp,2}$ was estimated, at each FBG location, from the difference between the measured average pile axial forces and the theoretical pile self-weight in two calibration centrifuge tests at N-g without soil (while assuming $\Delta N_{exp,1} = 0$); as shown in Fig. 3.8, $\Delta N_{exp,2}$ is within the range of 1-33 N, which is relatively small compared with the pile load capacity in centrifuge tests at 60 g ($\approx$ 1.6 kN, including base load and shaft friction).

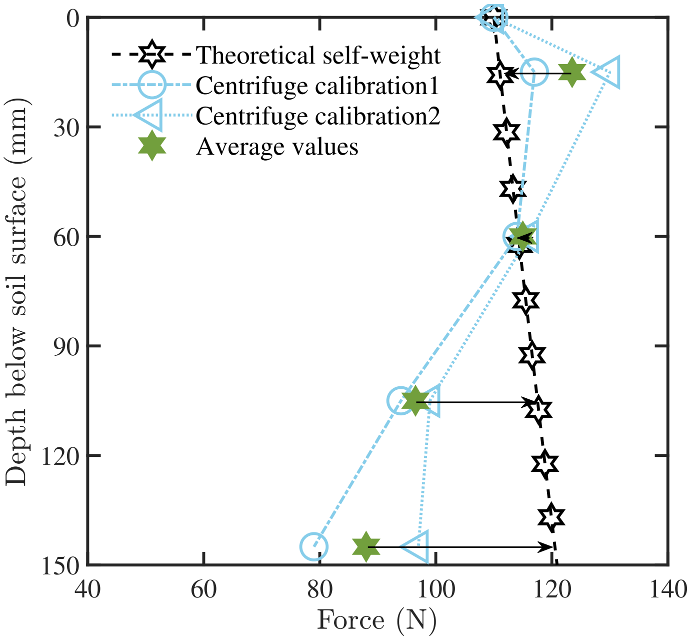

Fig. 3.8. Pile axial force offset at 60 g

3.3.3.3 Measurements of pile shaft roughness

Fig. 3.9 shows measurements along the circumferential direction over a portion of ≈ 10 mm of the pile shaft, of the arithmetic average roughness (R_a, i.e. arithmetic average of profile height deviations from the mean line) and root mean square roughness (R_q, i.e. root mean square average of the profile height deviations from the mean line) at four positions (i.e. shaft depth of 20, 45, 90, and 120 mm) of both a "new" (used in one centrifuge loading test: pile external load ≈ 1.6 kN and settlement ≈ 2 mm) and a "used" pile (used in ≈ 10 centrifuge loading tests: external load 0.7-2.0 kN and settlement 1-4 mm). A 10 mm wide laser (Micro Epsilon scanCONTROL 2900-10/BL, 1280 pixels) was used; pile was rotated during scans.

Results indicate that repeated centrifuge tests had little effect on R_a and R_q, although the "used" pile shows peaks in R_q ($R_q \approx 45$ µm for 90 and 120 mm depth in Fig. 3.9(d)), which might arise from local wear. This suggests that pile shaft roughness, thus shaft capacity, was maintained for repeated centrifuge tests of the experimental programme conducted.

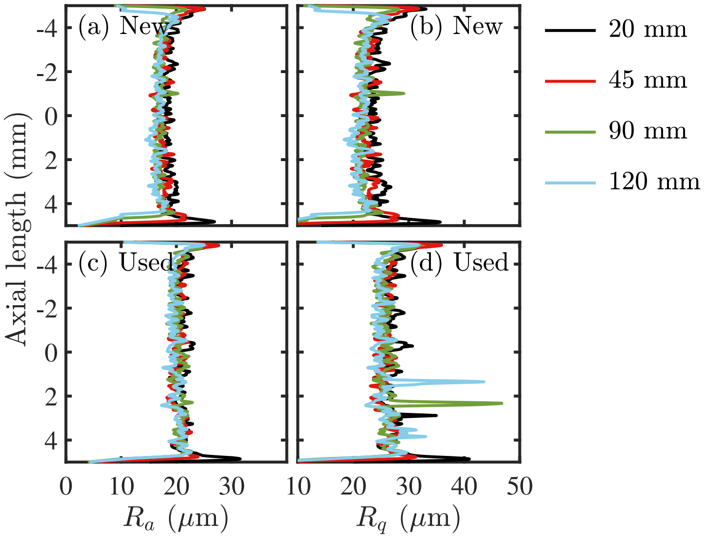

Fig. 3.9. Arithmetic average roughness and root mean square roughness of (a b) “new” and (c d) “used” piles

3.3.3.4 Use of a soft base for friction piles

The soft base, aiming to reduce pile base loads to model friction piles, consisted of an aluminium tube at the conical tip and an underlying cylinder of polystyrene foam (both pieces have 10 mm length and 12 mm diameter), as shown in Fig. 3.10(b). No sand was glued to the aluminium tube, so that the force at FBG4 was representative of the pile base load.

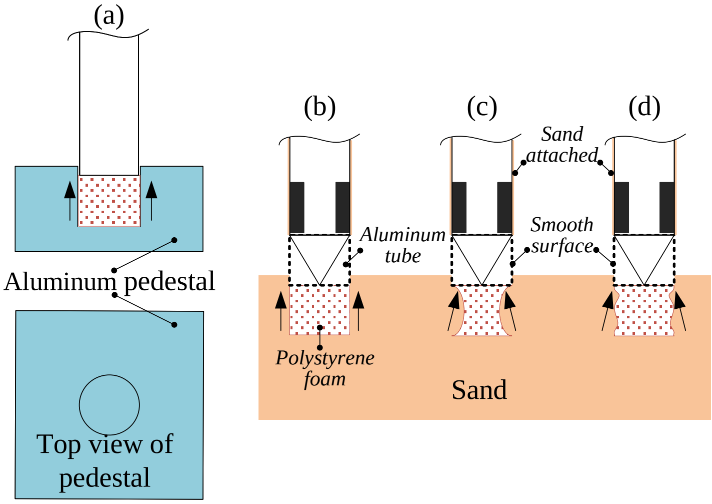

Fig. 3.10. Vertical force response of soft base: (a) 1 g test, and (b d) likely scenario in centrifuge tests

To test the response of the soft base in confined conditions, the pile was loaded at 1 g with the soft base embedded in a cavity (slightly larger than the pile diameter) machined into an aluminium pedestal (see Fig. 3.10(a)). The loading tests were performed at a rate of 0.1 mm/s on a "new" soft base which hadn't been used in centrifuge tests, as well as a "used" tip that had previously been used in two centrifuge loading tests (in case some permanent damage was incurred during tests which affected the loading response). Results in Table 3.3 show that the used soft base is slightly less stiff than the new soft base, but this variation is negligible.

Table 3.3. Base load of friction piles at 1 g and 60 g

	1 g		60 g	
	Used	New	Spin-up	Loading
Load (N)	11	12	150-200	200-300
Disp (mm)	6	6	~1.5	0.882

The ideal behaviour of the soft base is that it would maintain its shape radially while permitting axial compression with minimal reaction on the pile base, as shown in Fig. 3.10(b). However, in the centrifuge tests, the base load (after the centrifuge spin-up to 60 g and after pile loading with settlements reaching 7% of the pile diameter) was much larger than the ≈ 12 N measured in 1-g tests. The soft base decreased the mobilised base resistance by only 60-70% compared to the standard piles (at settlements of 7% pile diameter). Thus, the envisioned behaviour was not achieved during the centrifuge tests. It is likely that the polystyrene was compressed radially, as shown in Figs. 3.10(c)-(d), as a result of the confining stress from the surrounding soil, which would allow increased base resistance to be mobilized.

3.3.4 Centrifuge model package

The experimental package (see Fig. 3.11) developed by Song and Marshall (2020) and Xu et al. (2020a) for vertical loading of fibre-optic instrumented model piles above a displacement-controlled plane-strain model tunnel was used.

The tunnel was buried with a cover C of 180 mm in all tests, giving a cover-to-tunnel diameter ratio of C/D_t=2.0 (also see Fig. 3.4(a)). The tunnel volume loss was calculated based on the axial displacement of a hexagonal wedge shaped shaft which was measured by an LVDT. Two cameras positioned in front of the acrylic wall recorded soil deformations near the wall under amber LED lights. Piles/rafts were centrally located at 75 mm from the front/back walls of the strongbox. The foundation loading system consists of a stepper-motor driven actuator that can operate in load or displacement control, which transmits only vertical loads (perpendicular to the soil surface) to the foundations. The head load and displacement of the pile and raft models were measured by 2 kN load cells and 30 mm Linear Variable Differential Transformers (LVDT), while the variation of pile axial force was acquired using FBG strain sensors (Song and Marshall, 2020). To compensate FBG readings for temperature variation, three temperature sensors with a spacing of 70 mm were attached to the inner wall of a 'dummy' pile installed in the sand approximately 200 mm away from the tunnel centerline.

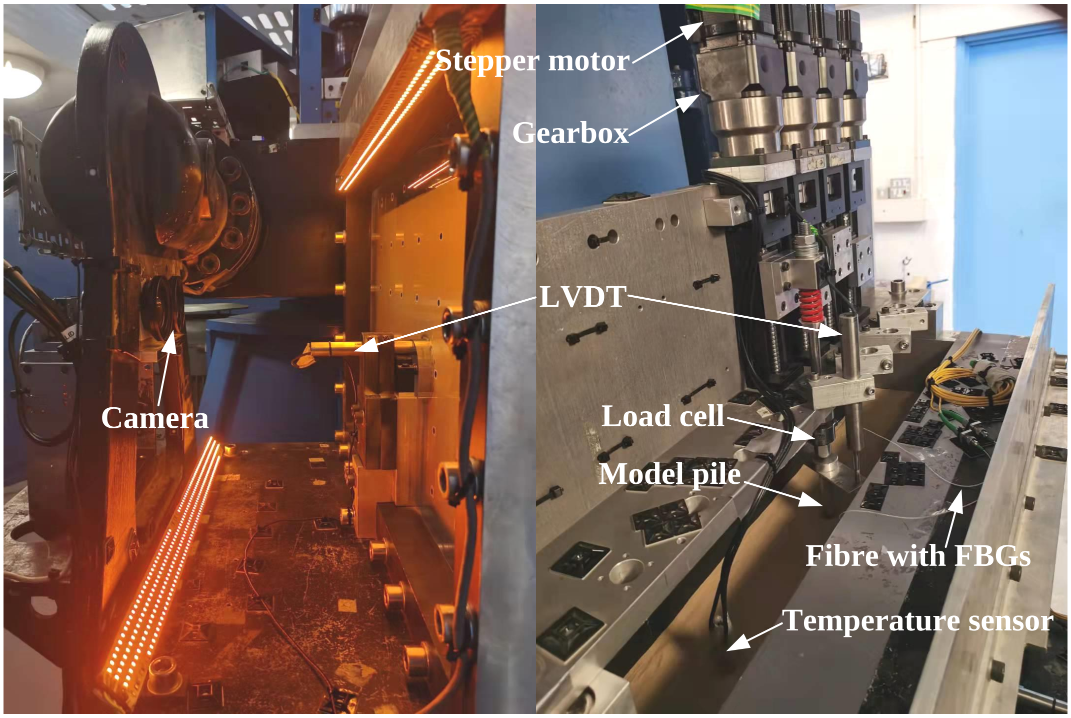

Fig. 3.11. Experimental package of pile loading and tunnelling (left: side view; right; view from above

3.3.5 Test plan

Table 3.4 summarises the tested configurations and corresponding load conditions for Chapter 4. Seven *loading tests* measured the external load-settlement response of the considered foundations. Identical foundations were tested twice to verify repeatability that was proved by consistent results between raft tests R1 and R2, reference pile tests P1 and P2, and friction pile tests FP1 and FP2 (see Fig. 4.3). Note that, in tests R1, R2, and CP1, the ultimate resistance was not measured because the capacity of the loading system was reached (2.2 kN). Also, P2 was not instrumented with FBGs and this test was done concurrently with P1. Nine *tunnelling tests* were performed, including one greenfield test and eight tests where pile foundations were located directly above the tunnel.

Table 3.4. Summary of centrifuge tests at model-scale dimensions

Test series	Test No.	Test label [a]	Offset (mm)	Measured load capacity Q (N) [MN[b]]	Assumed load capacity Q (N) [MN[b]]	Designed service load F_0 (N) [MN[b]]	WL	WL^*
Loading	1	R1	0	(≥) 2138 [7.7]	/	/	/	/
	2	R2	0	(≥) 1911 [6.88]	/	/	/	/
	3	P1	150	1558 [5.61]	/	/	/	/
	3	P2	300	1556 [5.6]	/	/	/	/
	4	CP1	150	(≥) 2017 [7.26]	/	/	/	/
	5	FP1	150	1025 [3.69]	/	/	/	/
	6	FP2	150	883 [3.18]	/	/	/	/
	7	FP3	0	705 [2.54]	/	/	/	/
Tunnelling	8	GF	/	/	/	/	/	/
	9	P3WL1	0	1422 [5.12]	/	1475 [5.31]	1	/
	10	P4.WL0.8[c]	0	/	1422 [5.12]	1085 [3.91]	0.8	/
	11	CP2.WL1[c]	0	/	1422 [5.12]	1475 [5.31]	1	0.7
	12	CP3WL0.8[c]	0	/	1422 [5.12]	1085 [3.91]	0.8	0.5
	13	CP4.WL0.6[c]	0	/	1422 [5.12]	901 [3.24]	0.6	0.4
	14	FP4.WL1	0	/	705 [2.54]	705 [2.54]	1	/
	15	FP5.WL0.7[c]	0	/	705 [2.54]	490 [1.76]	0.7	/
	16	CFP1.WL0.7[c]	0	/	705 [2.54]	490 [1.76]	0.7	0.2

[a] R: raft; P: reference pile without cap; CP: capped pile; FP: friction pile without cap; CFP: capped friction pile; GF: greenfield. [b] Prototype-scale. [c] These tests include post-tunnelling pile loading.

WL is working load level based on capacity of a pile; WL^* is working load level based on capacity of capped pile.

Load capacity (Q) is defined in this study as the resistance mobilised at a settlement S_p of 7% of the pile diameter d_p. In Figs. 4.3, the shaft loads of uncapped piles are fully mobilised at settlements of 6-7% d_p, while the pile external loads tend to continue to increase slightly because of the base loads. For all piles in Table 3.4, the working load level $WL = F_0/Q$ is the ratio between the applied service load F_0 and either measured or assumed load capacity Q of uncapped piles (Korff et al., 2016). The value of WL gives an indication of how far, in terms of applied load, the pile is from a state of failure due to the external head load change (where settlements reach a predefined limit; discussed in more detail in Chapter 4). Note that failure here relates more to pile stability than a serviceability state typically assumed for design (which would have much lower requirements for settlements of about 1-2% d_p (Poulos, 2001)). For the purposes of this study, a reference settlement was needed to obtain the load capacity Q; a value of 7% d_p was selected since, at this settlement, the shaft loads of uncapped piles were typically fully mobilised. The selection of reference settlement is somewhat arguable (i.e. a value of 6% could equally have been adopted with the same argument), however, within a reasonable tolerance, the assumed reference settlement will not affect the main outcomes and conclusions of this study.

As discussed in more detail in Chapter 4, the presence of the rigid model tunnel (before inducing any tunnel volume loss) decreased the load capacity of piles at large settlements for both reference and friction piles (compared to piles that were load tested at locations at an offset to the model tunnel). This resulted in the early onset of large pile settlements in tunnelling tests P3.WL1 and FP4.WL1; for these tests tunnelling ground loss was initiated after the pile had failed (i.e. $WL = 1$). The load capacity Q could be obtained either as a direct measurement from loading tests or from the tunnelling tests where $WL = 1$ (in which the applied service load F_0 resulted in a settlement $S_p \approx 7\%\, d_p$). When analysing the experimental data, the following approach was used to obtain the assumed load capacity Q. (1) For reference piles with no cap, the capacity from loading tests P1 and P2 (average 1557 N) at an offset of 150-300 mm was greater than the measured Q of 1422 N obtained from tunnelling test P3, which was directly above the rigid tunnel. The capacity $Q = 1422$ N from P3 was deemed the most representative for piles directly above the model tunnel; thus, service loads of 1475 N and 1085 N give working load levels (rounded to 1 decimal) of 1.0 and 0.8 for tests P3.WL1 and P4.WL0.8, respectively. (2) Similarly, the WL for capped piles in tests CP2.WL1, CP3.WL0.8, and CP4.WL0.6 corresponds to Q from test P3.WL1 (1422 N). (3) For friction piles, the capacity from loading tests FP1 and FP2 ($Q \approx 954$ N) at an offset of 150 mm from the tunnel also differs considerably to $Q = 705$ N during test FP3 directly above the tunnel; importantly, test FP4.WL1 also gave $Q = 705$ N for the friction pile loaded directly above the tunnel, confirming the impact of the rigid tunnel. Therefore, the WL of uncapped and capped friction piles for tunnelling tests (FP5.WL0.7, CFP1.WL0.7) was evaluated using $Q = 705$ N from FP3. Finally, to account for the soil resistance beneath an embedded cap, an alternative working load level WL^* is indicated in Table 3.4 for capped piles CP and capped friction piles CFP considering the load capacity from the loading test CP1.

3.3.6 Sand preparation

When preparing tests with reference piles (without caps or soft bases), the temporary plate was placed directly at the position of the soil surface ($C/D_t = 2$), sand was poured, the back wall was attached, the strongbox was rotated upright, and piles were pushed into place at 1 g using guides to get the piles in the correct position and ensure they stayed vertical during pushing. This procedure was modified slightly for tests with capped piles and rafts, where the temporary plate was placed at a level corresponding to the underside of the pile caps or rafts, sand was poured, the back wall was attached, the strongbox was rotated upright, the capped piles or rafts were installed, and further sand was poured up to the top of the cap/raft, achieving $C/D_t = 2$ at the top of the buried caps/rafts. For the uncapped/capped friction piles, the temporary plate was placed at the $C/D_t = 2$ level, 75 mm of sand was poured (reaching the middle of the strongbox width where piles are located), the piles were placed at their target positions, the remainder of the sand was poured, the back wall was attached, and the strongbox was rotated upright.

3.3.7 Test procedure

Prior to applying external loads at 60 g, two ‘stabilisation cycles’ were completed, spinning up/down to 60/10 g, with the aim of achieving uniformity in the sand (reducing localised stress concentrations) and getting better repeatability between tests; a notional 5 N load was applied to the load cell throughout this process. In pile loading tests, a velocity of 0.02 mm/s was imposed to the load cell until a settlement of 20% pile diameter (2.5 mm) or the capacity of the loading system (2.2 kN) was reached. An exception to this is loading test FP3, which was loaded using the pre-tunnelling pile loading procedure described below. The tunnelling tests (except greenfield GF) included three stages: pre-tunnelling loading, tunnel volume loss, and (in some cases) post-tunnelling loading. In the first stage, the pile external load was gradually increased to the target service load in intervals of 50 N. During tunnel volume loss, the service load was maintained and volume loss was induced in small increments. The post-tunnelling loading of piles (in tunnelling tests with $WL^{(*)} < 1$; refer to Table 3.4) used the same method as the loading tests, except that the loading speed was reduced to 0.01 mm/s. The reduced loading speed was adopted to avoid damage to the pile and tunnel, which at this stage of tests were relatively close to each other; the rigid tunnel was obviously present in these tests as well.

3.4 Development of a coupled centrifuge-numerical modelling (CCNM) approach for shallow strip foundations

3.4.1 CCNM method overview

The updated CCNM application aims to model the tunnel-masonry wall scenario under plane strain conditions illustrated in Fig. 3.12(a) (other structure types and layouts are also considered). Small-scale (1/70th) models of the strip foundation, soil, and tunnel are included in the centrifuge, while the masonry wall is simulated in Abaqus at full (prototype) scale (see also Fig. 3.15). The initial loads generated by geostatic wall self-weight based on an Abaqus analysis are first applied to the foundation. A small increment of tunnel volume loss (0.1-0.2%) is then initiated in the centrifuge and vertical footing displacement data are transferred to Abaqus, which calculates revised foundation loads based on the level of distortion caused to the wall. These revised loads are then applied within the centrifuge, which may result in displacement changes, which are then transferred again to Abaqus, and the cycle is repeated. Upon reaching a stable state where loads and displacements no longer change, an additional increment of tunnel volume loss is then applied. The “data exchange interface” between the centrifuge and numerical domains is programmed in LabVIEW, allowing the manipulation of data transferred at the interface (e.g. adjusting parameters between model and prototype scales) and the control of various test conditions, such as the activation of the numerical model (handing control of load actuation over to Abaqus), and the initiation of tunnel volume loss (Tang et al., 2024c).

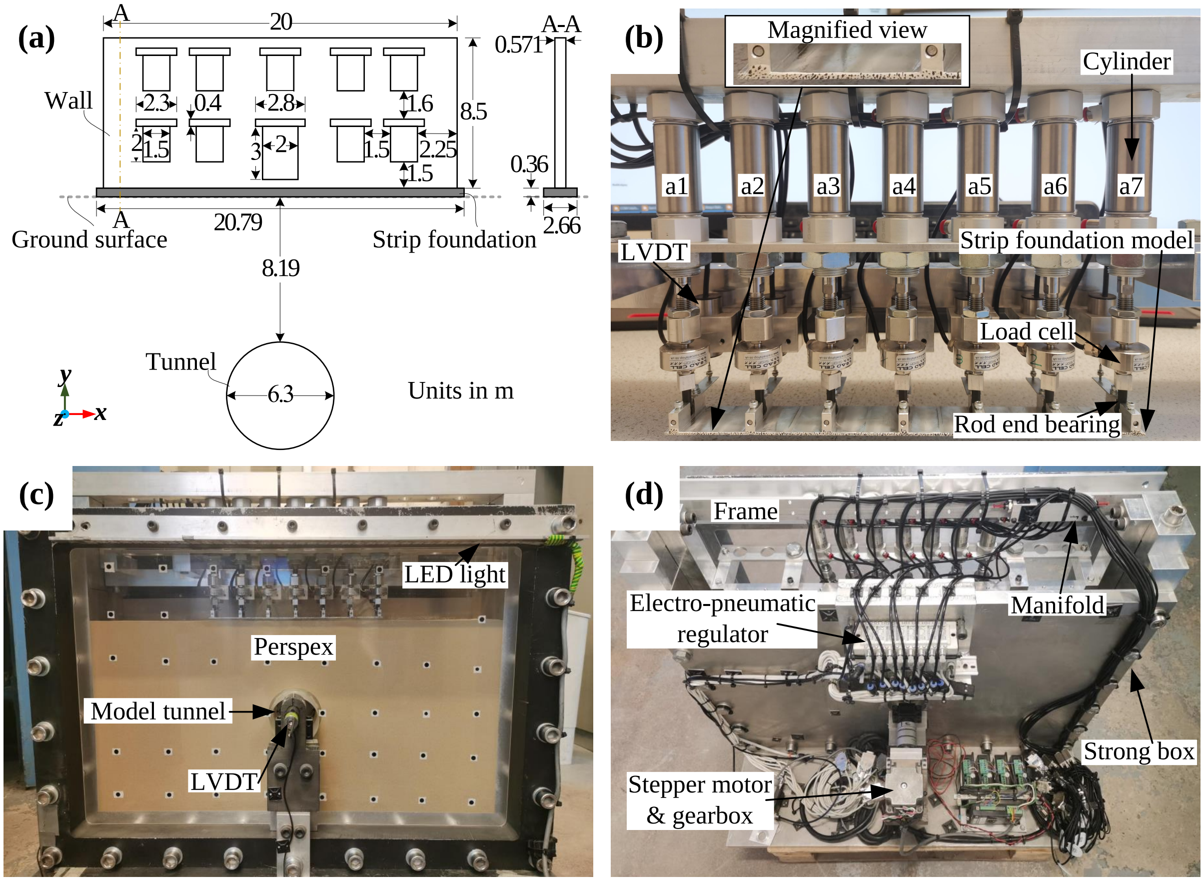

Fig. 3.12. (a) Layout of prototype-scale tunnel-strip foundation-wall, (b) loading system for strip foundation, and (c) front and (d) top views of centrifuge model

3.4.2 Centrifuge model

Fig. 3.12(b)-(d) show the configuration of the centrifuge model. The strong box has internal dimensions of 700 mm × 150 mm × 500 mm, with a front wall made of transparent acrylic that facilitates soil movement visualisation/measurement using two Dalsa Genie Nano-M4020 12.4 megapixel cameras and the GeoPIV-RG technique (Stanier et al., 2016). A fine, dry, poorly-graded silica sand known as Leighton Buzzard Fraction E sand was used. The sand is characterised by a typical average diameter D_{50} of 0.14 mm, a uniformity coefficient U_c of 1.58, a specific gravity G_s of 2.65, a maximum void ratio e_{max} of 1.01, and a minimum void e_{min} of 0.61 (Lanzano et al., 2016). The uniform dense sand ($I_d \approx 90\%$) was prepared using an automatic sand pourer. A 90 mm diameter eccentric rigid boundary mechanical model tunnel, driven by a stepper motor and gearbox (see Fig. 3.12(c-d)), with a maximum tunnel volume loss of 3.5% developed by Song and Marshall (2020) was used to achieve tunnel ground loss. The tunnel was buried with a cover-to-tunnel diameter C/D_t of 1.3, which represents a typical scenario for shallow buried tunnels.

The centrifuge tests were conducted at a gravitational acceleration of 70 g. An aluminium strip foundation model (297 mm × 38 mm × 1.8 mm, Young's modulus $E_a = 70\,\text{GPa}$) was located on the soil surface to simulate a prototype-scale masonry strip foundation (20.79 m × 2.66 m × 0.36 m, Young's modulus $E_m = 3\,\text{GPa}$); the model foundation has the same scaled bending stiffness as the prototype foundation ($EI = 31\,\text{MN}\cdot\text{m}^2$). The minimum width (in the direction of the tunnel) of the foundation was 38 mm to give sufficient space for the pneumatic cylinders used to apply loads (described later). The strip foundation is subjected to loading at seven predetermined positions at a spacing of 47.5 mm (see Fig. 3.12(b)) within raised beams along the foundation (the raised beams ensure load is applied evenly across the width of the foundation). The beams are loaded via rod end bearings (ensuring no bending action is applied) and 3 mm diameter steel rods inserted through the beams (a 6 mm length at the central position of the raised beams was removed to accommodate the rod end bearings).

The loading system consists of a frame, seven pneumatic cylinders (25 mm bore, 25 mm stroke, C85 series, double acting, maximum 1 MPa), a manifold, and eight compact electro-pneumatic regulators (ITV0050-3ML-Q, maximum 1 MPa pressure supply). The pressure within the lower chamber of each cylinder is connected to a unique regulator using 4 mm diameter pipe, while the pressure within the top chamber of all cylinders is linked to a common regulator using a manifold. A dedicated air compressor is used that supplies compressed air at approximately 950 kPa to the regulators. The frame, positioned on top of the strongbox, securely holds the manifold, cylinders, and 10 mm stroke linear variable differential transformers (LVDTs). Load cells with a 500 N range are connected in-line with the cylinder rods and the rod end bearings, enabling the application/measurement of loads onto the strip foundation.

3.4.3 Numerical model

The concrete damage plasticity (CDP) model was initially proposed by Lubliner et al. (1989) and later applied to concrete degradation under cyclic loading by Lee and Fenves (1998). The CDP model is also widely used in numerical modelling of masonry buildings (Furtmüller and Adam, 2011; Yiu et al., 2017; Yacila et al., 2019; Schiavoni et al., 2023). The CDP model is based on continuum and plasticity-damage, allowing for separate input of stress-strain relations and damage variables in tension and compression. The yield surface of the CDP model, modified from the Drucker-Prager strength hypothesis, is not circular in the deviatoric plane (the shape is controlled by K_c, the ratio of the tensile to the compressive meridian; see Fig. 3.13(a)), which enables different yield triaxial tension and compression stresses. The yield function is defined as (Lee and Fenves, 1998; Genikomsou and Polak, 2015):

$$\bar{F} = \frac{1}{1-\alpha}\left(q - 3\alpha p + \beta\sigma_{\max} - \gamma(-\sigma_{\max})\right) - \sigma_c = 0 \tag{3.4}$$

where q is the Mises equivalent effective stress, p is the hydrostatic pressure, $\sigma_{\max}$ is the maximum principal effective stress, and the parameters α, β, and γ are given by:

$$\alpha = \frac{(\sigma_{b0}/\sigma_{c0}) - 1}{2\,(\sigma_{b0}/\sigma_{c0}) - 1} \tag{3.5}$$

$$\beta = \frac{\sigma_c}{\sigma_t}(1-\alpha) - (1+\alpha) \tag{3.6}$$

$$\gamma = \frac{3(1-K_c)}{2K_c - 1} \tag{3.7}$$

where σ_b and σ_c are the biaxial and uniaxial compressive strengths, respectively, and σ_c and σ_t are the effective cohesion stresses for compression and tension, respectively. When $\sigma_{\max}$ is positive, β is active; when $\sigma_{\max}$ is negative, γ is active.

In the CDP model, the potential plastic flow of concrete materials is defined by the schematic dilation angle ψ and the flow potential eccentricity ϵ (see Fig. 3.13(b)), expressed as:

$$\bar{G} = \sqrt{\left(\epsilon\sigma_{t0}\tan\psi\right)^2 + q^2} - p\tan\psi \tag{3.8}$$

where σ_{t0} is the uniaxial tensile stress.

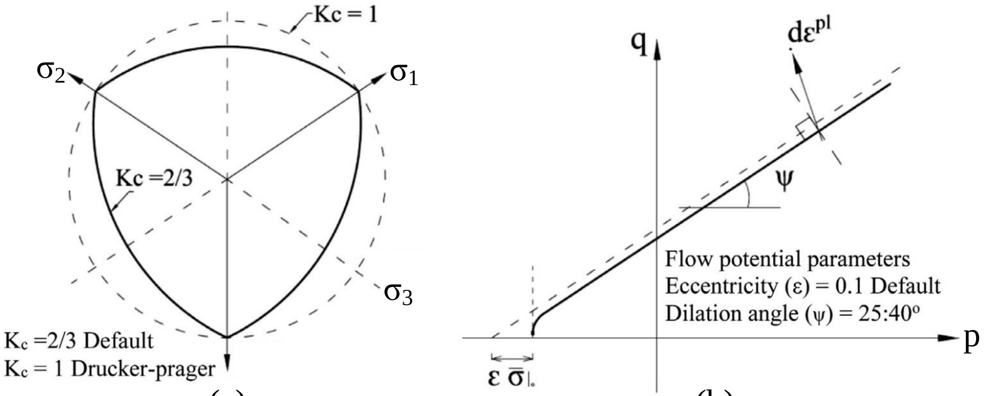

(a) (b)

Fig. 3.13. (a) Yield surfaces in the deviatoric plane and (b) dilation angle and eccentricity in meridian plane (modified from Othman and Marzouk (2018))

A reference masonry wall with dimensions of 20 m in length, 8.5 m in height, and an opening ratio of 19% is considered (H8.5O19, as shown in Fig. 3.12(a)); other walls in this thesis (Table 3.6 and 3.8) are variations based on the reference wall H8.5O19. The walls are modelled at prototype scale using 3D shell elements (S3) in Abaqus based on construction and dimensions derived from previous studies (Burd et al., 2000; Pickhaver et al., 2010; Yiu et al., 2017). According to Yiu et al. (2017), the CDP constitutive model of the masonry walls is characterised by a mass density of 2423.5 kg/m^3, a Poisson's ratio of 0.2, a Young's modulus E_m of 3 GPa, infinite compressive strength, and post-failure tensile stress that increases with a positive gradient of 0.01 E_m after reaching a tensile strength of 50 kPa (hardening failure), while the Young's modulus of the linear elastic lintel in the facade model is taken as 9 GPa. In Yiu et al. (2017), a 215 mm thick masonry wall rested on a 1 m wide strip foundation, resulting in a nominal bearing stress of 33.7 kPa. In the centrifuge, the prototype scale foundation width had to be increased to 2.66 m (as mentioned in the previous section, the minimum model foundation width was 38 mm due to experimental constraints); to achieve the same nominal bearing stress of 33.7 kPa beneath the foundation, the prototype wall thickness from the centrifuge tests was therefore scaled by the ratio of foundation widths (2.66) to 571 mm. This increased both bending stiffness EI and shear stiffness GA_s by the same factor of 2.66 (verified using the methodology provided in Section 3.5.1).

To establish planar conditions within a 3D environment, the numerical models impose global constraints on the displacement degrees of freedom in the z direction and the rotational degrees of freedom about the x and y axes (as defined in Fig. 3.12(a)). These conditions were primarily set to facilitate the implementation of the CCNM approach. Fig. 3.14 compares the tunnelling-induced tensile strain distributions within masonry walls without (i.e. plane stress conditions; H8.5O0** and H8.5O19**) and with these boundary conditions (i.e. plane strain conditions; H8.5O0* and H8.5O19*, which are also presented in Fig. 5.4, where more details are provided) at $V_{l,t} = 2.2\%$. The numerical results were acquired by applying fitted foundation settlements from conventional centrifuge constant-load tests (i.e. tests No. 2 and 4 in Table 3.6) on separate Abaqus models. The results indicate no significant effects from these different boundary conditions, and the assumption for the shell elements that no stress changes through the thickness in such conditions in Abaqus results in zero stress and strain in the z direction (i.e. the direction of the wall thickness). While plane stress conditions are typically considered for the walls, plain strain conditions yield similar results in such cases, thus the CCNM test results under plane strain conditions remain valid.

The boundary conditions applied to the 50 nodes along the base of the wall in Abaqus allowed free horizontal movement in the x-direction and rotation about the z-axis; vertical displacements (in the y-direction) are controlled according to centrifuge test measurements through a connection to the data exchange interface using a FORTRAN subroutine. The ex-

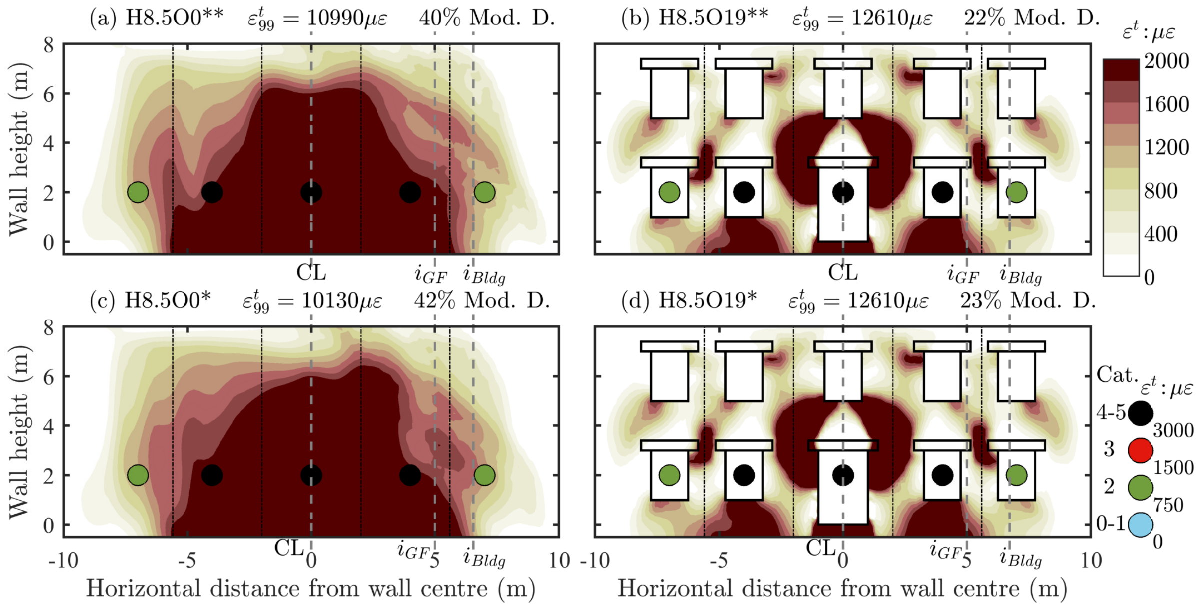

Fig. 3.14. Distributions of max principal strain (tensile strain) and wall damage assessment at $V_{l,t} = 2.2\%$ for walls with $e/L = 0$: (a)-(b) H8.5O** and H8.5O19** under plane stress conditions, (c)-(d) H8.5O* and H8.5O19* under plane strain conditions (gray dashed lines represent the tunnel centreline CL, and inflection points of greenfield surface i_{GF} and wall base settlements i_{Bldg})

perimental equipment has a limitation in that it does not allow measurement or control of (1) the rotation of the model foundation about the z-axis and (2) the horizontal (x-direction) displacements of the foundation. Limitation 1 may result in some disparity between centrifuge and numerical models, however comparison of the displaced shape of the base of the wall in Abaqus with the foundation settlements measured in the centrifuge demonstrate that this disparity is negligible (in Figs 5.2, 5.9, 6.10, and 6.11 compare 'LVDT fitting curve', which is the settlement imposed at the base of the wall in Abaqus, with 'foundation LVDT'). Regarding limitation 2, since measurements of lateral strains of the foundation could not be integrated into the CCNM control program (horizontal foundation displacements were only measured by post-test image analysis methods), it was decided to allow free horizontal movements along the base of the wall in the numerical model. Restraining horizontal displacements along the wall base would not have been realistic as strains need to occur due to wall bending. An approximated strain, calculated in real-time within the control program based on beam theory and the measured deformed shape of the wall, could have been imposed on the wall base in the numerical model; this approach would admittedly have been the best option, however it was overlooked during the experiment planning stages. To consider the implications of this limitation, the numerical modelling results from Yu (2024), who considered the effect of foundation-soil interface friction on a similar masonry wall within a numerical model, can be used; a detailed discussion of this is provided in Section 5.3. In summary, for central cases, the angular distortion (β) representing shear deformation could be underestimated by approximately within 10%, and minimal effect was observed in the extent and degree of (tensile) damaged area, when comparing results for a soil-foundation friction coefficient of $\mu = 0$ (comparable to the scenarios modelled in this paper) against results with $\mu = 0.3$ (a more typically adopted value). Note that the scenarios considered in this paper represent a 'pseudo' smooth interface between the wall and the ground surface because the foundation was physically modelled in the centrifuge, hence the effects of limitation 2 are expected to be less than those considered by Yu (2024).

Two analysis steps are implemented in Abaqus: the first involves the application of a gravity load to the walls within a single increment, while the second step is the subsequent coupled simulation with the centrifuge model through the data exchange interface, necessitating a substantial number of increments to cover the entire testing duration.

3.4.4 Coupled modelling

Firstly, each centrifuge model underwent three spin up/down/up “stabilisation cycles" (1-70-10-70-10-70 g), to reduce localised soil stress concentrations and improve test repeatability; the strip foundation is suspended from the load actuators during these cycles and is not in contact with the soil. The foundation is then lowered slowly onto the soil and a preliminary load of 2 N is simultaneously applied to the seven loading positions on the strip foundation using a LabVIEW load-control program, thereby ensuring the establishment of full contact between the bottom of the strip foundation and the soil surface. The test progresses as follows, with numbered items relating to the numbers in Fig. 3.15:

1. Initial loads (F_{f_0}) from the wall self-weight are simultaneously applied to the foundation in increments of 25% of the final load. Soil surface settlements are then initialised to 0.

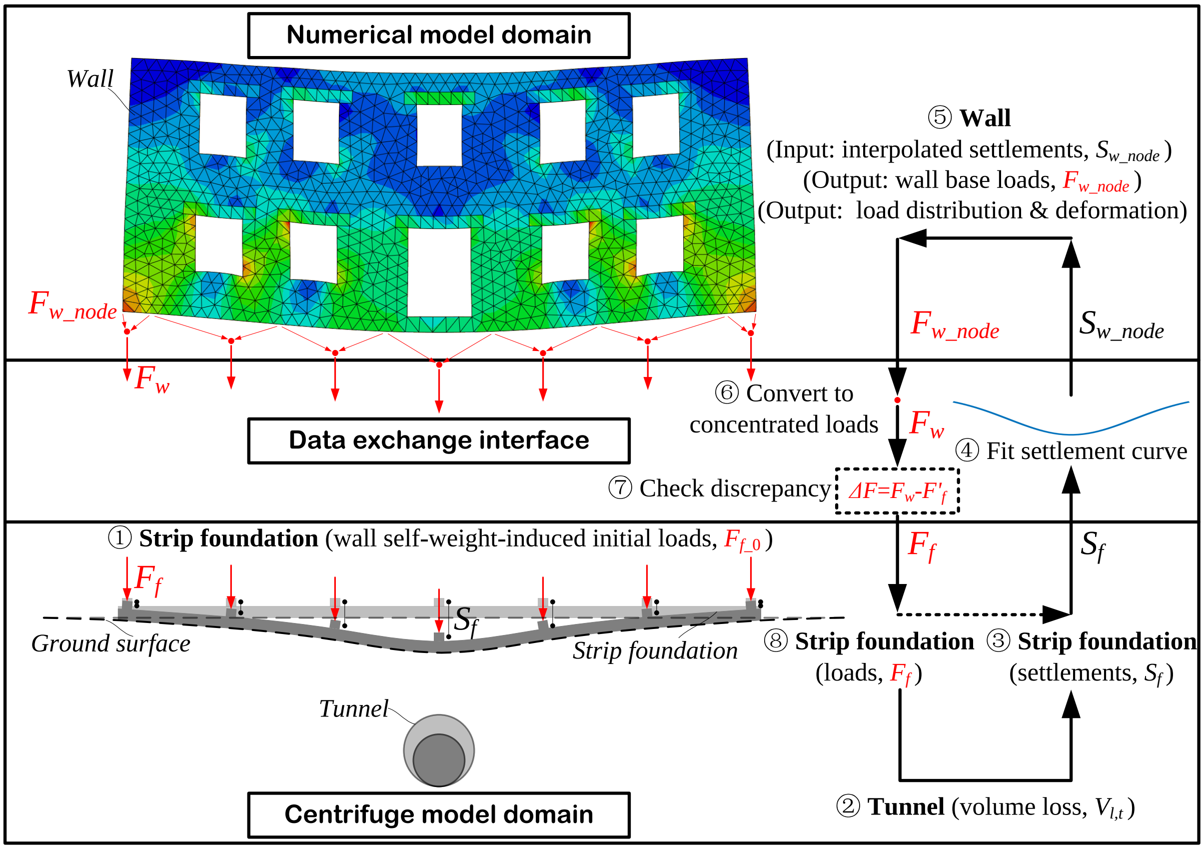

Fig. 3.15. Diagram of the coupled centrifuge-numerical modelling of shallow foundations

The data exchange interface is activated and control of the foundation load is passed to Abaqus.

2. An increment of tunnel volume loss is manually initiated ($\Delta V_{l,t} \approx$ 0.1-0.2%), causing settlements of the soil and the strip foundation.

3. The seven LVDT measurements of foundation settlements (S_f) are transferred to the data exchange interface when certain stabilisation criteria are met and a displacement threshold is reached ($|S_{f,tol}| \geq 15\,\mu$m).

4. The strip foundation settlements (S_f) are fitted using the fitting curves according to the tunnel-wall eccentricity ratio e/L (see Table 3.5) to get the input of settlement (S_{w_node}), after scaling to prototype scale and interpolating, of the 50 nodes along the base of the wall in the numerical model.

5. The wall base loads (F_{w_node}) are calculated in the numerical model according to the input wall base settlements (S_{w_node}); the change in settlement along the base of the wall in the numerical model is always from a 'reference' state corresponding to the final displacement profile at the end of the preceding volume loss increment ($S_{w\_node\_ref}$); this ensures that the numerical model state is not 'cycled' through intermediate states in the process of reaching its final equilibrium state.

6. Revised wall base loads (F_{w_node}) are transferred to the data exchange interface and distributed, after scaling to model scale, to the 7 concentrated (actuator) loads (F_w) according to the following convention: n1-3[3]:a1, n4-13[10]:a2, n14-21[8]:a3, n22-29[8]:a4, n30-37[8]:a5, n38-47[10]:a6, n48-50[3]:a7, where n#-# indicates the node number in Abaqus, [#] is the total number of nodes used to calculate the force for a given actuator, and a# is the actuator number in the centrifuge (see Fig. 3.12(b)).

7. The data exchange interface assesses whether loads are balanced ($F_f = F_w$). If yes, continue with step 8, and wait for the next tunnel volume loss increment (i.e. step 2, which is manually initiated; as long as the displacement threshold is not reached ($\left|S_{f,tol}\right| < 15\,\mu\text{m}$) and the stabilisation criteria are met). If not, continue with step 8 and repeat steps 3-8 (this process, i.e. steps 3-8, repeat automatically until a stable and balanced condition is achieved).

8. The new loads (F_f) from the data exchange interface are applied to the strip foundation, potentially resulting in new settlements of both the strip foundation and the underlying soil.

3.4.5 Data transfer principles

The following provides additional details relating to certain aspects of the control system and how data was managed in the data exchange interface.

Pneumatic cylinder air pressure control (load control): The bottom chamber of the pneumatic cylinders is controlled via the pressure regulators using a Proportional-Integral-Derivative

Table 3.5. Fitting curves

e/L	Curve type	Parameter
$e/L = 0$	Modified Gaussian curve (Vorster et al., 2005b): $f(x) = \frac{nS_{v,max}}{(n-1)+\exp[\alpha(x^2/i^2)]}$, where $n = \exp(\alpha)\frac{2\alpha-1}{2\alpha+1} + 1$	$S_{v,max}, \alpha, i$
$0 < e/L < 0.5$	Exponential Modified Gaussian curve: $f(x) = \exp(-\lambda x)\cdot\exp\left(-\frac{(x-\mu)^2}{2\sigma^2}\right)\cdot\left(1+\text{erf}\left(\beta\frac{(x-\mu)}{\sqrt{2}}\right)\right)$	$\lambda, \mu, \sigma, \beta$
$e/L = 0.5$	Second-order Fourier curve: $f(x) = a_0 + a_1\cos(\omega x) + b_1\sin(\omega x) + a_2\cos(2\omega x) + b_2\sin(2\omega x)$	$a_0, a_1, b_1, a_2, b_2, \omega$

(PID) algorithm within LabVIEW. Using the target load F_f (either manually input or obtained from Abaqus) and the load cell data, the PID algorithm adjusts the input voltage to the pressure regulator (i.e. the bottom chamber pressure) until the required target load is achieved. The test load range is typically set from -20 N (an upwards force of approximately 1/6 the foundation self-weight, representing the force needed to lift the (local) foundation off the surface) to half of the wall self-weight.

Settlement data transfer rules for centrifuge model (steps 3-4): The prerequisite for sending settlement data from the centrifuge to Abaqus is that the foundation system reaches a stable state and that displacements are above a certain threshold (such that insignificant changes in readings are not continually passed across the data exchange interface). The stabilisation criteria require ① the load tolerance $|F_{f,tol}| = |F_f - F_{f,cur}| \leq 5\,\text{N}$, where F_f is the target load and $F_{f,cur}$ is the current load cell reading, ② the maximum fluctuation of the foundation load cell readings $|F_{f,fluc}| \leq 3\,\text{N}$, and ③ the settlement fluctuation of the strip foundation $|S_{f,fluc}| \leq 5\,\mu\text{m}$; the displacement threshold condition is represented by the foundation settlement tolerance $|S_{f,tol}| = |S_{f,cur} - S'_f| \geq 15\,\mu\text{m}$, where $S_{f,cur}$ is the current LVDT reading and S'_f is the previous target from Abaqus (i.e. the settlement change is sufficiently large to be passed to Abaqus). Once these criteria are met for a time window of $ST = 5\,\text{s}$, the average of foundation settlement S_f over the preceding 1 s are transferred to the data exchange interface for fitting the modified Gaussian curves.

Settlement input rules for Abaqus (steps 4-5): The difference (ΔS) between the current target settlement (S_{w_node}) and the reference settlement for the wall base nodes after settlement curve fitting (i.e. the initialised soil/foundation settlement or the stable settlement at the end of the last tunnel volume loss process, $S_{w\_node\_ref}$) is applied in Abaqus in 10 increments to ensure the convergence of the Abaqus analysis of each increment. For the CDP masonry wall model, this process takes ≈ 4 s, with each increment taking ≈ 400 ms; the exact timing depends on the convergence time of the Abaqus analysis.

Load output rules for Abaqus (steps 5-6): According to the input foundation displacements, the Abaqus analysis provides a new load distribution along the building base (F_{w_node} for each of the 50 nodes). These are transferred to the data exchange interface after each assignment of nodal settlements in steps 4-5. The distributed loads at the complete settlement curve (S_{w_node}) are grouped into seven discrete loading points based on their proximity to the load actuation points in the centrifuge (see Fig. 3.15); the vertical loads from each node within a group are added together (F_w) to obtain the target actuator load (F_f).

Load application rules for centrifuge model (steps 6-8): The application of the target loads F_w from Abaqus directly to the centrifuge model caused stability issues, especially at the outset of tests where settlement magnitudes were low and building stiffness was greatest. Prior to the onset of yielding within the wall, fluctuations in foundation settlements caused relatively large variations in foundation load (and subsequently settlement) changes, ultimately preventing the overall system from stabilising. To overcome these issues, the loads from Abaqus were essentially 'damped' according to the following rules. If the load increment at a given actuation point $|\Delta F| = \left|F_w - F'_f\right| > 3\,\mathrm{N}$, where F'_f is the previous target load, the target load $F_f = 50\%\Delta F + F'_f$ is applied; if $|\Delta F| \leq 3\,\mathrm{N}$, the target loads are applied directly ($F_f = F_w$, i.e. load is balanced). If the application of ΔF causes settlements that satisfy the 'Settlement data transfer rules for centrifuge model (steps 3-4)' criteria, then a new cycle (steps 3-8) is initiated; if the stabilisation criteria are satisfied and the displacement threshold is not exceeded (i.e. the whole model is stable and balanced), the next tunnel volume loss trigger can be activated.

3.5 Centrifuge modelling of tunnel-soil-masonry wall interactions using CCNM

3.5.1 Calculation of wall bending stiffness EI and shear stiffness GA_s

It is generally the case that the length of a beam is much larger than the cross-sectional dimensions. In the walls considered in this thesis, for example, the length-to-height ratio is $L/H = 20/8.5 = 2.35$ for two-storey masonry walls, which does not conform to the traditional concept of a beam. Short 'beams' are more prone to erroneous estimates caused by significant local deformations when using beam theories. Fig. 3.16 shows the impact of wall length-to-height ratio (achieved by connecting multiple walls, e.g., four walls in Fig. 3.17) on the bending EI and shear stiffness GA_s of two-storey masonry walls without and with 19% openings (H8.5O0 and H8.5O19), where the strip foundation is also included but the coefficient $(L/H)/3$ is not considered (the detailed calculations are provided later). Fig. 3.16 demonstrates that the connection of four walls or more can provide more stable results.

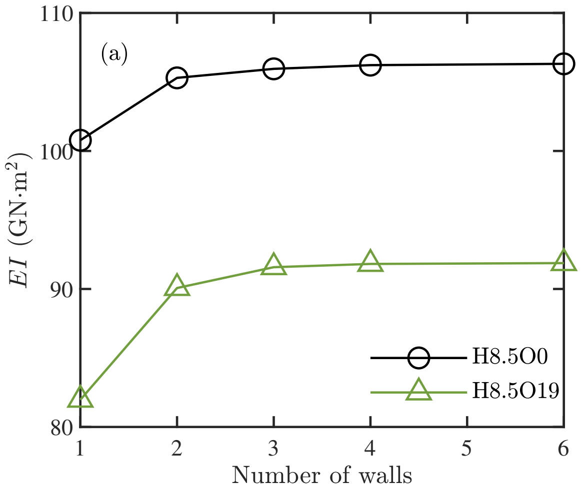

Fig. 3.16. Effect of wall number on (a) EI and (b) GA_s (foundation is considered, coefficient $(L/H)/3$ is not considered)

Therefore, to estimate the bending and shear stiffness of the walls, four two-storey masonry walls were connected together using the finite element analysis software Abaqus to form a longer beam model $4L/H = 20/8.5 = 9.4$ (see Fig. 3.17), subjected to three-point loading, four-point loading, and cantilever beam testing. The resulting maximum deflections δ_{tot} from these loading tests were used to calculate the bending (EI) and shear stiffness (GA_s) of the 'long' wall based on Timoshenko beam theory (Eqs. 3.9-3.11; this method was also adopted by Xu et al. (2020b)). To compensate for the size effect of the beam (i.e. the 'long' wall), the result is multiplied by a coefficient of $(L/H)/3 = 0.78$ (as suggested by Pickhaver et al. (2010) for beams with $L/H < 3$). Note that the walls tested here only incorporate the elastic properties of the CDP constitutive model; changes in wall stiffness due to yielding, which does occur during the CCNM tests, are not considered in this estimation of stiffness. The calculations are also applicable to other types of masonry walls in this thesis, with coefficient $(L/H)/3$ depending on the specific wall.

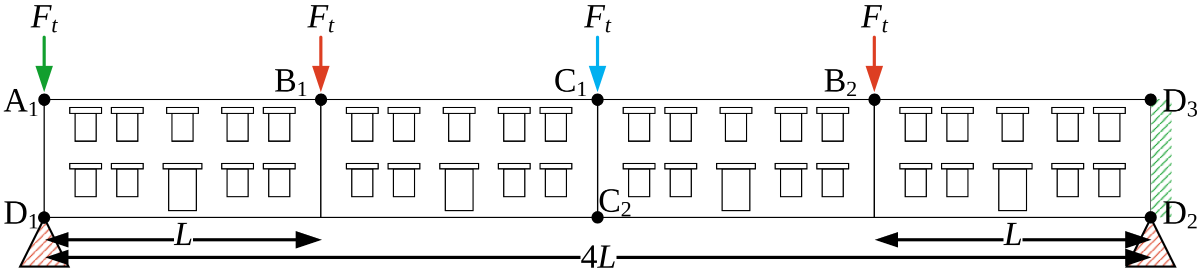

Fig. 3.17. Configuration of loading tests in Abaqus

For three-point loading tests, points D$_1$ and D$_2$ are supported vertically, and point C$_1$ is loaded by a concentrated vertical load F_t (the maximum deflection δ_{tot} is measured at the centre of line C$_1$C$_2$):

$$\begin{aligned} \delta_{tot} = \delta_{shear} + \delta_{bending} = \frac{F_t \cdot 4L}{4GA_s} + \frac{F_t(4L)^3}{48EI} \\ \frac{\delta_{shear}}{\delta_{bending}} = \frac{12EI}{(4L)^2 GA_s} = 12F_{sb} \end{aligned} \tag{3.9}$$

where $F_{sb} = EI/((4L)^2 GA_s)$ is a constant.

For four-point loading tests, points D$_1$ and D$_2$ are supported vertically, and points B$_1$ and B$_1$ are loaded (the maximum deflection δ_{tot} is measured at the centre of line C$_1$C$_2$):

$$\begin{aligned}
\delta_{tot} &= \delta_{shear} + \delta_{bending} = \frac{F_t L}{GA_s} + \frac{F_t L(3(4L)^2 - 4L^2)}{24EI} \\
\frac{\delta_{shear}}{\delta_{bending}} &= \frac{24EI}{(3(4L)^2 - 4L^2)GA_s} = \frac{24(4L)^2}{3(4L)^2 - 4L^2} F_{sb}
\end{aligned} \tag{3.10}$$

For cantilever beam testing, side D_2D_3 is fixed, and point A_1 is loaded (the maximum deflection δ_{tot} is measured at the centre of line A_1D_1):

$$\begin{aligned}
\delta_{tot} &= \delta_{shear} + \delta_{bending} = \frac{F_t \cdot 4L}{GA_s} + \frac{F_t(4L)^3}{3EI} \\
\frac{\delta_{shear}}{\delta_{bending}} &= \frac{3EI}{(4L)^2 GA_s} = 3F_{sb}
\end{aligned} \tag{3.11}$$

3.5.2 Test plan of verification and application of CCNM testing approach

This test plan is relevant to Chapter 5. Eight centrifuge tests (see Table 3.6) were carried out in the 50g-tonne centrifuge at the University of Nottingham Centre for Geomechanics (NCG), including one greenfield (GF) tunnelling test which serves as a reference, five tunnel-masonry wall interaction tests using the CCNM method for various tunnel-wall eccentricities (e), and two tunnel-masonry wall interaction tests using a constant wall dead load which provide a reference for evaluating the effect of wall load redistribution within the CCNM tests.

The effect of wall load redistribution on the tunnel-masonry wall interactions was first assessed by comparing CCNM test results against equivalent ‘conventional’ tests with constant dead loads applied to the foundation (indicated by an * in the test label); this was done for the 0% (H8.5O0) and 19% (H8.5O19) opening walls, but only for the case where the wall was located directly above the tunnel (i.e. $e/L = 0$, tests No.2-5 in Table 3.6).

The effect of the relative tunnel-wall location, quantified by $e/L = 0$ to 0.5 (see Fig. 3.18) was then considered using the CCNM method (tests No.5-8 in Table 3.6). Within the CCNM data transfer process, where experimental foundations settlements are fitted using a mathematical curve to obtain settlements at the 50 nodes along the numerical wall base (Step 4 from above and in Fig. 3.15), it was necessary to apply different fitting curves in tests with different e/L (see Table 3.5). A modified Gauss curve (Vorster et al., 2005b), previously employed by Marshall

Table 3.6. Test summary

No.	Label [a]	Testing method	e/L [b]
1	GF	/	/
2	H8.5O0*	Constant load	0
3	H8.5O0	CCNM	0
4	H8.5O19*	Constant load	0
5	H8.5O19	CCNM	0
6	H8.5O19	CCNM	1/6
7	H8.5O19	CCNM	1/3
8	H8.5O19	CCNM	1/2

[a] GF: greenfield; H: height; O: % of opening

[b] e: tunnel-wall eccentricity; L: wall length

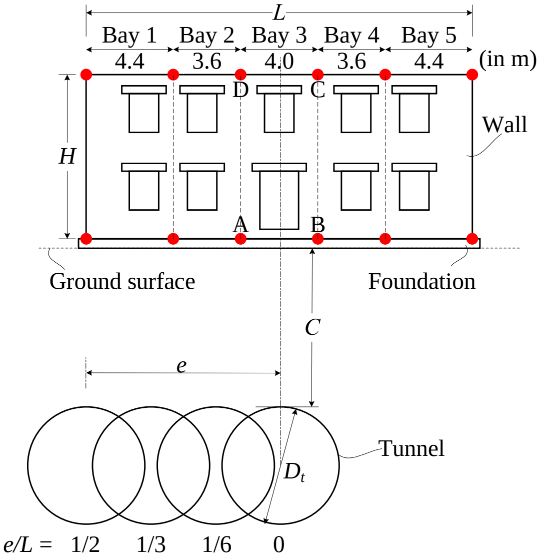

Fig. 3.18. Configuration of eccentric scenarios

et al. (2012) and Franza et al. (2019) to fit tunnelling-induced ground surface settlement, was adopted to acquire symmetric settlement curves when $e/L = 0$; an exponential modified Gaussian curve was used for eccentric cases with $0 < e/L < 0.5$; and a second-order Fourier curve for $e/L = 0.5$. Curve fitting parameters were obtained automatically within LabVIEW using a least-squares regression technique.

Franza et al. (2020a) proposed $F_{sag/hog}$ (see Eq. 2.30)) to distinguish wall deformations, where for $F_{sag/hog} < 0.04$, wall deformations are dominated by bending, whereas $F_{sag/hog} > 1$ indicates a wall will be characterised by shear deformations. The key parameter values for the cases considered in this study are provided in Table 3.7. In particular, note that the value of $F_{sag/hog}$ is typically between 0.04-1; this indicates that the wall in this study will exhibit mixed bending and shear response. In Table 3.7, values of EI and GA_s are provided for the wall only (for information) and for the wall with the foundation (used in subsequent parameter calculations).

Table 3.7. Parameters related to wall bending and shear stiffness

Wall	EI^a (GN$\cdot$m^2)	$GA_s{}^a$ (GN)	$F_{sag}{}^b$	$F_{hog}{}^b$
H8.5O0(*)	69.3/101.9	4.4/4.7	^{c}0.10, / , / , / ^{d}0.16, / , / , /	^{c}1.07, / , / , / ^{d}0.64, / , / , /
H8.5O19(*)	52/88.1	1.9/1.8	^{c}0.18, 0.18, 0.30, 0.71 ^{d}0.27, 0.27, 0.39, 1.07	^{c}1.86, 0.53, 0.25, 0.14 ^{d}1.11, 0.40, 0.20, 0.12

[a] Wall only / wall + foundation.

[b] Range relates to walls with varying $e/L = 0, 1/6, 1/3, 1/2$; [c] at $V_{l,t} = 1.1\%$; [d] 2.2%.

3.5.3 Test plan of tunnel-soil-masonry wall interaction mechanisms

This test plan is relevant to Chapter 6. Table 3.8 summarises the test configurations. There are ten centrifuge tunnelling tests, including one greenfield test without superstructures (GF, test No.1) and nine CCNM tests with masonry walls directly above the tunnel (labelled by the building height H, the door and window opening percentage O, and the masonry Young's modulus E and density d when applicable). The bending and shear stiffness of the masonry walls were scaled by the ratio of building length-to-height ratio L/H to a critical value of 3 when L/H< 3 to avoid an over-stiff response (Pickhaver et al., 2010).

In Table 3.8, the bending and shear stiffness of wall + foundation is, typically as expected, higher than that of a single wall, however, several counterintuitive values are also observed (for example, H8.5O19 and H8.5O27, where the existence of the foundation reduces the shear stiffness). This is probably because, after adding the foundation, the wall length-to-height ratio L/H is reduced (that directly affects the calculation results according to the rule of L/H< 3) and load distributions within walls are altered when loaded (especially for the two-storey wall with larger openings H8.5O27).

The test plan encompasses five standard walls (tests No.2-6), as shown in Fig. 3.19. The number of storeys in a wall significantly influences wall bending stiffness EI and self-weight (which determines the surface pressure; H4.5O20, H8.5O19, and H12.5O19), while openings notably affect shear stiffness GA (H8.5O0, H8.5O19, and H8.5O27). These tests were carried out on these masonry walls to study the role of wall geometries (i.e. the number of storeys and opening ratios) in tunnel-masonry building interaction scenarios.

Four non-standard wall tests (tests No.7-10, with the same geometry as H8.5O19), were con-

Table 3.8. Test summary (in prototype scale)

Test series	No.	Label [a]	Height (m)	Opening (%)	EI [b] (GN·m^2)	GA_s [b] (GN)	Surface pressure (kPa)
	1	GF	/	/	/	/	/
Standard	2	H4.5O20	4.5	20	12.7/26	0.8/1	17.7
	3	H8.5O19	8.5	19	52/88.1	1.9/1.8	33.6
	4	H12.5O19	12.5	19	106.6/161.6	1.9/2	49.6
	5	H8.5O0	8.5	0	69.3/101.9	4.4/4.7	41.7
	6	H8.5O27	8.5	27	47.5/71.8	1.1/0.9	30.3
Non-standard	7	H8.5O19E-	8.5	19	12.1/33.4	0.4/0.4	33.6
	8	H8.5O19E+	8.5	19	107.5/146.9	3.9/3.8	33.6
	9	H8.5O19d-	8.5	19	52/88.1	1.9/1.8	17.7
	10	H8.5O19d+	8.5	19	52/88.1	1.9/1.8	49.6

[a] GF: greenfield; H: height; O: opening percentage; E: Young's modulus; d: density; +: increase; -:decrease; [b] EI: bending stiffness; GA_s: shear stiffness; wall only / wall + foundation

ducted to further investigate the influence of bending stiffness and wall self-weight on building responses during tunnel excavation. H8.5O19E- and H8.5O19E+ are derived from H8.5O19, with Young's modulus being decreased and increased to achieve bending stiffness approximately equal to that of H4.5O20 and H12.5O19, respectively. Note that the Young's modulus of lintels is always 3 times that of masonry. Similarly, H8.5O19d-, H8.5O19, and H8.5O19d+ are characterised by masonry density, the former and the latter equipped with the same building self-weight (or surface pressure) as H4.5O20 and H12.5O19, respectively.

3.6 Summary

This chapter provided an overview of the testing methods, equipment, plans, and procedures, including the geotechnical centrifuge modelling technique, universal experimental package (for greenfield tunnelling), detailed testing configurations for TSPI, development of a coupled centrifuge-numerical modelling (CCNM) approach for shallow strip foundations, and detailed

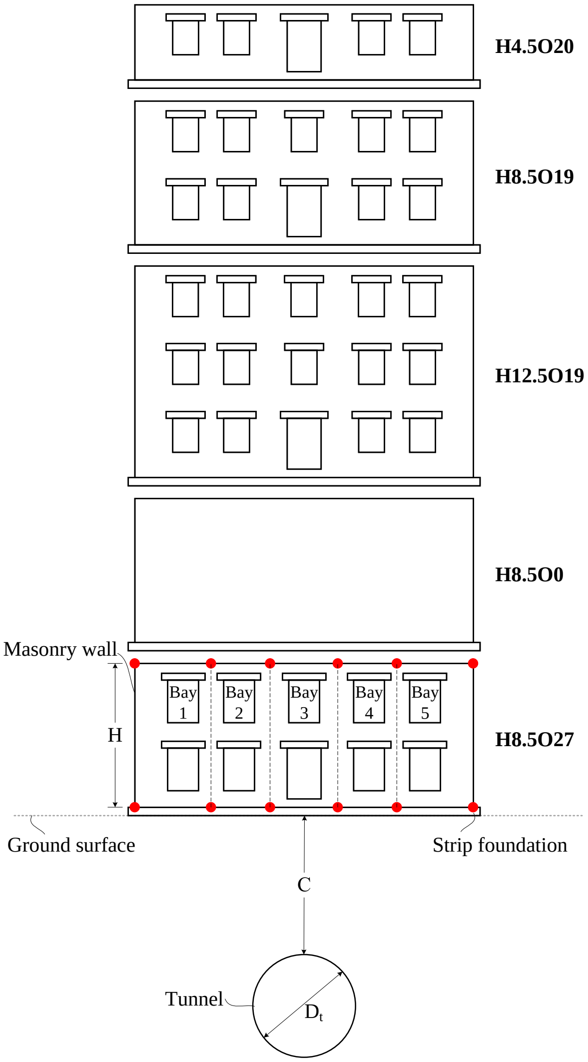

Fig. 3.19. Test layout with different building types

testing configurations for TSBI. These methods and equipment will serve the studies of TSPI (within Chapter 4) and TSBI mechanisms (within Chapters 5 and 6). The advanced coupled centrifuge-numerical modelling (CCNM) approach for shallow strip foundations, including its equipment and basic logic, is an important innovation of hybrid simulation technology in centrifuge testing.

Chapter 4

Load transfer mechanisms for capped piles

The expansion of urban areas requires the construction of tunnels, which often occurs close to existing pile foundations. As a result, design processes must include appropriate consideration of the effects of new tunnel construction on existing structures.

Centrifuge testing has been used to characterise the effects of tunnelling on single piles (Jacobsz et al., 2004; Lee and Chiang, 2007; Marshall and Mair, 2011; Williamson et al., 2017), pile groups with elevated rigid caps (Ng et al., 2014; Boonsiri and Takemura, 2015; Soomro et al., 2018), or piled buildings (Franza and Marshall, 2019a; Song and Marshall, 2020). These studies confirmed field observations (Selemetas and Standing, 2018; Mohamad et al., 2022) that, for isolated piles or a flexible superstructure, piles directly above the tunnel undergo settlements that are greater than surface greenfield settlements. However, in contrast to displacement (driven/jacked) piles, extremely large pile settlement or a steep increase in pile settlement with tunnel volume loss (defined as *geotechnical failure*) is not expected for non-displacement (bored) piles that have a service load lower than half of the load capacity, i.e. safety factor is greater than 2 (Marshall et al., 2020). The above experiments were carried out in the absence of a cap/grade beam that could be in contact with the soil surface, creating a "piled raft" foundation system described by Poulos (2001) (referred to here as a "capped pile" for the foundations where piles are the primary structural elements). Mair and Williamson (2014) reported field data that showed, for a piled building with a reinforced concrete grade beam, foundation settlements were similar to greenfield movements at the soil surface. The influence of such a connected shallow foundation in contact with the soil on the tunnel-pile interaction problem has not been adequately investigated. Research on tunnel-piled raft interactions has been conducted (Mu et al., 2012; Lu et al., 2020), however this has focused on rafts with multiple piles, which makes it difficult to isolate the fundamental mechanisms controlling the response of a single pile from load redistribution between piles through the connected raft.

This chapter uses data from geotechnical centrifuge tests in dry sand (see Table 4.1, which is the same as Table 3.4 in Section 3.3) to investigate how caps/beams in contact with the surface influence settlement and load transfer mechanisms of non-displacement piles prior to, during, and after tunnelling. Five foundation types are considered under varying vertical load conditions: an uncapped pile (the 'reference' pile for comparison), a capped pile in which the ideal cap is in contact with the ground (which may represent structurally connected grade beams, part of a connected raft foundation, or a single pad connected to the pile head), an uncapped friction pile (where the pile has a soft base such that base resistance is decreased compared to the reference pile), a capped friction pile, and a raft only (with the same size as the pile caps). Piles were instrumented with fibre Bragg grating (FBG) strain sensors to quantify the distribution of mobilised forces within the foundations during loading and tunnelling tests. This chapter presents prototype-scale results characterising the differences between capped and uncapped pile response to loading and tunnelling, including load transfer mechanisms, pile head-to-greenfield surface settlement ratios, and post-tunnelling behaviour of piles.

Piles with relatively high working load levels (i.e., low safety factors) were tested in this study as critical scenarios for large settlements induced by tunnelling. In addition, the base resistance in the tested piles was higher than typically assumed for capped piles in design; in the context of tunnel-pile interaction, this scenario (with relatively high base loads) may be considered as conservative, since tunnelling beneath piles predominately affects the base capacity of the pile. Important interaction mechanisms are demonstrated and quantified in this chapter, however readers should appreciate that the context of the outcomes does not necessarily align with design, where safety factors may be higher and pile base load resistance (as a proportion of total load capacity) may be lower. The contents of this chapter have been published (Tang et al., 2024a).

Table 4.1. Summary of centrifuge tests at model-scale dimensions

Test series	Test No.	Test label [a]	Offset (mm)	Measured load capacity Q (N) [MN[b]]	Assumed load capacity Q (N) [MN[b]]	Designed service load F_0 (N) [MN[b]]	WL	WL^*
Loading	1	R1	0	(≥) 2138 [7.7]	/	/	/	/
	2	R2	0	(≥) 1911 [6.88]	/	/	/	/
	3	P1	150	1558 [5.61]	/	/	/	/
	3	P2	300	1556 [5.6]	/	/	/	/
	4	CP1	150	(≥) 2017 [7.26]	/	/	/	/
	5	FP1	150	1025 [3.69]	/	/	/	/
	6	FP2	150	883 [3.18]	/	/	/	/
	7	FP3	0	705 [2.54]	/	/	/	/
Tunnelling	8	GF	/	/	/	/	/	/
	9	P3WL1	0	1422 [5.12]	/	1475 [5.31]	1	/
	10	P4.WL0.8[c]	0	/	1422 [5.12]	1085 [3.91]	0.8	/
	11	CP2.WL1[c]	0	/	1422 [5.12]	1475 [5.31]	1	0.7
	12	CP3WL0.8[c]	0	/	1422 [5.12]	1085 [3.91]	0.8	0.5
	13	CP4.WL0.6[c]	0	/	1422 [5.12]	901 [3.24]	0.6	0.4
	14	FP4.WL1	0	/	705 [2.54]	705 [2.54]	1	/
	15	FP5.WL0.7[c]	0	/	705 [2.54]	490 [1.76]	0.7	/
	16	CFP1.WL0.7[c]	0	/	705 [2.54]	490 [1.76]	0.7	0.2

[a] R: raft; P: reference pile without cap; CP: capped pile; FP: friction pile without cap; CFP: capped friction pile; GF: greenfield. [b] Prototype-scale. [c] These tests include post-tunnelling pile loading.

WL is working load level based on capacity of a pile; WL^* is working load level based on capacity of capped pile.

4.1 Pile axial force after centrifuge spin-up

Fig. 4.1 shows axial force N along the piles measured in tunnelling tests at the end of the spin-up and stabilisation process at 60 g, before applying the service external head load F_0, for capped/uncapped reference and friction piles respectively.

All piles have a base load mobilised greater than the weight of components above ground of 0.44 MN due to negative shaft friction. The axial force in the reference piles tends to increase with depth as a result of downwards (negative) shaft friction caused by the soil settling more than the pile during centrifuge spin-up, consistent with Song and Marshall (2020). Differently, friction piles show (i) positive shaft friction (i.e. decreasing trend of axial force) near the pile

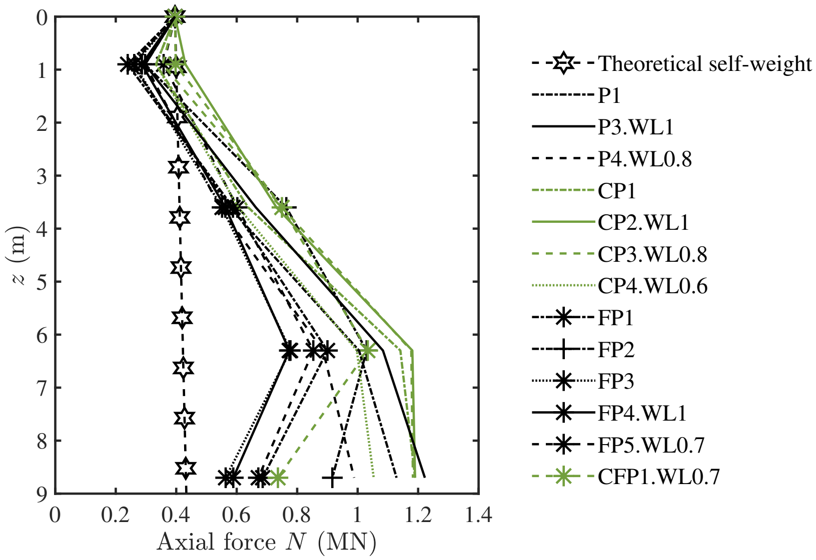

Fig. 4.1. Pile axial force after two 'stabilisation' cycles at 60 g (prototype-scale results)

base due to the soft tip and (ii) negative shaft load along the shaft that is lower than for reference piles, as the result of larger settlements of friction piles during spin-up than reference piles along with smaller mobilised base resistance. More importantly, despite the use of the soft base, all friction pile tests mobilised a base load significantly larger than the expected value of 0.04 MN (≈12 N at model scale). This expected base capacity was estimated from loading tests at 1-g of 10 mm long cylindrical samples of the soft base material placed within a cavity (slightly larger than the pile diameter) machined into an aluminium pedestal (thus providing radially confined conditions to the soft base material); further details can be found within Fig. 3.10. It is likely that the soft base was squeezed during spin-up and had to reach equilibrium at confining stresses with the surrounding sand that lead to a significant ultimate base load. In tunnelling tests, the effect of negative shaft friction and base pressure mobilised during spin-up should not significantly affect tunnelling-induced results considering that piles with relatively large working loads were tested, thus leading to positive shaft load prior to tunnelling, as shown from the N profile after service loading in Fig. 4.5.

Note that axial force N from FBG1 at 0.9 m depth (see Fig. 4.1) shows somewhat inconsistent values between 0.24 and 0.43 MN; ignoring shaft friction effects, the load at this position should be approximately 0.4 MN. This variability is likely due to some bending of the pile near the surface (from pile misalignment and the weight of the components above the ground surface) affecting FBG measurement of axial loads. This error is relatively small and does not impact the main outcomes of the study.

4.2 Pile response to loading

4.2.1 Effect of eccentric rigid boundary tunnel on pile load capacity

Fig. 4.2 shows the load-settlement curves of the main pile types from tests P1, P3.WL1, CP1, and FP3: namely, external, base, heading and shaft loads plotted against settlements S_p normalised by pile diameter d_p. Interestingly, shaft friction and base pressure were fully mobilised in uncapped piles (P1, P3.WL1 and FP3) by the settlement level of $S_p/d_p = 7\%$. Contrarily, capped pile CP1 displays a hardening external load trend up to $S_p/d_p \approx 8\%$, as heading, shaft, and base load do not reach an asymptotic value. This has implications on tunnelling effects, as discussed in Section 4.3.

To obtain insights into capped pile response to external loading, Fig. 4.3 compares the load-settlement curves of tests on raft (R1), reference piles (P1, P3.WL1 before tunnelling), and capped piles (CP1, CP2.WL1 before tunnelling). In the absence of a rigid tunnel, Fig. 4.3(a) shows that the load-settlement curve of the capped pile CP1 is similar to P1 during the initial stages of loading (external load < 2.5 MN), whereas at higher loads CP1 overlaps nearly with the raft R1. This is due to pile shaft resistance of capped pile CP1 being dominant over insignificant heading load at small settlements, whereas the heading load withstands a large portion of the external load at settlements greater than $7\%\,d_p$, as shown in Fig. 4.3(b)-(c). Additionally, the mobilised shaft load of CP1 in Fig. 4.3(d)-(e), which was less than that for P1 up to $S_p/d_p = 6.7\%$, continued to increase with settlements reaching a value greater than the ultimate shaft load of P1. This hardening trend of the shaft load of a capped pile is due to the cap-induced increase of mean effective stress of the soil beneath it, thereby increasing the shaft friction along the upper part of the pile. Consistent with this mechanism, the cap has a minor effect on mobilised base load (compare P1 and CP1 in Fig. 4.3(f)-(g)), resulting in a base load as a percentage of the external load at ultimate settlements being lower for capped piles than

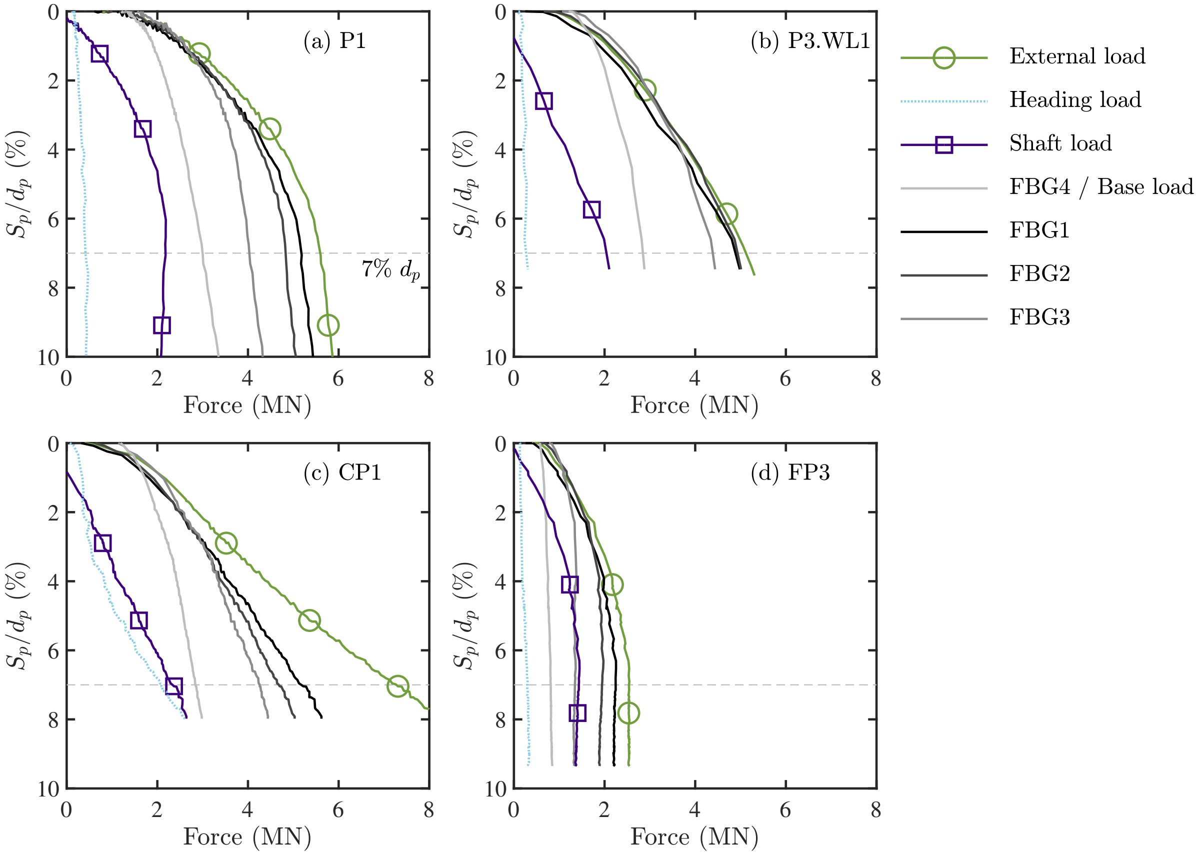

Fig. 4.2. External and axial forces along the pile plotted against normalised settlement during loading

uncapped piles.

As previously mentioned, the existence of the model tunnel had an effect on the pile response to loading (i.e. the load-settlement response of piles tested at an offset from the tunnel didn't match perfectly with piles tested directly above the tunnel). The use of physical models will always incur a degree of inaccuracy with respect to the full-scale scenario under consideration, so it's important to assess the impact of these issues where possible. To assess the effect of the rigid model tunnel (prior to tunnel volume loss) on pile load response, results from P3.WL1 and CP2.WL1 in the presence of the tunnel are compared with tests P1 and CP1 without it. At a given load, the pile in test P3.WL1 (above the rigid tunnel) tended to settle more than in test P1 (Fig. 4.3(a)); this is consistent with observations in Song and Marshall (2021), who suggested that the rigid model tunnel may have moved slightly during spin-up. However, from Fig. 4.3(d) it is clear that the base load of test P3.WL1 is consistent with P1, but Fig. 4.3(c) shows that

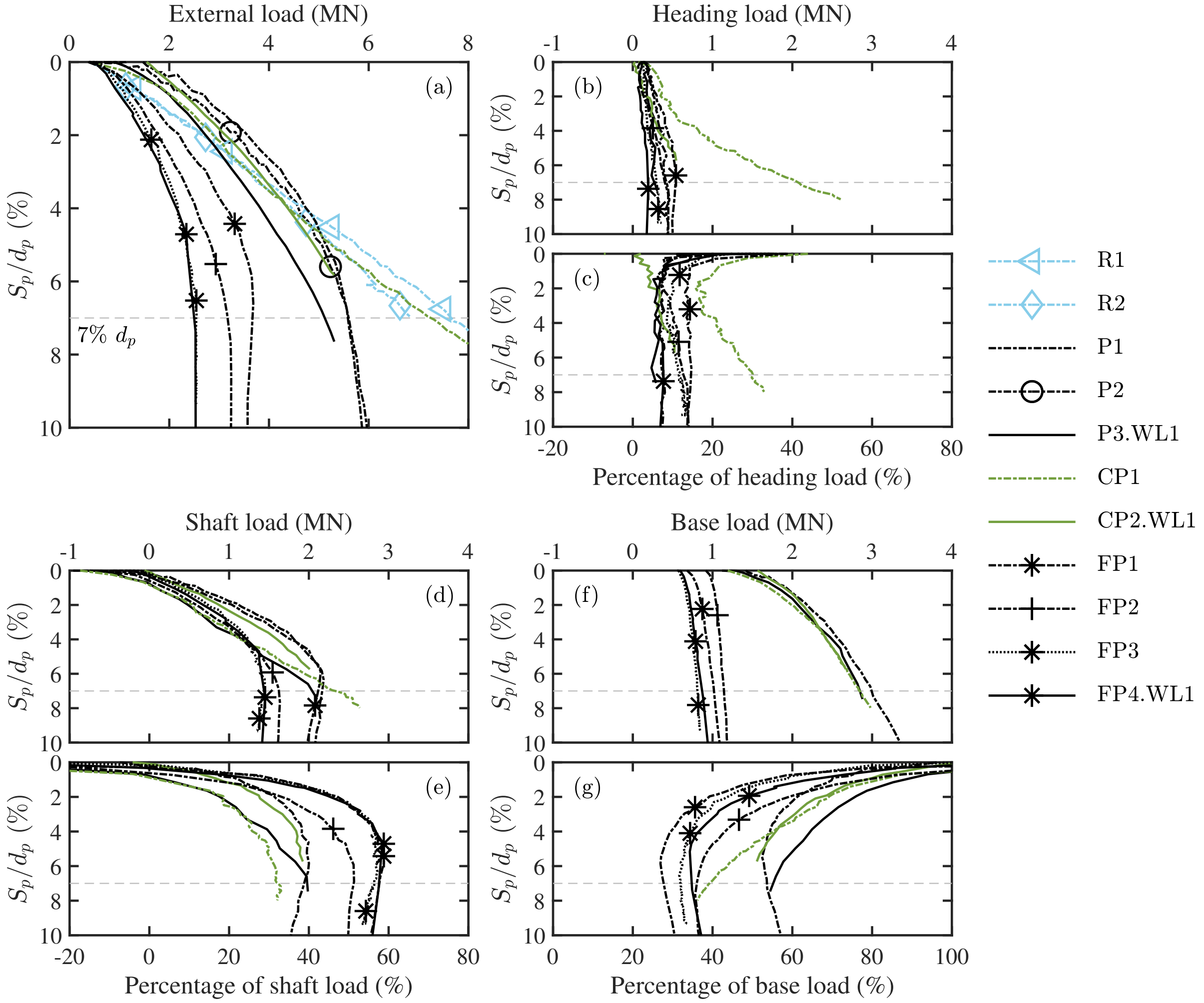

Fig. 4.3. Response to external loading of piles: (a) external load, (b) heading (cap) load, (d) shaft load, (f) base load, and their percentage to the external load where applicable (c), (e), (g)

shaft resistance is reduced. It is likely that the existence of the rigid model tunnel induced some stress arching within the soil above it, acting to reduce the soil mean effective stresses and thereby reduce the shaft capacity of pile P3.WL1 compared to P1. When comparing capped pile tests CP1 and CP2.WL1, the overall external load response in Fig. 4.3(a) for these tests was very similar, despite some discrepancies in Fig. 4.3(b) between the distribution of heading (cap) loads. Again, this is likely due to the presence of the rigid model tunnel in test CP2.WL1. The main parameter used in further data interpretation is the pile external load at a normalised settlement of 7%, which was similar for tests of a given pile type (e.g. tests P1 and P3.WL1 (Fig. 4.3(a)), hence the consequence of the discrepancies caused by the existence of the rigid model tunnel were deemed to be acceptable within the context of the aims of this study.

The response to loading of friction pile FP3 is shown in Fig. 4.3. Whilst not as effective as envisioned, the soft base still reduced the base load, causing a greater shaft load ratio (50–60 % for friction piles at $S_p/d_p = 7\%$, compared to 40 % in test P1) and base load of friction piles being fully mobilised during centrifuge spin-up (see marginal base load increases occurred during pile loading in Fig. 4.5). Similar to capped piles, the effect of the rigid model tunnel is once again seen with differences in axial forces of friction piles 150 mm away from (FP1-2) and above (FP3 and FP4.WL1) the tunnel. In particular, the shaft reduction was more significant for friction piles above the tunnel compared to the reference piles, since no additional base capacity could be mobilised in the friction piles. To avoid discrepancies when analysing tunnelling tests against loading tests, loading response is characterised from tests of piles directly above the rigid tunnel.

4.2.2 Pile settlement and axial force during pre-tunnelling loading

Next, pre-tunnelling service loading results from tunnelling tests are discussed. Fig. 4.4 plots external load versus normalised settlement data resulting in pile axial force N profiles in Fig. 4.5.

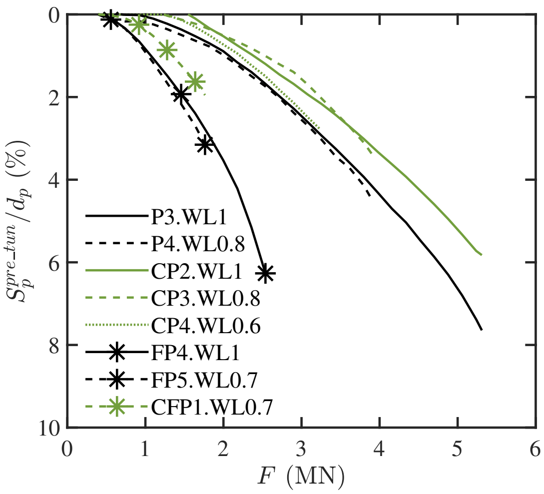

Fig. 4.4. Pile external load versus normalised settlement during pre-tunnelling loading

In these figures, there is good consistency between tests with the same foundation type (i.e. P3.WL1 consistent with P4.WL0.8, CP2.WL1 consistent with CP3.WL0.8 and CP4.WL0.6,

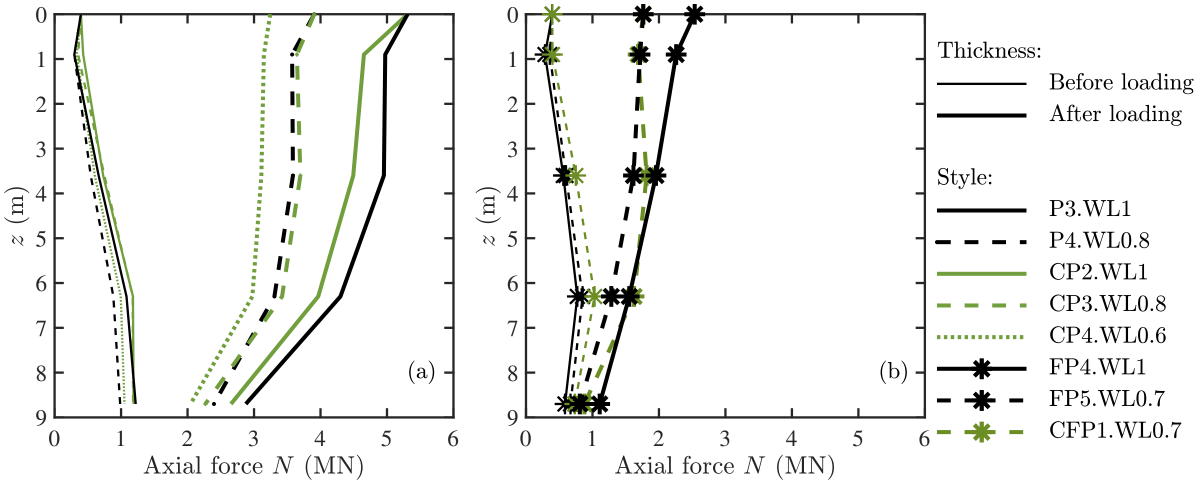

Fig. 4.5. Changes in pile axial force of capped and uncapped (a) reference and (b) friction piles before and after pre-tunnelling loading

etc) while the changes in response are according to expectations (i.e. for a given load, capped piles settle less than their un-capped equivalents; friction piles settle more than reference piles). In addition, pre-tunnelling service loads were noted to cause a shaft stress reversal, changing from negative shaft friction after centrifuge spin-up to positive friction after the application of service loads, creating a sensible load profile that generally agrees with expectations. However, from a design perspective, it should be noted that the proportion of load taken by the pile base was considerably higher than typically expected for a capped pile, which may have a serviceability settlement criteria of 1-2% of pile diameter (Poulos, 2001), which would not mobilise significant levels of base resistance. As such, the test procedure produced pile loading conditions which should be considered as conservative in the context of tunnel-pile interaction, since tunnelling will mostly impact the pile base capacity.

As the service load on a pile was increased (increasing WL; i.e. P4.WL0.8 to P3.WL1 and CP4.WL0.6 to CP2.WL1), the additional applied load was mainly mobilised as shaft friction in the middle (3.6-6.3 m) and lower (6.3-8.7 m) parts of the shaft and, where applicable, as cap (heading) load. In other words, prior to tunnelling, shaft and, where applicable, cap loads represent a greater ratio of the load distribution for heavily loaded piles (higher WL) compared to more lightly loaded piles.

4.3 Pile response to tunnelling

4.3.1 Pile settlement during tunnel volume loss

Fig. 4.6 shows the normalised pile settlement S_p^{Tun}/d_p versus tunnel volume loss $V_{l,t}$ along with greenfield settlements S_{GF} at the depth of the pile tip and the ground surface, which were measured at the front acrylic wall.

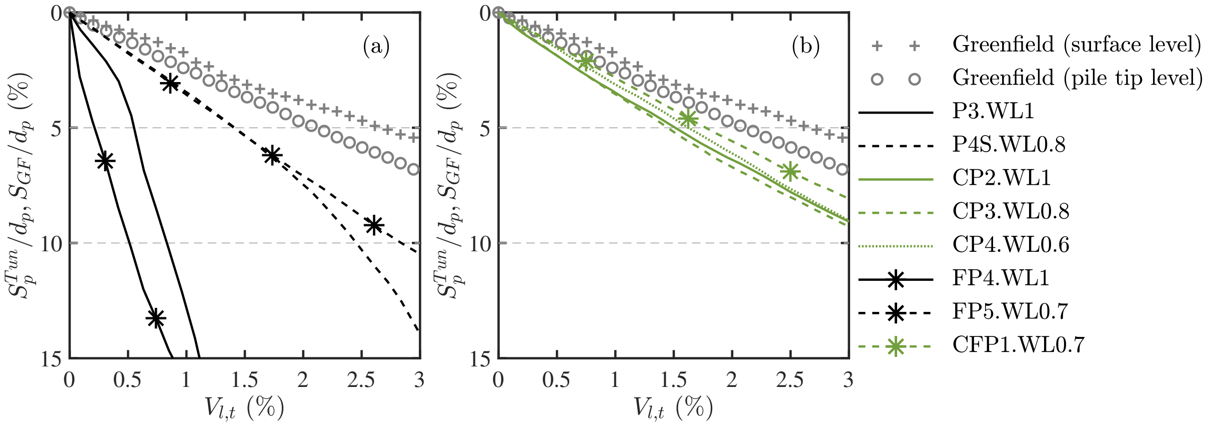

Fig. 4.6. Normalised pile settlement versus tunnel volume loss: (a) reference and friction piles and (b) capped (friction) piles

The results are discussed with respect to knowledge from literature. Tunnelling-induced settlements in Fig. 4.6 of all uncapped piles are greater than the greenfield surface and subsurface (pile base level) settlements. This is consistent with previous centrifuge tests of non-displacement piles having $SF = 1.5-2.5$ (i.e., $WL = 0.7$-0.4) in loose sand (Franza and Marshall, 2019a). Therefore, analytical interaction models (Korff et al., 2016) and literature review data (Mair and Williamson, 2014) that indicated pile settlements to be similar to the greenfield settlement at the pile tip for large base-to-external load ratio may lead to underestimation of pile settlements in sands (see Figs. 4.7 and 4.8). For uncapped piles (see Figs. 4.9-4.10), the changes of the distribution of mobilised shaft friction of piles in all tests show an increase in positive friction in the upper pile portion (0.9–3.6 m depth) (except FP4.WL1) and a reduction in the lower part (6.3–8.7 m depth). This increase in positive shaft friction is expected for tunnelling beneath tip level when base load reduces (Lee and Chiang, 2007); on the other hand, the reduction in shaft friction in the lower part is likely due to tunnelling-induced stress relief (Marshall et al., 2020). The experimental results also support indications from an analytical study from Marshall et al. (2020) that geotechnical failure is unlikely for $SF > 2$ (i.e., $WL < 0.5$).

Both uncapped friction (FP4.WL1) and reference (P3.WL1) piles having $WL = 1$ underwent *brittle failure* (extremely large settlements) at small values of $V_{l,t}$ (< 0.5%), whereas the reference pile with $WL = 0.8$ (P4.WL0.8) experienced a more gradual *softening failure* (with a distinct increase in the slope of the settlement-volume loss curve, but not as severe as the *brittle* cases) at a higher level of $V_{l,t} \approx 2\%$. The friction pile with $WL = 0.7$ did not show signs of equivalent 'failure' within the tested volume loss range.

4.3.2 Pile axial force transfer mechanism

Figs. 4.7 and 4.8 report changes of heading, shaft, and base loads, during the volume loss, both in magnitude as well as their ratio to the external load; this describes the load transfer mechanism between the pile and soil during the excavation. Figs. 4.9-4.10 present axial force profiles N and average shaft friction τ_s between FBG locations (i.e. the difference in axial force measured at adjacent FBG depths divided by the surface area of that segment of pile shaft, proportional to the reciprocal of the slope of N-z in Fig. 4.9).

The available data allow, for the first time, a link to be established between the measured load-transfer mechanism of uncapped piles (redistribution of loads between shaft and base) and the type of geotechnical failure, as follows. For $WL = 1$, as shaft resistance was already fully mobilised during pre-tunnelling loading, and because tunnelling stress relief reduces the maximum shaft resistance (through a reduction of mean effective stress around the pile shaft - note the drop in shaft load at $V_{l,t} < 0.5\%$ for P3.WL1 in Fig 4.7(b) and FP4.WL1 in Fig 4.8(b)) additional resistance has to be mobilised at the base to withstand the service load, which requires relatively large pile displacements and results in the *brittle failure* in Fig. 4.6 (see distinct increases in base load in plot (c) of Figs. 4.7 and 4.8 for P3.WL1 and FP4.WL1, respectively). In contrast, when $WL < 1$, if shaft resistance is not fully mobilised prior to tunnelling, a gradual transfer of load from the base to the shaft occurs with volume loss (see gradual decrease in base load for P4.WL0.8 in Fig 4.7(c) and FP5.WL0.7 in Fig 4.8(c)), which is accompanied by a gradual increase in shaft load (along the main part of the shaft for P4.WL0.8 in Fig 4.7(b) and

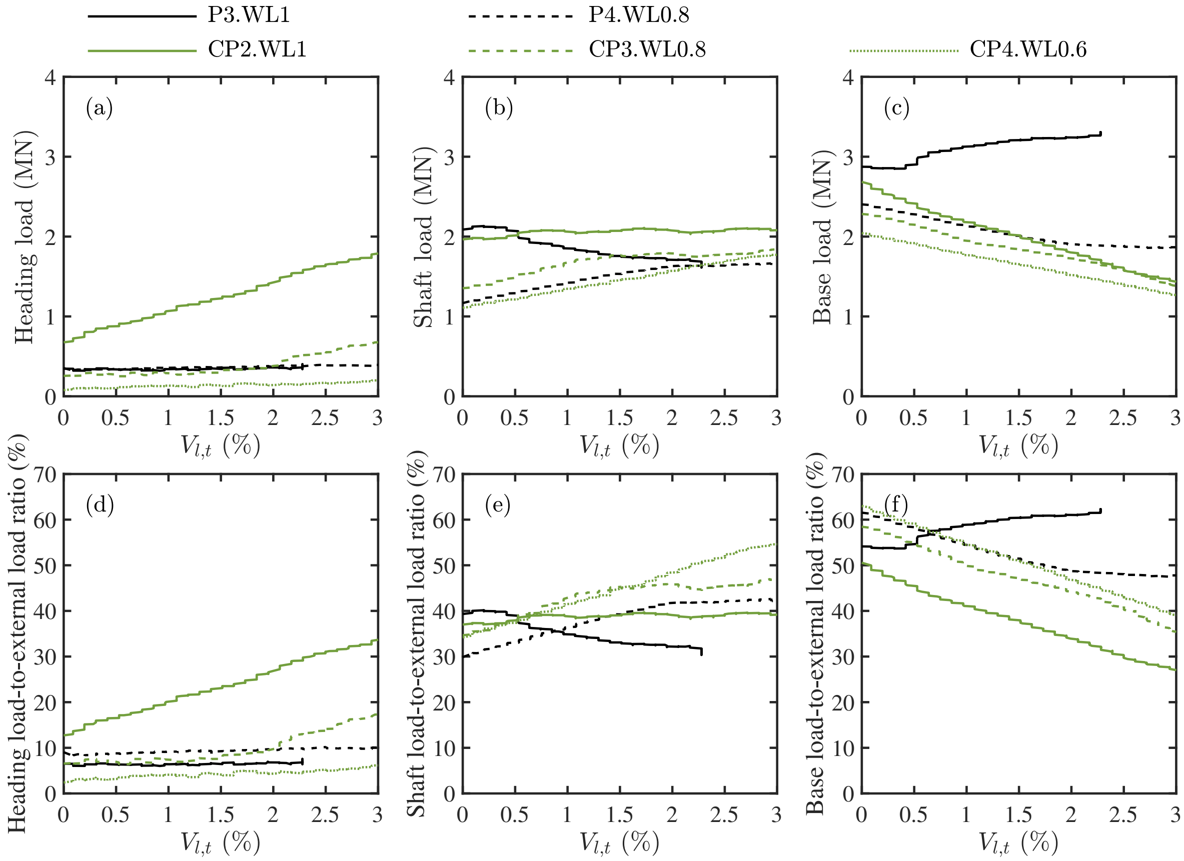

Fig. 4.7. Changes in axial force of reference and capped piles during tunnel volume loss

along the upper-most part of the shaft (the heading load) for FP5.WL0.7 in Fig 4.8(a)). It is interesting that, for P4.WL0.8, the point of *softening failure* at $V_{l,t} \approx 2\%$ coincides closely with a levelling off of the shaft and base load data; in other words, at this volume loss, the mobilised shaft resistance can not increase any further, and to maintain the base load required for equilibrium, the pile began to settle more rapidly. Also, at $V_{l,t} \approx 2\%$, the shaft load of P4.WL0.8 and P3.WL1 converge to a similar value (Fig. 4.7(b)), indicating that the shaft resistance will ultimately tend to a unique state regardless of the initial state of shaft load (akin to a critical state). For FP5.WL0.7, within the tested range of volume loss, the reduction of base load (and to some degree shaft load at $V_{l,t} > 2\%$) was accommodated by an increase in heading load; there was no levelling off of the shaft load and the gradual *softening failure* was not observed. In summary, if pre-tunnelling shaft load is fully mobilised, volume loss leads to a reduction of shaft load and likely a *brittle failure* of the pile; in contrast, when the pre-tunnelling shaft load

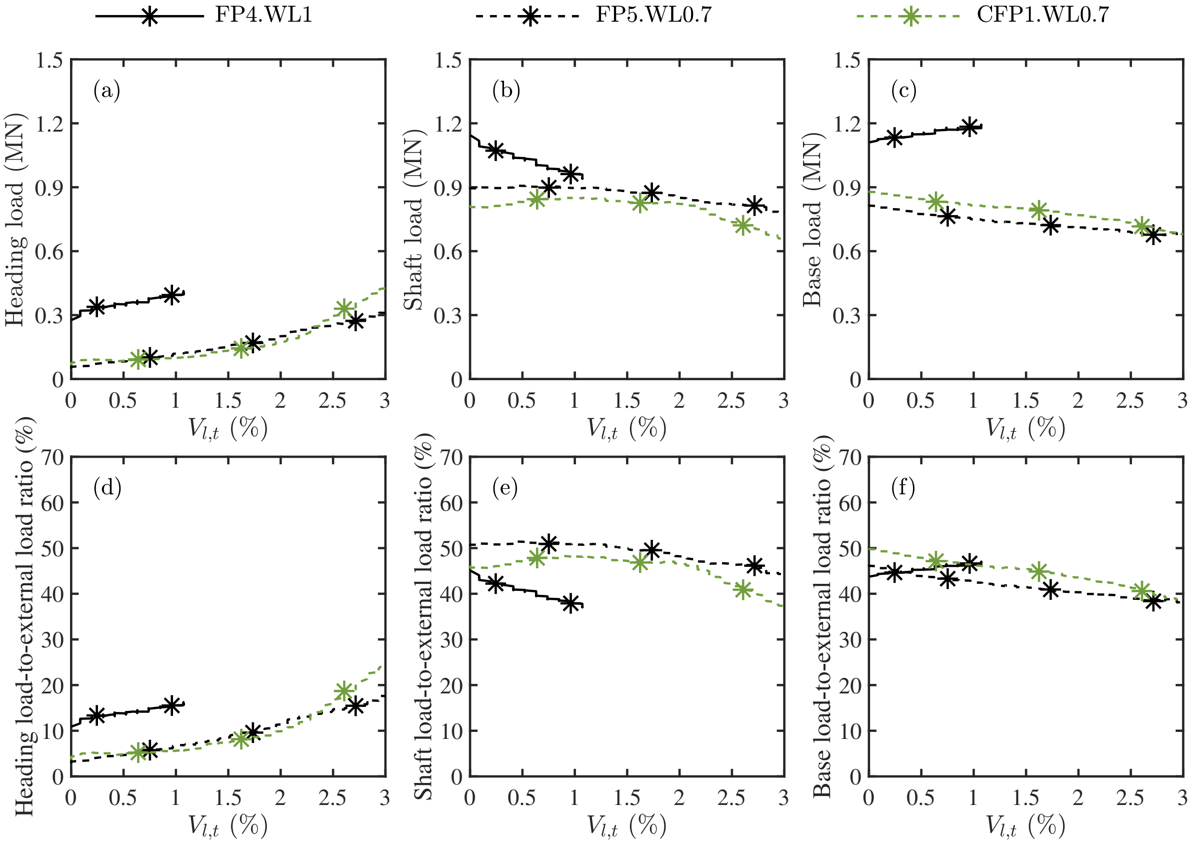

Fig. 4.8. Changes in axial force of capped and uncapped friction piles during tunnel volume loss

is not fully mobilised, there may be a gradual increase of shaft load and, possibly, a gradual *softening failure*.

There isn't a significant difference between the response of the friction and corresponding reference piles (both in the case of capped and uncapped piles), with friction piles with $WL < 1$ settling less than the corresponding reference piles due to smaller base-to-external load ratios. In particular, alike tunnelling-induced settlement trends of friction and reference piles correspond to similar load transfer mechanisms for a given WL: (i) tunnelling reduced the base load and shaft load in the lower portion of the pile (the base load reduction, as a percentage of external load, was greater for the reference pile), resulting in an increase in shaft load in the upper portion of the pile for reference pile P4.WL0.8 and friction pile FP5.WL0.7. Note that the strain hardening shaft load response noted previously for P4.WL0.8 (linked to the *softening failure* of the pile) is only evident within the upper-most portion of the friction pile (heading load in Fig. 4.8(a)). The similar trends for friction and reference piles under the same working load level are not overly surprising given the fact that the proportion of load carried by the base was not significantly different (because the polystyrene tip was not as effective as intended, as mentioned previously).

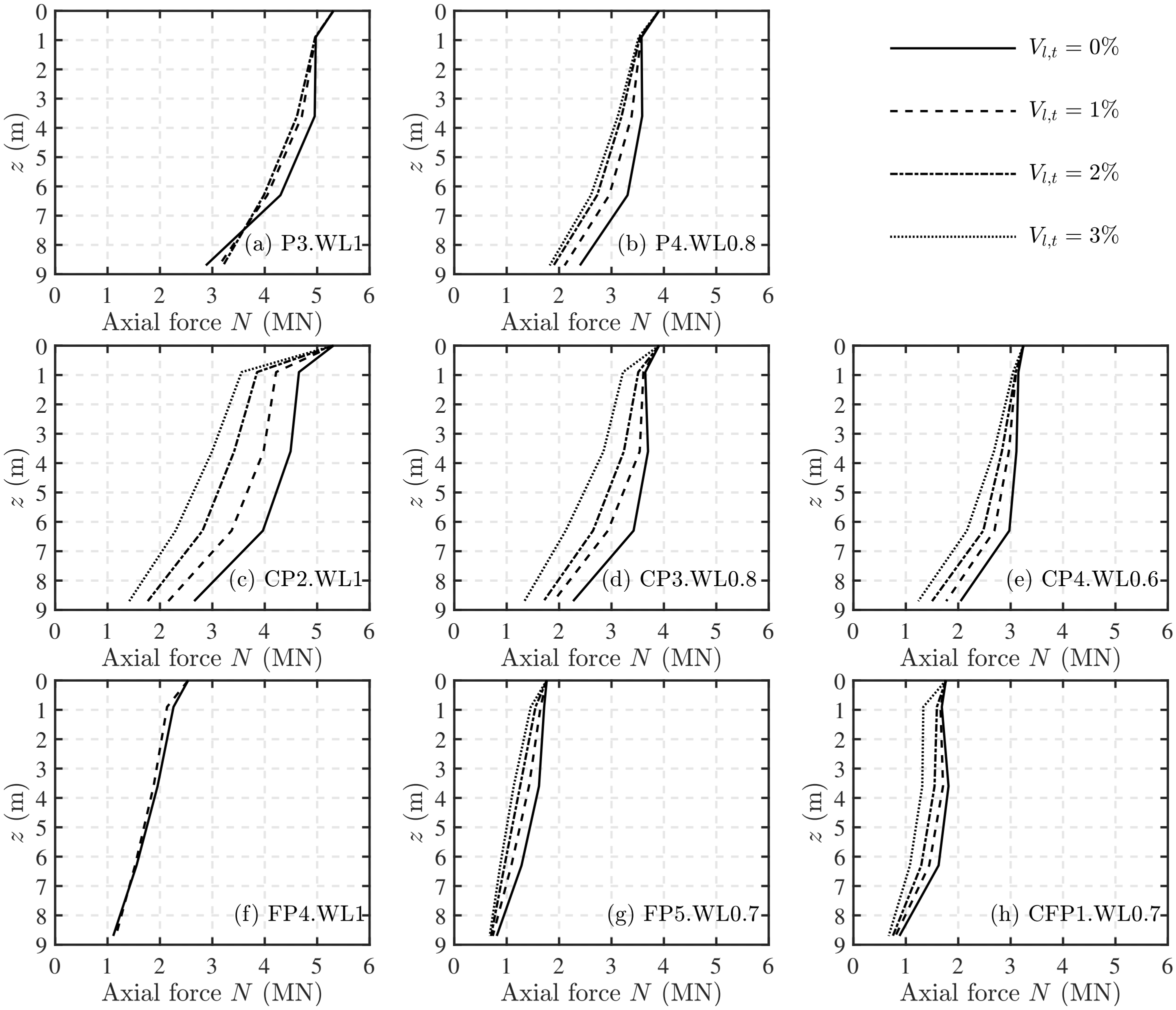

Fig. 4.9. Pile axial force during tunnel volume loss

Next, the response of capped piles is discussed. Fig. 4.6 shows that all capped piles (including reference and friction) at varying WL levels settled nearly linearly with tunnel volume loss and slightly more than subsurface greenfield movements, with minimal influence of the working load level on resulting settlements. The pile caps prevented all forms of pile failure and, for $WL < 1$, slightly decreased settlements compared to corresponding uncapped piles. Figs. 4.7-4.8 demonstrate that the cap prevented geotechnical failure by (i) mobilising surface

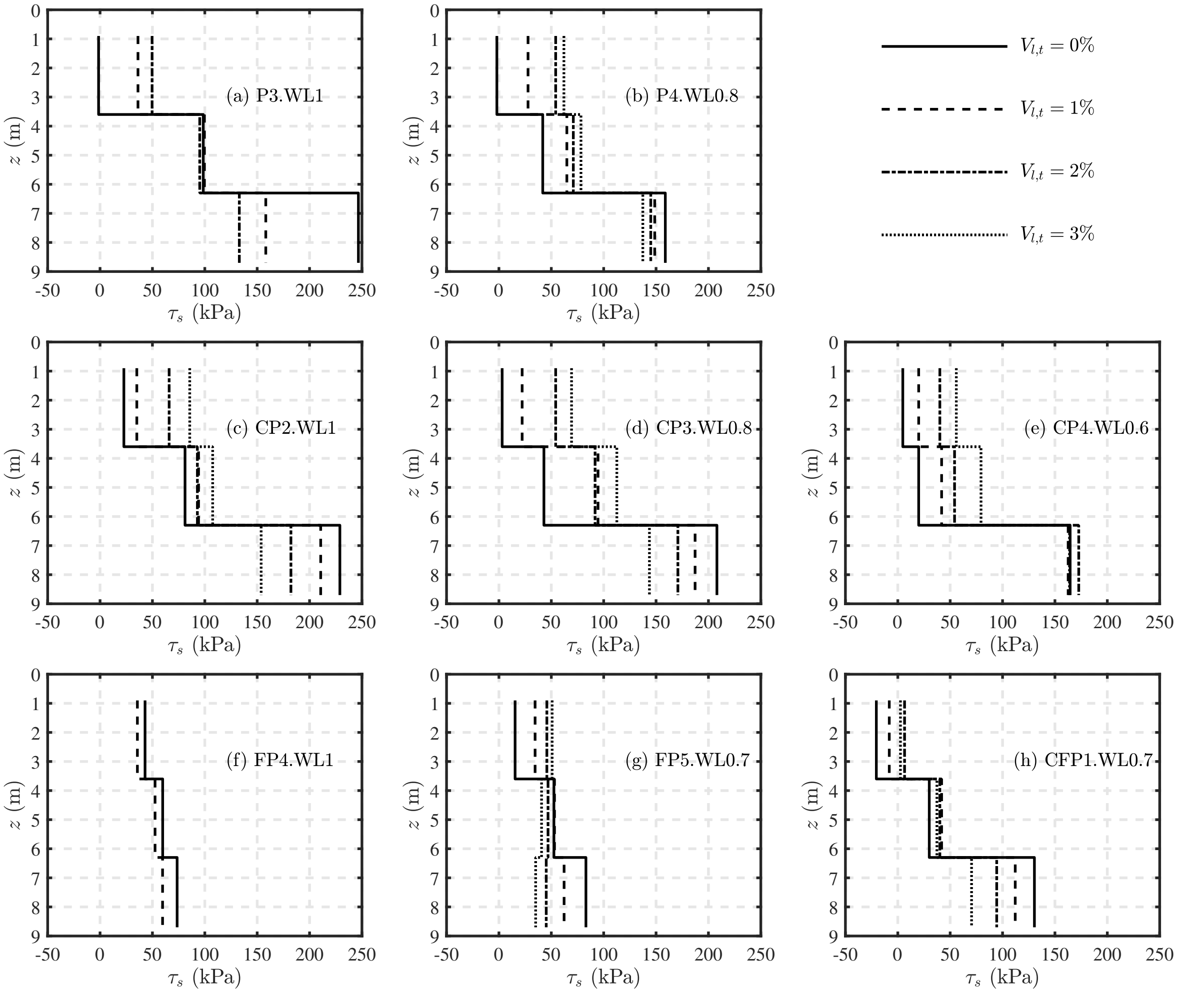

Fig. 4.10. Pile average shaft friction during tunnel volume loss

contact pressure (increase in the magnitude and percentage of load carried by the cap (heading load)), (ii) by increasing mobilised shaft friction in the upper and middle portions of the pile (mainly in the middle portion in Figs. 4.9-4.10; explained next), and thus (iii) reducing the magnitude and percentage of load carried by the base (where greenfield settlements are largest; particularly for reference piles with no soft base). The change in pile axial force N and shaft resistance τ_s with tunnel volume loss are provided in more detail in Figs. 4.9-4.10. The average vertical shear stress within a segment of a pile (related to the reciprocal of the slope of the axial force data) is informative in understanding how shaft loads move during volume loss. Considering Figs. 4.9-4.10 and focusing on piles and capped piles with a consistent WL (for example compare: P3.WL1 with CP2.WL1; P4.WL0.8 with CP3.WL0.8; also FP5.WL0.7 with

CFP1.WL0.7), in the upper-most portion of the pile shaft, the increase in shaft friction during tunnel volume loss for both reference piles and capped piles is about the same, i.e. the effect of the cap does not seem to be significant (due to the combined effect of enhanced confining stress and reduced relative soil-pile displacement). At the mid-depth region of the pile, however, the capped piles show a more significant increase in resistance than the reference piles.

Again, it is interesting to observe that, for CP3.WL0.8, where shaft load levels off at $V_{l,t} > 1.5\%$ (Fig. 4.7(b)) and base loads continue to decrease (for P4.WL0.8 this trend resulted in *softening failure* of the pile), we see that the cap (heading) load increases to maintain equilibrium and effectively prevent any geotechnical failure (this does require some additional settlement to mobilise the cap resistance, as shown in Fig. 4.6(b)). For CP2.WL1, where the equivalent uncapped pile P3.WL1 experienced *brittle failure* at a low value of $V_{l,t} < 0.5\%$, the cap (heading) load is noted to increase significantly right from the start of volume loss (Fig. 4.7(a)) to accommodate the loss of base load (Fig. 4.7(c)), which could not be taken by the shaft since it had already fully mobilised its resistance (constant shaft force in (Fig. 4.7(b)). For the higher $WL = 0.6$ with CP4.WL0.6, the loss of base load in Fig. 4.7(c) is observed to be taken solely by the shaft load (Fig. 4.7(b)), which does not level off during the range of volume loss; no appreciable increase in cap load is noted in Fig. 4.7(a) since pile shaft resistance is mobilised for smaller settlements compared to the bearing resistance beneath the cap.

4.3.3 Discussion of pile head-to-greenfield surface settlement ratio

For quick risk assessments, engineers relate tunnelling-induced pile head settlement to surface greenfield movements using the *settlement ratio* $R = S_p^{Tun} / S_{GF}^0$. For both drained and undrained conditions, field trials indicated a settlement ratio for piles directly above the tunnel greater than unity (Kaalberg et al., 2005), as confirmed by centrifuge tests of uncapped piles (among others, Williamson et al. (2017) and Franza and Marshall (2019a)).

To characterise the behaviour of capped piles, settlement ratios R from all tunnelling tests are as shown in Fig. 4.11, along with uncapped reference piles NSF1.5 and NSF2.5 in loose sand from Franza and Marshall (2019a) having $WL = 0.7$ and 0.4 (equivalent to the reference pile from this study). These outcomes are interpreted within Fig. 4.12, relating R to the risk for

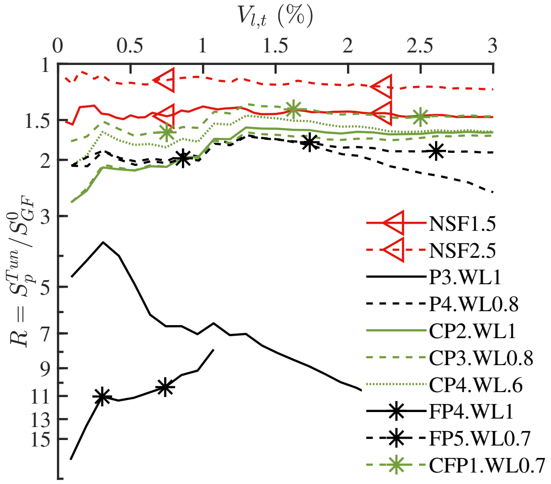

Fig. 4.11. Centrifuge settlement ratio against tunnel volume loss; NSF1.5 and NSF2.5 uncapped piles in loose sand from Franza and Marshall (2019a)

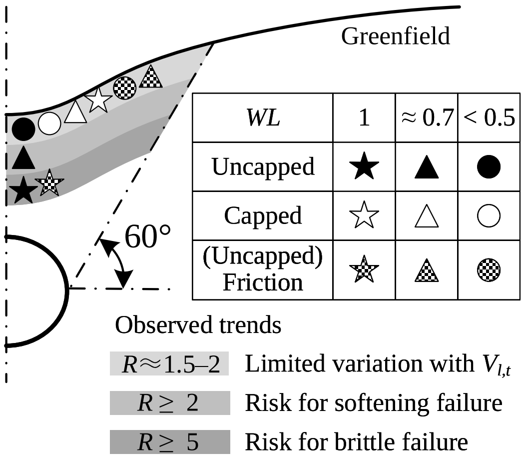

WL	1	≈ 0.7	< 0.5
Uncapped	★	▲	●
Capped	☆	△	○
(Uncapped) Friction	✯	▲	◍

Observed trends

R≈1.5–2	Limited variation with $V_{l,t}$
$R \geq 2$	Risk for softening failure
$R \geq 5$	Risk for brittle failure

Fig. 4.12. Observed settlement ratios for non-displacement capped and uncapped (friction) piles in sand located directly above a tunnel

the identified geotechnical failure types, i.e. *brittle failure* and *softening failure*. For a given service load, the presence of the cap (i) prevents geotechnical failure associated with $R > 3$ and (ii) effectively reduces R of both reference and friction piles for the investigated range of volume loss (the only exception is reference piles at small volume losses $V_{l,t} < 0.5\%$). Also, results show a tendency of R to slightly decrease with volume loss for capped piles, in contrast to uncapped reference and friction piles.

There is strong experimental evidence that, regardless of tunnel volume loss and even for relatively high $WL = 0.8$-1.0 (as estimated from uncapped piles), the pile cap will effectively reduce R to approximately 1.5-2.0 and prevent geotechnical failure for non-displacement piles located directly above a tunnel, which may experience, without the cap, either softening or brittle failure. Considering (i) test results from uncapped non-displacement piles in loose sand (indicating $R \approx 1.1$-1.2 for $WL = 0.4$) and (ii) the observed reduction in the settlement ratio induced by the cap, in the absence of interaction modelling, a design value of $R \approx 1.5$ is suggested for both capped and uncapped piles when $WL \leq 0.4$, whereas $R \approx 2$ may be considered for uncapped piles with $WL \approx 0.7$, capped piles with $WL = 0.7$-1 (with load capacity estimated from uncapped piles), and friction piles with $WL \leq 0.7$.

4.4 Pile load capacity after tunnel volume loss

4.4.1 Pile load capacity and axial force

Post-tunnelling load-settlement curves are studied, as shown in Fig. 4.13, to evaluate the impact of tunnelling on the serviceability and ultimate performance of the foundations, which may be particularly relevant in cases where building foundations are re-purposed rather than replaced. As an operational value, post-tunnelling load capacity is estimated in Table 4.2 when the settlement $S^* = S_p^{pre-tun} + S_p^{post-tun}$ reaches 7 % d_p, where S^* is given by the sum of pre- and post-tunnelling settlements due to change in external load F.

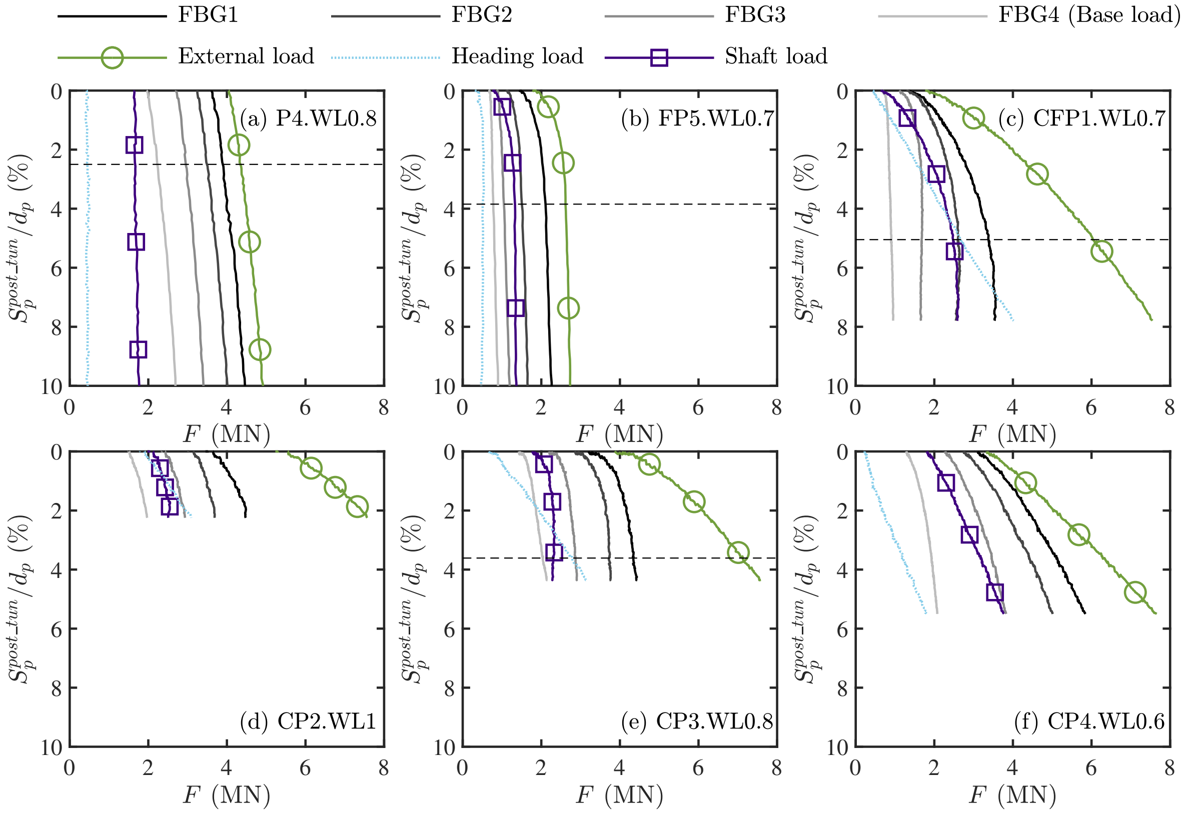

Fig. 4.13. External and axial forces along the pile plotted against normalised settlement during post-tunnelling loading

Table 4.2 compares load capacities from loading tests (piles without or above rigid tunnel) and post-tunnelling (piles directly above tunnel). There was no reduction in post-tunnelling load capacity of friction piles (when considering piles FP3 and FP5.WL0.7 directly above the

Table 4.2. Comparison of pre- and post-tunnelling load capacity (defined as external load at $S^*/d_p = 7\%$)

	Reference pile	Friction pile	Capped pile	
Pre-tunnelling load capacity (MN)	P3.WL1	FP3	CP1[a]	
	5.12	2.54	>7.26	
Post-tunnelling load capacity (MN)	P4.WL0.8	FP5.WL0.7	CP3.WL0.8	CFP1.WL0.7
	4.34	2.62	>7.13	>6.03
Normalised pre-tunnelling settlement	$4.5\%\, d_p$	$3.2\%\, d_p$	$3.4\%\, d_p$	$2\%\, d_p$

[a] CP1 was tested at an offset from the tunnel (see Table 3.4); all other piles were located directly above the tunnel.

rigid tunnel) and capped piles. On the other hand, load capacity of reference pile P4.WL0.8 decreased by 15% with respect to P3.WL1. Also, Table 4.2 confirmed the significant reduction in capacity due to the boundary conditions from the presence of the rigid tunnel.

4.4.2 Loading-induced changes in pile tangent stiffnes

The tangent stiffness for an increment of external load ($K = dF/dS^*$) is plotted against normalised S^*/d_p for selected tests in Fig. 4.14. There is good consistency in the pre-tunnelling loading data between equivalent pile tests (i.e. P3.WL1 matches well with P4.WL0.8; FP4.WL1 matches well with FP5.WL0.7, etc), which gives reassurance on the repeatability of tests. The data show that tunnelling, to some degree, ‘resets’ the initial loading stiffness (i.e. the initial post-tunnelling loading stiffness is higher than the stiffness at the end of the pre-tunnelling loading). This is most true for the capped piles where the initial and post-tunnelling loading stiffness profiles are very similar. The post-tunnelling stiffness of the capped piles also maintains a reasonable value at larger settlements, whereas the stiffness of the uncapped piles all tend to zero as S^*/d_p approaches 10%. For the friction pile FP5.WL0.7, the initial post-tunnelling stiffness increased the least compared to the stiffness at the end of pre-tunnelling loading, but gradually tended to an ultimate, near-zero, value at $S^*/d_p = 10\%$. In contrast, for the reference pile P4.WL0.8, the post-tunnelling stiffness rapidly reduced to a near-zero value at $S^*/d_p \approx 6\%$, which was notably lower than the stiffness of P3.WL1 at the same settlement.

In summary, for non-displacement piles, there is the possibility of a slightly negative impact of tunnelling on the post-tunnelling stiffness (and capacity) of piles that rely on base resistance,

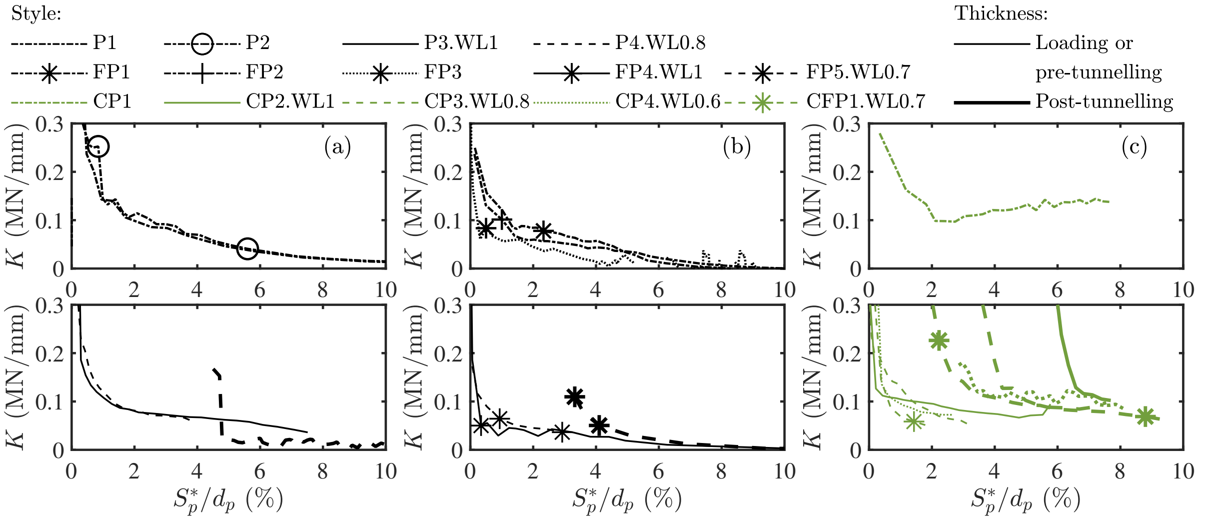

Fig. 4.14. Tangent stiffness of (a) reference piles, (b) friction piles, and (c) capped friction piles in loading tests (up plots) and in pre- and post-tunnelling loading tests (low plots)

whereas for piles with a cap that is in contact with the surface, the pre- and post-tunnelling responses are nearly identical. Also, Song and Marshall (2020) observed a post-tunnelling capacity for displacement piles in dense sand similar to that of greenfield pile-jacking. Consequently, for both displacement and non-displacement piles, assessments of tunnelling beneath piles in sand should primarily concern induced settlements (rather than post-tunnelling bearing capacity). For instance, the analytical method from Marshall et al. (2020) could be used to estimate risk for geotechnical failure in terms of settlements only.

4.5 Summary

This chapter presented data from geotechnical centrifuge tests of tunnelling beneath loaded non-displacement piles and focused on the effect of a pile cap (representative also of a raft or grade beam) in contact with the soil surface. Results from 16 centrifuge tests in dry dense sand were presented, including loading tests to ascertain the foundation capacity and load-displacement response in the absence of a tunnel, and tunnelling tests in which ground loss from a model tunnel occurs directly beneath the foundation. Individual 'reference' pile response is compared for cases with and without a pile cap, including pile displacements and load distributions between the head, shaft, and base; the case of 'friction' piles with a compressible foam base are also considered. Uncapped piles experience ‘geotechnical failure’, undergoing large settlements or a significant increase in settlement rate with tunnel volume loss in order to mobilise further base or shaft resistance to achieve vertical equilibrium under the applied load. Test results are used to quantify the beneficial effect of the pile caps in reducing settlements compared to uncapped piles and, importantly, preventing geotechnical failure of both reference and friction piles, even when the applied load approaches the uncapped pile capacity. It is also demonstrated that pile caps improve the post-tunnelling foundation performance, providing higher post-tunnelling tangent stiffness for both friction and reference piles. The chapter provides valuable quantitative evidence to allow engineers to confidently consider the beneficial role of pads/grade beams/rafts in contact with the surface on both the serviceability and ultimate performance of pile foundations during, and subsequent to, tunnelling.

Chapter 5

Verification and application of CCNM testing approach in tunnelling under masonry walls

In many cities, tunnel excavation often occurs beneath low-rise masonry buildings with shallow foundations. The resulting ground movements can cause deformations and stress redistribution in the overlying structures. An accurate estimation of the impacts of tunnelling on masonry buildings on shallow foundations is therefore imperative.

Researcher relating to the tunnel-masonry building interaction problem often makes use of small-scale physical models, or full-scale numerical models. Physical models at 1 g (where g is gravity) provide indications of some important relationships and trends in tunnel-masonry building interactions, yet the direct applicability of results to the full-scale is questionable because of the mismatch in ground stress conditions, which affects soil behaviour (i.e., 1 g model stresses are much lower than full-scale conditions) (Giardina et al., 2012; Nghiem et al., 2014; Al Heib et al., 2020). Centrifuge models at elevated gravity levels provide a more realistic reproduction of full-scale ground stress conditions, benefiting from the reduced model dimensions and controlled laboratory environment (Ritter et al., 2017, 2018). Centrifuge models, however, necessitate certain simplifications, in particular in relation to the structural details, varying from beams and plates (Mair, 2013; Farrell et al., 2014) to 3D printed miniature buildings (Ritter et al., 2018). Numerical models are capable of reproducing many detailed aspects of the construction and material complexities involved in real tunnelling projects (Burd et al., 2000; Yiu et al., 2017; Miliziano and de Lillis, 2019). Nonetheless, the reliability/fidelity of numerical modelling results is difficult to verify unless corresponding experimental/full-scale data are available.

Hybrid tests are a form of the substructure approach (Blakeborough et al., 2001) and can combine the strengths of both physical and numerical modelling by analysing, within the respective physical/numerical domain, the part of the problem that is best suited to that domain, with data being transferred between models at a shared boundary (Kong et al., 2015). For tunnel-building interaction problems, a real-time hybrid testing method known as coupled centrifuge-numerical modelling (CCNM) was developed at the University of Nottingham Centre for Geomechanics (NCG) (Idinyang et al., 2018, 2019). This technique has, to now, been applied to the study of elastic framed buildings on piled foundations, where the tunnel, soil, and piles were modelled in the centrifuge, and the framed building was modelled numerically, with data of pile vertical displacements and loads shared between the two model domains (Franza and Marshall, 2019a; Song and Marshall, 2020).

This chapter presents the verification and application of the recent novel developments of the CCNM technique which allows testing of a continuous shallow foundation (strip foundation) along with a more accurate (compared to elastic) nonlinear representation of the structure. Results from eight geotechnical centrifuge tests (see Table 5.1, which is the same as Table 3.6 in Section 3.3), including one greenfield tunnelling test, five CCNM tests, and two ‘conventional’ constant building dead load tests, are presented to investigate tunnel-masonry wall interactions under plane strain conditions. In the updated CCNM method, masonry walls are simulated using the concrete damage plasticity (CDP) constitutive model in the finite element (FE) numerical simulation software Abaqus (Simulia, 2014), while the centrifuge model includes the soil, tunnel, and a strip foundation. The chapter summarises the treatment of data shared at the continuous foundation interface between the experimental domain (controlled by Labview) and the numerical domain (Abaqus). Two masonry wall schemes (with 0 and 19% openings) and four wall-to-tunnel positions (with the wall moving from directly above the tunnel to where one side of the wall is located directly above the tunnel) are considered. The chapter first provides test results demonstrating the significance of wall stress redistribution (from CCNM tests) compared to the 'conventional' centrifuge tests where a constant wall dead load is applied. Results from the CCNM tests are then used to investigate the effect of the wall-to-tunnel eccentricity, including a demonstration of the level of load redistribution that occurs with the wall for the eccentric cases, an evaluation of wall distortion and damage parameters, and, by examining the contribution of settlements caused by bending and shear, providing insights into how the masonry wall response, due to the adopted non-linear CDP model, evolves during the tunnel volume loss process.

Table 5.1. Test summary

No.	Label [a]	Testing method	e/L [b]
1	GF	/	/
2	H8.5O0*	Constant load	0
3	H8.5O0	CCNM	0
4	H8.5O19*	Constant load	0
5	H8.5O19	CCNM	0
6	H8.5O19	CCNM	1/6
7	H8.5O19	CCNM	1/3
8	H8.5O19	CCNM	1/2

[a] GF: greenfield; H: height; O: % of opening

[b] e: tunnel-wall eccentricity; L: wall length

5.1 Comparison between CCNM and ‘conventional’ constant dead load method

To quantify the effect of load redistribution within the wall on tunnelling-induced wall settlements and distortions, data from ‘conventional’ constant load tests (indicated with an *; see Table 5.1) and the CCNM tests are presented in this section; only cases where the wall was located directly above the tunnel (eccentricity $e = 0$) are used. Note that all results are presented in prototype scale unless otherwise stated.

5.1.1 Loads and displacements

Fig. 5.1 presents data from both the centrifuge (i.e. foundation) and numerical model (i.e. wall base) domains at a tunnel volume loss of $V_{l,t}$ = 2.2%, including (a) the load distribution along the foundation and wall base, and (b) the settlement of the foundation and wall base; greenfield (GF) settlements from a separate centrifuge test are also included for reference. Note that in Fig. 5.1(a), the 7 centrifuge load magnitudes are much larger than the 50 Abaqus loads because the centrifuge values are obtained by summing up the loads from nodes close to the centrifuge load actuation points. The settlement profiles along the wall base in Abaqus (fitted using LVDT data; Fig. 5.1(b)) are consistent with the foundation settlement profiles from the centrifuge LVDT measurements (PIV data was also checked to verify readings;see Fig. 5.2). It was assumed that no gaps formed between the bottom of the foundation and the soil surface (due to not reaching the uplifting force threshold from actuators to pull up the foundation within centrifuge).

The model foundation in the centrifuge, through its bending stiffness, will distribute the load from the seven actuators to the underlying soil, the aim being to achieve a load profile in the underlying soil that is similar to the wall base load profile from Abaqus. The settlement profile in Fig. 5.1(b), to some degree, gives confidence that this is achieved. The load data in Fig. 5.1(a), noting that the initial loading in the CCNM tests (H8.5O0 and H8.5O19) is the same as the data plotted for the constant load tests (H8.5O0* and H8.5O19*), shows that, as a result of wall distortions caused by tunnelling ground movements, wall load is generally transferred from

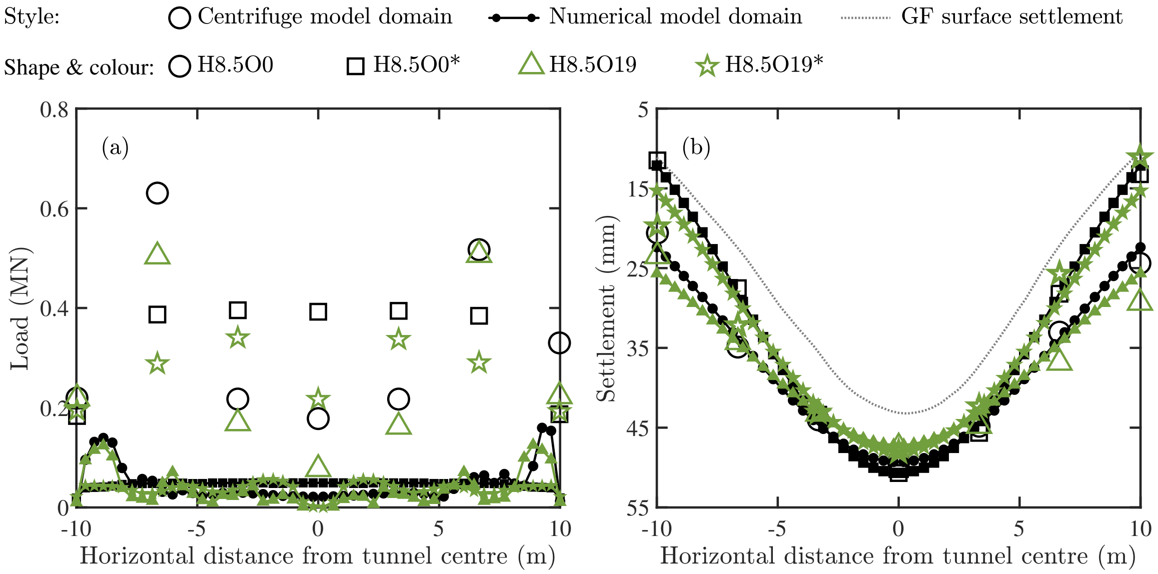

Fig. 5.1. (a) Load and (b) settlement at the interface between the centrifuge (7 positions) and numerical model (50 nodes) domains at $V_{l,t} = 2.2\%$ for walls with $e/L = 0$

the centre of the foundation towards its ends. This load redistribution has a notable effect on the foundation settlements, as shown in Fig. 5.1(b), where the settlement at the foundation centre is reduced in the CCNM tests compared to the constant load tests, and the relative displacements between the foundation centre and its ends are reduced. Fig. 5.1(b) also demonstrates that the modified Gaussian curve fitted to the seven data points from the centrifuge settlement gives a sensible input of settlements at the 50 nodes along the base of the wall in the Abaqus model (for the central cases with $e/L = 0$). There is some asymmetry of settlements to the left and right sides of the tunnel, however this level of variability is typical for these types of centrifuge tests.

Fig. 5.2 presents settlement profiles at the foundation base level at $V_{l,t} = 2.2\%$. The foundation PIV result for H8.5O0* is not included (also for Fig. 5.3) because, in that test, there was insufficient texture on the front face of the model foundation to obtain accurate PIV measurements (a white background with black dots was subsequently painted onto the foundations; the textured foundation is displayed in Fig. 3.12(b)). Foundation settlements were measured using LVDT (solid star) and PIV technique (hollow circle), showing good agreement. The settlement profiles of the wall base and the foundation should ideally match, thus the fitted settlement profiles (solid curves, fitted by LVDT data), which also align well with PIV-measured foundation settlement troughs, were applied to the wall base in Abaqus. The foundation settlement appears marginally greater than the corresponding surface settlement (dashed curves) because the strip foundation model did not completely contact the inner face of the acrylic wall of the strongbox thereby preventing the sand settlement near the acrylic wall, which often happens in such tests.

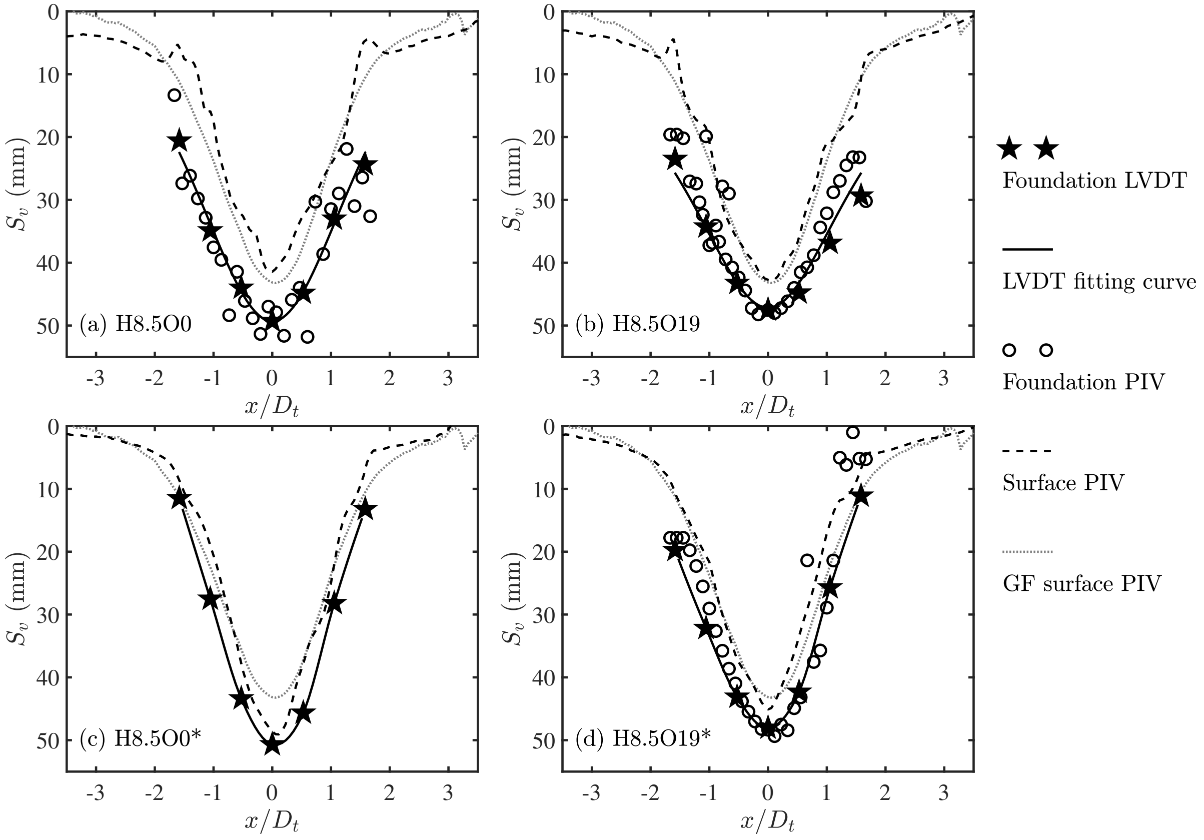

Fig. 5.2. Vertical displacements at foundation base level at $V_{l,t} = 2.2\%$

Fig. 5.3 illustrates the PIV-measured horizontal displacements of both the foundation and the underlying soil at $V_{l,t} = 2.2\%$, as well as the greenfield (GF) surface data. The foundation result for H8.5O0* is not included for the same reason as Fig. 5.2(c): in that test, there was insufficient texture on the front face of the model foundation to obtain accurate PIV measurements (a white background with black dots was subsequently painted onto the foundations; the textured foundation is displayed in Fig. 3.12(b)). In contrast to the greenfield scenario, the soil surface horizontal displacements are noticeably reduced by the effect of the foundation. The foundation horizontal displacements, compared with foundation settlements in Fig. 5.1(b) and Fig. 5.2, are relatively small, as expected for the continuous foundation applied in these tests (consistent with Farrell et al. (2014), Xu et al. (2020b)). Ideally, horizontal displacements would be measured and controlled in the same way that vertical displacements are, however this is beyond the current capabilities of the experimental equipment (note that the image-based measurements of horizontal displacements in Fig. 5.3 can not be acquired quickly enough to integrate within the CCNM control program; a discussion of this limitation was provided in Section 5.3).

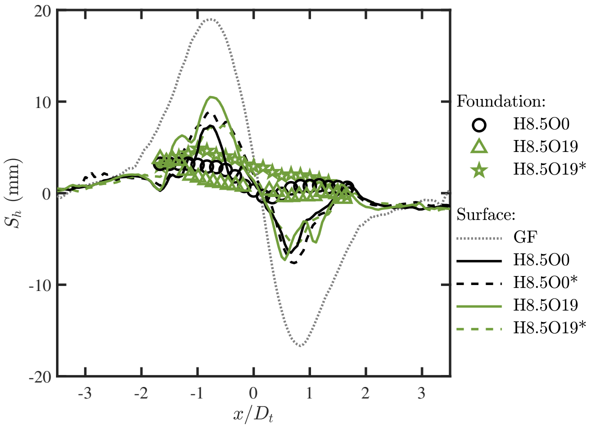

Fig. 5.3. Horizontal displacements at foundation base level at $V_{l,t} = 2.2\%$ for walls with $e/L = 0$ (excluding foundation data of H8.5O0*)

5.1.2 Wall deformation and damage assessment

The wall tensile strain ε^t induced by tunnelling at $V_{l,t} = 2.2\%$ is provided in Fig. 5.4 for CCNM and constant-load (*) tests of walls directly above the tunnel ($e/L = 0$). The values of ε^t for the constant-load tests were obtained by applying the measured foundation settlements to the Abaqus wall models after the centrifuge tests. Included in Fig. 5.4 are values of characteristic strain ε^t_{99}, which is the maximum tensile strain that is not exceeded in 99% of the total area of the masonry wall, as adopted by Yiu et al. (2017) and Yu (2024); values reported here are of similar magnitude to those in Yu (2024) where a similar wall was modelled. Finally, the damage category of each bay, defined according to Mair et al. (1996) based on limiting tensile strains, is included (0-1 negligible to very slight, 2 slight, 3 moderate, 4-5 severe to very severe), as well as the area of the wall experiencing moderate damage or above (indicated as % Mod. D., defined as $\varepsilon^t > 1500\mu\varepsilon$).

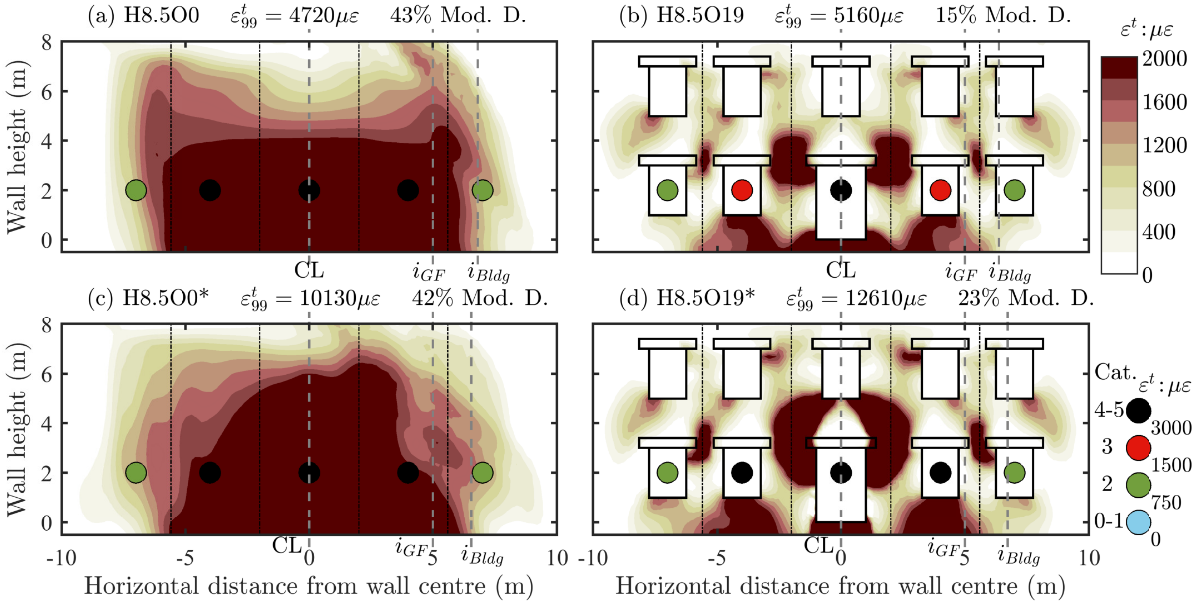

Fig. 5.4. Distributions of max principal strain (tensile strain) and wall damage assessment at $V_{l,t} = 2.2\%$ for walls with $e/L = 0$ (gray dashed lines represent the tunnel centreline CL, and inflection points of greenfield surface i_{GF} and wall base settlements i_{Bldg})

Regions with the highest magnitude of tensile strains are observed in the vicinity of the lower parts of the wall centre, predominately within the sagging region (the greenfield inflection point is noted to be $i \approx 5$ m; see also Fig. 5.8(b)) and, for the wall with openings, around the door and windows in the central region. Note that, due to some asymmetry of the numerical mesh adopted within Abaqus, the strain profiles are not perfectly symmetric. For all tests, the size of the regions experiencing large strains and the magnitude of characteristic strain is greater in the constant load tests (*) compared to the CCNM tests. For example, ε^t_{99} is $10130\mu\varepsilon$ for H8.5O0* and $4720\mu\varepsilon$ for H8.5O0; the constant load test increased ε^t_{99} by 115%. For the H8.5O019 wall, ε^t_{99} was increased by 144% in the constant-load test compared to the CCNM test (from $5160\mu\varepsilon$ to $12610\mu\varepsilon$). For the wall without openings, the effect of the constant-load test on the damage level and the percentage of the wall experiencing moderate damage or above (Mod. D.) is marginal, however for the wall with openings, Mod. D. is increased from 15% to 23% and the damage category is increased from 3 to 4 in bays 2 and 4 (refer to Fig. 3.18 for bay numbers).

These outcomes demonstrate that the use of constant dead loads in these types of tests will overestimate the extent and/or severity of damage in masonry walls, highlighting the novelty and value of the advanced CCNM tests.

5.1.3 Soil shear strains

To further investigate the differences between the 'conventional' constant-load tests and the CCNM tests, Fig. 5.5 plots the distribution of engineering shear strain γ obtained from the PIV analyses. The distributions of shear strains are roughly consistent across the different cases, in particular around the tunnel at greater depth. However, soil shear bands near the surface exhibit different phenomena under these two test methods. Specifically, the constant dead load method (H8.5O0*, H8.5O19*) generates more continuous shear zones near the surface (beneath the foundations), whereas the CCNM method (H8.5O0, H8.5O19) shows more discontinuous shear regions due to the changes in applied loads. These variations in foundation loads and shear strain magnitudes will affect the response of the soil; as a result the CCNM method achieves a more realistic simulation of the tunnel-wall interaction scenarios than the constant dead load method. The issue of under- or over-estimating building damage/deformation associated with conventional methods (for example, assuming a fully flexible building (Franza and Marshall, 2018) or estimating building stiffness by simplified physical modelling (Xu et al., 2020b)) are overcome through real-time adjustments of wall loads (as a function of the wall/foundation scheme and wall material properties) in the CCNM method.

5.2 CCNM results including eccentric scenarios

5.2.1 Global wall deformation and damage assessment

This section provides further experimental data from the CCNM tests, which have been demonstrated to provide a more accurate simulation of the tunnel-masonry wall interactions than constant-load tests, for the wall with openings (H8.5O19; considered to be of more practical rel-

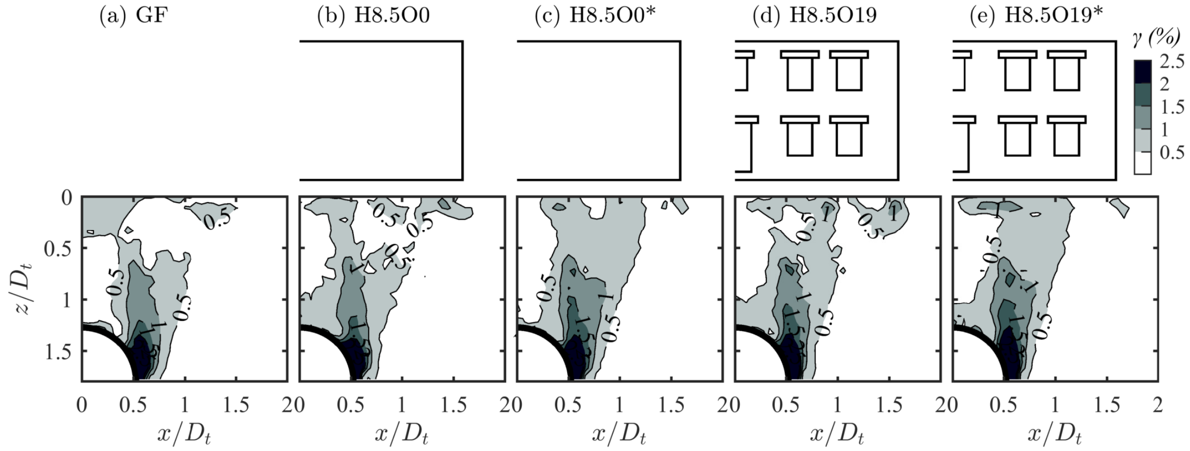

Fig. 5.5. Soil engineering shear strains at $V_{l,t} = 2.2\%$ (the global scene is symmetrical about the tunnel centreline)

evance than the wall with no openings) for varying relative tunnel-wall positions ($0 \leq e/L \leq 1/2$; refer to Fig. 3.18). These data may provide a reference for risk assessments or for verification of related numerical modelling studies. Displacements below a tunnel volume loss of approximately 0.2% were very small and caused scatter within results; for this reason only data above $V_{l,t} = 0.2\%$ was used.

Fig. 5.6 shows the distribution of applied loads (in prototype scale) at the seven actuator positions along the strip foundation at $V_{l,t} = 2.2\%$. In addition, the locations of the greenfield surface and wall base inflection points are indicated with a dashed line marked i_{GF} and i_{Bldg}, respectively. Consistent with the observation for the symmetric case ($e/L = 0$), for the cases where $e/L > 0$, the foundation load above the tunnel reduces as a consequence of the ground movements caused by tunnel volume loss and is shifted towards the ends of the wall (in order to maintain equilibrium); the exception to this is $e/L = 1/2$ where the edge of the wall is directly above the tunnel. In general, the foundation load is reduced around the sagging areas and increased in hogging areas; this general trend is not always observed due to the effects of building rotation, for example on the left edge of the $e/L = 1/3$ wall which shows an increase in load in the sagging zone caused by the rotation of the wall driving the wall corner into the soil. The data in Fig. 5.6 demonstrate that, similar to the symmetric case, the changes in load that occur during tunnel volume loss are significant for the eccentric building cases, again demonstrating the value of the CCNM technique.

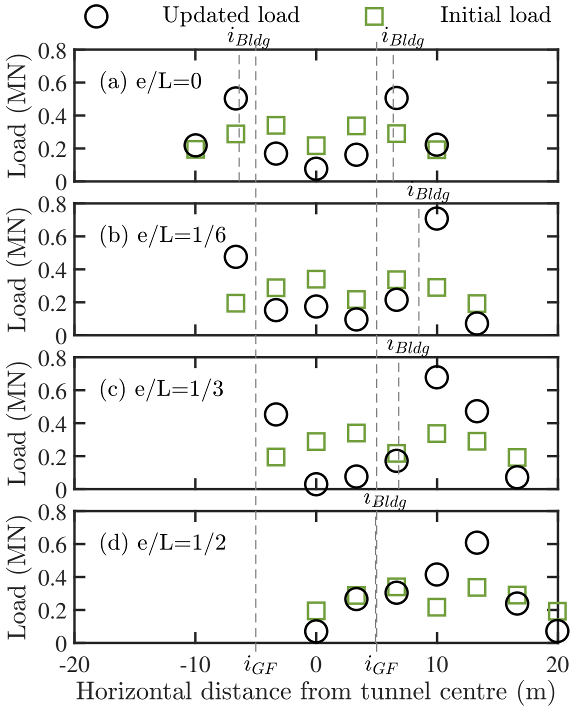

Fig. 5.6. Load distribution on the foundation (7 positions) at $V_{l,t}$ = 2.2% (gray dashed lines represent inflection points of greenfield surface i_{GF} and wall base settlements i_{Bldg})

Fig. 5.7 exhibits the load distributions of nodes along the wall base in Abaqus at $V_{l,t}$ = 2.2%. Compared with the loads applied by the actuators Fig. 5.6 (each force represents the sum of several nearby node forces), these node loads show more complex changes caused by wall deformation. However, the stresses transmitted from the wall to the ground through the foundation are usually relatively continuous and uniform, and the actuator forces are expected to achieve this effect after being transmitted to the ground through the foundation.

Fig. 5.8(a) presents settlement profiles of the wall base at $V_{l,t} = 2.2\%$. Due to the wall length ($L/D_t = 3.2$, where D_t is the tunnel diameter), settlement patterns are primarily influenced by either sagging or hogging regions. As the wall becomes further away from the tunnel with e/L increasing from 0 to 1/2, the dominant interaction gradually transitions from sagging to hogging. Additionally, the more eccentric cases give relatively higher levels (but still very small) of foundation horizontal displacements (see Figs. 5.9-5.10 for detailed vertical and horizontal displacements).

Fig. 5.8(b) displays the horizontal distance from the tunnel centreline to the inflection point

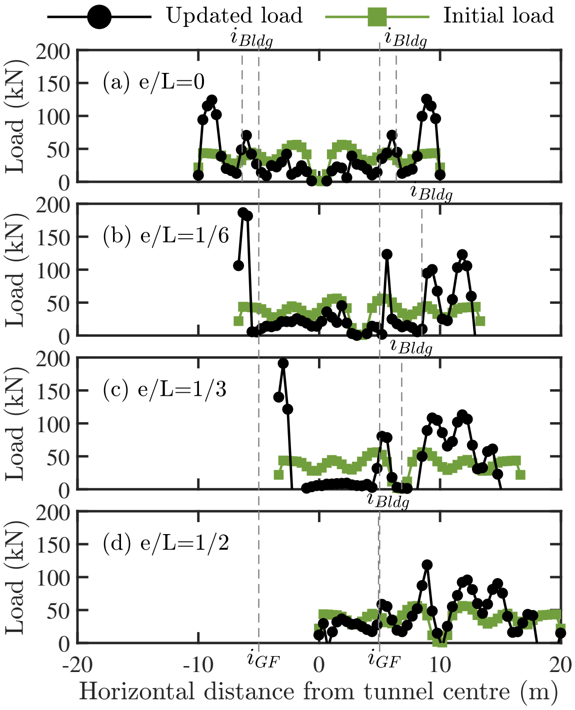

Fig. 5.7. Load distribution at wall base (50 nodes) at $V_{l,t} = 2.2\%$ (gray dashed lines represent inflection points of greenfield surface i_{GF} and wall base settlements i_{Bldg})

i of the greenfield surface or wall base settlement profile as it relates to tunnel volume loss. In all cases, a gradual reduction of i with increasing tunnel volume loss is observed (consistent with Marshall et al. (2012), Franza et al. (2019)). Note that for $e/L = 0$, at volume loss $< 0.7\%$, the wall base settlements did not exhibit an inflection point (i.e. only sagging deformations were measured), hence no data is included in Fig. 5.8(b) for this range of $V_{l,t}$. The inflection point of the wall tends to be greater than the greenfield surface settlement, in particular for $e/L = 0$ and $1/6$; the inflection point moves closer to the tunnel as e/L increases (consistent with numerical results by Zhao et al. (2019)). Interestingly, for $e/L = 1/2$, the inflection point of the wall base is relatively consistent with the greenfield values. The magnitude of i is noted to decrease faster for $e/L = 0$ than for $e/L = 1/6$; this is likely due to the higher levels of strains and damage induced within the wall with $e/L = 0$ (illustrated later with Fig. 5.12), making the wall relatively more flexible.

Based on Fig. 5.8(b), the masonry walls can be divided into sagging and hogging regions. Fig. 5.11 shows the ratio of wall to greenfield hogging/sagging length $M^{L,hog/sag} =$

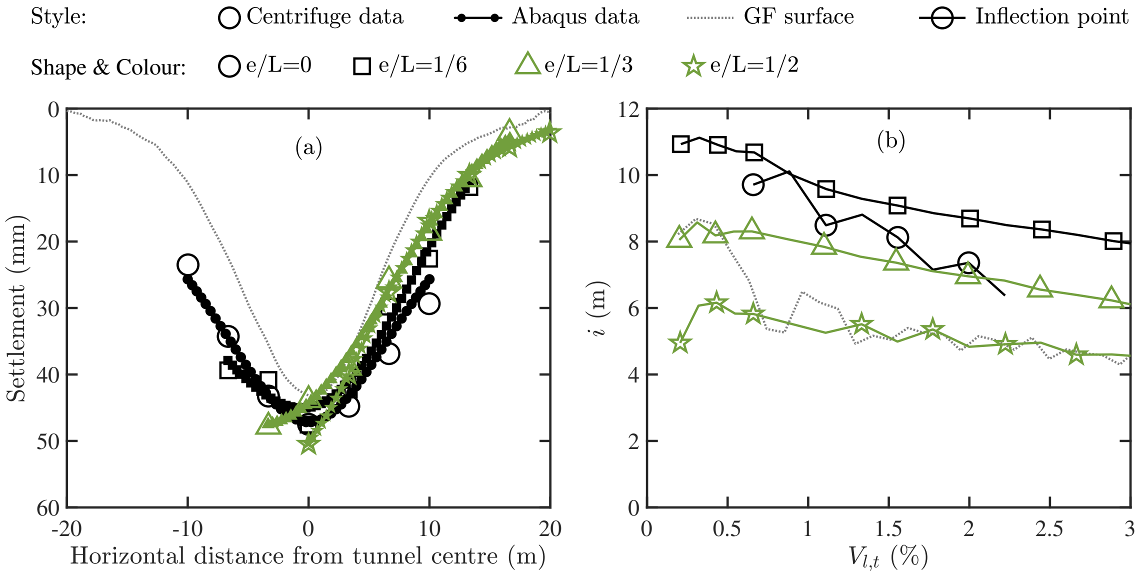

Fig. 5.8. (a) Wall base settlement profiles at $V_{l,t} = 2.2\%$ and (b) horizontal distance from tunnel centreline to wall base inflection point i against tunnel volume loss

$L_{hog/sag,Bldg}/L_{hog/sag,GF}$, which was also adopted by Franza et al. (2020b). The ratios $M^{L,hog}$ generally increase with eccentricity (i.e. $M^{L,hog}$ is lowest for $e/L = 0$ and highest for $e/L = 1/2$); the ratios of $M^{L,sag}$ correspondingly tend to decrease with increasing eccentricity. These trends are consistent with the outcomes of elastic continuum solution analyses from Franza et al. (2020b), however the outcomes provided here are additionally affected by soil and wall non-linearity, as well as the shear deformability of the wall (note that Potts and Addenbrooke (1997) suggested that $M^L = 1$ should be adopted for structures deforming in pure shear; as illustrated in Table 3.7, the walls in this study are characterised by a mixed bending and shear response). The ratios $M^{L,hog/sag}$ generally stabilise after $V_{l,t} \approx 1\%$, except for $M^{L,hog}$ with $e/L = 0$. These results may provide a useful reference when directly using greenfield data within wall risk assessments, or for validation of further analytical/numerical studies which, for example, could focus on the effects of shear deformability on M^L, as suggested by Franza et al. (2020b).

Fig. 5.12 illustrates the distribution of tensile strains within the walls; as before, the characteristic tensile strain ϵ_t^{99}, damage category for each bay, and amount of the wall experiencing moderate damage or above (% Mod. D.) is provided. As the tunnel-wall eccentricity increases, both ε_{99}^t and % of Mod. D. first decrease, reaching minimum values at $e/L = 1/3$ where the

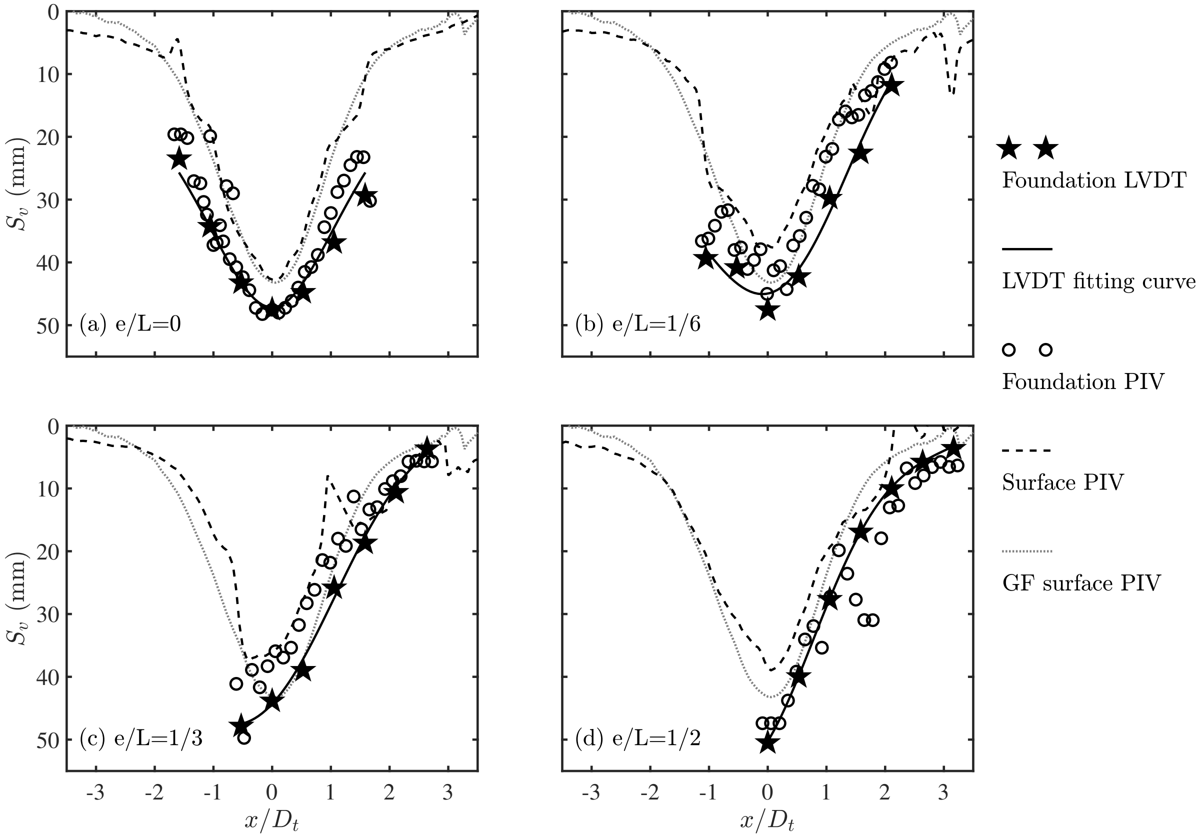

Fig. 5.9. Vertical displacements at foundation base level at $V_{l,t} = 2.2\%$

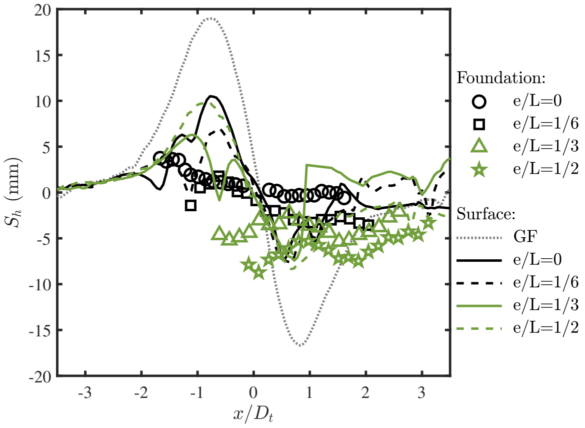

Fig. 5.10. Horizontal displacements at foundation base level at $V_{l,t} = 2.2\%$

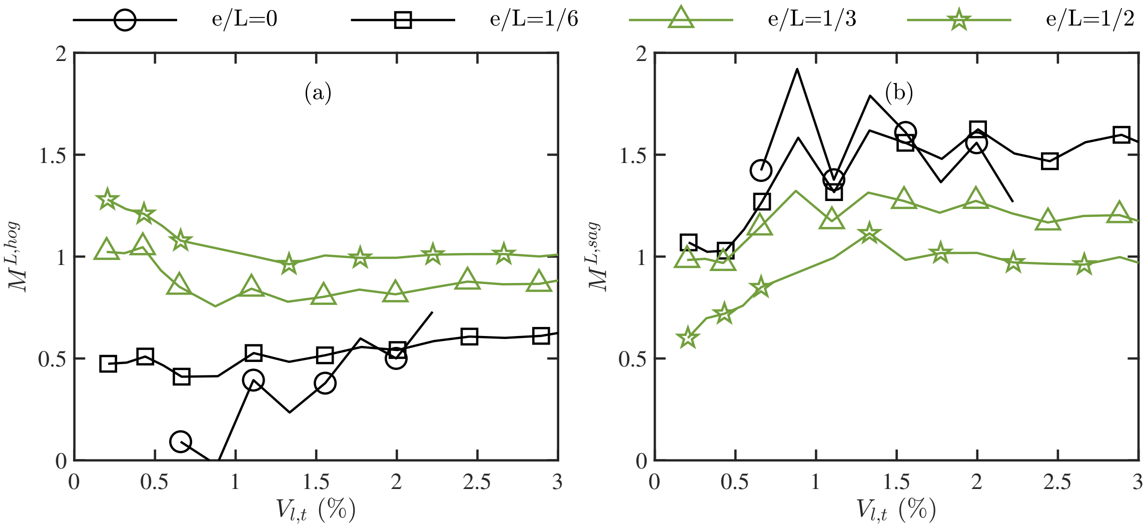

Fig. 5.11. Ratio of wall to greenfield hogging/sagging length $M^{L,hog/sag}$ against tunnel volume loss: (a) hogging and (b) sagging

maximum damage level is category 2, then increase slightly at $e/L = 1/2$ where bays 3 and 4 experience a moderate damage category 3, but only 3% Mod. D (consistent with Amorosi et al. (2014), Yiu et al. (2017), Burd et al. (2022), Yu (2024)). The regions of high-magnitude tensile strains are observed near the centre and lower part of the wall when $e/L < 1/3$, while these areas shift to the upper parts of the wall when $e/L > 1/3$; the most severe strains are noted to occur near the middle of either sagging (for $e/L = 0$ and 1/6) or hogging (for $e/L = 1/2$) regions.

For $e/L = 1/3$, the centre of the wall coincides closely with the wall base and greenfield inflection points ($i \approx$ 6-8 m, gradually decreasing with tunnel volume loss; see also Fig. 5.8(b)); because of the wall length and position, it does not experience the most 'extreme' effect of either of the sagging or hogging zones, explaining why wall strains are lowest for this case.

Fig. 5.13(a) shows how deflection ratios DR in sagging and hogging change with tunnel volume loss; Fig. 5.13(b) presents this data using the modification factor M^{DR} (Eq. 2.25) for $V_{l,t} \geq 0.2\%$. The hogging region for $e/L = 0$ and the sagging region for $e/L = 1/2$ are omitted as they experienced very low levels of curvature and the M^{DR} values are not entirely reliable. Both sagging and hogging deflection ratios exhibit relatively linear changes with tunnel volume loss for $V_{l,t} \geq 0.5\%$ (Fig. 5.13(a)); sagging deflection ratios DR_{sag} tend to decrease with e/L for a given $V_{l,t}$, whereas hogging deflection ratios DR_{hog} increase with e/L (similar findings were

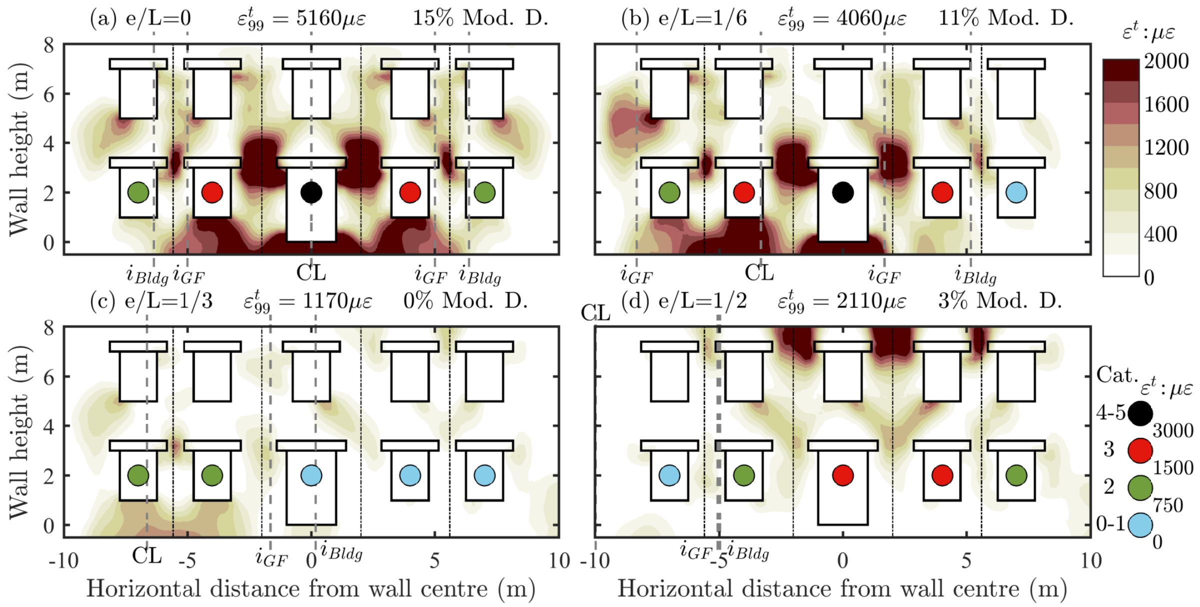

Fig. 5.12. Distributions of max principal strain (tensile strain) of H8.5O19 with different e/L at $V_{l,t} = 2.2\%$ (gray dashed lines represent the tunnel centreline CL, and inflection points of greenfield surface i_{GF} and wall base settlements i_{Bldg})

reported by Goh (2011), Ritter et al. (2017)).

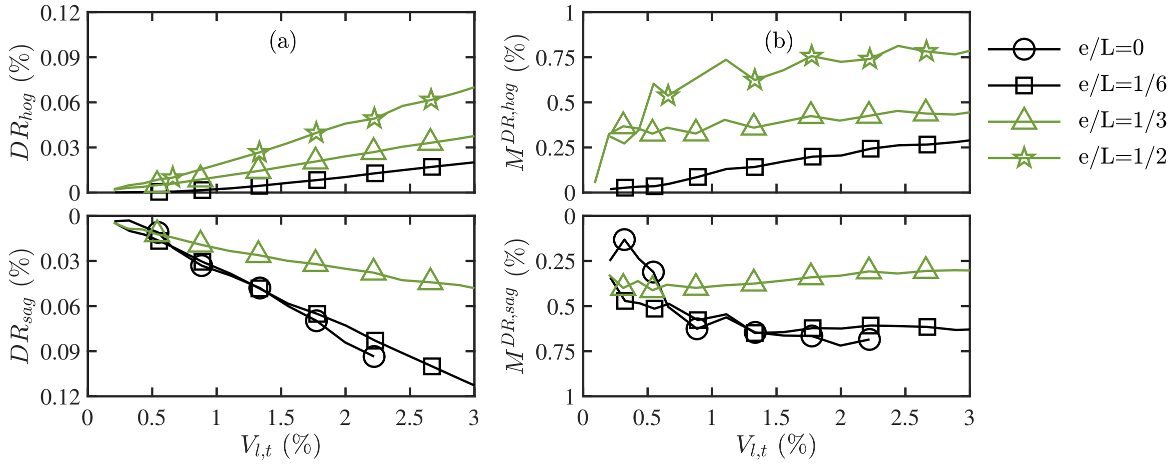

Fig. 5.13. (a) Deflection ratios and (b) corresponding modification factors of wall hogging (upper plot) and sagging regions (lower plot) against tunnel volume loss

Values of M^{DR} in Fig. 5.13(b) generally exhibit a consistent pattern of increasing with tunnel volume loss, but unlike the values of DR, M^{DR} tends to a constant value at higher $V_{l,t}$; for sagging this levelling off occurs at $V_{l,t} \approx 1\%$, whereas for hogging the values continue to increase slowly even at $V_{l,t} = 3\%$. These results reaffirm the dominance of sagging deformation in central cases ($M^{DR_{sag}} \approx 0.7$ for $V_{l,t} \geq 1\%$) and hogging deformation in eccentric cases ($M^{DR_{hog}} = 0.6 - 0.8$ for $V_{l,t} \geq 1\%$).

5.2.2 Local wall deformation/damage assessment

Fig. 5.14 illustrates bay top and base horizontal strains ($\varepsilon_{h,top}$, $\varepsilon_{h,base}$), relative vertical settlement ($S_{v,tot}$), slope (s), tilt (θ), and angular distortion (β), respectively, at $V_{l,t} = 2.2\%$ (refer to Fig. 2.40 for calculation processes). The horizontal strain exhibits typical patterns of top compression and base tension when the wall is located directly above the tunnel (sagging dominates; $e/L = 0$). As the eccentricity ratio e/L increases from 0 to 1/2, the base tensile strain gradually shifts to compressive, while the top compressive strain gradually transitions to tensile. The position of peak horizontal strain (including both top and base), typically located near the middle of the dominant sagging/hogging region, corresponds to the wall damage location in Fig. 5.12, i.e. the top of Bay 3 for $e/L = 1/2$ (Fig. 5.14(b)) and the base of Bay 3 for $e/L =$ 0-1/6 (Fig. 5.14(a)).

The relative settlement ($S_{v,tot}$) increases (positively or negatively, depending on the bay horizontal location relative to the tunnel) from the tunnel centreline towards both ends of the wall until reaching the vicinity of the inflection point of the wall settlement profile (approximately $1 \leq x/D_t \leq 1.5$), except for bay 1 for $e/L = 1/2$. Similar patterns are observed in terms of bay slope, tilt, and angular distortion in Figs. 5.14(d)-(f).

The relationship between angular distortion β and $V_{l,t}$ is shown in Fig. 5.15. The bays nearest the tunnel centreline (filled markers) generally exhibit relatively small angular distortion (except for $e/L = 1/3$, discussed later in this paragraph). Tunnel excavation causes the inflection point to move towards the tunnel centreline; for the central case ($e/L = 0$ in Fig. 5.15(a)) this results in the angular distortion of bays 2 and 4 to increase at the greatest rate, overtaking the values of angular distortion in bays 1 and 5 after $V_{l,t} \approx 2\%$. For the eccentric scenarios ($0 < e/L \leq 1/2$), there is generally a consistent trend with tunnel volume loss of the bays with the maximum value of angular distortion. There is a significant difference in the angular distortion between the first and third bays for $e/L = 1/6$ and the first and second bays for $e/L = 1/3$

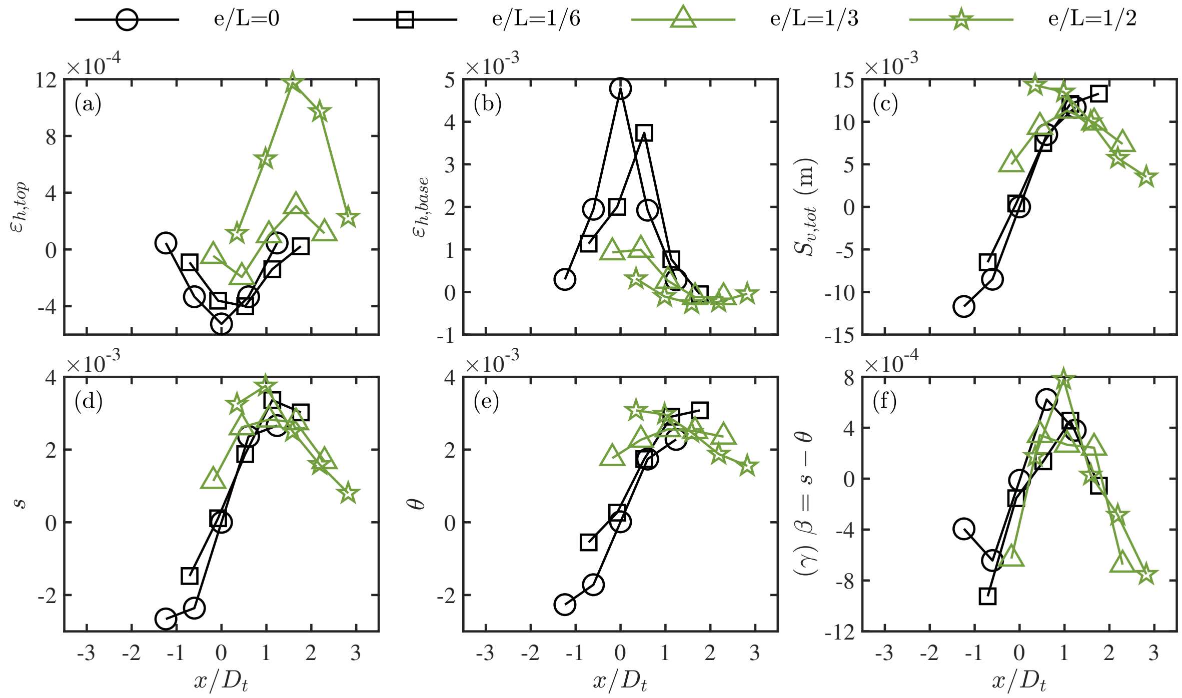

Fig. 5.14. Comparison of bay deformation parameters (markers represent bay centre; Bay 1-5 going from left to right, refer to Fig. 3.18): (a) top and (b) base horizontal strain (+ is tension); (c) relative settlement; (d) slope; (e) tilt (+ is anticlockwise); and (f) angular distortion at $V_{l,t}$ = 2.2%

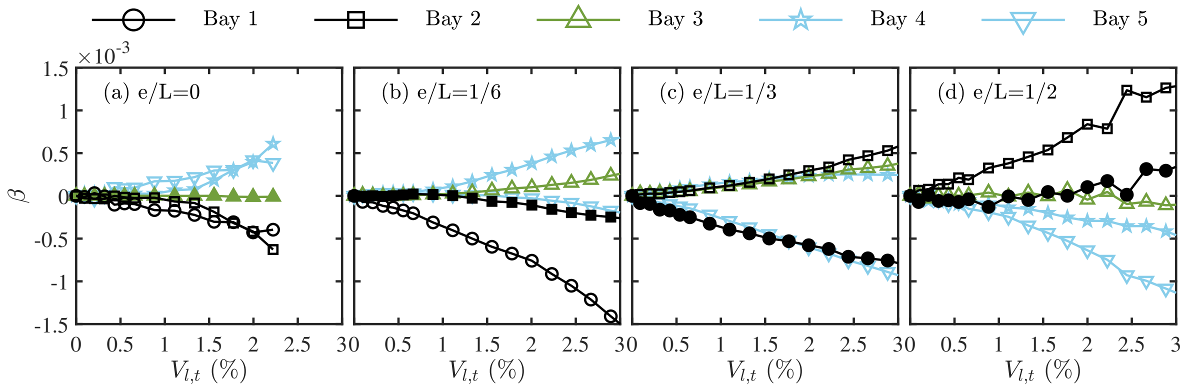

Fig. 5.15. Angular distortion of bays against tunnel volume loss (the filled markers represent the bays nearest the tunnel centreline)

(where the selected two bays in each case are roughly symmetrical about the tunnel centreline), indicating that the shorter side of the wall (relative to the tunnel centreline; within the sagging zone) undergoes more pronounced shear distortion in the eccentric scenarios than the longer part that spans both sagging and hogging zones. This can also explain why, for $e/L = 1/3$, the magnitude of angular distortion of the bay above the tunnel (Bay 1) is higher compared to the other tests (mentioned earlier).

An interesting outcome that can be gleaned from this study is the effect of structural non-linearity on the of wall response to tunnelling. This can, in part, be evaluated by considering how the components of wall bay settlements change during volume loss. Fig. 5.16 presents the settlement components induced by tilt, bending, and shear behaviours from the bay total relative settlement (Fig. 5.14(c); refer to Fig. 2.41 for calculation processes). The primary component of vertical displacement of bays is due to tilt (note the y-axis scale in Fig. 5.16(a) compared to (b) and (c)). The bays that experience more bending settlement are located near the tunnel centreline for cases where the wall centreline is close to the tunnel (Bay 3 for $e/L = 0$, Bays 2-3 for $e/L = 1/6$); for the eccentric case $e/L = 1/2$, bending occurs outside of the inflection point in the hogging zone (Bay 3). Shear induced settlements are less affected by e/L, as bays at the same position, for example at positions ①-④, exhibit similar shear induced settlements. Shear induced settlements increase from tunnel centreline towards both sides until reaching the inflection points, and then decrease to 0 before increasing again. These trends are consistent with Fig. 5.14(f).

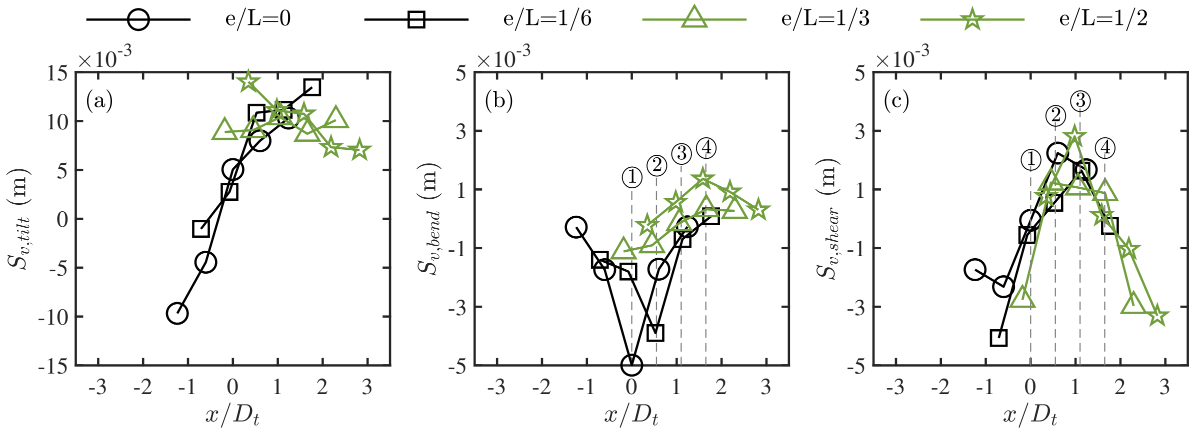

Fig. 5.16. Composition of the total settlement of bays at $V_{l,t} = 2.2\%$: (a) tilt, (b) bending, and (c) shear-induced settlement (numbered items relate to Fig. 5.17)

Going further, it is also informative to consider the wall deformation parameters (as a means of understanding the predominant deformation mode: bending or shear) in contrast to the degree of plasticity of the wall. Fig. 5.17 presents the value F_{bay} (refer to $F_{sag/hog}$ in Eq. 2.30),

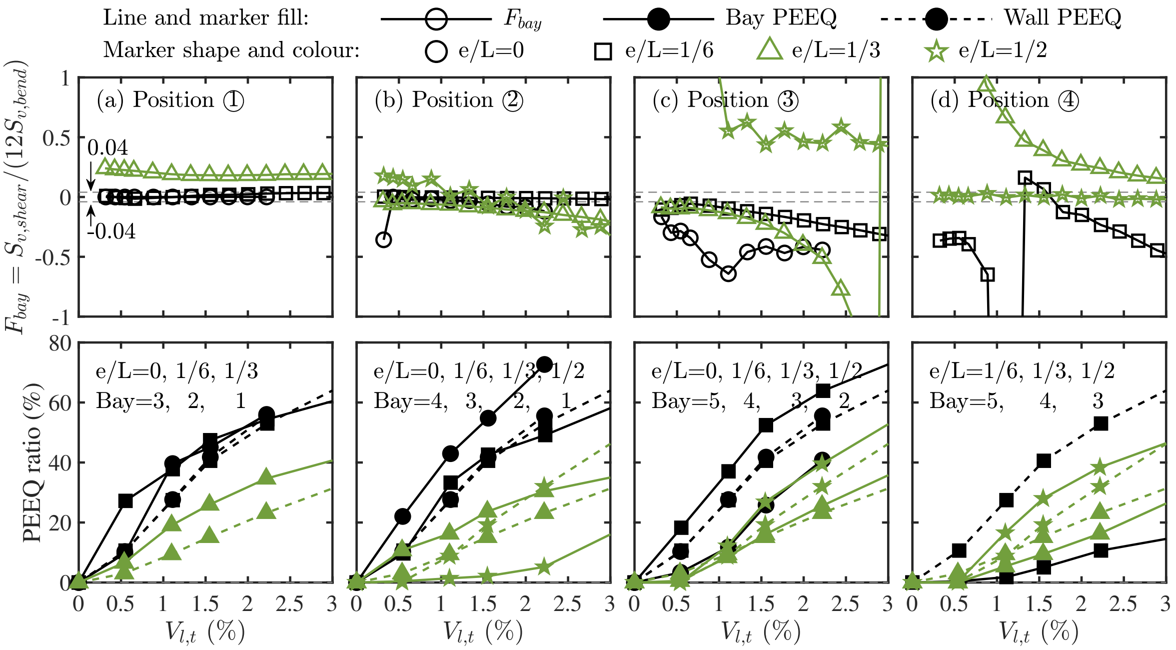

Fig. 5.17. Coefficient F_{bay} (proportional to the ratio of bay shear-to-bending settlement; upper plots) and ratio of equivalent plastic strain area (PEEQ) against tunnel volume loss (lower plots) from tunnel centreline in (a) outwards in (b)-(d) (i.e. position ①-④ in Fig. 5.16(b)-(c), where position ③ is approximately on the wall inflection points)

which is proportional to the ratio of shear-to-bending settlement of bays at position ①-④ in Fig. 5.16(b)-(c), along with the proportion of equivalent plastic strain area (PEEQ) within each bay and the entire wall (i.e. the percentage of the bay/wall that has yielded; obtained from the Abaqus model) as they relate to $V_{l,t}$. Bays closer to the tunnel (i.e. position ①-② in Fig. 5.17(a)-(b)) exhibit relatively obvious bending-dominated behaviour ($|F_{bay}| < 0.04$ or close to this limit) during the entire tunnel volume loss process and a reducing trend of PEEQ with e/L (bay PEEQ tending to exceed the overall wall PEEQ, except for Bay 1 at $e/L = 1/2$ in Fig. 5.17(b)). Bays above inflection points or further from the tunnel (i.e. position ③-④ in Fig. 5.17(c)-(d)) tend to exhibit mixed bending and shear response ($0.04 < |F_{bay}| < 1$). In general, the data shows a tendency towards shear-dominated response as volume loss increases (i.e. the absolute value of F_{bay} increases with $V_{l,t}$). The exceptions to this trend include: Bay 2 and 3 at $e/L = 1/2$ (position ③ and ④) remain stable (mixed and bending response, respectively); Bay 4 at $e/L = 1/3$ (position ④) is reduced (i.e. indicating a trend towards bending response). Position ③ shows the maximum percentage of PEEQ for Bay 4 at $e/L = 1/6$ (with bay PEEQ values being higher than the overall wall PEEQ, except for Bay 5 at $e/L = 0$) while position ④ shows a trend of increasing PEEQ with e/L (with bay PEEQ values being close to or lower than the overall wall PEEQ). The mixed bending and shear response, the main distortion mode, of bays is consistent with the values of $F_{sag/hog}$ for sagging and hogging regions of the wall in Table 3.7. The negative values of F_{bay} (composed of positive $S_{v,shear}$ and negative $S_{v,bend}$) in Fig. 5.17 indicate that the overall settlement of these bays is reduced by the effects of bending deformations.

The masonry wall at $e/L = 1/3$ exhibits minimal differences between bays in these parameters in Figs. 5.14-5.16 and lowest plastic strain areas in Fig. 5.17. This provides further evidence that short masonry walls, when subject to tunnel excavation within $0 \leq e/L \leq 1/2$, pose the lowest risk of damage if the spans of the sagging and hogging regions are the same in contrast to cases of dominating by either sagging or hogging zones.

5.3 Discussion - effect of horizontal displacements in the CCNM approach

Based on the numerical study by Yiu et al. (2017), Yu (2024) conducted a series of numerical modelling studies on tunnel-soil-masonry wall interactions under the influence of various friction coefficients between the soil and a strip foundation (μ = 0-1; μ = 0.3 is commonly adopted in such modellings). The scenario involved a 40×8.5×0.215 m masonry wall with openings resting on a 1 m-wide and 0.5 m-high foundation, with the wall buried 0.5 m deep below the surface, directly above an 11 m diameter tunnel ($C/D_t = 2.3$). Yu (2024) reported that, at $V_{l,t} = 1.5\%$, comparison of a smooth interface ($\mu = 0$) with $\mu = 0.3$ showed almost unchanged wall settlements (S_v), contact stress (i.e. pressure under the foundation base), bay top horizontal strain ($\varepsilon_{h,\mathrm{top}}$), and bay slope ($s$); increased horizontal sliding between foundation and surface (the maximum value $\Delta S_{h,max} \approx 20$ mm with $\mu = 0$ vs $\Delta S_{h,max} \approx 15$ mm with $\mu = 0.3$), bay base horizontal strain (maximum horizontal tensile strain in the central bays $\varepsilon_{h,\mathrm{base,max}} = 300\mu\varepsilon$ with $\mu = 0$ vs compression strain $\varepsilon_{h,\mathrm{base,max}} = -40\mu\varepsilon$ with $\mu = 0.3$), bay tilt (maximum value θ_{max} increased by $\approx$ 78%); and reduced bay angular distortion (maximum value β_{max} reduced by

≈ 12%), characteristic tensile strain (ε_{99}^{t} reduced by ≈ 6%), and areas of medium damage and above (Mod. D. reduced by ≈ 2%). The results demonstrate that ignoring soil-foundation friction with $\mu = 0$ tends to underestimate wall shear deformations and damage areas compared to a more realistic assumption of $\mu = 0.3$, however the degree of underestimation is reasonable.

For this study, the continuous foundation model was relatively stiff, however no restrictions on the horizontal movement of the wall base were imposed, hence the friction coefficient between the wall base and the top of the foundation can be considered to be zero, allowing for sliding between the wall and the foundation. Therefore, a 'pseudo' smooth interface existed between the wall and the ground surface due to the foundation's condition. Based on the findings from Yu (2024), in central cases of this study, the base horizontal strain of the central bay was overestimated (conservative), and the angular distortion (β) representing shear deformation could be underestimated by approximately within 10%, with minimal variation observed in the (tensile) damaged area.

5.4 Summary

This chapter presents outcomes from a geotechnical centrifuge modelling study of tunnel-masonry wall interaction. A hybrid modelling technique, known as coupled centrifuge-numerical modelling (CCNM), was used, combining the advantages of centrifuge modelling (providing accurate soil stresses/deformations and soil-foundation interactions) with those of numerical modelling (capturing complex structural details/behaviour). A previously developed CCNM method (for discrete loading of pile foundations) was extended to enable, for the first time, the simulation of a continuous strip foundation beneath a masonry wall using this hybrid modelling technique. Through a shared boundary condition between the centrifuge and numerical model, the CCNM tests are able to accurately replicate the global tunnel-masonry wall interaction problem. Novel aspects of this work include the consideration of the nonlinear response of the masonry wall, which was simulated using the Concrete Damage Plasticity constitutive model, and, by virtue of the hybrid modelling approach, accounting for the effect of load redistribution within the masonry wall during tunnel volume loss (highlighted in the chapter by comparing

CCNM results against ‘conventional’ constant load tests. The chapter also provides CCNM test results which examine wall deformation/damage and soil movements for different scenarios of tunnel-wall eccentricity, as well as insights on how masonry wall response, in terms of bending and shearing, evolve during the tunnel volume loss process.

Chapter 6

Tunnel-soil-masonry wall interaction mechanisms

The excavation of shallow tunnels may pose a risk of damage to overlying masonry buildings with strip foundations, however the tunnel-soil-masonry building interaction (TSBI) mechanisms are not well understood due to the difficulty in accurately reproducing and predicting complex real-world situations (such as structural details and building materials). The CCNM technique (Tang et al., 2024c) was demonstrated in Chapter 5 to provide, compared with conventional constant load methods, the most accurate experimental data of the global tunnel-masonry wall analysis problem by reproducing the tunnelling-induced load redistribution within CDP masonry walls. The CCNM approach was therefore adopted in this chapter to further investigate the mechanisms of how tunnelling activities induce soil displacements and cause distortion and damage to different masonry walls with strip foundations.

This chapter presents findings from ten geotechnical centrifuge tests using the CCNM approach (see Table 6.1, which is the same as Table 3.8 in Section 3.3), including one greenfield tunnelling test and nine tunnel-masonry wall interaction tests (representing classic cases of tunnelling directly underneath masonry walls, with a wall-to-tunnel eccentricity $e/L = 0$). The study considers five standard masonry walls (with different height and opening ratios) and four additional non-standard walls (with variations in Young's modulus or density within the standard two-storey masonry wall H8.5O19) designed to isolate the influence of wall bending stiffness and self-weight. The non-standard walls H8.5O19E- and H8.5O19E+ have similar bending stiffness to the standard walls H4.5O20 and H12.5O19, respectively. The non-standard walls H8.5O19d- and H8.5O19d+ have the same self-weight as the standard walls H4.5O20 and H12.5O19, respectively.

This chapter first presents the results of tunnelling-induced tensile and angular distortions within different masonry walls, followed by an anslysis of the deformation parameters (such as settlement S_v, deflection ratio DR, and modification factors of deflection ratio M^{DR}) based on the wall base and greenfield surface settlement profiles. This is followed by results relating to the foundation settlement (measured by LVDT and PIV) and its compatibility with wall base settlement (fitted LVDT curve) in Abaqus and the underlying surface settlement (measured by PIV) in the centrifuge. Finally, tunnelling-induced soil movement is presented along with a discussion on how these affect and are affected by the masonry walls. This chapter reveals the influence of the geometric factors of walls (including height and openings) and internal factors within masonry walls (i.e. bending/shear stiffness, self-weight) on the TSBI problem.

Table 6.1. Test summary (in prototype scale)

Test series	No.	Label [a]	Height (m)	Opening (%)	EI [b] (GN·m^2)	GA_s [b] (GN)	Surface pressure (kPa)
	1	GF	/	/	/	/	/
Standard	2	H4.5O20	4.5	20	12.7/26	0.8/1	17.7
	3	H8.5O19	8.5	19	52/88.1	1.9/1.8	33.6
	4	H12.5O19	12.5	19	106.6/161.6	1.9/2	49.6
	5	H8.5O0	8.5	0	69.3/101.9	4.4/4.7	41.7
	6	H8.5O27	8.5	27	47.5/71.8	1.1/0.9	30.3
Non-standard	7	H8.5O19E-	8.5	19	12.1/33.4	0.4/0.4	33.6
	8	H8.5O19E+	8.5	19	107.5/146.9	3.9/3.8	33.6
	9	H8.5O19d-	8.5	19	52/88.1	1.9/1.8	17.7
	10	H8.5O19d+	8.5	19	52/88.1	1.9/1.8	49.6

[a] GF: greenfield; H: height; O: opening percentage; E: Young's modulus; d: density; +: increase; -:decrease; [b] EI: bending stiffness; GA_s: shear stiffness; wall only / wall + foundation

6.1 Tensile and angular distortions within masonry walls

Figs. 6.1-6.2 illustrate the distribution of tensile strain within different masonry walls at $V_{l,t}$ = 2.2%, along with corresponding characteristic tensile strains ε_{99}^{t} (the strain that is not exceeded in 99% of the total volume of the masonry wall, as adopted by Yiu et al. (2017)) and the percentages of moderate and above damage areas (Mod. D., defined as $\varepsilon^{t} > 0.0015$ according to Mair et al. (1996); results rounded to nearest integer value). Tensile damage phenomena tend to concentrate in the centre and lower part of the walls (i.e. beneath the door and near its top corners when applicable) and radiate to the surroundings (spanning approximately −5 m to 5 m horizontally, roughly representing sagging regions on the surface settlement curves).

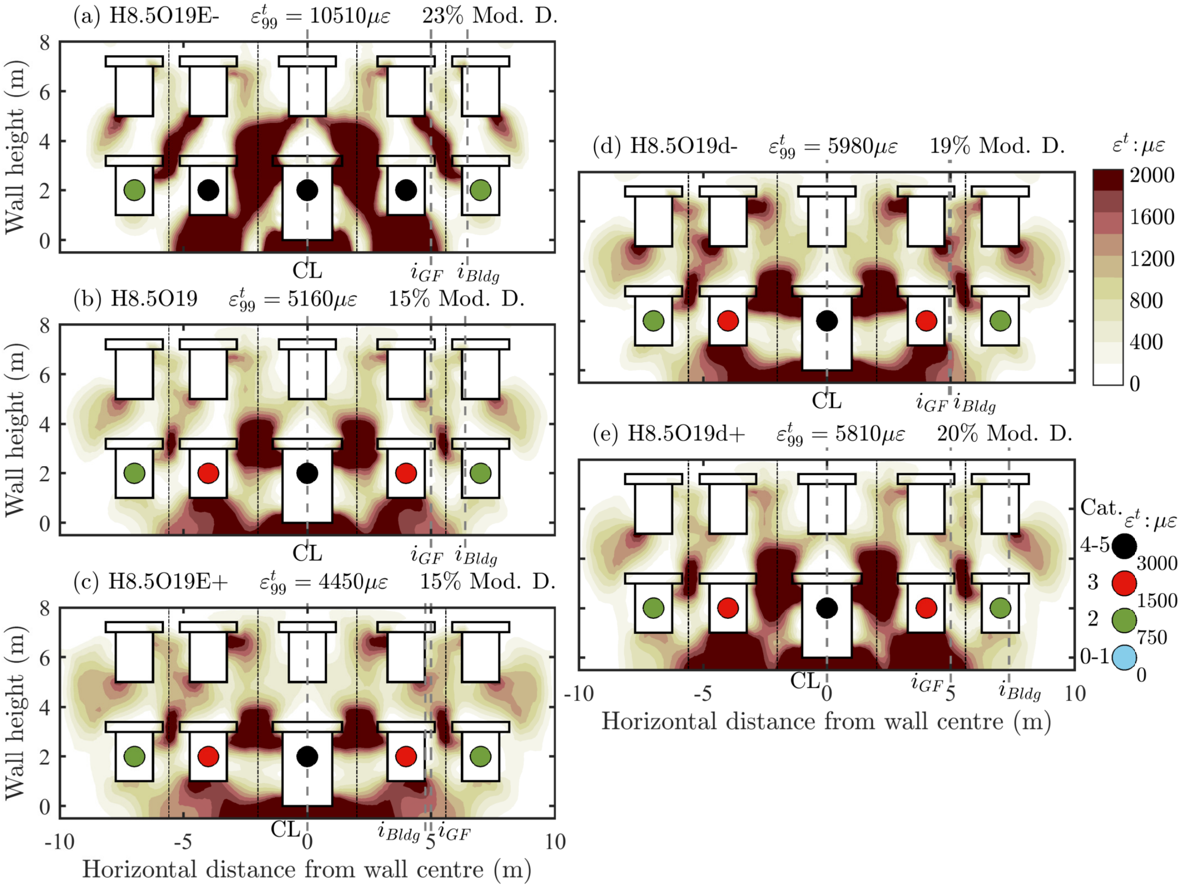

Fig. 6.1. Distributions of max principal strain (tensile strain) of non-standard walls at $V_{l,t}$ = 2.2%

Firstly, the effect of bending stiffness EI of the masonry walls (determined by Young's modulus E) in Fig. 6.1(a-c) is discussed. The low-E wall (H8.5O19E-) with the lowest bending stiffness is most susceptible to tensile deformation, with the highest severity (ε_{99}^{t}) and area of damage (Mod. D.). As the bending stiffness was enhanced (H8.5O19E- vs H8.5O19 vs H8.5O19E+), both the characteristic tensile strain ε_{99}^{t} and the area of Mod. D. are reduced. Considering the relative values of bending stiffness of the three walls (0.4:1:1.7, including foundation), higher bending stiffness is seen to have a limited effect on reducing wall deformation, whereas lower bending stiffness significantly increases the risk of wall damage. The high Young's modulus of H8.5O19E+, compared to H8.5O19, results in a more dispersed distribution of tensile damage within the wall, with more significant damage occurring around the two windows adjacent to the middle upper one and between the lintels of the lower layer windows; the main area where damage is concentrated (i.e. around the door) is slightly smaller.

Note that for the masonry walls without a foundation and with identical structural details (i.e. H8.5O19, H8.5O19E+, and H8.5O19E-), the shear stiffness GA_s is proportional to the bending stiffness EI in the elastic range ($EI/GA_s \approx$ 27-30, see Table 6.1). When considering the walls with the foundation together, the ratio $EI/GA_s \geq 39$, indicating a greater proportion of bending behaviour. Additionally, it was demonstrated in Section 5.2.2 that bending distortions (in sagging regions above the tunnel) are dominant in such cases. Thus, the bending stiffness EI is primarily considered to describe tunnelling-induced building deformations; the shear stiffness GA_s also affects wall behaviour (discussed later in this section) but could not be analysed independently among H8.5O19, H8.5O19E+, and H8.5O19E-.

Figs. 6.1(d, b, e) examine the effect of an increase or decrease in wall self-weight on the characteristic tensile strain ε_{99}^{t} and areas of Mod. D., with self-weight ratios for H8.5O19d-, H8.5O19, and H8.5O19d+ being 0.5:1:1.5. Higher self-weight walls (H8.5O19d+, H8.5O19) exhibit concentrated damage at the bottom of the lower openings and between their lintels primarily stemming from excessive gravitational loads, while the lower self-weight wall (H8.5O19d-) shows scattered damage, partly around the upper openings, due to significant distortions.

It is observed that the geometries of damage between local tensile damage areas within the walls are influenced by wall material properties. Low bending stiffness and high self-weight, through different mechanisms, tend to create vertical connections between local damage areas;

conversely, high bending stiffness and low self-weight contribute to horizontal connections.

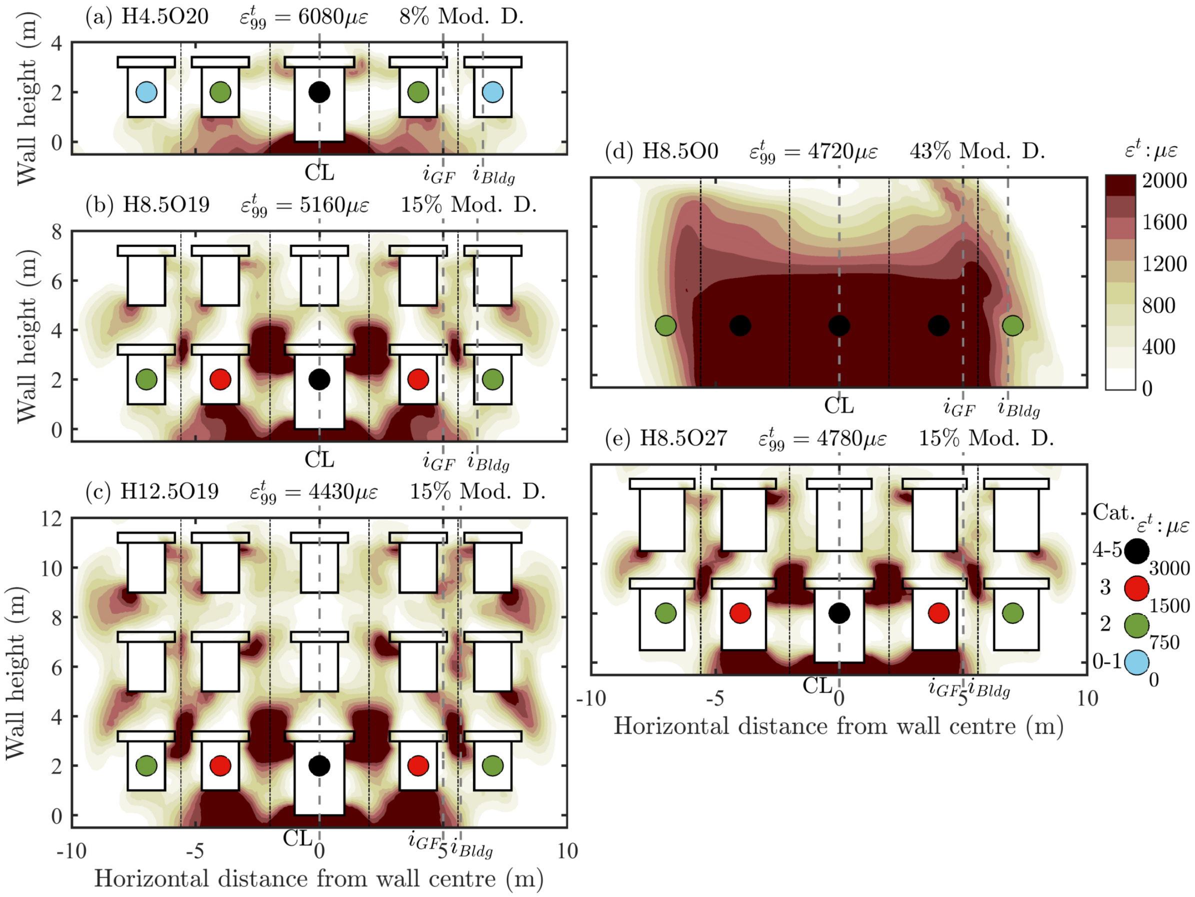

Fig. 6.2. Distributions of max principal strain (tensile strain) of standard walls at $V_{l,t} = 2.2\%$

Next, the standard masonry walls are analysed. Comparing H8.5O0, H8.5O19, and H8.5O27 in Figs. 6.2(d, b, e), the presence of openings slightly increases the characteristic tensile strain ε^t_{99} and significantly reduces the (ratio of) damage areas within the masonry walls. The wall without openings (H8.5O0) exhibits beam-like behaviour, characterised by significant tensile damage at the lower part of the wall and relatively uniform strain gradients. The higher bending stiffness and self-weight (mentioned earlier), coupled with the absence of openings in the structure, impose more significant local constraints within the wall H8.5O0, collectively resulting in a larger and more continuous damaged area in the wall. The proportion of damage area in H8.5O19 and H8.5O27 is identical, with the latter having slightly lower bending stiffness and self-weight than the former. However, the significantly reduced shear stiffness of H8.5O27 allows the entire wall greater flexibility (i.e. the ‘columns’ and ‘beams’ around (between) the openings are more prone to deformation), resulting in lower characteristic tensile strain ε_{99}^{t} and a more dispersed distribution of damaged areas.

As shown in Figs. 6.2(a-c), changes in wall height (or the number of storeys) involve various factors including bending stiffness, shear stiffness, and self-weight of the masonry wall. Taller walls exhibit more damage areas of high-magnitude tensile strains on the ground floor. Comparing the two- and three-storey walls (H8.5O19 and H12.5O19 with the same shear stiffness), they have the same ratio of Mod. D. (15%), whereas the characteristic tensile strain ε_{99}^{t} of the three-storey wall is lower. The damage distribution within H12.5O19 shows a concentration in the middle and lower layers of the wall (caused by higher self-weight) and a small area of dispersion (caused by higher bending stiffness). The values of the characteristic tensile strain ε_{99}^{t} and the ratio of Mod. D. areas are close to the two-storey wall H8.5O19E+, which has a similar bending stiffness to H1.25O19. Compared to the two-storey wall (H8.5O19), the characteristic tensile strain ε_{99}^{t} of the one-storey wall (H4.5O19) is higher (similar to the value of the two-storey wall H8.5O19d- which has the same self-weight as H4.5O20), however the proportion of medium damaged areas is only 8%, roughly half of that of the two-storey wall. The tensile strain around the two window openings near the edge of the one-storey wall is minimal, which is different from other walls, possibly due to the larger length-to-height ratio $L/H = 4.4$. The lower bending stiffness, shear stiffness, and wall self-weight all contribute to significant differential settlement of the wall during tunnelling (see Fig. 6.6), the primary factor influencing the internal tensile strain of the wall.

The masonry walls can be divided into five bays according to the locations of openings, as illustrated by the red dots and dashed lines in Fig. 3.19. Fig. 6.3 provides the angular distortions β of all bays during tunnel volume loss and demonstrates that bays 2 and 4, immediately adjacent to the central bay (the walls are symmetric about the central bay), generally have the highest values of β, except for H4.5O20 where β for bays 1 and 5 are only slightly higher. As such, Fig. 6.4 shows β_{max} obtained from bay 4, which generally represents the maximum values of angular distortion. Taking the two-storey masonry wall H8.5O19 as a baseline, reduced shear stiffness (H8.5O27) and self-weight (H8.5O19d-) result in a significant increase in angular distortion, while increased self-weight (H8.5O19d+) causes a slight reduction. The

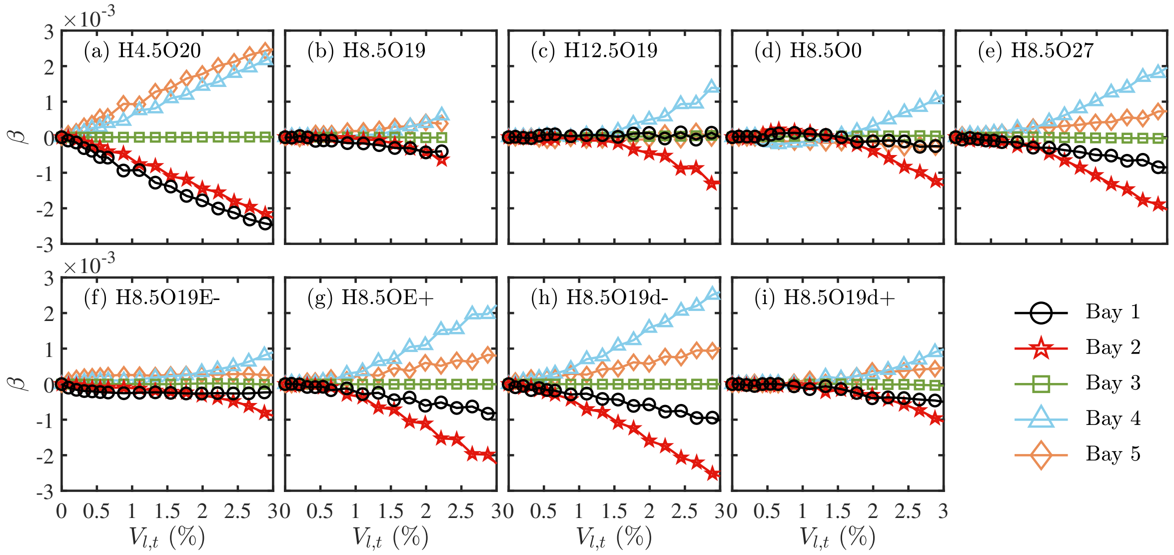

Fig. 6.3. Angular distortion of bays (from left to right in walls) against tunnel volume loss

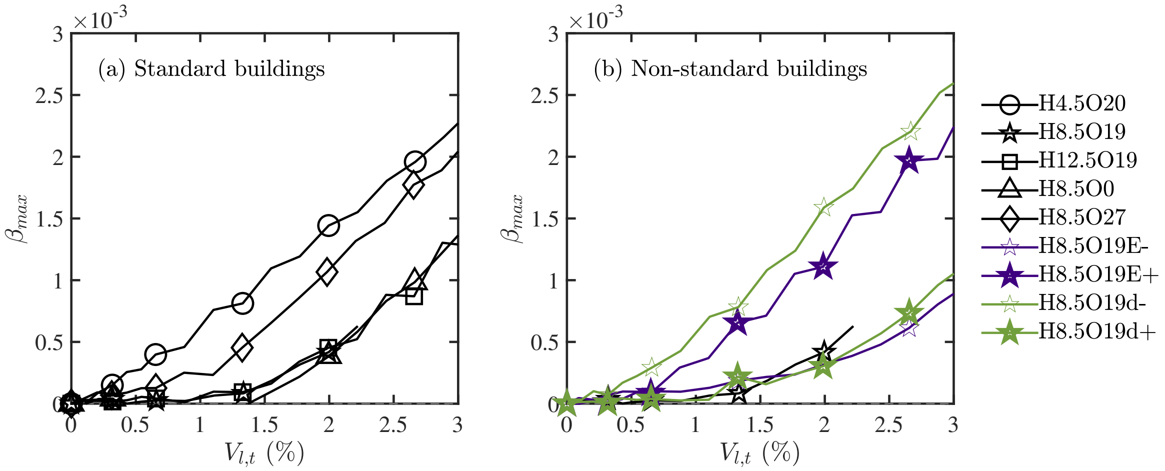

Fig. 6.4. Angular distortion of bay 4 against tunnel volume loss

higher bending stiffness (H8.5O19E+) homogenizes the local damage area (below the door, extending to both sides; see Figs. 6.1(b-c)), but instead increases the bay angular distortion; reducing the bending stiffness (H8.5O19E-) forms a vertical continuous damage area on both sides of the middle openings (see Figs. 6.1(a-b)), maintaining the integrity of adjacent bays after $V_{l,t} \geq 1.6\%$, i.e. slightly reducing the bay angular distortion. Consequently, the one-storey wall H4.5O20, featuring low bending/shear stiffness and self-weight, exhibits the maximum increase in magnitude in bay angular distortion. In contrast, the bays of the three-storey wall H12.5O19 and the wall without openings H8.5O0 behave similarly to that of H8.5O19.

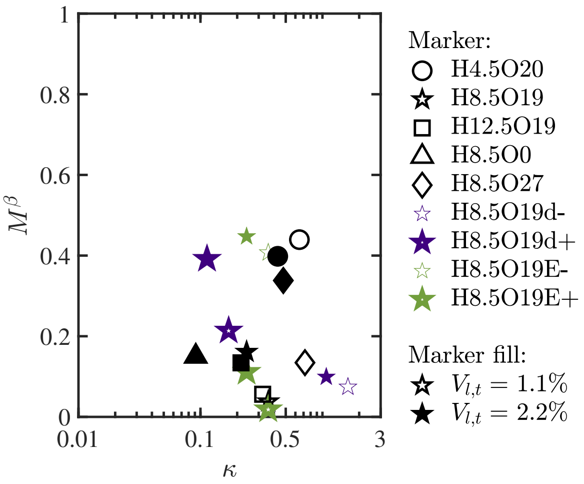

Fig. 6.5. Modification factors of angular distortion M^{β} against relative soil/building shear stiffness κ at $V_{l,t} = 1.1\%$ and 2.2%

Fig. 6.5 presents the relationship between modification factors of the maximum angular distortions M^{β} and corresponding relative soil/building shear stiffness κ (which considers χ in the same way as Eq. 2.31, i.e. $GA_s^* = GA_s/(\chi l)$ where $\chi = (20.79 \times 2.66)/(20 \times 0.571) = 4.8$ representing the foundation-to-wall bottom area ratio, as proposed by Franza et al. (2020b) to describe buildings with strip foundations) at $V_{l,t} = 1.1\%$ and 2.2%. With increases in tunnel volume loss, the relative shear stiffness κ decreases due to soil stiffness degradation, and the modification factors tend to increase, consistent with Fig. 6.4. The modification factors of the maximum angular distortions M^{β} for different walls roughly increase with corresponding relative soil/building shear stiffness κ; similar increasing trends were reported by Son and Cording (2005); Xu et al. (2020b); Yu (2024) using comparable methods.

In summary, the impact of wall height when going from two to three storeys (H8.5O19, H12.5O19) on tensile and bay angular distortion is relatively minimal (consistent with findings by Yiu et al. (2017); Xu et al. (2020b)). Compared with the reference two-storey wall H8.5O19, special attention is needed for (1) the increased tensile damage areas and the different tensile damage distributions within walls with no openings (H8.5O0, without opening-induced stress concentrations inside the walls) and (2) for the increased bay angular distortions of larger-opening walls (H8.5O27) and one-storey walls (H4.5O20) due to lower bending/shear stiffness and self-weight.

6.2 Deformation parameters of wall base settlement

Fig. 6.6 illustrates the wall base settlement profiles under the influence of wall height, opening areas, bending stiffness, and self-weight at $V_{l,t} = 2.2\%$. Figs. 6.7-6.8 present the deflection ratios of wall sagging/hogging regions and corresponding modification factors relative to greenfield data during tunnel volume loss, respectively.

Under identical or similar wall geometry conditions as the reference wall H8.5O19, lower shear stiffness (H8.5O27 in Fig. 6.6(b)), bending stiffness (represented by Young's modulus; H8.5O19E- in Fig. 6.6(c)), and self-weight (H8.5O19d- in Fig. 6.6(d)) results in, as expected, a significant increase in differential settlement, whereas the maximum settlement (i.e. at the centre of the settlement trough) remains nearly unchanged. The higher bending stiffness case H8.5O19E+ in Fig. 6.6(c) reduces the settlements by 2-5 mm, however causes an increase in differential settlement (especially in the central region between −5 m and 5 m). This counter-intuitive outcome occurs because of the non-linear response within the CDP model; the elevated Young's modulus of H8.5O19E+ induces a more dispersed region of yield within the wall, thereby resulting in a reduction in effective secant stiffness of the wall and more severe localised distortion. The higher self-weight case H8.5O19d+ in Fig. 6.6(d) exhibits a similar settlement profile to the reference wall H8.5O19, except for a slightly higher settlement and differential settlement in the central part.

Compared to the reference two-storey wall H8.5O19, the differential settlement of the one-storey wall H4.5O20 in Fig. 6.6(a) is increased markedly (with a lower maximum settlement) due to the lower bending stiffness, shear stiffness, and self-weight. Conversely, the three-storey wall H12.5O19 has a settlement profile similar to that of H8.5O19, however, with settlement values being reduced by approximately 2-3 mm and, different from H8.5O19E+ and H8.5O19d+, reduced differential settlement attributed to the combined influence of higher bending stiffness and self-weight. This implies that the construction characteristics of the walls also contribute to the tunnel-building interaction process, influencing the deformation and load re-

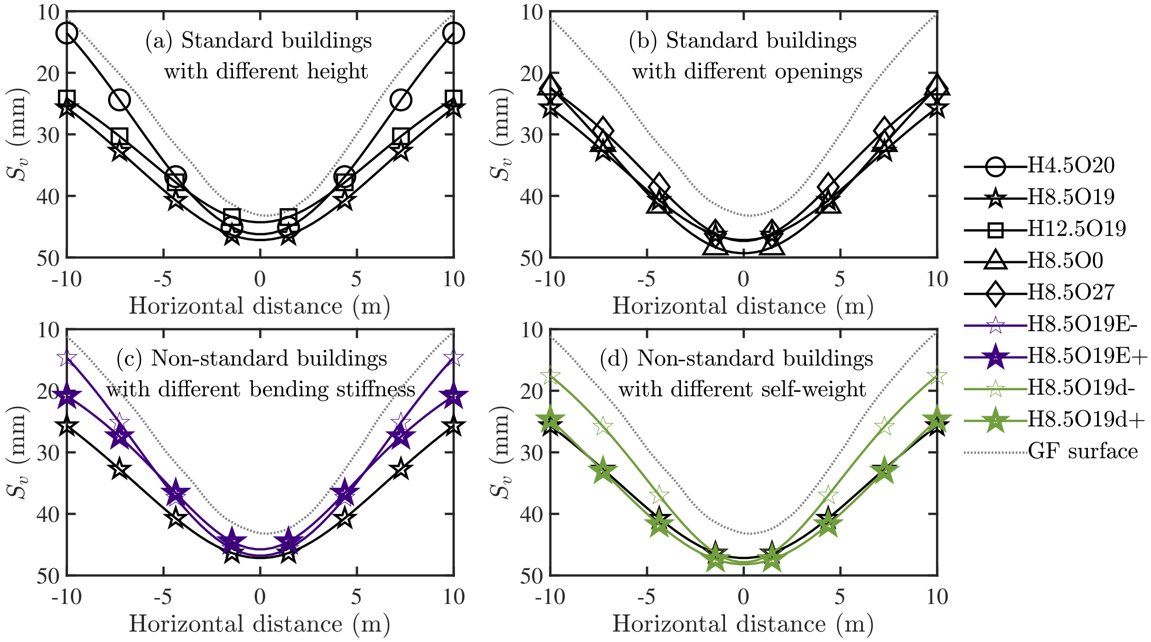

Fig. 6.6. Settlement troughs of wall base and greenfield surface at $V_{l,t} = 2.2\%$

distribution inside the walls. The wall without openings H8.5O0 in Fig. 6.6(b) exhibits greater differential settlement and maximum settlement due to the continuous stress distribution (i.e. without structural concentrated stress) within the wall and the higher weight at the positions of openings.

There is an approximately linear relationship between the wall sagging/hogging deflection ratios $DR_{sag/hog}$ and tunnel volume loss in Fig. 6.7. The masonry walls predominantly experience sagging, with high-magnitude sagging and low-magnitude hogging deflection ratios. Consistent with the changing trends of the differential settlements of entire walls, compared with the reference wall H8.5O19, more flexible/lighter walls related to the one-storey wall (H4.5O20. H8.5O189E-, H8.5O19d-) show higher sagging deflection ratios during tunnel volume loss, close to that of the greenfield surface; H8.5O27 behaves similarly to H8.5O19 before $V_{l,t} = 1\%$, after which the sagging deflection ratios of H8.5O27 exhibit a higher level; an increase in bending/shear stiffness or self-weight (H8.5O19E+, H8.5O19d+, H8.5O0) slightly increases the sagging deflection ratios, while the three-storey wall (H12.5O19) slightly reduces the sagging deflection ratios.

The modification factors of deflection ratios $M^{DR,sag/hog}$ in Fig. 6.8 reproduce the relation-

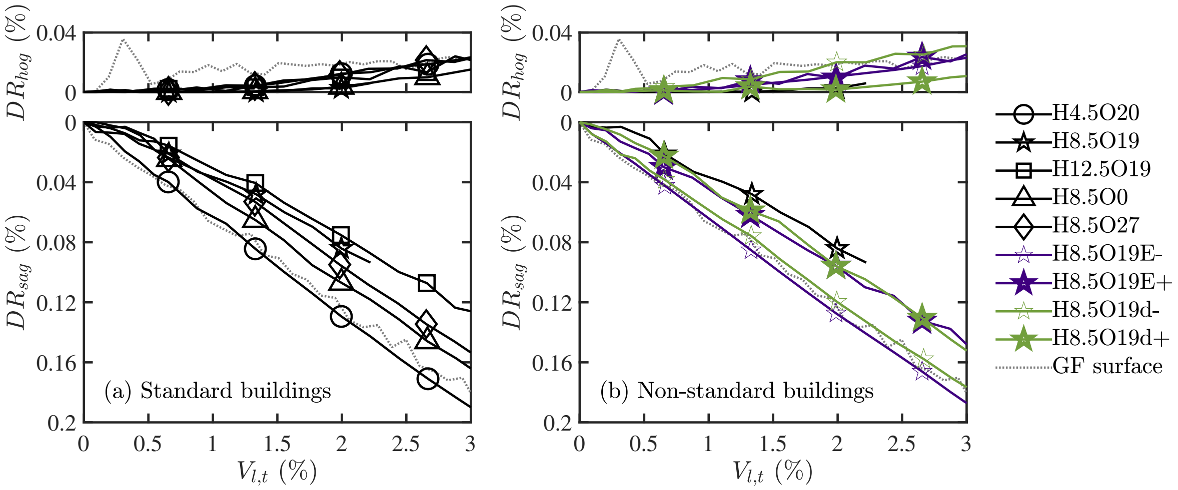

Fig. 6.7. Building deflection ratios in sagging and hogging zones against tunnel volume loss

ships between the magnitude of sagging/hogging deflection ratios of different walls in Fig. 6.7, and the changes in the hogging zones are more pronounced. Hogging deflection ratio modification factors exhibit a gradual increase before reaching 1% tunnel volume loss, followed by a rapid ascent (towards 1, where a value of 1 indicates it matches with greenfield conditions). This trend arises from the initial small span and differential settlement in hogging areas, both of which increase with tunnel volume loss. The sagging deflection ratio modification factors rapidly increase before 1% tunnel volume loss and remain relatively constant (in the 0.7-1 range) thereafter. These results underscore the credibility of evaluating wall deformation deflection ratios through the greenfield data.

Fig. 6.9 presents the deflection ratio modification factors of wall sagging/hogging regions $M^{DR,sag/hog}$ against relative building/soil stiffness (a) $\rho_{sag/hog}$ (see Eq. 2.29, Goh and Mair (2011)) and (b) $\eta_{sag/hog}$ (see Eq. 2.30, which factors in wall shear stiffness, Franza et al. (2020a)) at $V_{l,t}$ = 1.1-2.2%. The greenfield soil secant stiffness ($E_s \approx 43.2$ MPa and 65 MPa at $V_{l,t}$ = 1.1% and 2.2%, respectively, from Xu et al. (2020b)), was used to calculate the relative stiffness in all cases, and thus the influence of wall self-weight (increasing the effective soil stiffness by less than a factor of two in a logarithmic scale) is ignored. Note that previous estimations of the relative stiffness tend to employ greenfield sagging/hogging spans (Franza et al., 2017; Xu et al., 2020b), while the calculation in this study adopted the spans of the wall base

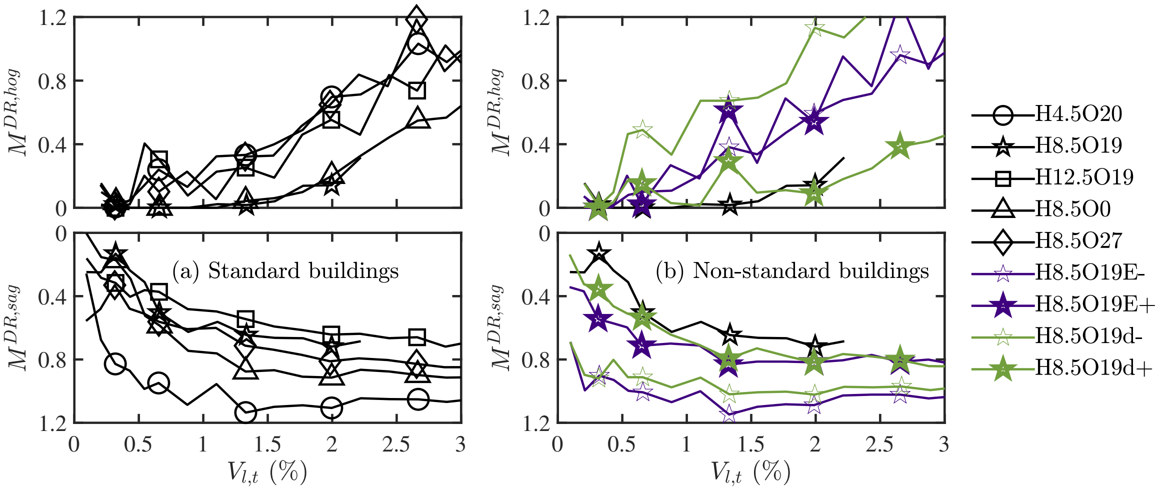

Fig. 6.8. Modification factors of sagging/hogging deflection ratios against tunnel volume loss

(Franza et al., 2020b); this does not cause any obvious differences in the adopted log-scale.

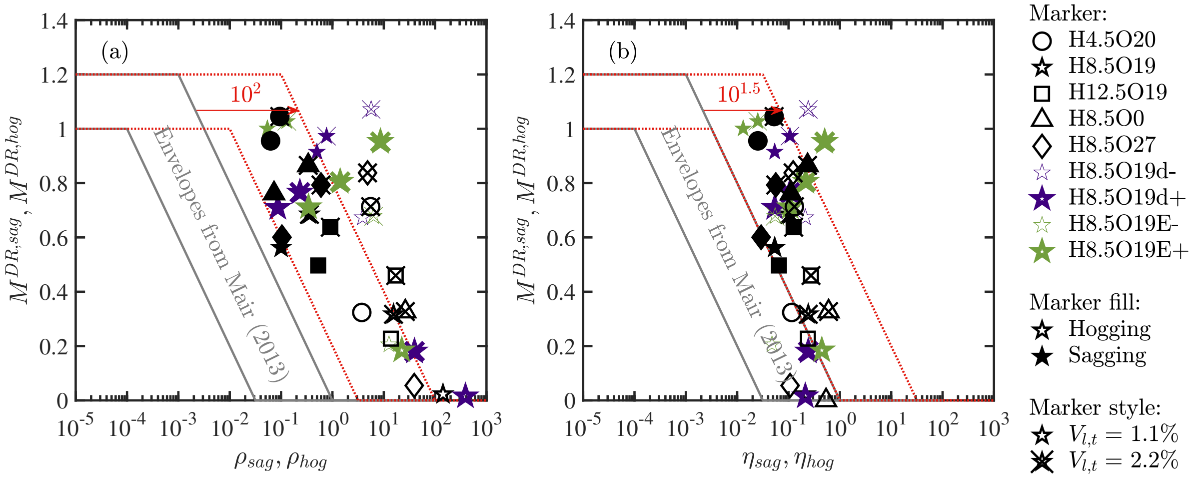

Fig. 6.9. Modification factors of deflection ratio $M^{DR,sag/hog}$ against relative building/soil stiffness (a) $\rho_{sag/hog}$ and (b) $\eta_{sag/hog}$ at $V_{l,t} = 1.1\text{-}2.2\%$

The distribution patterns of the modification factors exhibit similarities for both types of relative stiffness, i.e. the wall sagging/hogging deflection ratio modification factors (representing wall deformation) are reduced with higher relative stiffness values. This is less true in Fig. 6.9(b), which has a more concentrated (vertical) grouping of results with respect to $\eta_{sag/hog}$. From a practical perspective, these results may, therefore, not be very useful, since for a given value of $\eta_{sag/hog}$ one could obtain a large range of values of $M^{DR,sag/hog}$. In other words, applying $\eta_{sag/hog}$ is not particularly suitable for the cases in this thesis.

The relative stiffness of hogging areas tends to surpass that of sagging areas due to the shorter hogging spans (note that, in the calculation of relative stiffness here, sagging/hogging span was the only variable that affects the sagging/hogging relative stiffness for a wall at a certain tunnel volume loss). Higher sagging/hogging relative stiffness is typically associated with higher wall bending stiffness and self-weight, both of which could change the wall settlement profiles. As tunnel volume loss increases, deteriorated soil stiffness and reduced sagging span result in an increase in the relative stiffness of sagging regions.

The envelopes in Fig. 6.9 (i.e. the grey solid lines) were proposed by Mair (2013) to match field and numerical and centrifuge modelling data of buildings with shallow foundations affected by tunnelling or deep excavations. The envelope positions are primarily determined using sagging data (sagging regions are predominant; see Fig. 6.7), with hogging data not necessarily covered considering the possible errors in the response of the shorter hogging regions (discussed later). The relative stiffness of sagging regions exceeds the envelope range by approximately 1.5-2 orders of magnitude (see the red dotted envelopes); the cause of this can be related to two reasons.

First, the normalised bending stiffness EI^* of the single walls in this work might be greater than entire buildings in realistic cases. For example, H8.5O19 has $EI = 88.1\,\mathrm{GN{\cdot}m^2}$ and $EI^* = 31.9\,\mathrm{GN{\cdot}m^2/m}$ (Eq. 2.31, where $\chi = 4.8$, mentioned in Section 6.1); comparable field cases from DeJong et al. (2019) have EI = 13-41 GN·m^2 and EI^* = 0.5-2.8 GN·m^2/m (where $\chi = 1$ representing raft foundation), contributing to approximately 1 order of magnitude offset. The use of χ for single walls in this work is reasonable, because an assumed complete masonry building comprised of two H8.5O19 walls (i.e. front and back walls) connected by two 10 m-long plane walls gives the normalised bending stiffness of the entire building $EI^* = 88.1 \times 2/(10\chi) = 23.5\,\mathrm{GN{\cdot}m^2/m}$ (where $88.1 \times 2 = 176.2\,\mathrm{GN{\cdot}m^2}$ is the sum of bending stiffness of the front and back walls H8.5O19 that is used to roughly represent the bending stiffness of the complete building, and $\chi = (20.79\times2.66\times2+7.34\times2.66\times2)/(20\times10) = 0.75$ represents the ratio of the bottom area of the strip foundations to that of the complete building) that is comparable to the EI^* of the single wall H8.5O19 ($31.9\,\mathrm{GN{\cdot}m^2/m}$).

Second, shorter sagging and hogging spans $L_{sag/hog}$ give larger relative stiffness value (see

Eqs 2.29-2.30). In this study, the values of $L_{sag/hog} \leq 15$ m , whereas they are 15-28 m in Goh and Mair (2011)). This difference would contribute to approximately 1 order of magnitude offset (the $(1/L_{sag/hog})^3$ ratio $((15+28)/2)^3/((5+15)/2)^3 = 9.9$). Goh (2011) reported the results of 10-60 m long buildings near deep excavations falling within the envelopes from Mair (2013), however the results could not provide enough reference for short buildings spanning both sagging and hogging zones (such as $L = 20$ in this study) due to the longer spans ($L_{sag/hog} \geq 20$ m, except for the 10 m-long building). Short buildings tend to exhibit relatively rigid behaviours Goh and Mair (2011); Amorosi et al. (2014), which would affect the calculations of relative building/soil stiffness. Goh (2011); Mair (2013) also reported the possible phenomenon of approximately an order of magnitude increment in relative stiffness under the influence of building length and eccentricity.

6.3 Foundation displacement

Figs. 6.10-6.13 present the foundation settlement measured by seven LVDTs, its fitting curve (representing the wall base settlement in Fig. 6.6 as well), foundation settlement/horizontal displacement acquired using the GeoPIV-RG technique, and settlement/horizontal displacement of the ground surface with and without the foundation/wall by GeoPIV-RG. Due to the strip foundation model not being immediately against the inner face of the acrylic wall of the strongbox (to avoid friction effects), the surface soil settlements are less than the foundation settlements (see Figs. 6.10-6.11); this outcome is not realistic, i.e. it indicates that the soil and foundation overlap by about 5-10 mm, or 0.07-0.14 mm in model scale; similar phenomena were also observed within centrifuge modelling tests reported by Farrell et al. (2014); Ritter et al. (2017); Xu et al. (2020b)).

In centrifuge simulations of excavating a tunnel directly beneath a building, gaps between the bottom of the building (or shallow foundation) and the ground surface have been observed (Farrell et al. (2014); Ritter et al. (2020) for $V_{l,t} \geq 1.4$-2%). However, employing more flexible, lighter, or shorter building models in centrifuges or numerical modelling is less likely to generate such gaps (demonstrated in Farrell et al. (2014); Yiu et al. (2017); Xu et al. (2020b) at

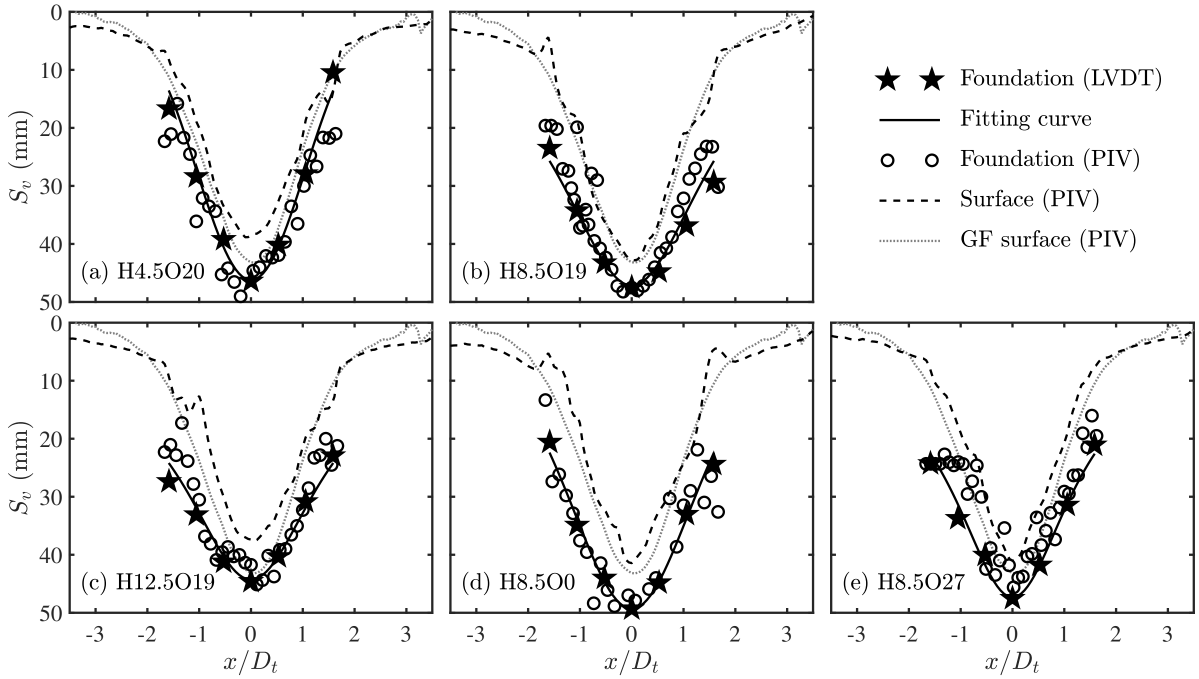

Fig. 6.10. Vertical displacements at foundation base level for standard walls at $V_{l,t} = 2.2\%$

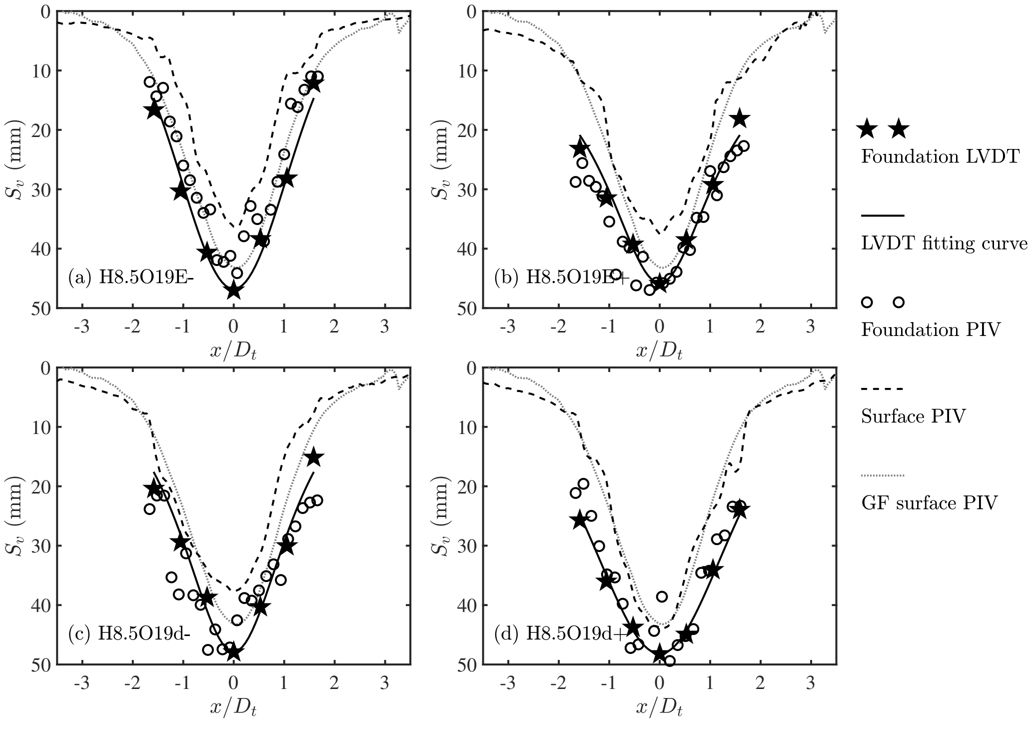

Fig. 6.11. Vertical displacements at foundation base level for non-standard walls at $V_{l,t} = 2.2\%$

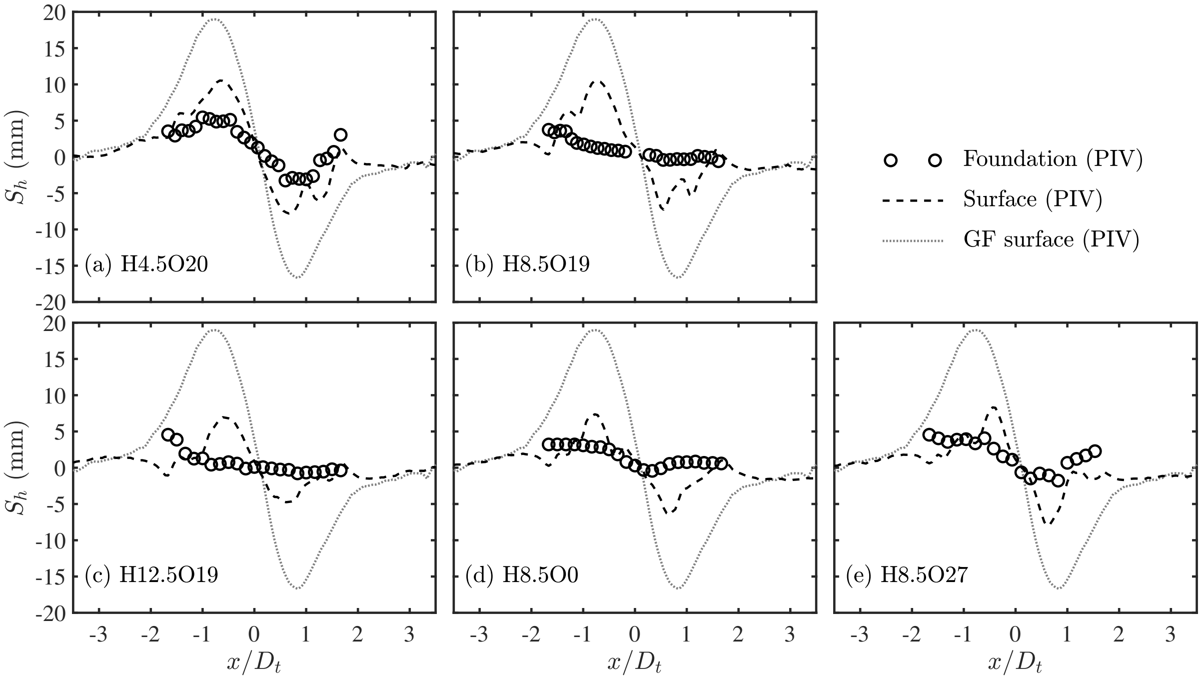

Fig. 6.12. Horizontal displacements at foundation base level for standard walls at $V_{l,t} = 2.2\%$

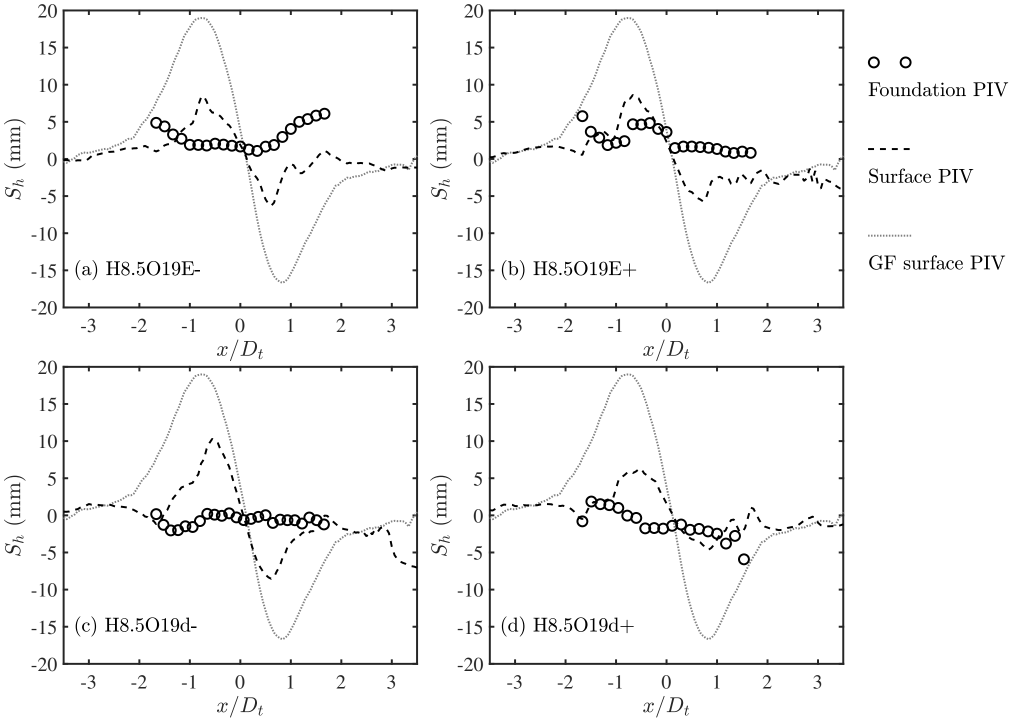

Fig. 6.13. Horizontal displacements at foundation base level for non-standard walls at $V_{l,t} = 2.2\%$

comparable volume losses indicated above).

In this study, a minimum nominal load of -20 N (an upwards force accounting for the self-weight of the load actuation components below the load cell and approximately 1/6 the foundation self-weight, representing the force needed to lift the (local) foundation off the surface) was adopted; the control program never allowed the foundation load to go below this value. This was done to ensure no obvious soil-foundation separation, which could cause, upon possible subsequent reloading, an impact force on the soil (since the actuators are load-controlled and the separation distance would not be controllable). Fig. 6.14 shows the change in foundation loads for the central load actuator (i.e. actuator a4 that was directly above the tunnel, see Fig. 3.12(b)), and Fig. 6.15 shows the actuator force from a1-3. The load adjustments show variability from one volume loss stage to the next; this reflects the variability in the experimental settlement data which feeds into the numerical calculation of foundation loads. Despite this variability, the CCNM method still provides a reliable overall trend of the load adjustment within the masonry walls.

Figs. 6.14-6.15 indicate that the actuator loads are transferred from the central part of the strip foundation (a3-4) to its ends (a1-2) during tunnel volume loss. Similar phenomenon can also be observed in eccentric cases in Fig. 5.6 in Chapter 5. Fig. 6.14 shows that most tests maintain a load above 10 N throughout the tests, indicating that a gap is unlikely to form (in particular the heavier H8.5O0 and H8.5O19d+ cases where the load remained above 20 N). The non-standard walls with a high stiffness (H8.5O19E+) and low density (H8.5O19d-) have loads < 0 N, indicating that a gap would likely form for these cases.

The PIV-measured foundation settlement profiles in Figs. 6.10-6.11 (circular markers), despite measurement errors due to experimental constraints such as the small foundation thickness, align closely with the LVDT (fitting) data (star markers and solid lines). The fitted curves from the LVDT data are sent to Abaqus to obtain a revised loading on the foundation (see Section 3.4.4), hence the agreement of the fitted curve (based on only 7 points) with respect to the distributed settlements obtained from PIV is important. The close resemblance in the fitted LVDT and PIV settlement profiles of the strip foundation therefore indicates that the load distribution at the base of the wall in the numerical model is consistent with the load distribution

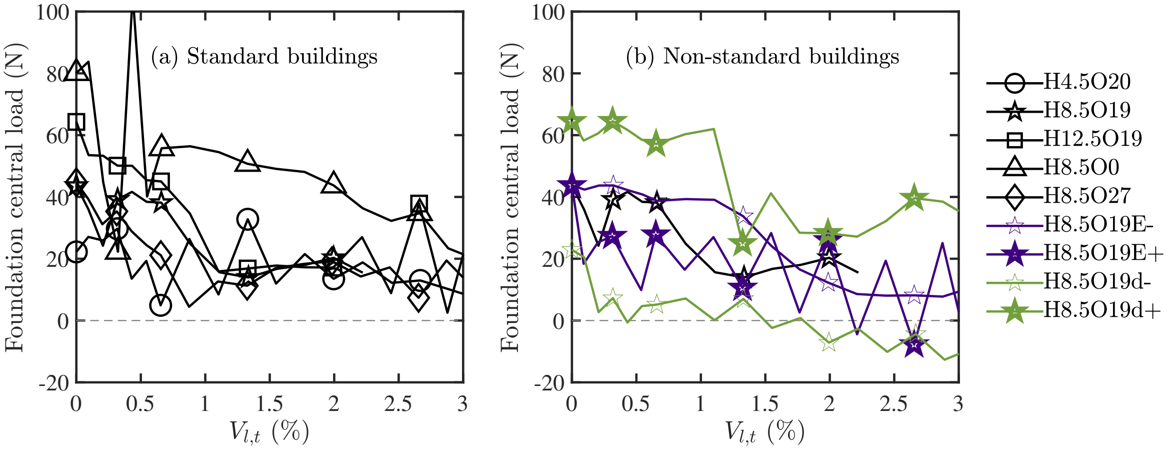

Fig. 6.14. Changes in vertical load (in model-scale) applied to the centre of the strip foundation (from actuator a4) with tunnel volume loss

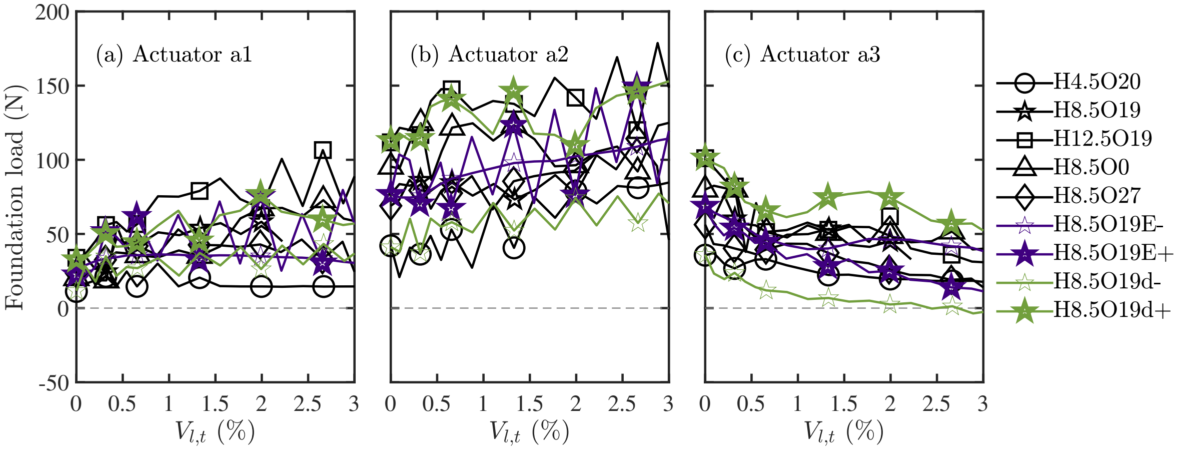

Fig. 6.15. Changes in vertical load (in model-scale) applied to the strip foundation (from actuators a1-3) with tunnel volume loss

applied to the strip foundation in the centrifuge model. The similar profiles of foundation and surface PIV data (excluding the offset between them due to gaps between the foundation model and the acrylic wall of the strongbox, explained at the beginning of this chapter) indicate that the wall loads are appropriately transferred to the underlying soil (through the model foundation). The impact of the walls on ground surface settlements is reflected in the changes at the base of the wall in Fig. 6.6, with relatively smaller differential settlements between the foundation centre and ends compared to the greenfield condition.

Compared to the greenfield surface in Figs. 6.12-6.13, masonry walls notably constrain soil horizontal movement beneath and around them, resulting in a sudden change in surface horizontal displacement near both ends of the foundation. In turn, both ends of the foundation tend to be embedded in the soil, restricting the foundation's movement. In previous centrifuge modelling studies, the horizontal displacement of buildings (base) on dense sand in symmetrical tunnelling cases was deemed negligible due to the large stiffness and weight of the buildings (Farrell et al., 2014; Yiu et al., 2017; Xu et al., 2020b). However, in this study, the strip foundation, considered separately from the walls, exhibits greater flexibility, making it more susceptible to the influence of surface movement. Under forced vertical distributed loads, the horizontal displacement of the foundation belonging to the most rigid and heaviest wall, H12.5O19, is the lowest, consistent with previous studies (Farrell, 2011), while the foundation's horizontal displacement profile for the most flexible and lightest wall H4.5O20 closely mirrors the surface horizontal displacement.

6.4 Soil movement

Soil movements are important in tunnel-soil-masonry wall interaction problems, which affect the movements and deformations of the walls. A better understanding of soil movement patterns would help predict the impact of current tunnelling activities on existing superstructures.

Figs. 6.16-6.19 present the soil vertical and horizontal displacements and engineering shear and volumetric strains, respectively. The soil movement around the tunnel is minimally affected by the masonry walls and exhibits similar displacement and strain profiles in all tests in Figs. 6.16-6.19. Compared to the greenfield case, the presence of walls increases the overall effective stress and stiffness of the soil beneath them. A significant phenomenon in soil movement is a decrease in differential horizontal and vertical displacement (Figs. 6.16-6.17) and the dilative response (Figs. 6.18-6.19) near the bottom of the walls, and a lower level of vertical displacement (Figs. 6.16-6.17) and the presence of shear strains (Figs. 6.18-6.19) near the tunnel crown.

Taking the standard two-storey masonry wall H8.5O19 as a reference, more flexible/lighter walls (H8.5O19E-, H8.5O19d-, H8.5O27, H4.5O20) tend to cause the range of soil vertical

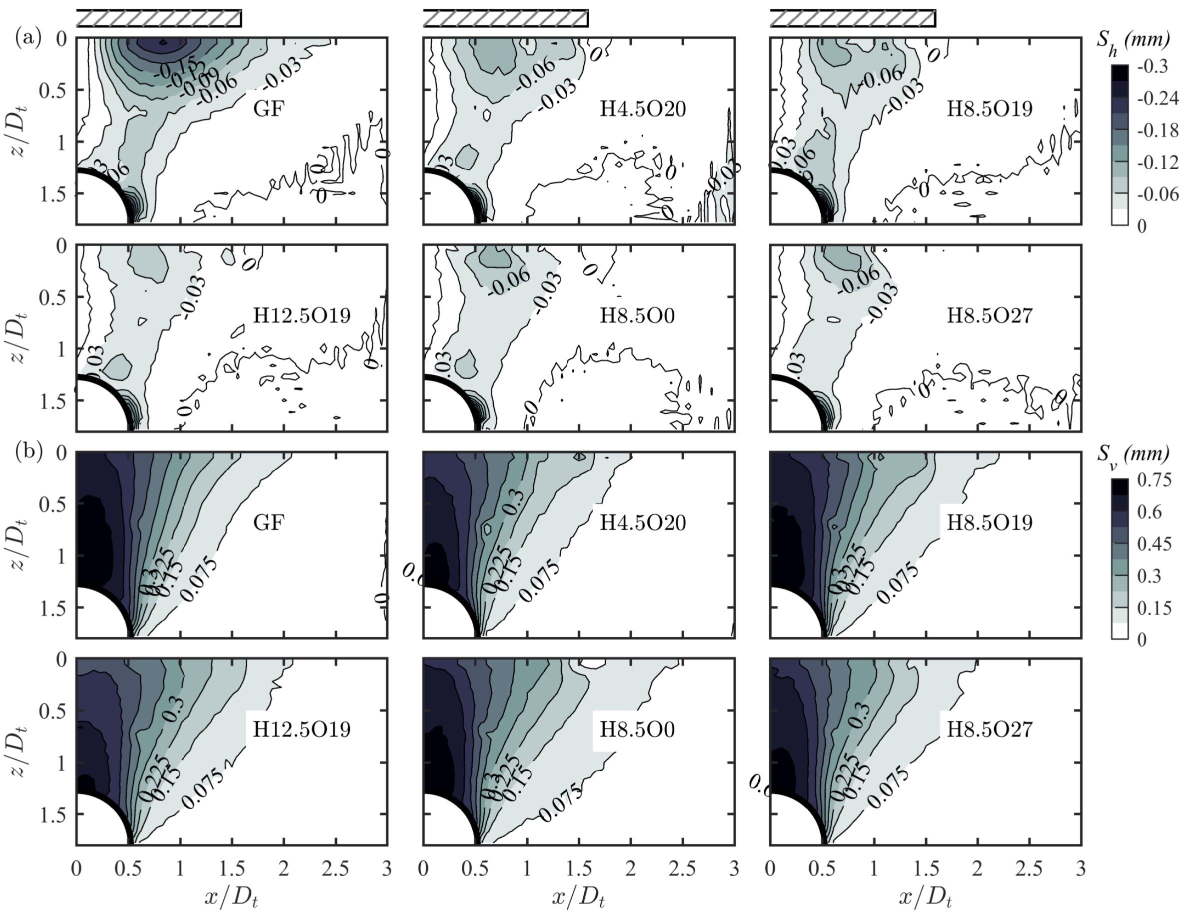

Fig. 6.16. Soil (a) horizontal and (b) vertical displacements at $V_{l,t} = 2.2\%$ (rectangular area on surface shows the position of the wall, where applicable; the global scene is symmetrical about the tunnel centreline)

displacement and shear below to contract towards the tunnel centreline, and the soil settlement near the tunnel crown to be prevented. The reduction of wall bending and shear stiffness and self-weight promotes the formation of a more complete and continuous soil shear zone near the wall base. On the contrary, the stiffer/heavier walls (H8.5O19E+, H8.5O19d+, H8.5O0, H12.5O19) expand the vertical displacement and shear range of the soil, moving away from the centerline of the tunnel. The increase in self-weight, bending stiffness, and shear stiffness promotes the formation of more dispersed soil shear zones near the wall base. These more rigid masonry walls are also capable of causing a slight reduction in soil settlement above the tunnel crown (especially H12.5O19), despite the expected increase in soil settlement due to higher wall self-weight (as observed in H8.5O19d+).

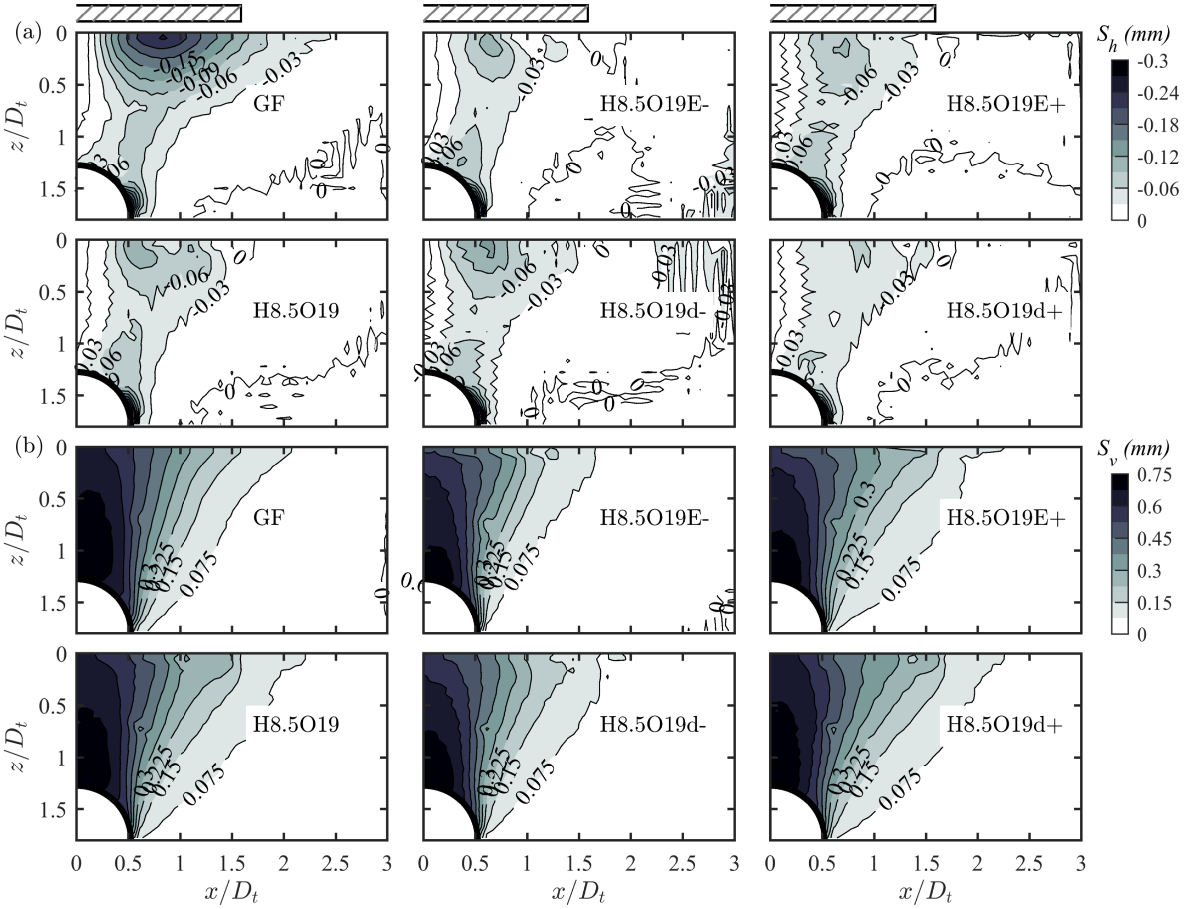

Fig. 6.17. Soil (a) horizontal and (b) vertical displacements at $V_{l,t} = 2.2\%$ (rectangular area on surface shows the position of the wall, where applicable; the global scene is symmetrical about the tunnel centreline)

Fig. 6.20 illustrates ground settlement profiles at different depths normalised by cover depth: $z/C = 0.1$, 0.25, and 0.5. The relationship between settlement troughs in different cases at the same depth aligns with the relationship between the wall base settlements shown in Fig. 6.6 (where the wall base/foundation settlement can be considered equivalent to surface settlement for these cases with no gaps, discussed in Section 6.3). This consistency reveals the connection between soil movement and the induced wall deformation. In addition, the wall also affects soil movement with this influence diminishing with soil depth. Taking greenfield and H8.5O19 as a reference, the subsurface settlement profiles gradually resemble the reference cases at greater depths, with smaller differences between the central (maximum) settlement. This is also supported by the trend of less difference in soil volume loss in difference cases at deeper positions

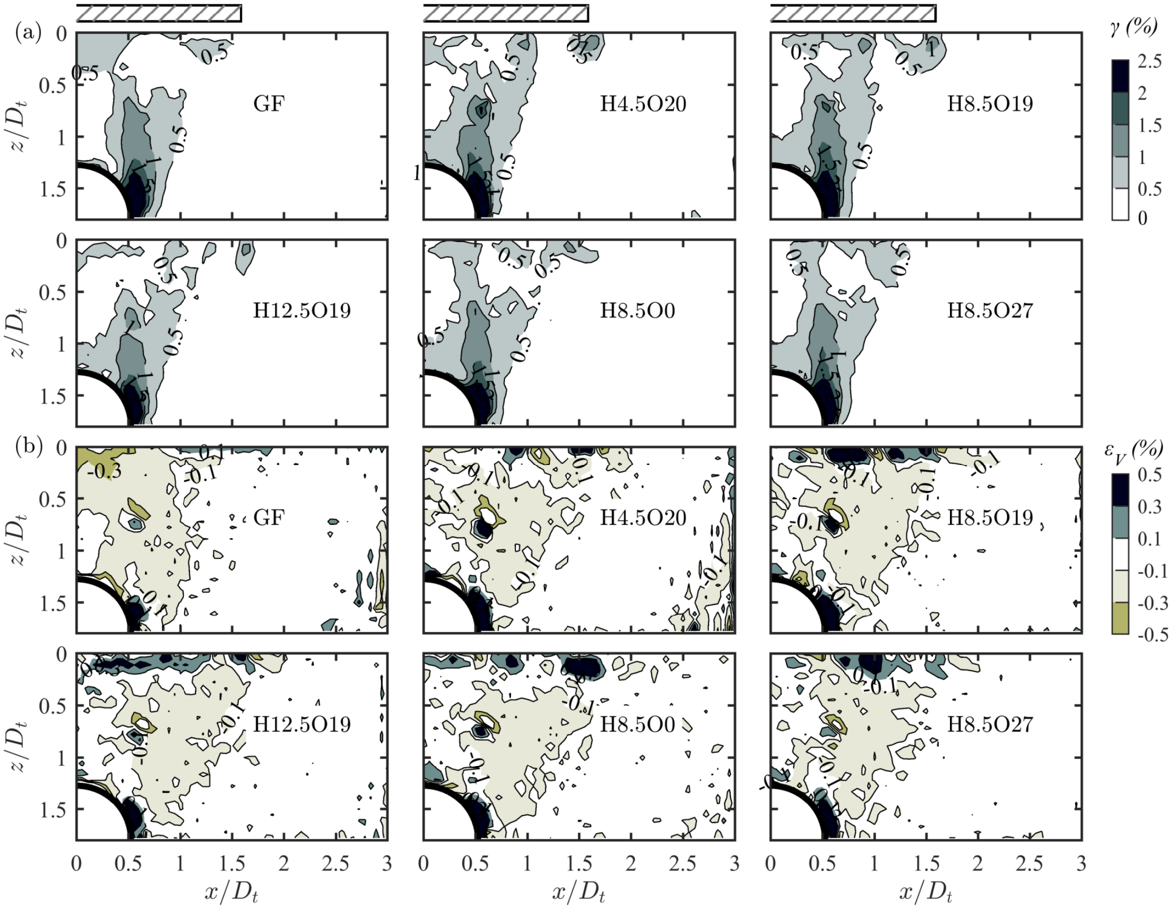

Fig. 6.18. Soil (a) engineering shear and (b) volumetric strains (+ is dilation) at $V_{l,t}$ = 2.2% (rectangular area on surface shows the position of the wall, where applicable; the global scene is symmetrical about the tunnel centreline)

in Fig. 6.22.

Tunnel excavation in drained soil would result in an overall contraction or dilatant response of the soil (Marshall, 2009; Franza et al., 2019). Fig. 6.21 presents the relationship between surface soil volume loss $V_{l,s}$ and tunnel volume loss $V_{l,t}$, where the gray dashed line represents $V_{l,s} = V_{l,t}$. The surface volume loss slightly exceeds the tunnel volume loss before $V_{l,t}$ = 1.5%, representing soil contraction, and then it is observed that the surface volume loss caused by overall soil dilation gradually decreases compared to the tunnel volume loss (except for H8.5O19E-). In test H8.5O19E-, the centrifuge was stopped after a full stabilisation process (i.e. 1-10-70-10-70-10-70-1 g) due to experimental reasons, and then the identical stabilisation process was repeated before testing resumed, which means the soil was fully unloaded to 1 g

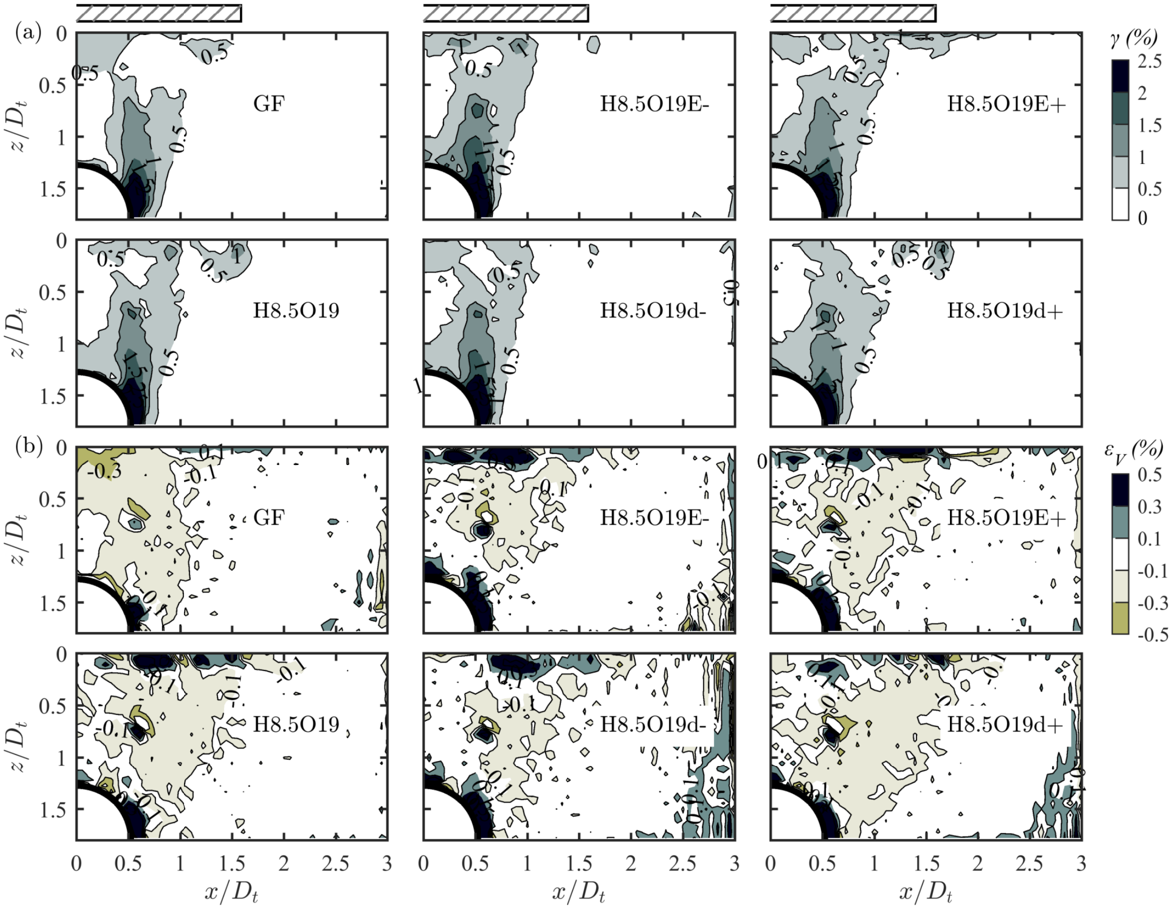

Fig. 6.19. Soil (a) engineering shear and (b) volumetric strains (+ is dilation) at $V_{l,t}$ = 2.2% (rectangular area on surface shows the position of the wall, where applicable; the global scene is symmetrical about the tunnel centreline)

and experienced twice the number of stabilisation cycles as other tests. The results suggest that this process had an effect on the response of the soil; the more dilatant response suggests that the soil in this test was more dense before tunnel volume loss than other tests. However, this issue is acceptable because the soil movement in test H8.5O19E- is comparable to other tests (Figs. 6.16-6.20).

The subsurface soil volume loss in Fig. 6.22 provides a detailed explanation of the degree of soil contraction or dilation at varying depths above the tunnel crown. In the range of z/C = 0.2-1, soil volume loss decreases with increasing depth, indicating that the soil is contracting. Near the surface (z/C = 0-0.2), the soil beneath the walls experiences a small increase (soil dilation) or almost constant soil volume loss; the effect of the wall acts to diminish or reverse the tendency

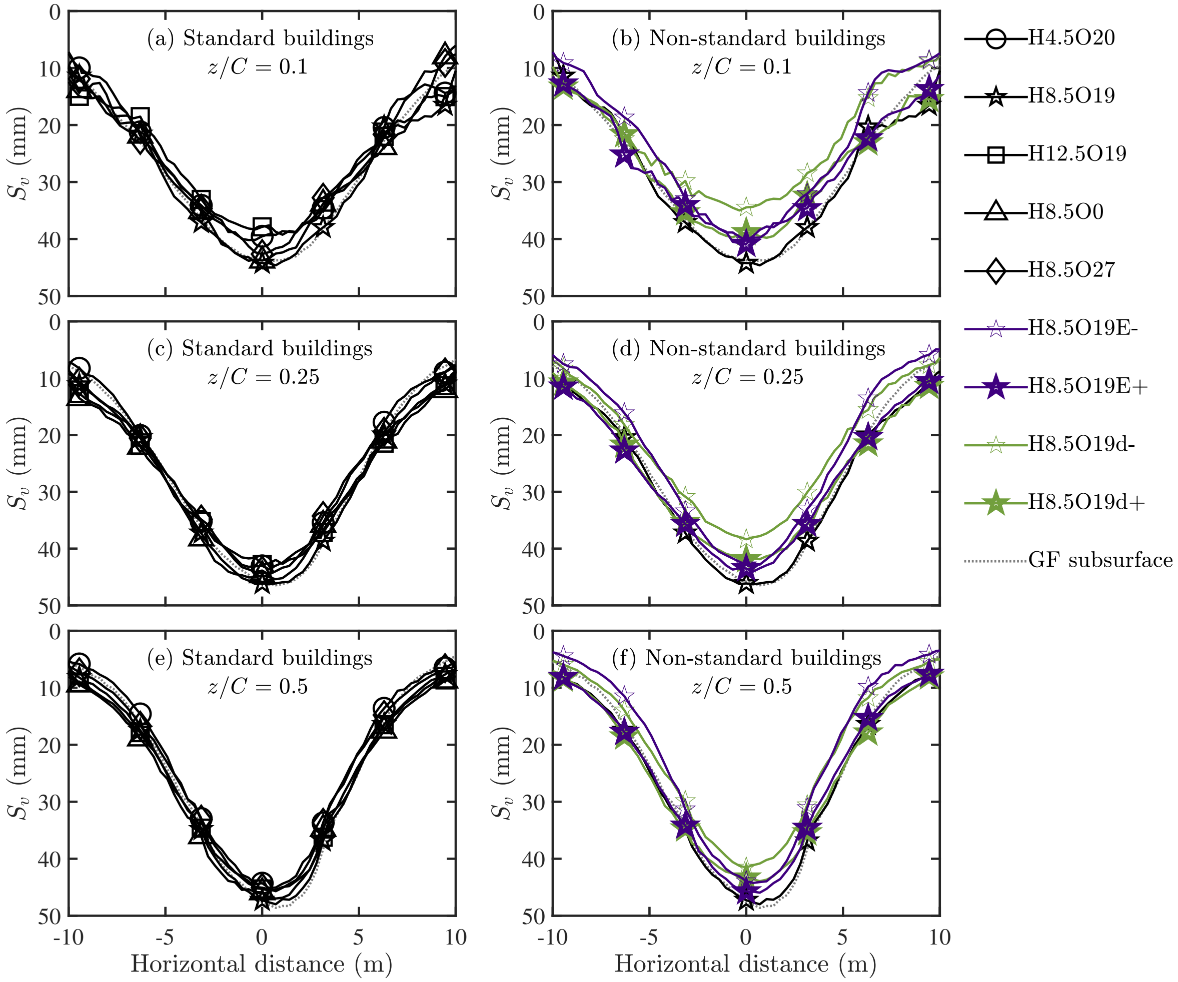

Fig. 6.20. Subsurface settlement troughs at depth of $z/C = 0.1$, 0.25, and 0.5 at $V_{l,t} = 2.2\%$

for soil contraction (which would otherwise occur in this range of soil depth, as demonstrated by the greenfield data). Near the tunnel, soil dilation causes $V_{l,s} \approx 1.5\%$ at $z/C \approx 1$. The local soil contraction or dilation phenomena are consistent with Figs. 6.18(b) and 6.19(b) where the regions near the strip foundation and around the tunnel exhibit volumetric strains indicative of dilation while other areas situated between the tunnel and the surface exhibit volumetric strains associated with contraction. Stiffer or heavier walls contribute minimal differences to the effects on the soil, while more flexible or lighter walls tend to cause relatively smaller surface and subsurface soil volume loss (such as H4.5O20, H8.5O35, H8.5O19E-, and H8.5O19d-).

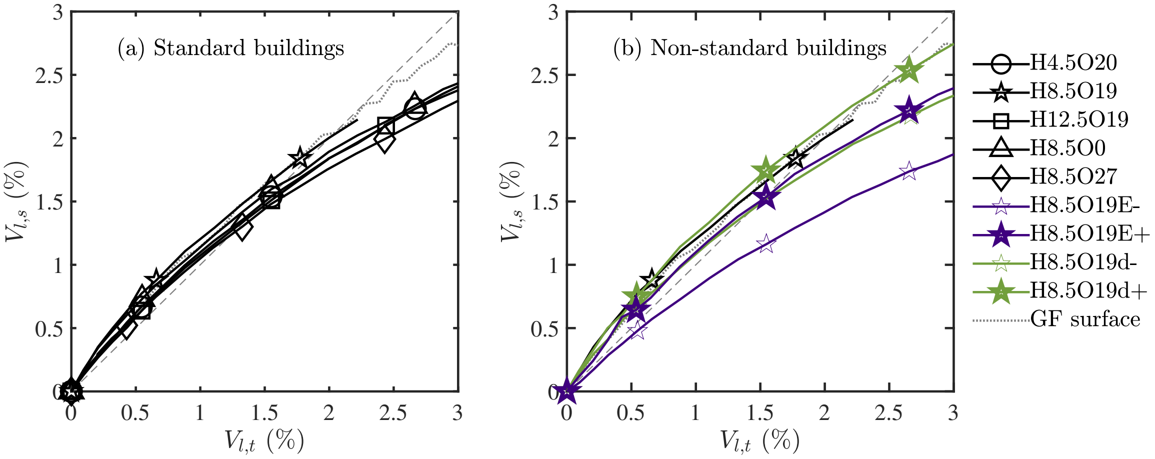

Fig. 6.21. Ground surface volume loss against tunnel volume loss

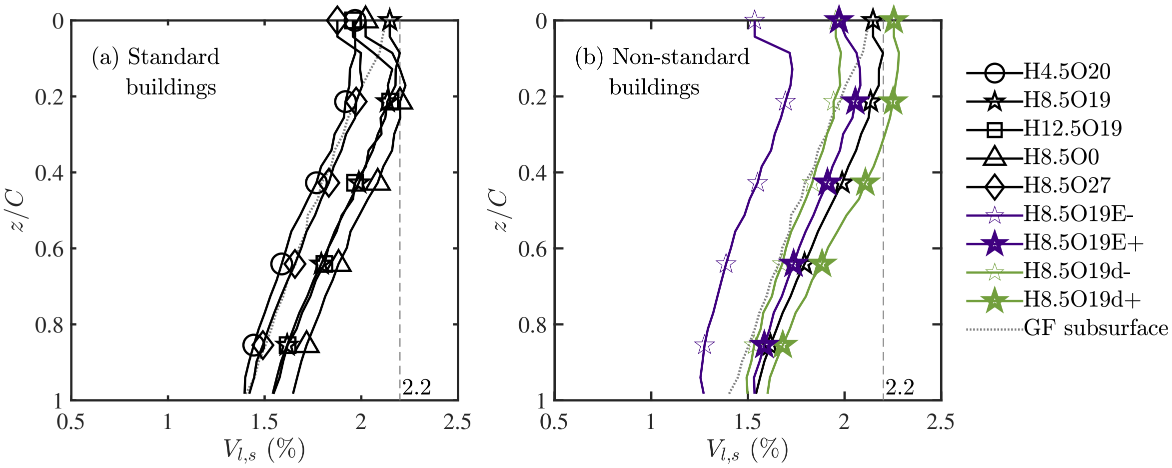

Fig. 6.22. Changes in soil volume loss with normalised depth at $V_{l,t} = 2.2\%$

6.5 Summary

The damage mechanisms of masonry walls affected by tunnel excavation are complex and remain an area of uncertainty within building damage assessment procedures. This chapter presents the results from a centrifuge modelling study to investigate the interaction mechanisms between tunnels and existing masonry walls on strip foundations. A new coupled centrifuge-numerical modelling (CCNM) method was adopted, where foundation settlements and load information are shared between a physical model domain in the centrifuge comprising the tunnel, soil, and strip foundation, and a numerical model domain in Abaqus comprising of a masonry wall. The physical and numerical domains have a shared boundary at the interface between the wall and the foundation. The role of wall stiffness and self-weight are distinguished by varying Young's modulus and density of a reference two-storey masonry wall with openings. Wall distortion and damage parameters are used to evaluate the responses of standard masonry walls (with different heights/storeys and door/window openings) to tunnel excavation. High bending stiffness and low self-weight cause a dispersed distribution and horizontal propagation (along the wall length direction) of tension damage areas within the walls; low bending stiffness and high self-weight result in a concentrated distribution and vertical propagation (along the wall height direction). Some counter-intuitive results are presented, such as the possibility of slightly greater wall differential settlement with stiffer or heavier structures. This chapter also explores the influence of the existing walls on soil movements during tunnelling, considering key factors such as wall self-weight and stiffness.

Chapter 7

Conclusions and recommendations for future work

The escalating demand for underground space by humans necessitates the construction of new tunnels in close proximity to existing structures (including underground foundations and surface buildings), thus it is vital to gain a deep understanding of how tunnelling impacts these existing structures. This thesis provided insights into the mechanisms of tunnel-soil-pile interactions (TSPI) and tunnel-soil-masonry building interactions (TSBI) with shallow strip foundations through geotechnical centrifuge modelling tests in dense sand. Particularly noteworthy is the development of an advanced coupled centrifuge-numerical modelling (CCNM) approach with a continuous interface between physical and numerical domains to study, but not limited to, TSBI problems. This chapter reviews the primary conclusions of this thesis (from Chapters 4, 5, and 6) and proposes potential avenues for future research in related areas.

7.1 Conclusions

7.1.1 Load transfer mechanisms for capped piles

Chapter 4 investigated the effect of a model cap on the response to loading and tunnelling of single pile foundations using data from sixteen 60-g geotechnical centrifuge tests in dense sand. All piles were tested during tunnelling at a constant service load that was relatively close to the load capacity of the corresponding uncapped pile, giving a nominal working load level WL between 0.6 and 1.0 in all cases. In addition, the influence of the base load transfer mechanism was studied to distinguish 'reference' and 'friction' piles, with the latter having a compressible foam pile tip. The following main conclusions can be drawn.

- Spin-up mobilised relatively large pile base loads between 30%-50% of the external load for all piles (due to the mass of instrumentation above the ground level and negative shaft friction caused by the compression of the surrounding soil). The rigid tunnel reduced the load capacity of piles located directly above the tunnel, likely due to a reduction in shaft resistance caused by a stress arching mechanism above the model tunnel. Consequently, pile capacity was assessed from tests where the pile was located directly above the model tunnel. It was demonstrated that the presence of the rigid tunnel did not affect the trends of load transfer mechanisms nor significantly affect their magnitudes; thus, tunnelling tests were deemed to be acceptable within the context of the study aims.

- Results of uncapped non-displacement piles confirmed that piles would settle more than greenfield movements (both at the surface and pile tip level) in dense sand, which was consistent with previous studies in loose sand. Also, the tendency of the service load (increase of WL) to increase tunnelling-induced pile settlements was confirmed. In this study, the distributed measurements of axial force within the piles gave novel insights into the link between geotechnical failure and the equilibrium state of piles during tunnelling. Namely, (i) *brittle failure* with extreme pile settlements (5-10 times greater than greenfield values) was observed for uncapped non-displacement piles with $WL \approx 1$ at small volume losses; because shaft capacity had already been fully mobilised during pre-tunnelling loading, large pile settlements were needed to mobilise additional base capacity to compensate for the reduction of shaft load caused by tunnelling-induced stress relief (reducing mean effective stresses at the shaft). On the other hand, (ii) *softening failure* associated with a gradual increase in settlement rate with volume loss (pile settlements 2-4 times greater than greenfield values) was observed for uncapped non-displacement piles with $WL \leq 0.7$ at large volume losses; because the shaft capacity had not been fully mobilised during pre-tunnelling loading, at low volume losses, the reduction in base load was transferred to the shaft without incurring significant pile displacements; when at higher volume losses, the shaft capacity was fully mobilised and the rate of pile settlement with volume loss increased to mobilise a constant pile base load.

- Pile caps reduced tunnelling-induced settlements of non-displacement piles (pile head-to-greenfield settlement ratio typically lower than ≈ 2) and prevented their geotechnical failure (compared against equivalent uncapped piles). The load transfer mechanism of capped piles during tunnelling depends on the service load. (i) For lower WL, the cap does very little at lower values of $V_{l,t}$ when the reduction of base load can be accommodated by the shaft, whereas cap load is gradually mobilised at higher volume losses ($V_{l,t} = 2\%$), preventing the *softening failure* that uncapped piles may be susceptible to. (ii) In contrast, for piles with WL close to 1, where shaft resistance is fully mobilised prior to tunnel volume loss, the cap load increases from very low values of volume loss (taking load lost at the pile base), preventing the risk of *brittle failure* by taking a significant proportion of the external load.
- Post-tunnelling loading tests indicated no impact on load capacity for friction piles and all capped piles; a minor reduction of ≈15% was observed for the reference pile. Regarding tangent stiffness during pile loading, (i) tunnelling 'reset' the loading stiffness profiles (to a lesser degree for the reference and friction piles), while (ii) the pre- and post-tunnelling stiffness tended to converge at high values of pile settlement of about 10% of pile diameter, except for the notable rapid drop in post-tunnelling loading stiffness for the reference pile characterised by the reduction in load capacity. Therefore, tunnelling-stress relief

in drained conditions may detrimentally affect non-displacement piles that rely on base pressure, whereas the effect on frictional piles and capped piles is likely to be secondary.

- Ratios between pile head and greenfield surface settlements are summarised as a design guideline, including the influence of load level, pile type, and cap on the possible geotechnical failure. In the absence of more rigorous modelling, a design value of $R \approx 2$ is suggested for both capped and uncapped non-displacement piles when $WL \leq 0.7$ (with load capacity estimated from uncapped piles). Note that centrifuge test data from the literature for uncapped piles has indicated relatively low values of $R \approx 1.2$ for a WL of 0.4 (instead of 0.7); therefore, WL should be carefully considered when modelling these interaction scenarios.

The outcomes presented in this thesis relate to a conservative tunnel-pile interaction condition where piles are relatively highly loaded and have proportionally higher base load mobilised than would typically be expected for capped pile foundations. As such, from a design perspective, the effect of the key interaction mechanisms demonstrated in this thesis should be judged more qualitatively with respect to the specific foundation and loading conditions under consideration. For design scenarios, in which mobilised base load is relatively low, engineers may consider the friction pile test results presented here as being more representative.

7.1.2 Verification and application of CCNM testing approach in tunnelling under masonry walls

Chapter 5 introduced a newly developed coupled centrifuge-numerical modelling (CCNM) technique for studying tunnel-masonry wall interaction problems related to non-linear building materials and shallow strip foundations under plain strain conditions. In the CCNM approach, the tunnel, soil, and foundation are included in the centrifuge, the masonry walls are created in Abaqus, with the vertical loads and settlements exchanged between the strip foundation and the wall base (representing a continuous interface between the physical and numerical model domains). Results from eight geotechnical centrifuge tests at 70 g were presented to verify the effectiveness of the CCNM approach and its application in scenarios with different relative wall-to-tunnel positions. The following main conclusions can be drawn.

- The CCNM approach includes flexible fitting curves for wall settlement to adapt to scenarios of different wall-to-tunnel eccentricities e/L: the modified Gaussian curve, the exponential Gaussian curve, and the second-order Fourier curve apply to $e/L = 0$ (i.e. the wall centre is directly above the tunnel), $0 < e/L < 1/2$, and $e/L = 1/2$ (i.e. the wall side is directly above the tunnel) scenarios, respectively. The wall settlement (fitted from seven LVDT displacements), the strip foundation settlement (measured from both LVDT and PIV), and the surface settlement (measured from PIV) profiles exhibited good consistencies in CCNM tests. Satisfactory results were obtained from the CCNM testing method.
- Compared with the conventional constant dead load method (where constant loads representing initial load distributions within the masonry walls before tunnelling were applied on the strip foundation during the tunnelling process), the CCNM testing on tunnelling directly under two-storey masonry walls (with and without openings, $e/L = 0$) achieved load redistribution within the masonry walls during tunnelling and captured the resulting wall settlement profiles and soil movements. The CCNM test results exhibited wall loads being transferred from the wall centre to both ends, lower differential settlement at the wall base, lower characteristic tensile strain ε_{99}^{t} and similar/less areas of moderate damage and above inside the wall, and more discontinuous shear regions near the surface. These findings underscore the significance of incorporating load redistribution within masonry walls in the CCNM approach for precise evaluations of wall distortions and damage induced by tunnelling.
- It was demonstrated that the concentrated loads applied to the strip foundation by the seven load actuators were adequately transferred to the underlying soil, as expected, due to the foundation stiffness. During tunnel volume loss, the wall loads were transferred towards the ends (if the ends were located in sagging regions) and the hogging regions (if the ends were in hogging regions) in eccentric scenarios. With the wall-to-tunnel eccentricity e/L increasing from 0 to 1/2, the inflection point of the wall base settlement

profiles moved towards the tunnel centreline (with inflection points for $e/L = 1/2$ and greenfield being similar), the location of tensile damage shifted from the lower part of the wall to the upper part (near the middle of sagging/hogging regions), and the predominant settlement pattern transitioned from sagging to hogging. The wall relative settlements and tensile strain distributions indicated a deformation/tensile damage process characterized by an initial decrease followed by an increase (with minimal deformation/tensile damage occurring when the wall centre coincided with the inflection point for $e/L = 1/3$).

- The bay deformation parameters (such as top and base horizontal strains, relative settlement, slope, tilt, and angular distortion) also supported the wall deformation/tensile damage process with e/L. The vertical displacement of bays can be divided into tilt-, bending-, and shear displacement, where tilt displacement was predominant; bays experienced more bending distortions when located near the tunnel centreline and inflection points, while other bays underwent more shear distortions. The bays near the tunnel centreline exhibited more bending behaviour (characterised by $|F_{bay}|$, proportional to the bay shear-to-bending settlement ratio, of < 0.04) with equivalent plastic strain areas (PEEQ) reducing with e/L; in contrast, those at inflection points or further away showed mixed bending and shear response ($0.04 < |F_{bay}| < 1$) with PEEQ for bays further away tending to increase with e/L. The minimal difference between bays in these parameters and the lowest equivalent plastic strain areas for $e/L = 1/3$ again supported the lowest damage of risk in this case.

7.1.3 Tunnel-soil-masonry wall interaction mechanisms

Chapter 6 presented results from ten 70-g geotechnical centrifuge tests using the CCNM technique to study tunnel-soil-masonry wall interaction mechanisms. The effects of mechanical properties (including bending stiffness, shear stiffness, self-weight) and structural elements (such as height, door and window openings) on wall deformations and damage during tunnelling directly beneath masonry walls were elucidated based on a reference two-storey masonry wall with 19% openings H8.5O19. The varying bending stiffness and self-weight of the reference wall H8.5O19, i.e. representing non-standard masonry walls, replicated the values of corresponding standard one- and three-storey masonry walls. The following main conclusions can be drawn.

- For non-standard masonry walls, an increase in bending stiffness, corresponding to masonry walls with one to three storeys, led to a decrease in characteristic tensile strain ε_{99}^{t} and moderate damage areas and above (except the same ratios of damaged areas in the cases with the bending stiffness of two- and three-storey walls). Changes in wall self-weight, compared with the standard reference wall H8.5O19, resulted in an equal degree of increase in characteristic tensile strain and damage areas. Through different mechanisms, low bending stiffness and high self-weight tended to centralise damage around the door (i.e. at the centre and lower part of the walls) and established vertical connections (along wall height direction) between local damage areas; conversely, high bending stiffness and low self-weight and shear stiffness contribute to a dispersed distribution of damage, the formation of horizontal connections (along wall length direction), and higher maximum angular distortions (for the bays located above the inflection points on surface settlement curves).

- For standard one- to three-storey masonry walls, damage to the same location (e.g. the ground floor) increased with wall height due to elevated wall self-weight loads. The one-storey wall, characterised by the largest length-to-height ratio and the lowest bending/shear stiffness and self-weight, exhibited the lowest proportion of tensile damage areas and the highest maximum bay angular distortion, with damage concentrated below the door. The two- to three-storey walls (with identical shear stiffness and opening ratio) demonstrated a consistent proportion of damage areas and maximum angular distortion, indicating a minimal impact of increased bending stiffness and self-weight on overall wall damage. The characteristic tensile strain and damage area ratio of the three-storey wall can be reproduced by the non-standard two-storey wall with the same bending stiffness. The wall without openings, compared to those with openings, showed a slightly lower characteristic tensile strain, however a significantly larger damage area (proportion) due to greater local constraints inside the structure. The two-storey wall with larger openings

(27%; i.e. with less shear stiffness and more flexibility) lowered the characteristic tensile strain while not altering the proportion of damaged area.

- More flexible or lighter walls, as anticipated, produced greater differential settlements, with sagging deflection ratios closely resembling greenfield surface conditions, while more rigid or heavier walls may also result in slightly larger differential settlements, with a reduction observed only in the case of the standard three-storey wall. Greater wall bending stiffness (relative to soil secant stiffness) corresponds to reduced deformation in local areas of the structure, as indicated by lower levels of modification factors for sagging and hogging deflection ratios. The maximum settlements of walls occurring directly above the tunnel exhibit no significant difference, posing a challenge in establishing a clear relationship between the maximum settlement values of different walls in complex tunnel-building interaction scenarios, however the impact of this phenomenon on building damage assessment is minimal. The sagging relative building/soil stiffness was higher than previous studies by approximately 1.5-2 orders of magnitude due to the higher stiffness and shorter spans of the walls in this work.

- It was assumed no gap existed between the strip foundation and the surface since the actuator loads were insufficient to lift the foundation. Compared with greenfield conditions, the presence of masonry walls increased the overall effective stress and stiffness of the underlying soil, resulting in a decrease in differential horizontal and vertical displacement of soil near the wall base, where more obvious soil dilation behaviours appeared. Simultaneously, the vertical displacement of soil around the tunnel crown decreased, accompanied by observable shear strains. Based on the reference wall H8.5O19, more flexible (stiffer) or lighter (heavier) walls caused the settlement and shear range of the underlying soil to shrink towards (expand away from) the centerline of the tunnel, with more continuous (dispersed) shear zones near the wall base. The impact of walls on soil settlement troughs diminished with depth. Walls induced macroscopic soil dilation phenomenon (i.e. surface soil volume loss less than tunnel volume loss; at $V_{l,t} \approx 1.5\%$) earlier than greenfield conditions (at $V_{l,t} \approx 2\%$) by affecting the surrounding soil, while subsurface soil volume loss tended to exceed that in greenfield conditions due to the wall gravitational loads. Soil in the depth range $z/C = 0.2$-1 above the tunnel was contracted on a macro scale.

7.2 Recommendations for future work

This thesis investigated the three-dimensional TSPI mechanisms and TSBI mechanisms under plane strain conditions through centrifuge modelling tests in dense sand. The TSPI scenarios involved single piles with different elements (i.e. pile cap and soft base) located directly above the tunnel. The TSBI scenarios involved CDP masonry walls with diverse characteristics (including wall height, openings, Young's modulus, and density) above the tunnel. These findings provide valuable guidance for engineers and researchers in field predictions and numerical and theoretical analyses. Based on the work in this thesis, further investigations into tunnelling scenarios could explore the following areas:

(1) **Pile foundations**

- This thesis delved into the load transfer mechanisms of capped piles. In future research, diversifying the size and shape of piles and caps could enhance the understanding of mechanical behaviours of engineering structures such as capped piles and pile-raft composite foundations. The performance of the soft bases of friction piles fell short of ideal, failing to achieve minimal pile base resistance (i.e. approximating zero). Exploring alternative methods, such as employing radially stiffer soft bases (diminishing the squeezing of the soft base by surrounding sand; but flexible axially) or leaving pile bases unsealed (directly reducing base load), could offer new insights into replicating the mechanical characteristics of friction piles.
- This thesis investigated the pile failure mechanisms under high working load levels ($WL \geq 0.6$). In practical engineering, the pile working load level requirements tend to be more conservative (for example, $WL \leq 0.4$), underscoring the necessity of more studies to comprehend pile responses under lower working load levels that align with practical demands.

Also, capped piles exhibited more complex load transfer mechanisms, warranting a scientific redefinition of the WL.

- This thesis studied pile loading (away from the tunnel model or without a tunnel) and the impacts of tunnel excavation on piles (with piles located directly above the tunnel), where the piles are not subjected to horizontal disturbances. In reality, piles are often positioned in proximity to tunnels, so it is possible to supplement research on the horizontal response of adjacent piles during tunnelling.
- This thesis studied single-pile responses, whereas multiple piles are usually fixed beneath buildings in realistic scenarios. Hence, the newly developed CCNM approach could be adjusted appropriately for application in studying tunnelling effects on piled buildings.

(2) **Masonry buildings with shallow strip foundations**

- The newly developed CCNM approach has been applied to the TSBI problems. In the CCNM technique, the strip foundations and masonry walls existed in centrifuge and numerical domains, respectively, which would cause a certain degree of coupling errors between the two separate domains. In the future, it is necessary to explore new methods (such as novel theories, machine learning, and artificial intelligence) to more accurately achieve coupling between the two model domains.
- This thesis exclusively employed a CDP constitutive model with a hardening failure characteristic for masonry walls, and future work could apply more constitutive models according to actual needs. Different structural characteristics and building positions relative to the tunnel could also be considered.
- This study used 2D masonry wall models in Abaqus, and the CCNM approach allows for the use of 3D building models under experimental plain strain conditions, which provides more possibilities for simulating TSBI scenarios.
- The strip foundation model in this thesis was situated on the ground surface. Future research could explore embedding the foundation into the soil at different depths. Differ-

ent shallow foundations (with various sizes, shapes, and smooth/rough contact surfaces) could be considered as well.

(3) **Tunnelling and soil conditions**

- This thesis investigated the influence of tunnel excavation under plane strain conditions. However, since tunnel excavation is inherently a 3D problem, future work could focus on establishing 3D tunnelling scenario testing.
- This thesis only used dense dry fine silica sand, and various soil types (such as clay, sand, gravel, and their mixture) along with different densities could be considered according to specific requirements, as well as the location of tunnels, buildings, and foundations.

References

Al Heib, M., Emeriault, F., and Nghiem, H.-L. (2020). On the use of 1g physical models for ground movements and soil-structure interaction problems. *Journal of Rock Mechanics and Geotechnical Engineering*, 12(1):197–211.

Amorosi, A., Boldini, D., De Felice, G., Malena, M., and Sebastianelli, M. (2014). Tunnelling-induced deformation and damage on historical masonry structures. *Géotechnique*, 64(2):118–130.

Attewell, P. B. and Yeates, J. (1984). Tunnelling in soil. *Ground movements and their effects on structures*, pages 132–215.

Attewell, P. B., Yeates, J., and Selby, A. R. (1986). *Soil movements induced by tunnelling and their effects on pipelines and structures*.

Blakeborough, A., Williams, M. S., Darby, A. P., and Williams, D. M. (2001). The development of real–time substructure testing. *Philosophical Transactions of the Royal Society of London. Series A: Mathematical, Physical and Engineering Sciences*, 359(1786):1869–1891.

Bolton, M. D., Gui, M.-W., Garnier, J., Corte, J. F., Bagge, G., Laue, J., and Renzi, R. (1999). Centrifuge cone penetration tests in sand. *Géotechnique*, 49(4):543–552.

Boone, S. J. (1996). Ground-movement-related building damage. *Journal of geotechnical engineering*, 122(11):886–896.

Boonsiri, I. and Takemura, J. (2015). Observation of ground movement with existing pile groups due to tunneling in sand using centrifuge modelling. *Geotechnical and Geological Engineering*, 33(3):621–640.

Boscardin, M. D. and Cording, E. J. (1989). Building response to excavation-induced settlement. *Journal of Geotechnical Engineering*, 115(1):1–21.

Burd, H., Houlsby, G., Augarde, C., and Liu, G. (2000). Modelling tunnelling-induced settlement of masonry buildings. *Proceedings of the institution of civil engineers-geotechnical engineering*, 143(1):17–29.

Burd, H., Yiu, W., Acikgoz, S., and Martin, C. (2022). Soil-foundation interaction model for the assessment of tunnelling-induced damage to masonry buildings. *Tunnelling and Underground Space Technology*, 119:104208.

Burland, J. B., Broms, B. B., and De Mello, V. F. B. (1977). Behaviour of foundations and structures on soft ground. In *Proceedings of the 9th International Conference on Soil Mechanics and Foundations Engineering*, volume 2, pages 495–546.

Burland, J. B. and Wroth, C. (1974). Settlement of buildings and associated damage. In *Proceedings of the conference on settlement of structures*, pages 611–654. Pentech Press Cambridge, UK.

Camós, C., Molins, C., and Arnau, O. (2014). Case study of damage on masonry buildings produced by tunneling induced settlements. *International Journal of Architectural Heritage*, 8(4):602–625.

Celestino, T. B., Gomes, R. A., and Bortolucci, A. A. (2000). Errors in ground distortions due to settlement trough adjustment. *Tunnelling and underground space technology*, 15(1):97–100.

Chen, L., Poulos, H., and Loganathan, N. (1999). Pile responses caused by tunneling. *Journal of Geotechnical and Geoenvironmental Engineering*, 125(3):207–215.

Cheng, C., Dasari, G., Chow, Y., and Leung, C. (2007). Finite element analysis of tunnel–soil–pile interaction using displacement controlled model. *Tunnelling and Underground Space Technology*, 22(4):450–466.

Clough, G. W. and Schmidt, B. (1981). Design and performance of excavations and tunnels in soft clay.

Cook, D. (1994). Studies of settlement and crack damage in old and new facades. In *Proc., 3rd Int. Masonry Conference., London, England*, volume 6, pages 203–211.

Cording, E. (1991). Control of ground movements around tunnels in soil. In *Ninth Pan American Conference, Vina del Mar, Chile. Sociedad Chilena de Geotechina*, volume 4, pages 2195–2244.

DeJong, M. J., Giardina, G., Chalmers, B., Lazarus, D., Ashworth, D., and Mair, R. J. (2019). Impact of the crossrail tunnelling project on masonry buildings with shallow foundations. *Proceedings of the Institution of Civil Engineers-Geotechnical Engineering*, 172(5):402–416.

Dias, T. G. S. and Bezuijen, A. (2015). Data analysis of pile tunnel interaction. *Journal of Geotechnical and Geoenvironmental Engineering*, 141(12):04015051.

Elkayam, I. and Klar, A. (2019). Nonlinear elastoplastic formulation for tunneling effects on superstructures. *Canadian Geotechnical Journal*, 56(7):956–969.

Ellis, E., Cox, C., Yu, H., Ainsworth, A., and Baker, N. (2006). A new geotechnical centrifuge at the university of nottingham, uk. In *6th International Conference of Physical Modelling in Geotechnics: ICPMG*, volume 6, pages 129–33.

Farrell, R., Mair, R., Sciotti, A., and Pigorini, A. (2014). Building response to tunnelling. *Soils and Foundations*, 54(3):269–279.

Farrell, R. P. (2011). *Tunnelling in sands and the response of buildings*. PhD thesis, University of Cambridge.

Finno, R. J., Voss Jr, F. T., Rossow, E., and Blackburn, J. T. (2005). Evaluating damage potential in buildings affected by excavations. *Journal of geotechnical and geoenvironmental engineering*, 131(10):1199–1210.

Franza, A. (2017). *Tunnelling and its effects on piles and piled structures*. PhD thesis, University of Nottingham.

Franza, A., Acikgoz, S., and DeJong, M. J. (2020a). Timoshenko beam models for the coupled analysis of building response to tunnelling. *Tunnelling and Underground Space Technology*, 96:103160.

Franza, A., Idinyang, S., Heron, C., Marshall, A., and Abdelatif, A. (2016). Development of a coupled centrifuge-numerical model to study soil-structure interaction problems. In *Proc., 3rd European Conf. on Physical Modelling in Geotechnics (Eurofuge 2016)*, pages 135–140.

Franza, A. and Marshall, A. M. (2018). Centrifuge modeling study of the response of piled structures to tunneling. *Journal of Geotechnical and Geoenvironmental Engineering*, 144(2):04017109.

Franza, A. and Marshall, A. M. (2019a). Centrifuge and real-time hybrid testing of tunneling beneath piles and piled buildings. *Journal of Geotechnical and Geoenvironmental Engineering*, 145(3):04018110.

Franza, A. and Marshall, A. M. (2019b). Empirical and semi-analytical methods for evaluating tunnelling-induced ground movements in sands. *Tunnelling and Underground Space Technology*, 88:47–62.

Franza, A., Marshall, A. M., Haji, T., Abdelatif, A. O., Carbonari, S., and Morici, M. (2017). A simplified elastic analysis of tunnel-piled structure interaction. *Tunnelling and Underground Space Technology*, 61:104–121.

Franza, A., Marshall, A. M., and Zhou, B. (2019). Greenfield tunnelling in sands: the effects of soil density and relative depth. *Géotechnique*, 69(4):297–307.

Franza, A., Miraei, S., Boldini, D., and Losacco, N. (2022). An equivalent beam approach for assessing tunnelling-induced distortions of frames with infills. *Tunnelling and Underground Space Technology*, 129(December 2020):104686.

Franza, A., Ritter, S., and Dejong, M. J. (2020b). Continuum solutions for tunnel–building interaction and a modified framework for deformation prediction. *Géotechnique*, 70(2):108–122.

Franzius, J. N. (2003). *Behaviour of buildings due to tunnel induced subsidence*. PhD thesis, Imperial College London.

Franzius, J. N., Potts, D. M., and Burland, J. B. (2006). The response of surface structures to tunnel construction. *Proceedings of the Institution of Civil Engineers-Geotechnical Engineering*, 159(1):3–17.

Fraser, R. and Wardle, L. (1976). Numerical analysis of rectangular rafts on layered foundations. *Geotechnique*, 26(4):613–630.

Furtmüller, T. and Adam, C. (2011). Numerical modeling of the in-plane behavior of historical brick masonry walls. *Acta mechanica*, 221(1):65–77.

Geddes, J. D. (1991). Discussion of "building response to excavation-induced settlement" by marco d. boscardin and edward j. cording (january, 1989, vol. 115, no. 1). *Journal of Geotechnical Engineering*, 117(8):1276–1278.

Genikomsou, A. S. and Polak, M. A. (2015). Finite element analysis of punching shear of concrete slabs using damaged plasticity model in abaqus. *Engineering structures*, 98:38–48.

Giardina, G., Marini, A., Hendriks, M. A., Rots, J. G., Rizzardini, F., and Giuriani, E. (2012). Experimental analysis of a masonry façade subject to tunnelling-induced settlement. *Engineering Structures*, 45:421–434.

Goh, K. (2011). *Response of ground and buildings to deep excavations and tunnelling*. PhD thesis, University of Cambridge.

Goh, K. and Mair, R. (2011). Building damage assessment for deep excavations in singapore and the influence of building stiffness. *Geotechnical Engineering Journal of the SEAGS & AGSSEA*, 42(3):1–12.

Goh, K. H. and Mair, R. J. (2014). Response of framed buildings to excavation-induced movements. *Soils and Foundations*, 54(3):250–268.

Grant, R. and Taylor, R. (2000). Tunnelling-induced ground movements in clay. *Proceedings of the Institution of Civil Engineers-Geotechnical Engineering*, 143(1):43–55.

Gutiérrez-Ch, J., Song, G., Heron, C., Marshall, A., and Jimenez, R. (2021). Centrifuge tests on rock-socketed piles: effect of socket roughness on shaft resistance. *Journal of Geotechnical and Geoenvironmental Engineering*, 147(11):04021125.

Horikoshi, K. and Randolph, M. (1996). Centrifuge modelling of piled raft foundations on clay. *Geotechnique*, 46(4):741–752.

Hussien, M. N., Tobita, T., Iai, S., and Karray, M. (2014). On the influence of vertical loads on the lateral response of pile foundation. *Computers and Geotechnics*, 55:392–403.

Idinyang, S., Franza, A., Heron, C., and Marshall, A. (2018). Millisecond interfacing of physical models with abaqus. In *Physical Modelling in Geotechnics*, pages 209–214. CRC Press.

Idinyang, S., Franza, A., Heron, C. M., and Marshall, A. M. (2019). Real-time data coupling for hybrid testing in a geotechnical centrifuge. *International Journal of Physical Modelling in Geotechnics*, 19(4):208–220.

Jacobsz, S., Standing, J., Mair, R., Hagiwara, T., and Sugiyama, T. (2004). Centrifuge modelling of tunnelling near driven piles. *Soils and foundations*, 44(1):49–56.

Jones, B. D. (2010). Low-volume-loss tunnelling for london ring main extension. *Proceedings of the Institution of Civil Engineers-Geotechnical Engineering*, 163(3):167–185.

Kaalberg, F., Teunissen, E., Van Tol, A., and Bosch, J. (2005). Dutch research on the impact of shield tunnelling on pile foundations. In *Geotechnical Aspects of Underground Construction in Soft Ground, Proceedings of 5th International Conf. of TC*, volume 28, pages 123–133.

Klaassen, R. K. and Creemers, J. G. (2012). Wooden foundation piles and its underestimated relevance for cultural heritage. *Journal of cultural heritage*, 13(3):S123–S128.

Kong, V., Cassidy, M. J., and Gaudin, C. (2015). Development of a real-time hybrid testing method in a centrifuge. *International Journal of Physical Modelling in Geotechnics*, 15(4):169–190.

Korff, M., Mair, R. J., and Van Tol, F. A. (2016). Pile-soil interaction and settlement effects induced by deep excavations. *Journal of Geotechnical and Geoenvironmental Engineering*, 142(8):04016034.

Kutter, B. L., Chang, J. D., and Davis, B. C. (1994). Collapse of cavities in sand and particle size effects. In *Proceedings of International Conference Centrifuge 94*, pages 809–815, Singapore. Balkema.

Lanzano, G., Visone, C., Bilotta, E., and Santucci de Magistris, F. (2016). Experimental assessment of the stress–strain behaviour of leighton buzzard sand for the calibration of a constitutive model. *Geotechnical and Geological Engineering*, 34:991–1012.

Lee, C. (2013). Numerical analysis of pile response to open face tunnelling in stiff clay. *Computers and Geotechnics*, 51:116–127.

Lee, C. and Jacobsz, S. (2006). The influence of tunnelling on adjacent piled foundations. *Tunnelling and Underground Space Technology incorporating Trenchless Technology Research*, 21(3):430–430.

Lee, C.-J. and Chiang, K.-H. (2007). Responses of single piles to tunneling-induced soil movements in sandy ground. *Canadian Geotechnical Journal*, 44(10):1224–1241.

Lee, C.-J., Wu, B.-R., Chiou, S.-Y., et al. (1999). Soil movements around a tunnel in soft soils. *Proceedings of the National Science Council, Republic of China, Part A: Physical Science and Engineering*, 23(2):235–247.

Lee, J. and Fenves, G. L. (1998). Plastic-damage model for cyclic loading of concrete structures. *Journal of engineering mechanics*, 124(8):892–900.

Lee, S.-H. and Chung, C.-K. (2005). An experimental study of the interaction of vertically loaded pile groups in sand. *Canadian Geotechnical Journal*, 42(5):1485–1493.

Lee, Y.-J. and Bassett, R. H. (2007). Influence zones for 2D pile–soil-tunnelling interaction based on model test and numerical analysis. *Tunnelling and underground space technology*, 22(3):325–342.

Leung, C. F., Lim, J., Shen, R., and Chow, Y. (2003). Behavior of pile groups subject to excavation-induced soil movement. *Journal of Geotechnical and Geoenvironmental Engineering*, 129(1):58–65.

Li, C., Chi, Y., Sun, X., Han, Y., Chen, X., Zhao, L., and Zhang, H. (2017). Construction technology of high-rise pile cap foundation of offshore wind power in taiwan strait. In *IOP Conference Series: Earth and Environmental Science*, volume 93, page 012037. IOP Publishing.

Liu, S., Li, H., and Tong, L. (2021). Simulation of pile cap contribution to the lateral pile performance due to adjacent excavation. *Acta Geotechnica*, 16:1895–1907.

Loganathan, N., Poulos, H., and Stewart, D. (2000). Centrifuge model testing of tunnelling-induced ground and pile deformations. *Geotechnique*, 50(3):283–294.

Loganathan, N. and Poulos, H. G. (1998). Analytical prediction for tunneling-induced ground movements in clays. *Journal of Geotechnical and geoenvironmental engineering*, 124(9):846–856.

Lu, H., Shi, J., Ng, C. W., and Lv, Y. (2020). Three-dimensional centrifuge modeling of the influence of side-by-side twin tunneling on a piled raft. *Tunnelling and Underground Space Technology*, 103:103486.

Lubliner, J., Oliver, J., Oller, S., and Onate, E. (1989). A plastic-damage model for concrete. *International Journal of solids and structures*, 25(3):299–326.

Mair, R. (2013). Tunnelling and deep excavations: Ground movements and their effects. In *Proc., 15th European Conf. on Soil Mechanics and Geotechnical Engineering—Geotechnics of Hard Soils—Weak Rocks (Part 4)*, pages 39–70. IOS Press, Amsterdam.

Mair, R. and Taylor, R. (1997). Bored tunnelling in the urban environment. In *Proceedings of the fourteenth international conference on soil mechanics and foundation engineering*, pages 2353–2385. Rotterdam.

Mair, R. and Taylor, R. (2001). 14 elizabeth house: settlement predictions. In *Building response to tunnelling: Case studies from construction of the Jubilee Line Extension, London*, pages 195–216. Thomas Telford Publishing.

Mair, R., Taylor, R., and Bracegirdle, A. (1993). Subsurface settlement profiles above tunnels in clays. *Geotechnique*, 43(2):315–320.

Mair, R. and Williamson, M. (2014). The influence of tunnelling and deep excavation on piled foundations. *Geotechnical Aspects of Underground Construction in Soft Ground*, pages 21–30.

Mair, R. J. (1979). *Centrifuge modelling of tunnel construction in soft clay*. PhD thesis.

Mair, R. J., Taylor, R., and Burland, J. (1996). Prediction of ground movements and assessment of risk of building damage due to bored tunnelling. In *Proceedings of Geotechnical aspects of underground construction in soft ground*, pages 713–718.

Mandolini, A., Russo, G., and Viggiani, C. (2005). Pile foundations: Experimental investigations, analysis and design. In *Proceedings of the 16th International Conference on Soil Mechanics and Geotechnical Engineering*, pages 177–213. IOS Press.

Marshall, A. (2009). *Tunnelling in sand and its effect on pipelines and piles*. PhD thesis, University of Cambridge.

Marshall, A., Farrell, R., Klar, A., and Mair, R. (2012). Tunnels in sands: the effect of size, depth and volume loss on greenfield displacements. *Géotechnique*, 62(5):385–399.

Marshall, A. M., Elkayam, I., and Klar, A. (2009). Ground behaviour above tunnels in sand-dem simulations versus centrifuge test results. In *Euro: Tun 2009, Proceedings of the 2nd International Conference on Computational Methods in Tunnelling, Bochum, Germany*, pages 9–11. Aedificatio Verlag, Bochum, Germany.

Marshall, A. M., Franza, A., and Jacobsz, S. W. (2020). Assessment of the posttunneling safety factor of piles under drained soil conditions. *Journal of Geotechnical and Geoenvironmental Engineering*, 146(9):04020097.

Marshall, A. M. and Mair, R. J. (2011). Tunneling beneath driven or jacked end-bearing piles in sand. *Canadian Geotechnical Journal*, 48(12):1757–1771.

Meyerhof, G. G. (1953). Some recent foundation research and its application to design. *The Structural Engineer*, 31(6):151–167.

Miliziano, S. and de Lillis, A. (2019). Predicted and observed settlements induced by the mechanized tunnel excavation of metro line c near s. giovanni station in rome. *Tunnelling and Underground Space Technology*, 86:236–246.

Moh, Z., Ju, D. H., and Hwang, R. (1996). Ground movements around tunnels in soft ground. In *Proceedings International Symposium on Geotechnical Aspects of Underground Construction in Soft Ground*, volume 730, pages 725–730. London: Balkema AA.

Mohamad, W., Bourgeois, E., Le Kouby, A., Szymkiewicz, F., Michalski, A., Branque, D., Berthoz, N., Soyez, L., and Kreziak, C. (2022). Full scale study of pile response to epbs tunnelling on a grand paris express site. *Tunnelling and Underground Space Technology*, 124:104492.

Moussaei, N., Khosravi, M. H., and Hossaini, M. F. (2019). Physical modeling of tunnel induced displacement in sandy grounds. *Tunnelling and Underground Space Technology*, 90:19–27.

Mroueh, H. and Shahrour, I. (2002). Three-dimensional finite element analysis of the interaction between tunneling and pile foundations. *International Journal for Numerical and Analytical Methods in Geomechanics*, 26(3):217–230.

Mu, L., Huang, M., and Finno, R. J. (2012). Tunnelling effects on lateral behavior of pile rafts in layered soil. *Tunnelling and Underground Space Technology*, 28:192–201.

Nematollahi, M. and Dias, D. (2019). Three-dimensional numerical simulation of pile-twin tunnels interaction–case of the shiraz subway line. *Tunnelling and Underground Space Technology*, 86:75–88.

Ng, C. W. W., Hong, Y., and Soomro, M. A. (2015). Effects of piggyback twin tunnelling on a pile group: 3d centrifuge tests and numerical modelling. *Géotechnique*, 65(1):38–51.

Ng, C. W. W., Soomro, M. A., and Hong, Y. (2014). Three-dimensional centrifuge modelling of pile group responses to side-by-side twin tunnelling. *Tunnelling and Underground Space Technology*, 43:350–361.

Nghiem, L., Al Heib, M., and Emeriault, F. (2014). Understanding subsidence consequences on masonry structures using large small-scale physical modeling. In *8th International Conference on Physical Modelling in Geotechnics (ICPMG 2014)*, pages 1195–1202. CRC Press. Leiden.

O'Reilly, M. P. and New, B. (1982). Settlements above tunnels in the united kingdom-their magnitude and prediction. Technical report.

Othman, H. and Marzouk, H. (2018). Applicability of damage plasticity constitutive model for ultra-high performance fibre-reinforced concrete under impact loads. *International Journal of Impact Engineering*, 114:20–31.

Pang, C., Yong, K., and Chow, Y. (2005). Three-dimensional numerical simulation of tunnel advancement on adjacent pile foundation. *Underground space use: analysis of the past and lessons for the future*, 2:1141–1148.

Peck, B. (1969). Deep excavation and tunnelling in soft ground, state of the art volume. In *7th ICSMFE*, volume 4, pages 225–290.

Phienwej, N., Hong, C. P., and Sirivachiraporn, A. (2006). Evaluation of ground movements in epb-shield tunnelling for bangkok mrt by 3d-numerical analysis. *Tunnelling and Underground Space Technology incorporating Trenchless Technology Research*, 21(3):273–273.

Pickhaver, J., Burd, H., and Houlsby, G. (2010). An equivalent beam method to model masonry buildings in 3d finite element analysis. *Computers & structures*, 88(19-20):1049–1063.

Piddington, J., Nicol, S., Garrett, H., and Custard, M. (2020). *The Housing Stock of The United Kingdom*. BRE Trust.

Polshin, D. E. and Tokar, R. (1957). Maximum allowable non-uniform settlement of structures. In *Proc., 4th Int. Conf. on Soil Mechanics and Foundation Engineering*, volume 1, pages 402–405. Butterworth's London.

Potts, D. and Addenbrooke, T. (1997). A structure's influence on tunnelling-induced ground movements. *Proceedings of the Institution of Civil Engineers-Geotechnical Engineering*, 125(2):109–125.

Potts, D. and Bond, A. (1994). Calculation of structural forces for propped retaining walls. In *International conference on soil mechanics and foundation engineering*, pages 823–826.

Poulos, H. (2001). Piled raft foundations: design and applications. *Geotechnique*, 51(2):95–113.

Rankin, W. (1988). Ground movements resulting from urban tunnelling: predictions and effects. *Geological Society, London, Engineering Geology Special Publications*, 5(1):79–92.

Ritter, S., Giardina, G., DeJong, M. J., and Mair, R. J. (2017). Influence of building characteristics on tunnelling-induced ground movements. *Géotechnique*, 67(10):926–937.

Ritter, S., Giardina, G., DeJong, M. J., and Mair, R. J. (2018). Centrifuge modelling of building response to tunnel excavation. *International Journal of Physical Modelling in Geotechnics*, 18(3):146–161.

Ritter, S., Giardina, G., Franza, A., and DeJong, M. J. (2020). Building deformation caused by tunneling: Centrifuge modeling. *Journal of Geotechnical and Geoenvironmental Engineering*, 146(5):04020017.

Schiavoni, M., Giordano, E., Roscini, F., and Clementi, F. (2023). Numerical modeling of a majestic masonry structure: A comparison of advanced techniques. *Engineering Failure Analysis*, 149:107293.

Selemetas, D. (2006). *Response of full-scale piles and piled structures to tunnelling*. PhD thesis, University of Cambridge.

Selemetas, D. and Standing, J. (2018). Response of full-scale piles to epbm tunnelling in london clay. In *Tunnelling in the Urban Environment: Géotechnique Symposium in Print 2017*, pages 123–136. ICE Publishing.

Shahin, H. M., Nakai, T., Ishii, K., Iwata, T., and Kuroi, S. (2016). Investigation of influence of tunneling on existing building and tunnel: model tests and numerical simulations. *Acta Geotechnica*, 11:679–692.

Simulia, D. S. (2014). Abaqus 6.14. *Providence, RI, USA*.

Skempton, A. W. and MacDonald, D. H. (1956). The allowable settlements of buildings. *Proceedings of the Institution of Civil Engineers*, 5(6):727–768.

Son, M. and Cording, E. J. (2005). Estimation of building damage due to excavation-induced ground movements. *Journal of geotechnical and geoenvironmental engineering*, 131(2):162–177.

Son, M. and Cording, E. J. (2007). Evaluation of building stiffness for building response analysis to excavation-induced ground movements. *Journal of geotechnical and geoenvironmental engineering*, 133(8):995–1002.

Song, G. (2019). *The use of protective structures to reduce tunnelling induced damage to buildings*. PhD thesis, University of Nottingham.

Song, G. and Marshall, A. M. (2020). Centrifuge study on the influence of tunnel excavation on piles in sand. *Journal of Geotechnical and Geoenvironmental Engineering*, 146(12):04020129.

Song, G. and Marshall, A. M. (2021). Tunnel–piled structure interaction: Numerical simulation of hybrid centrifuge tests. *Computers and Geotechnics*, 140:104477.

Song, G., Xu, J., Heron, C. M., Marshall, A. M., Correia, R., and Korposh, S. (2022). Centrifuge application of fibre bragg gratings: pile axial loads and wall bending moments. *International Journal of Physical Modelling in Geotechnics*, 22(4):192–207.

Soomro, M. A., Mangi, N., Xiong, H., Kumar, M., and Mangnejo, D. A. (2020). Centrifuge and numerical modelling of stress transfer mechanisms and settlement of pile group due to twin stacked tunnelling with different construction sequences. *Computers and Geotechnics*, 121:103449.

Soomro, M. A., Ng, C. W. W., Memon, N. A., and Bhanbhro, R. (2018). Lateral behaviour of a pile group due to side-by-side twin tunnelling in dry sand: 3d centrifuge tests and numerical modelling. *Computers and Geotechnics*, 101:48–64.

Standing, J. and Selemetas, D. (2013). Greenfield ground response to EPBM tunnelling in london clay. *Géotechnique*, 63(12):989–1007.

Stanier, S. A., Blaber, J., Take, W. A., and White, D. (2016). Improved image-based deformation measurement for geotechnical applications. *Canadian Geotechnical Journal*, 53(5):727–739.

Tang, C., Franza, A., Xu, J., and Marshall, A. M. (2024a). Load transfer mechanisms for capped and uncapped non-displacement piles above tunnels: a centrifuge modelling study. *Géotechnique*, pages 1–36. doi.org/10.1680/jgeot.23.00201.

Tang, C., Marshall, A. M., Franza, A., and Xu, J. (2024b). Setup and calibration of piles with FBG strain sensors in a geotechnical centrifuge. In *Proceedings of XVIII European Conference on Soil Mechanics and Geotechnical Engineering*, pages 2667–2670. CRC Press.

Tang, C., Selvaraj, S. P., Heron, C. M., and Marshall, A. M. (2024c). Coupled centrifuge-numerical modelling of shallow strip foundations. In *Proceedings of the 11th International*

Symposium of Geotechnical Aspects of Underground Construction in Soft Ground, pages 404–412. CRC Press.

Tawadros, H., Farag, M., and Mehanny, S. (2022). Extent and hierarchy of seismic induced inelastic demands in the substructure system of bridges on piled foundation crossing waterways. *Bulletin of Earthquake Engineering*, 20(8):3889–3919.

Taylor, R. N. (1995a). *Geotechnical centrifuge technology*. Blackie Academic and Professional, London.

Taylor, R. N. (1995b). Tunnelling in soft ground in the uk. In *Underground construction in soft ground*, pages 123–126.

Teparaksa, W., Tangpraprutgul, T., Boonsong, C., and Boonard, J. (2006). Ground and bridge displacement due to epb shield tunnel bored underneath bridge pile foundation. In *Proceedings of the International Symposium on Underground Excavation and Tunnelling*, pages 299–307.

Timoshenko, S. P. (1955). Strength of materials part 1. *Elementary theory and problems*, pages 165–310.

Toyosawa, Y., Itoh, K., Kikkawa, N., Yang, J.-J., and Liu, F. (2013). Influence of model footing diameter and embedded depth on particle size effect in centrifugal bearing capacity tests. *Soils and foundations*, 53(2):349–356.

Vorster, T., Klar, A., Soga, K., and Mair, R. (2005a). Estimating the effects of tunneling on existing pipelines. *Journal of Geotechnical and Geoenvironmental Engineering*, 131(11):1399–1410.

Vorster, T. E. B., Klar, A., Soga, K., and Mair, R. J. (2005b). Estimating the effects of tunneling on existing pipelines. *Journal of Geotechnical and Geoenvironmental engineering*, 131(11):1399–1410.

Wang, X., Li, S., and Li, J. (2023). Experimental and numerical study on lateral response of pile-group for offshore wind turbines in sand. *Marine Georesources & Geotechnology*, 41(5):524–543.

Wang, Z.-F., Cheng, W.-C., Wang, Y.-Q., and Du, J.-Q. (2018). Simple method to predict settlement of composite foundation under embankment. *International Journal of Geomechanics*, 18(12):04018158.

Williamson, M., Mair, R., Devriendt, M., and Elshafie, M. (2017). Open-face tunnelling effects on non-displacement piles in clay–part 2: tunnelling beneath loaded piles and analytical modelling. *Géotechnique*, 67(11):1001–1019.

Williamson, M. G. (2014). *Tunnelling effects on bored piles in clay*. PhD thesis, University of Cambridge.

Xu, J., Franza, A., and Marshall, A. M. (2020a). Centrifuge modelling of tunnel-soil-pile interaction considering the presence of rigid caps. In *4th European Conference on Physical Modelling in Geotechnics: ECPMG 2020*, pages 193–200. Luleå University of Technology Luleå, Sweden.

Xu, J., Franza, A., and Marshall, A. M. (2020b). Response of framed buildings on raft foundations to tunneling. *Journal of Geotechnical and Geoenvironmental Engineering*, 146(11):04020120.

Yacila, J., Camata, G., Salsavilca, J., and Tarque, N. (2019). Pushover analysis of confined masonry walls using a 3d macro-modelling approach. *Engineering Structures*, 201:109731.

Yiu, W., Burd, H., and Martin, C. (2017). Finite-element modelling for the assessment of tunnel-induced damage to a masonry building. *Géotechnique*, 67(9):780–794.

Yu, Y. (2024). *The effect of nonlinear structural behaviour within tunnel-building interaction analyses*. PhD thesis, University of Nottingham.

Yuan, Y., Wang, Y., and Ding, M. (2021). Deformation control analysis of unequal-length bridge piles of urban rail transit tunnel crossing urban expressway elevated bridge. In *Hydraulic and Civil Engineering Technology VI*, pages 66–72. IOS Press.

Zhao, C., Schmüdderich, C., Barciaga, T., and Röchter, L. (2019). Response of building to shallow tunnel excavation in different types of soil. *Computers and Geotechnics*, 115:103165.

Zhou, B. (2015). *Tunnelling-induced ground displacements in sand*. PhD thesis, University of Nottingham.

Zhou, B., Marshall, A. M., and Yu, H.-S. (2014). Effect of relative density on settlements above tunnels in sands. In *Tunneling and Underground Construction*, pages 96–105.

Zhu, Y., Zeng, B., Ye, S., He, L., Zheng, Y., and Ma, R. (2023). Physical model tests and discrete-element simulation of pile and soil displacement response induced by dot shield tunneling based on transparent soil technology. *International Journal of Geomechanics*, 23(8):04023124.